JAERI-M
89-119

JAERI TANDEM, LINAC & V.D.G. ANNUAL REPORT 1988

April 1, 1988—March 31, 1989

September 1989

Department of Physics

日本原子力研究所
Japan Atomic Energy Research Institute

JAERI-Mレポートは，日本原子力研究所が不定期に公刊している研究報告書です。
入手の問合わせは，日本原子力研究所技術情報部情報資料課（〒319－11茨城県那珂郡東海村）あて，お申しこしください。なお，このほかに財団法人原子力弘済会資料センター（〒319-11茨城県那珂郡東海村日本原子力研究所内）で複写による実費頒布をおこなっております。

JAERI-M reports are issued irregularly.
Inquiries about availability of the reports should be addressed to Information Division, Department of Technical Information, Japan Atomic Energy Research Institute, Tokai-mura, Naka-gun, Ibaraki-ken 319-11, Japan.

編集兼発行　日本原子力研究所
印　　刷　日立高速印刷株式会社

JAERI-M 89-119

JAERI TANDEM, LINAC & V.D.G.
Annual Report
1988

April 1, 1988 - March 31, 1989

Department of Physics
Tokai Research Establishment
Japan Atomic Energy Research Institute
Tokai-mura, Naka-gun, Ibaraki-ken

(Received August 7, 1989)

This annual report describes research activities which have been performed with the JAERI tandem accelerator, the electron linear accelerator and the Van de Graaff accelerator from April 1, 1988 to March 31, 1989. Summary reports of 45 papers, and list of publications, personnel and cooperative researches with universities are contained.

Keywords: JAERI TANDEM, e-LINAC, V.D.G., Synchrotron Radiation, Atomic Physics, Radiation Chemistry, Solid State Physics, Material Science, Nuclear Chemistry, Nuslear Physics, Neutron Physics, Annual Report

Editors: Naomoto Shikazono
Mitsuhiko Ishii
Yuuki Kawarasaki
Yukio Kazumata
Chiaki Kobayashi
Yohta Nakai
Yoichi Suto

JAERI－M 89－119

原研タンデム，リニアック，バンデグラフ加速器1988年度年次報告

日本原子力研究所東海研究所
物理部

（1989年8月7日受理）

本年次報告は，原研タンデム，リニアック及びバンデグラフ加速器で，1988年4月1日から1989年3月31日までの間に東海研で行われた研究活動をとりまとめたものである。

1） 加速器運転と開発研究　2） 原子分子及び化学　3） 固体物理及び材料の放射線効果　4） 核化学　5） 核物理及び　6） 中性子物理の6部門にまたがる45編の研究報告，公表された文献，関与した職員及び大学等との協力研究のリストを収録している。

東海研究所：〒319-11　茨城県那珂郡東海村白方字白根2－4
（編集者）鹿園直基・石井三彦・河原崎雄紀・数又幸生・小林千明
中井洋太・須藤洋一

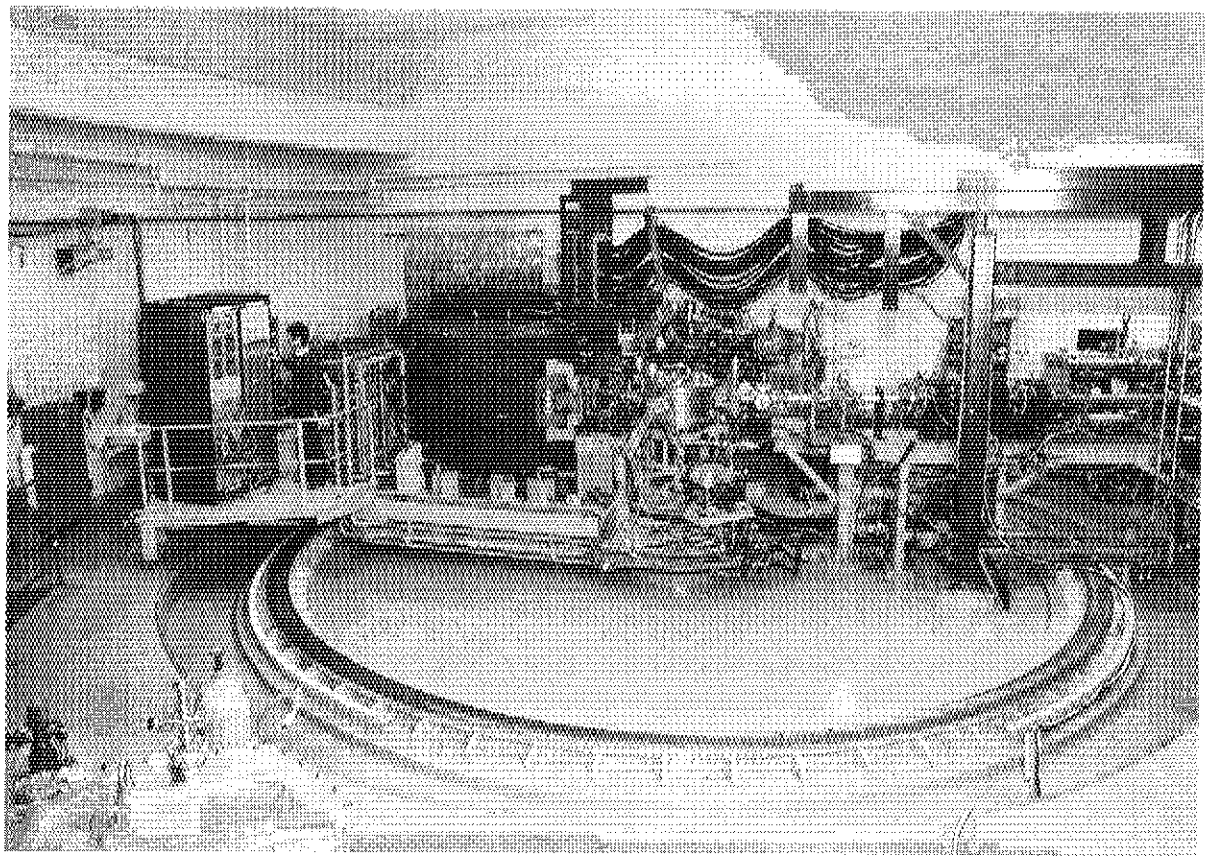

Heavy Ion Spectrometer "ENMA"

PREFACE

This report covers activities of research and development carried out during the period from April 1 1988 through March 31 1989. The activities which were performed by using accelerators of Department of Physics are described in this report.

All the accelerators, i.e. the tandem accelerator, the electron linear accelerator and the Van de Graaff accelerator, have been operated stationarily and satisfactorily throughout the period. The tandem accelerator, with which a majority of the research activities have been done, operated on a regular schedule in accordance with the cycle of three months operation for the research activities and one month for the maintenance. A construction of a post accelerator to boost the energy of the heavy ion beams has begun in the period. The goal of our project is to obtain a 30 MV of accelerating voltage by using 40 superconducting quater wave resonators. The electron linear accelerator was newly equipped by a positron generator and by a small storage ring JSR. A project of free electron laser has progressed remarkably in this period.

Main subjects of our research activities contain; 1) atomic physics and chemistry, 2) solid state physics and radiation effects in materials, 3) nuclear chemistry, 4) nuclear physics, and 5) neutron physics.

During the period, more than 60 staff members of JAERI have worked in the above mentioned fields of researches, and about 100 colleagues have joined from universities and institutes outside JAERI for collaboration in these studies.

An international symposium, organized and sponsored by JAERI, on heavy-ion reaction dynamics in tandem energy region was held at Hitachi, August 1-3, 1988. Sixty five participants including 20 guests from countries outside Japan gathered together and discussed on new and interesting aspects of heavy ion physics. Some of the studies presented in the symposium are included in this annual report.

Naomoto Shikazono

Naomoto Shikazono
Director
Department of Physics

Contents

I ACCELERATOR OPERATION AND DEVELOPMENT 1
1.1 Tandem Accelerator Operation 3
1.2 Electron Linac Operation and Improvements 6
1.3 Present Condition of Ion Source and Ion Injection System 12
1.4 Superconducting Booster 16
1.5 Production of Intense Monochromatic Positron Beam and its Application to Materials Science 19
1.6 Status of the JAERI Free Electron Laser System 24
1.7 Estimation of FEL's Gain:Design Studies for the Total System in Phase-I 27
1.8 Injector Gun of the Linac for a FEL Oscillator 31
1.9 Design of the Electrode Shape of the Injection Gun for the JAERI Free Electron Laser 35
1.10 Space Charge Effects on Bunched Beam 39
1.11 Higher Brightness Injector:Survey on Photocathode Injector Development and Preliminaly Design Consideration 43
1.12 Construction of a Compact Electron Storage Ring, JSR 47
1.13 Fabrication and RF Properties of the S-band TM010 Microwave Cacity Made of $YBa_2Cu_3O_{7-\delta}$ 51
1.14 Data Oriented Programming using LSSolver 60
1.15 FORTH-HODAL Preparative: Implementation of a Forth Monitor Nucleus into a 16-bit PC 64
II ATOMIC PHYSICS AND CHEMISTRY 69
2.1 High-Resolution Zero-Degree Electron Spectroscopy(I) 71
2.2 Ion Channeling Spectroscopy of Single Crystal Austenitic Stainless Steel 75
2.3 Perturbed Angular Correlation Measurement using Pb-100/Rh-100 Nuclear Probes 79
2.4 Ionization Measurement in a Gas Traversed by A Beam of High-Energy Heavy Ion 83
2.5 Heavy Ion Irradiation Induced Radicals in Polyvinylidene Fluoride 87
III SOLID STATE PHYSICS AND RADIATION EFFECTS IN MATERIALS 91
3.1 Ion Conductivity of Lithium Oxide Irradiated With Oxygem and Lithium Ions 93

3.2 Swelling of Lithium Oxide Irradiated with High Energetic Lithium Ions 97
3.3 Damage Structure Obtained by Cross-sectional Observation in He-Ion Irradiated SiC 101
3.4 Electron Microscopic Observation of Lithium Aluminate Irradiated with Oxygen Ions 105
3.5 Defect Production by Electron Excitation in FCC Metals Irradiated with High Energy Heavy Ions 108
3.6 A Study of X-Ray Diffraction of Ion Irradiated GaAs Crystal 111
3.7 Precise X-Ray Observation of Si Single Crystals Irradiated with Energetic Heavy Ions(7) 115
3.8 Effect of 120 MeV ^{16}O Ion Irradiation on Electronic Properties of La_2CuO_4 119
3.9 Effects of He Ion Irradiation on Superconductivity of Bi-Sr-Ca-Cu-O Films 123
IV NUCLEAR CHEMISTRY 127
4.1 Complex Fragment Emission in the Reaction $^{37}Cl + ^{68}Zn$ 129
4.2 A Fission Barrier Study in Actinides 132
4.3 Bsta-Decay Studies of ^{123}La, ^{125}La and ^{127}La with an On-Line Isotope Separator 136
4.4 A Study of Short-lived Aetinides by means of On-line Chemical Separation System 139
V NUCLEAR PHYSICS 143
5.1 Contribution of Nucleon Transfer to Elastic Scattering of $^{28}Si + ^{58,64}Ni$ near the Coulomb Barrier 145
5.2 Measurements of Pre-Fission ^{4}He Multiplicity to Investigate the Temperature Dependence of Level Density Parameter 149
5.3 Detection of the ^{8}Be Nuclei from the Reactions $^{28}Si + ^{68}Zn$ and $^{32}S + ^{64}Ni$ 152
5.4 Shift of Neutron Resonance Levels in Periodic Structure 155
5.5 Electromagnetic Transition Probabilitles in the Natural-Parity Rotational Band of ^{157}Gb 159
5.6 Electromagnetic Transition Probabilities in the Natural-Parity Rotational Band of ^{173}Yb 161
5.7 Lifetimes and G-factors of Excited States in ^{106}Sn 165
5.8 Nuclear Structure of ^{105}In 167
5.9 Invariant Fission Path in the Multi-Dimensional Parameter Space 168

5.10 Structure of Actinide Nuclei and the SPDF Boson Model 172
VI NEUTRON PHYSICS 175
6.1 Scattering of 28.15 MeV Neutrons from ^{12}C 177
6.2 Gamma-Ray Production Cross Sections of Al, Si, Fe, Pb and Bi at 10 and 11.5 MeV 180
VII PUBLIGATIONS 185
VIII PERSONNEL AND COMMITTEES 209
IX Co-OPERATIVE RESEARCHES 221

I ACCELERATOR OPERATION AND DEVELOPMENT

1.1 TANDEM ACCELERATOR OPERATION

Tandem Accelerator Group

Department of physics, JAERI

Accelerator operation

During the year from April 1, 1988 to March 31, 1989, the tandem accelerator has been operated for many kinds of research programs. As the accelerator ran without serious troubles in this period, almost all of the experimental programs were performed under the arranged schedule. The following are summary of the operation and the maintenance. The running time was 4852 hours.

1) Time distribution by terminal voltage

>16 MV	3 days	1.5 %		11-12 MV	5 days	2.4 %
15-16	85	41.9		10-11	8	3.9
14-15	61	30.0		9-10	6	3.0
13-14	18	8.9		8- 9	1	0.5
12-13	6	3.0		< 8	20	4.9

2) Time distribution by projectile

H	14 days	6.9 %		S	32 days	15.7 %
D	8	3.9		Cl	5	2.5
Li	6	3.0		Ca	1	0.5
B	18	8.9		Sc	2	1.0
C	22	10.8		Ni	36	17.6
O	17	8.4		Ge	4	2.0
F	16	7.9		Br	4	2.0
Si	11	5.4		I	5	2.5
				Au	2	1.0

3) Time distribution by activity

Operation for research	203 days	55.6 %
Atomic and solid state physics	(49 days)	
Radiation effects in materials	(9)	
Nuclear chemistry	(33)	

Nuclear physics	(75)	
Fast neutron physics	(30)	
Accelerator development	(7)	
Voltage conditioning	10	2.7 %
Operation training	0	0.0
Scheduled maintenance	82	22.5
Unexpected repair	28	7.7
Holidays and vacation	42	11.5

Major troubles

1) January 6 - 9, 1988 (tank open)
The trouble of The high voltage power supply for the terminal electrostatic quadrupole lens.

2) May 14 - 17,1988 (tank open)
Damage of the vacuum valve's bellows at the bottom of the high energy tube by a failure. Consequently, three ion pumps power supplies in the major dead sections were damaged.

3) May 23 - June 1,1988 (tank open)
About thirty of the terminal foil stripper holders with support clip dropped into the foil changer housing. One of then dropped further into the low energy tube and intercepted the beam pass. The cause of trouble, by our guess, was poor welding of the support clips to the stainless steel belt or over tension of the stainless belt.

4) August 31 - September 16,1988 (tank open)
One foil stripper holder dropped into the low energy tube again and same trouble occurred as the item 3).
The movement of the foil changer was replaced with new ones.

maintenance

1) Two coils of the switching magnet exchanged for new ones on January 1989 because of the layer insulator deterioration on the upper coil occurred on end of December 1987. We made a ten ton hoist for this work. We presumed that the cause of the trouble was bad fabrication of the coils in the factory.

Improvement and development

1) In order to observe the aspect of the terminal stripper foil under irradiating by ion beams, a black and white TV monitor system has been developed. Fig.1 shows the schematic diagram of the system. Some modifications were needed for the video camera to protect it against the gas pressures in the tank. A plastics optical fiber(1mm dia.) which communicates light signals from the terminal to outside of the tank is laid along the insulation columns with self supporting. The monitor system gives us many information not only the states of the stripper foils but the beam spot size or position by luminescence on the foil. Fig.2 is an example of monitoring picture.

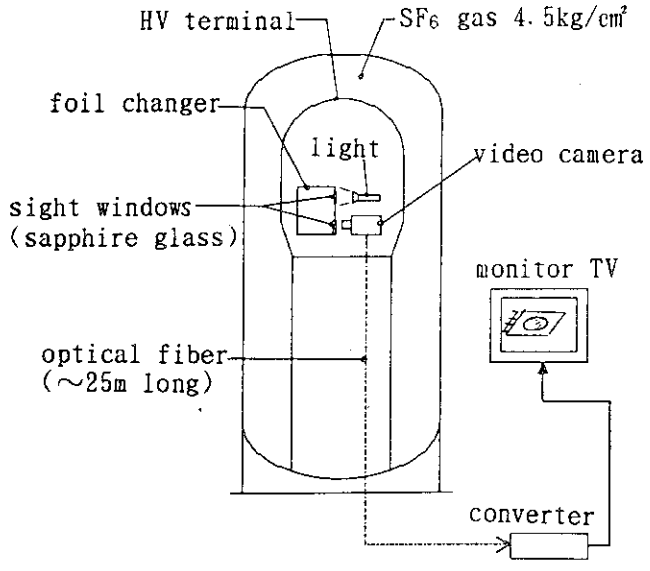

Fig. 1 schematic diagram of the foil monitor

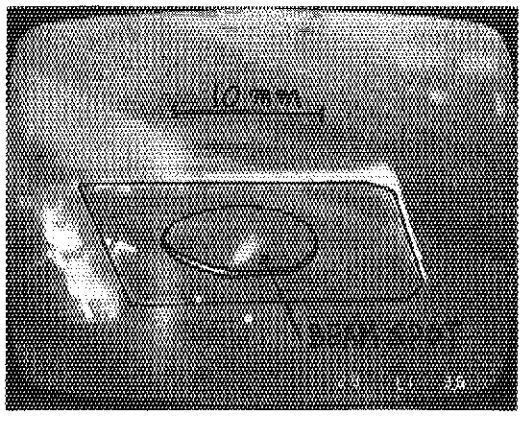

Fig. 2 An example of monitoring picture

1.2 ELECTRON LINAC OPERATION AND IMPROVEMENTS

Electron Linac Group

Departments of Physics

1. Operation

The JAERI 120 MeV electron linear accelerator (linac) have been smoothly operated with a repetition rate of less than 150 pps during the 1988 fiscal year. The total beam time was summed up to 278 hours for various experimental researches.

A summary of the linac operating conditions between April, 1988 and March, 1989 is shown in Table 1 for each experimental program. The linac machine times were used as follows; (1)the neutron cross section measurements, (2)the neutron radiography, (3)the monoenergetic positron emission and its applications to material researches, (4)the radio-isotope productions, and (5)the experiments for the free electron laser (FEL).

Table 1 Machine Time and Output Beam for Research Programe in 1988

Research Program	Time (h)	Ratio (%)	Energy (MeV)	Rate (pps)	Length (nsec)	Current Ave (μA)
Neutron Cross Section (Time of Flight Method)	72.3	26.0	120	150	25	12
Neutron Radiography	108.6	39.1	120	150	1000	12
Radioisotope Production	48.4	17.4	60	150	1000	9
Positron Experiment (Emission of monoenergetic Positron	20.3	7.3	100	25~50	1000	12
Free Electron Laser	15.4	5.5	100	50	1000	~2
Tuning and Test Operation	13.0	4.7	100~180	50~150	1000	~30
Total	278.0	100.0				

The several construction and repairing works have been carried out during this fiscal year,

(1) roof of the linac building (2 weeks),

(2) radiation monitoring system (2 weeks),

(3) ceiling of the linac building (5 weeks),

2. Main parameters

To realize the infrared(10.6μm) operation, the system is designed consisting of an electron gun with a grid-pulsed thermoionic cathoad, a sub-harmonic buncher, a buncher, a pre-accelerator, an α-magnet and a main accelerator.[1] The peak current is guessed to be more than 100mA at the exit of the gun, and 9.14A after the bunching process using the sub-harmonic buncher, the buncher and the pre-accelerator. At the exit of the gun, the emittance of the beam is estimated less than 10π mm·mr by using the SLAC electron trajectory program, E-gun[2]. At the final stage, the emittance is guessed 15π mm·mr. The beam energy amounts to 25MeV at the end of the main accelerator. Main parameters of our system are listed in table 2.

Table 2 Main parameters

Beam energy	25MeV
Normalized emittance	10π mm·mr
Energy spread	80keV
Micropulse(at Gun)	4ns(10.6MHz)
Macropulse	1ms(10Hz)
Peak current	9.14A
Bunch length	1.31cm

3. The calculation of the gain

The oscillation wave-length(λ) can be expressed[3] as,

$$\lambda=\frac{\lambda_q}{2\gamma^2}(1+K^2) \tag{1}$$

where λ_q is the undulator period, γ is the beam energy and K is the undulator parameter. When a planar undulator is used,

$$K=\frac{eB\lambda_q}{2\sqrt{2}\pi mc^2}. \tag{2}$$

The gain(g) depends strongly on K value and can be written as,

$$g\propto\frac{K^2}{(1+K^2)^{3/2}}\left\{J_0\left[\frac{K^2}{2(1+K^2)}\right]-J_1\left[\frac{K^2}{2(1+K^2)}\right]\right\}^2 \tag{3}$$

where J_0 and J_1 are the Bessel function of order n. Eq.(3) leads to the maximum value of g at K=1.1. The value of K can then fix the undulator period and the magnetic field strength(B) under the condition of γ=49.9 (E=25MeV), λ=10.6μm, through eq.(1) and (2). The system is now assumed to work under the homogeneous broadening regime. The constraints between the parameters can be expressed as,

$$\sigma_E<\frac{\lambda_q}{4L}=\frac{1}{4N} \tag{4}$$

$$\gamma\varepsilon_y < \frac{1}{\sqrt{2}h}\frac{1+K^2}{2K}\frac{\lambda_q^2}{L} \tag{5}$$

where σ_E is the energy spread given by $\delta E/E$, L is the undulator length, N is the number of the undulator periods, $\gamma\varepsilon_y$ is the normalized emittance and h is a constant. At the end of the main accelerator the energy spread was estimated to be $\pm$80kV. Eq. (4) requires that N must be less than 78. In our case we chose N as 60. From eq. (5) $\gamma\varepsilon_y$ must be less than 63π mm·mr. The small signal gain[4] is given by,

$$g_0 = 32\sqrt{2}\pi^2\lambda^{\frac{3}{2}}\lambda_q^{\frac{1}{2}}\frac{K^2}{(1+K^2)^{3/2}}\frac{I_p}{I_a}\frac{N^3}{\Sigma}f(x)F(K) \tag{6}$$

where Ip is the peak current and is estimated to be 9.14A, Ia is the Alfven current(17045A), Σ is the mean transverse area of the optical mode, f(x) and F(K) are given by next equations, respectively,

$$f(x) = \frac{1}{x^3}\left(\cos x - 1 + \frac{1}{2}x\sin x\right) \tag{7}$$

$$F(K) = \left\{J_0\left[\frac{K^2}{2(1+K^2)}\right] - J_1\left[\frac{K^2}{2(1+K^2)}\right]\right\}^2 \tag{8}$$

The optimum value of Σ is provided as $L\lambda/\sqrt{3}$. Taking account of the fact that the maximum value of f(x) is 0.0675 for x=2.61 and F(K) is 0.715 for K=1.1, we obtain the gain as 55.9% from eq. (6).

Real beam has many factors to decrease the gain, that is, the energy spread(μ_E), the emittance(μ_y), the slippage(μ_z), etc. Taking those factors into account, we define the real gain that can roughly be expressed,

$$g = g_0\frac{1}{(1+\frac{\mu_c}{3})(1+\mu_y^2)(1+1.7\mu_E^2)} \tag{9}$$

Here μ_E, μ_y, μ_c are given by next equations.

$$\mu_E = 4\sigma_E N \tag{10}$$

$$\mu_y = \frac{4K}{1+K^2}\frac{\gamma\varepsilon_y}{\lambda_q}N \tag{11}$$

$$\mu_c = \frac{\lambda N}{\sigma_z} \tag{12}$$

where σ_Z is the bunch length and estimated as 1.31cm(8° at 508MHz). Substituting each value into the eq. (10), (11) and (12),

$\mu_E = 0.768$, $\mu_y = 0.229$, $\mu_Z = 0.0485$

The gain was calculated as 26% from eq. (9). Furthermore, assuming that the optical cavity output coupling(ε) is 5% and the mirror loss(δ) is 2%, we obtained the final gain as 19%.

(5) Operation of Repetition Rate 1pps

The 1 pps operation is required for the injection to the JSR. The pulse repetition rate of the JAERI linac modulator was designed to be from 50 to 600 pps. The line-type pulse circuits are used to charge PFN (pulse forming network) with the 40 kV choke-transformer. The decay constant (~ 0.8 sec) from PFN is determined by a product between the resistance (5 MΩ) of breeder resistors of reverse circuits and the capacitance (0.16 μF) of PFN condensers. Therefore, the 1 pps operation (1 sec) of the linac can not be made. The grid pulser of the electron gun was modified to cope with the problem with the 50 pps operation of the main pulse modulator. The trigger pulse is also send to the JSR.

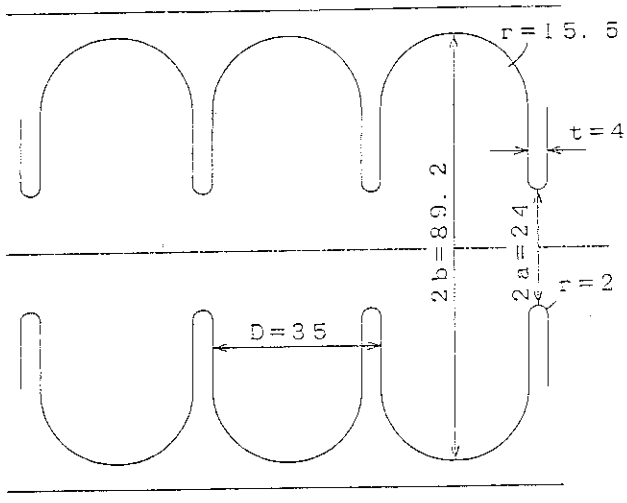

Fig.1 New Structure Wave Guide

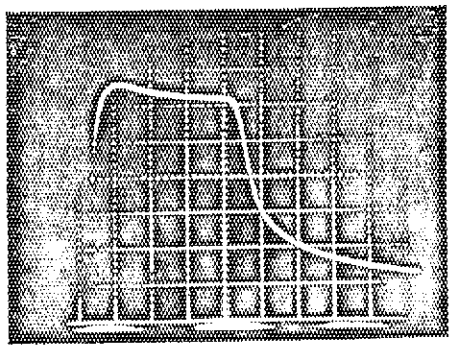

X:1μ s/div Y:0.1V/div
Fig.3 RF Drive Amplifer Output Waveform

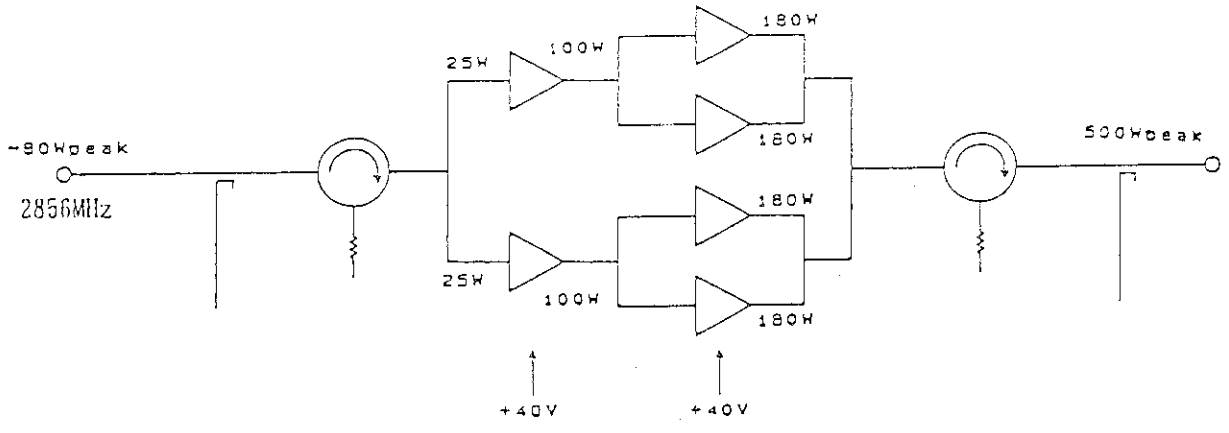

Fig.2 S Band RF Driver Circuit

and to prepare the JSR operation, the 300 kVA motor generator was installed (this is the same system as the linac in the Electrotechnical Laboratory). The test result shows that the input AC line is stabilized within 1 % and the beam quality has been remarkably improved.

(3) Design of a new traveling wave type accelerator structure

The field characteristics for the new accelerator structure has been calculated with the computer code SUPERFISH. The new structure is shown in Fig. 1. The target specification of the accelerator structure is as follows; energy gain (no load) is 22.5 MV/m, shunt impedances 70 MΩ/m, Q value is more than 14,500. The new structure will be fablicated and installed as the alternate of the #1 accelerator structure (2 m long) of the JAERI linac. The actual beam test is planned to carry out before the end of this fiscal year. The test data of the new accelerator structure will be useful for the STA SR Project (Science Technology Agency Synchrotron Radiation Project).

(4)Replacement of the RF driver amplifier by the solid state amplifier for the main klystrons.

We have been replacing all the hard tube circuits with the solid state components for the "maintenance free" stable operations. The remaining parts are the main klystrons, the main thyratrons and the RF driver klystron. The RF driver klystron has been used to drive the six sets of main klystrons with 10 kW pulse operation. The replacement of this component with solid state circuit had been planned because the CW transistor with an output power of 125 W had been developed for the S-band (2856 MHz). It is found that the kW power amplifiers can be technically available with multi-staged and phase-synthesized circuit.

In October, 1988, the circuit with the output power of 500 kW was ordered as shown in Fig. 2 and has been built in February, 1989. This circuit was installed and tested as the RF driver amplifier for the #1 klystron (20 MW). The actual 50 pps beam operation gave the satisfactory result with the almost same property as the klystron amplifier, although the beam energy spread of 2 ~ 3 % occurred at the initial part of the pulse due to the phase modulation. The output RF pulse shape is shown in Fig. 3. This new JAERI's development is the first time application of the 500 W class S-band pulse amplifier in Japan.

(4) boring of the 4 m shielding wall (1 week),
(5) installation of JSR (JAERI Storage Ring) (about 4.5 months),
(6) shielding for JSR in the north target room (5 weeks),
(7) installation of the 300 kVA Motor Generator (5 weeks),
(8) maintenances of the vacuum system and the IVR power supply (2 ~ 3 weeks).

For these construction and repairing works, the total machine time for the experiments was reduced compared to the previous years.

2. Maintenance

The unscheduled shut-down was only due to the replacement work of the heat exchanger assembly for the klystron cooling system, which is caused by the trouble of pinhole.

Several parts of the linac components were replaced as the scheduled maintenance. Those replaced parts were as follows;

(1) all the beam transport tubes of stainless steel were replaced with those of aluminum.
(2) the beam monitor was installed in the beam line TL,
(3) the driving motor in the IVR was replaced and its interlock circuit was newly prepared,
(4) the linac pulse trigger system was installed, by which the 1 pps operation becomes available,
(5) the TL beam line was realigned.

3.Improvements

(1) The installation of JSR

The JSR was installed in the north target room in the linac building during the period from October 25, 1988 to March 10,1989. The manufacturing companies responsible for the installation were Mitsubishi Electric Co., Hitachi Ltd., Toshiba Co. and Sumitomo Heavy Industry, Ltd. The acceptance test for the whole systems including electromagnet, radiofrequency (RF) cavity, beam duct and computer have been satisfactorily performed.The beam injec-tion test has started in April, 1989.

(2) The installation of the 300 kVA Motor Generator (MG)

The input AC line to the RF modulator power supplies for the JAERI linac has not been stabilized so far. In order to improve this situation

1.3 PRESENT CONDITION OF ION SOURCE AND ION INJECTION SYSTEM

Tadashi YOSHIDA, Eisuke MINEHARA, Shinichi ABE

Department of Physics, JAERI

1. Operation of the ion source system

The ion source and ion injection system for the JAERI tandem accelerator has been operated since the installation to generate new ion beam species and larger output current. Middle of 1987, we introduced a new type ion source so-called inverted sputter ion source that could produced large current than before.

This ion source is the inverted type sputter ion source (SNICS-II as an abbreviation) manufactured by NEC (National Electrostatic Corporation, Middleton, U.S.A.).

In June 1987, the SNICS-II ion source was installed to an ion source test apparatus and the test operation was carried out for about 6 months.

After the test operation, the ion source was installed to the ion injection system and the routine operation started for various experiments.

Since 1988, the SNICS-II ion source has been operated for most of the operation of the ion injection system.

The 2nd ion injection system is scheduled to be completed within several months. The vacuum system is in operation already. A part of the control system was completed for their checking.

After the 2nd ion injection system is completed, two ion injection systems will be operated alternately for the service of delivering a variety of ion beams more efficiently.

2. Status of each ion source system

2.1 Sputter ion source (HICONEX 834)

The HICONEX 834 type ion source was manufactured by GIC (General Ionex Corporation, Massachusetts, U.S.A.), and used for the generation of the various ion beams for the JAERI tandem accelerator.

In 1988, this ion source was removed from the ion injection system to investigate the serious degradation of the output current.

At present, the ion source was moved to the ion source test apparatus

and now under investigation.
This type of ion source had been used in many tandem laboratories. However, many of those ion sources had been shut down due to the similar problems. Apart from the degradation problem, this ion source can be operated stably for a very long time without maintenance.
If the problem can be removed through the investigation, we will install it to the injection system again for the actual operation.

2.2 Duoplasmatron ion source (DEDP type manufactured by NEC)

Ion beams of proton and deuteron are often demanded for large current operation and the DEDP ion source is the most suitable ion source for them.
It is the inevitable ion source to pulsed beam operation for the tandem accelerator.
At the beginning, bare tungsten filament is used for this ion source, but the lifetime of the filament is short for the stable pulsed beam operation. Therefore, the filament material was exchanged to a nickel mesh coated by oxide compounds from bare tungsten wire several years ago. As for the present, long time operation of the DEDP ion source is also possible very stably.

2.3 Heinicke Penning ion source (HPIG type manufactured by NEC)

The HPIG ion source is used for the production of halogen family ions. This type of the ion source consumes a large amount of gases to maintain stable discharge. As the result of the discharge, it produces a much amount of fluorine, chlorine and other active gases which give serious damages to the mechanical parts of the vacuum system.
We had to save the operation for these ion species as few as possible.

3. Operation of each ion source

The operation of each ion source in every machine time period, from October 1987 up to now, is summarized in figure 1.
The SNICS-Ⅱ ion source has become the major or main ion source for the JAERI tandem accelerator from 1988. It is currently used for the production of
all ion species except proton and deuteron.

4. Performance of SNICS-II ion source

The test operation of the SNICS-II ion source started at June 1987 and continued for 6 months, producing about 110 kinds of ions.
The test results are shown in figure 2.
Poisonous samples were excluded in the test operation of the ion source.
The summary of the test results shows that half of the samples are usable and have sufficient current intensity for various experiments.

5. Present condition of the 2nd ion injection system

Construction of the 2nd ion injection system is near to the end.
The vacuum system is now under operation.
As soon as the extension of the control system to the 2nd injection system is commissioned, the first ion beam from the system will be scheduled to test the whole acceleration system.
Also, the expansion and other works of control system, a minor adjustment of the injection beam line that requires beam optical alignment are still remained. The construction work is mainly performed during an interval between machine time periods.
It is scheduled to carry out a minor adjustment of the injection beam line in a machine time period of June.

References

1) E.Minehara et al.: JAERI tandem, linac & V.d.G. annual report 1986.
2) E.Minehara et al.: 6th symposium on accelerator science and technology, Tokyo, October 27-29, 1987.
3) E.Minehara et al.: JAERI tandem, linac & V.d.G. annual report 1987.

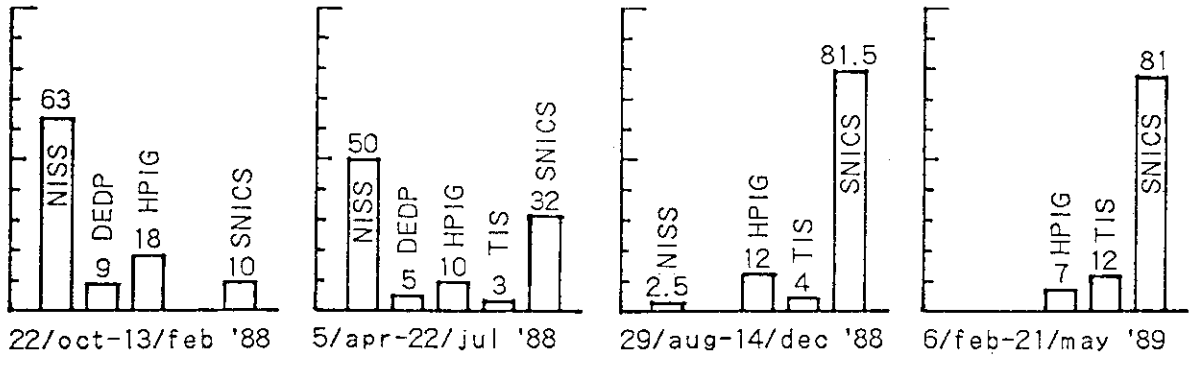

Fig.1 Operation of each ion source

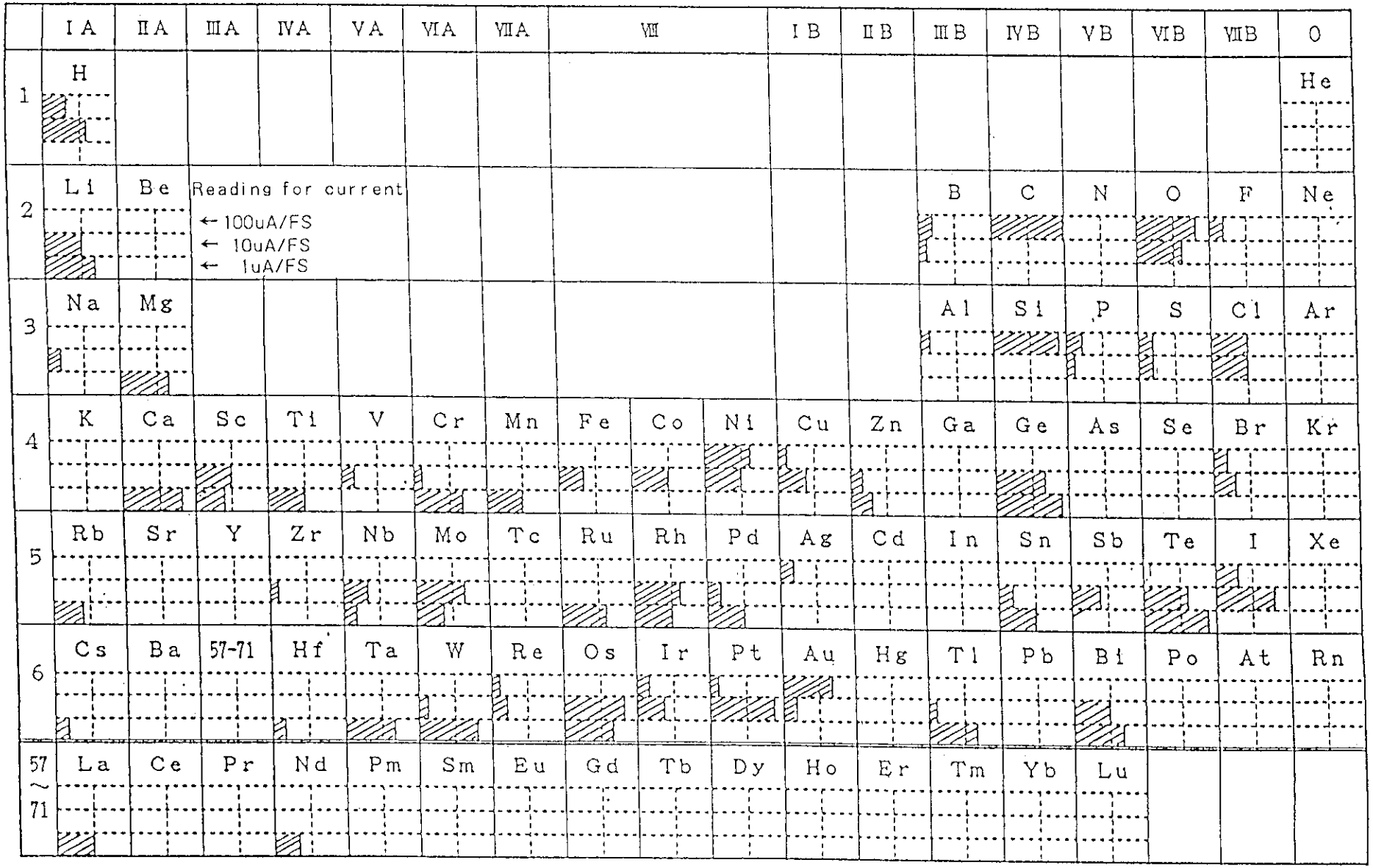

Fig.2 Performance of SNICS-II ion source

1.4 SUPERCONDUCTING BOOSTER

Booster Project Group

Department of Physics

1. Accelerating structure

The superconducting booster will be composed of a double-drift buncher, ten linac units and a de-buncher.

The buncher will consist of a 260 MHz unit and a 130 MHz unit. The 130 MHz unit has been made already. And its superconducting QWR resonators have shown a high performance of 5 - 6 MV/m at an rf loss of 4 watts. The resonator performance was confirmed with a beam test using 164 MeV(v/c=0.1) Cl^{10+} beams; the resonator field levels obtained in the previous off-line tests were only 0 - 2 % less than those measured in the beam test. The buncher was sent to a manufacturer at the beginning of 1989 to modify the tubing for resonators pre-cooling and radiation shield cooling in order to make use of cold helium gas instead of liquid nitrogen as a coolant. The modification continues to the next fiscal year.

Each linac unit comprises four 130 MHz QWRs in a cryostat. Four of the ten linac units were funded and the design and fabrication works began at an industry(Mitsubishi Electric Corp. in Kobe). The design of the QWRs is entirely the same as that of the 130 MHz buncher resonators. With respect to the cryostats, we have been giving re-considerations to the design of a liquid helium dewar for four resonators, connection to a liquid helium transfer line and magnetic shields. The fabrication proceeds in meeting requirements of the safety regulations for refrigerators and will be completed by March of 1991. Two sets of rf control stations were ordered for the four units(16 resonators) from Applied Superconductivity Inc. in U.S.A. The rest six units are going to be funded in the fiscal years of 1989 to 1991.

The de-buncher which is officially called as the prototype acceleration unit was completed and its two 130 MHz QWRs were tested in off line. Their performances were as good as those obtained with the buncher resonators. The maximum accelerating field levels were about 7

MV/m and the levels at an rf loss of 4 watts were about 5.5 MV/m. These results are shown in fig. 1 together with those for the buncher resonators. A set of rf control station was delivered from A.S.I. We examined it with a de-buncher resonator cooled at 4.2K. It worked well but it was a little bit difficult to set the resonator field level as we wanted with the control station. A few modifications are necessary to have a perfect match with our resonators.

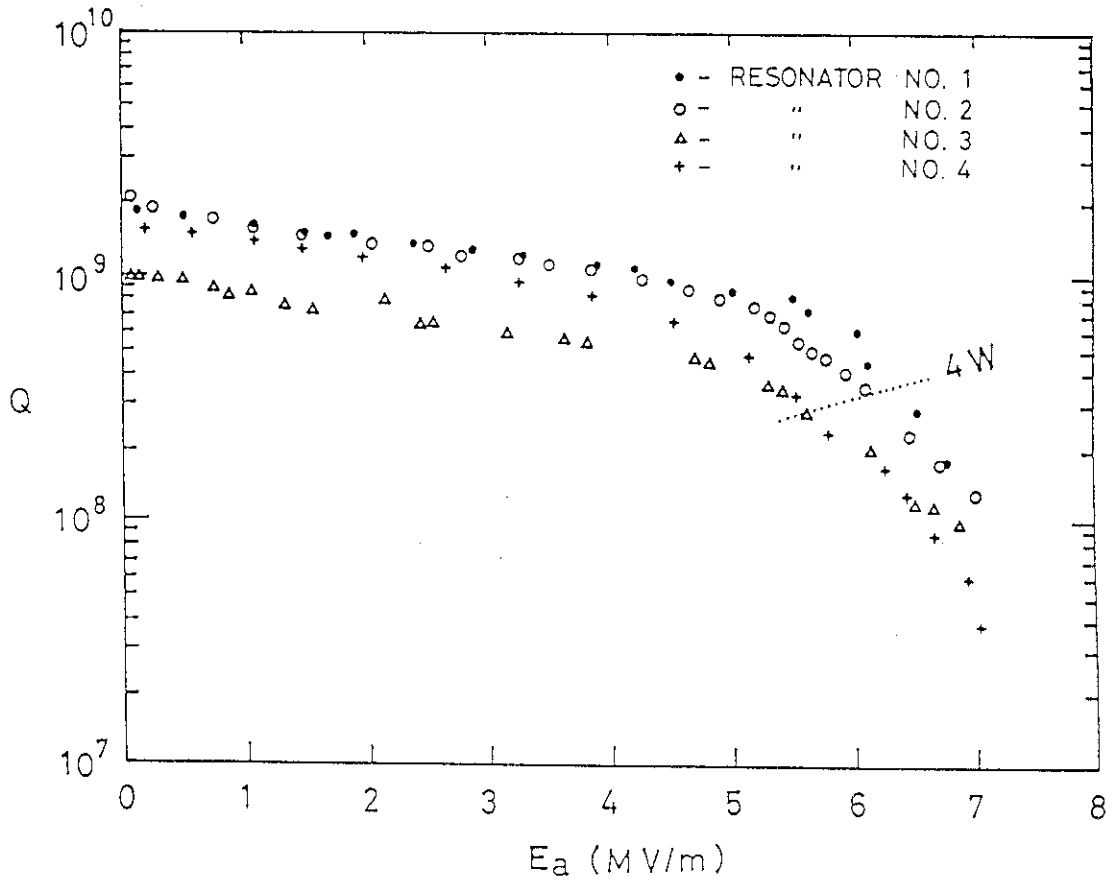

Fig. 1 Resonator performances at 4.2 K. The resonators No.1 and 2 belong to the buncher and the No.3 and 4 the de-buncher.

2. Cryogenic system

We have decided to operate the resonators and the refrigeration system under the safety regulations for refrigerators. In the regulations, refrigerators are classified by their refrigeration power or by the power of compressors as of the first, the second and the third

group. A liquid helium refrigerator which can provide refrigeration power of more than 350 watts at 4.5K belongs to the first group. To operate such a refrigerator, at least two of us need to have licences of the highest grade and three years operating experience with a big refrigerator. There is unfortunately no refrigerator which is big enough for the three years experience in JAERI. As a result of considerations on such restriction and operational advantages and disadvantages, we decided to have two identical refrigerators which belong to the second group.

The specifications of the liquid helium and cold helium gas transfer lines and the dual refrigerator system are being studied by our cryogenic group with cooperation from several manufacturers. The fabrication of the cryogenic system is planned in 1990 and 1991.

3. Booster layout

The layout plan of the booster components, the target room and the utility rooms is, at present, essentially not different from that of the previous annual report. Its refinement and the design work of the building will be made in 1989. The building construction is scheduled in 1990 and 1991.

1.5 PRODUCTION OF INTENSE MONOCHROMATIC POSITRON BEAM AND ITS APPLICATION TO MATERIALS SCIENCE

Yasuo ITO*, Saburo TAKAMURA, Osamu SUEOKA*2
and Sohei OKADA*3

Department of Physics, JAERI, *RCNST, Univ. of Tokyo,
*2College of Arts and Sciences, Univ. of Tokyo,
*3Takasaki Radiation Chemistry Establishment, JAERI

Extraction of intense monochromatic positron beam (or slow positrons) has been carried out using the electron Linac of Tokai Establishment, JAERI. The intensity of the slow positron beam was 3×10^{8} sec^{-1}, which is one of the most intense of the world. Since the slow positrons are obtained as a pulsed beam, it is stretched in time into a quasi-DC beam using a linear storage tube. Further improvements of the positron beam, which are necessary before it is used for the study of materials, are under way.

1. Introduction

Production of intense slow positron beam is a matter of recent great concern, since it has potential usefulness for a variety of new studies of materials science. The principle of producing the slow positron beam is to moderate fast positrons at the surface of suitable moderator materials and then, by virtue of the negative positron work function, to expel them to vacuum. Since the efficiency of conversion from fast to slow positrons is of the order of 10^{-4}, positron intensity larger than about 10^{6} sec^{-1} cannot be reached when β^{+}-decay radioisotopes are used as the positron source. In order to get an even more intense beam, the use of an electron Linac is promising: by irradiating high-energy electron beam on a high-Z target (Ta in the present case), intense fast positrons are produced by the cascade of Bremsstrahlung and pair-production. The fast positrons are then converted to slow positrons by thin W moderator. This method was proven successful in a previous work using the 30 MeV electron Linac of University of Tokyo[1], and the present work follows it with the aim of obtaining a positron beam for practical use.

When an electron Linac is used, the slow positrons are obtained as a pulsed beam. The positron density in a pulse is too large and causes pulse

pile-up problems in many measurements such as lifetime, energy or angular correlation. We have tried to produce intense positron beams and to shape them into a quasi-DC beam by using a pulse stretching technique. This beam will further be collimated by using the brightness enhancement technique[2] and will be used for RHEPD (Reflecting High Energy Positron Diffraction) and PAD (Positron Annihilation induced Desorption).

2.Production of slow Positrons

The beam characteristics of the electron Linac are typically 120 MeV, 1 μs width, 600 pps, and 150 μA average current. The expected slow positron yield is c.a. 10^9 sec^{-1}, but for the preliminary runs the beam was reduced to 1/10 of the full power in order to compromise with the health physics problem caused by the activation at the target. Fig.1 shows the horizontal view of the slow positron beam line. The electron beam comes from the right side of the figure and hits the water-cooled Ta target. The fast positrons produced enter the vacuum chamber and get into the W moderator (25 μm thick x 2 mm width W ribbons stacked in the shape of a vane). The slow positrons are extracted and transported through a long solenoid tube (90° bent twice) to the positron counting room which is shielded by a concrete wall (2 m thick). At the end of the solenoid tube are a linear storage tube and a positron counting chamber.

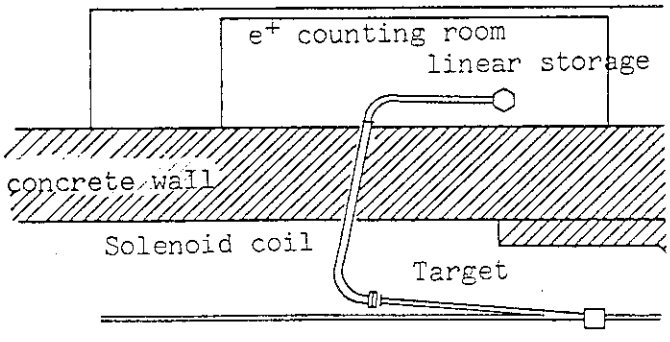

Fig.1 Horizontal View of the Slow Positron Beam Line

The slow positrons were first measured using a Ceratron, a kind of channel electron multiplier. Since this detector becomes easily saturated at high counting rates we are mostly observing a deformed pulse shape, but it is still the best way to get rough view of the pulse shape. Fig.2 is the oscillogram of the output of the detector. It consists of two components: the burst and the slow positrons. Since a retarding potential against electron (-500 V) is applied at the head of the detector, the burst is due to secondary electrons with energies larger than 500 eV and fast positrons. The burst can apparently be avoided by applying a high-voltage pulse to the deflector plate synchronous to the passage of the

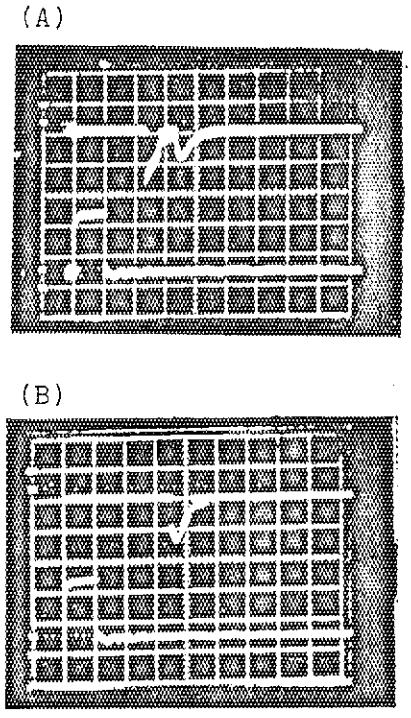

Fig.2 Oscillogram of the Ceratron output signal (upper trace). The double peaks in (A) correspond to burst and slow e^+. By properly adjusting the beamline, it is possible to direct only the slow e^+ to Ceratron (B).

burst component (Fig.2B), or by adjusting the magnetic fields. But this does not mean that the burst is eliminated. For the complete elimination it is necessary to resort to a more sophisticated way. One possible way is to use the energy analyzing characteristics of a ExB drift field at the head of the slow electron extraction, and this is being prepared at the time of writing of this report.

The slow positron intensity was measured using a Faraday cup after properly adjusting the beam line and preventing the electrons from entering the Faraday cup. The measured positron current was 5 pA (3×10^7 e^+/sec). This is the intensity obtained at 10% full power operation and is close to the expected level. Since there is enough room for optimizing various parameters (focusing of the electron beam, thickness of the Ta target, conditions of the W moderator, etc.), extraction of even more intense positron beam is quite probable.

3. Storage and Stretching

The principle of storage and stretching of the positron pulses is illustrated in Fig.3: prior to the arrival of the slow positron pulse, the electrode G_2 is biased positive while G_1 is grounded. The positrons entering this tube is reflected back at G_2, and just before the front of the positron pulse come back to G_1, it is switched to positive, too. The length of the linear storage tube (1.2 m) is approximately equal to half the length of the 1 μs positron pulse and thus the whole positrons are confined in the tube. This is the principle of the linear storage. A quasi-DC beam is obtained when the stored positrons are released by lowering the potential of G_2 gradually.

The operation of the storage and the stretching is demonstrated in Fig.4. In each oscillogram the upper trace is the Ceratron output and the lower one is the potential G_2. It is seen that the bunch of slow

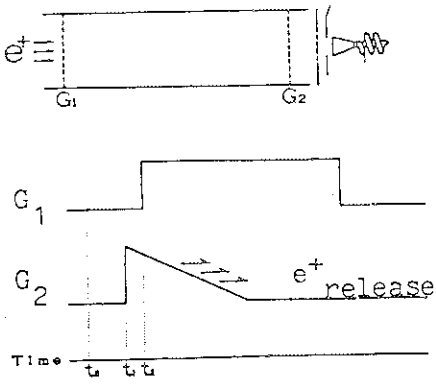

Fig.3 Principle of the linear storage and pulse stretching

positrons is stored and, when the potential G_2 is switched to ground, is released spontaneously. When G_2 is lowered gradually as in Fig.4B, the positrons come out stretched in time. The feasibility of the linear storage and the stretching has thus been demonstrated, but it is necessary to lengthen the storage time from the previously achieved level (c.a. 300 μs) to about 1 ms.

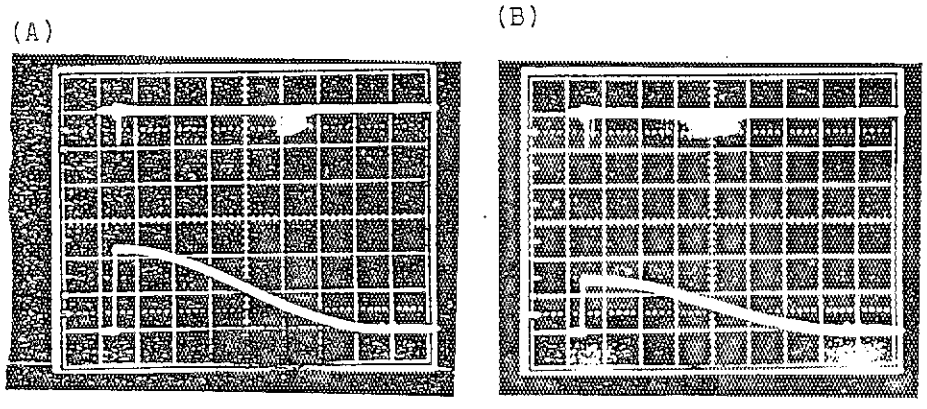

Fig.4 Example of pulse stretching operation
The upper trace in each oscillogram is the Ceratron output signal of e^+ released when the potential G_2 (lower trace) is being lowered.

4.Radiation Damage of the W Moderator

We could observe a gradual decrease of the slow positron yield. Fig.5 shows how the output signal intensity of Ceratron is decreased after 5 hours continuous irradiation. Since the Ta target and the W moderator were situated along the electron beam directions, some fraction of the high energy electrons can hit W moderator to induce radiation damage. The Linac was operated at 1/10 full power at this occasion, and the decrease of the yield due to the damage would be more significant when operated at the full power. It may be possible to minimize the damage by making a suitable choice of the geometry. An alternative choice may be to anneal the moderator from time to time. In order to test at what temperature the damage of the W moderator is recovered, positron lifetimes were measured for the damaged moderator material. A long lifetime component which can be ascribed to micro-void formation was apparently observed, which, by isochronal annealing experiments, was found to start to move at about 600 ℃ and be annealed completely above 900℃ (Fig.6).

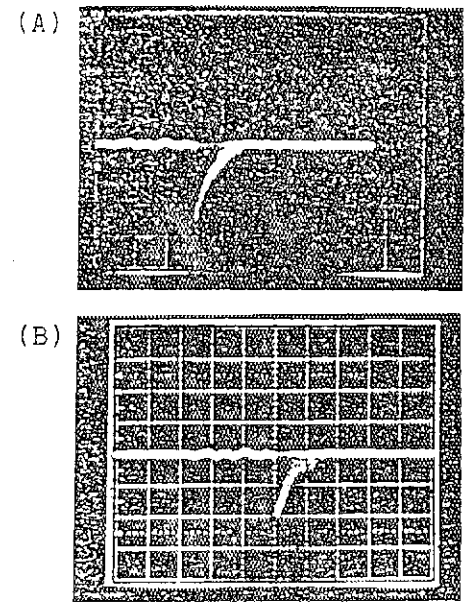

Fig.5 Ceratron output at the beginning (A) and after 5 hours irradiation (B)
Although the pictures are not clear, it is seen that the peak height is smaller for B compared to A.

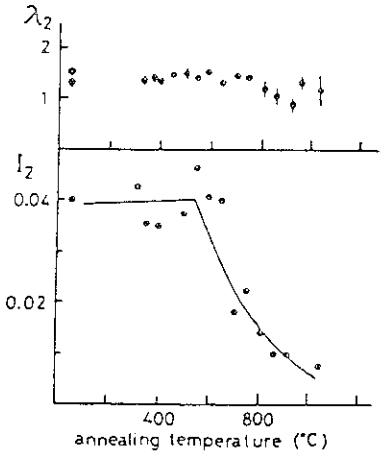

Fig.6 Effect of Annealing of radiation-damaged W moderator

5. Conclusion

There has been a substantial progress in the production of intense slow positron beam, and the results have been reported at ICPA-8. Further improvements are under way in which are included:

1) Elimination of the burst component by using ExB separation technique.
2) Transfer of the positron beam from the magnetic field to non-magnetic field. This is necessary for the positron scattering experiments.
3) To lengthen the storage and stretching time of positrons.
4) Brightness enhancement and formation of positron micro-beam.
5) To float the whole beamline to a high potential (10-20 kV). This is a fundamental necessity for most of the positron beam applications: the brightness enhancement, micro-beam, positron microscopes, etc..

References

1) O.Sueoka, Y.Ito, T.Azuma, H.Kobayashi and Y.Tabata; Jpn. J. Appl. Phys., 24(2), 222-224 (1985)
2) A.P. Mills. Jr., "Positron Solid State Physics", pp.432-509 (North-Holland Pub. Co.)
3) Y.Ito, O.Sueoka, S.Takamura; Proc. 8th ICPA, pp.583-585, (Gent,1988)

1.6 STATUS OF THE JAERI FREE ELECTRON LASER SYSTEM

Makio OHKUBO, Masayoshi SUGIMOTO, Masaru SAWAMURA,
Katsuo MASHIKO, Masayuki TAKABE, Jyun SASABE
and Yuuki KAWARASAKI

Department of Physics, JAERI

Design and construction of JAERI FEL system based on a superconducting linac are continued aiming at the FEL oscillation in 10 - 20 μm infrared wave length. A subharmonic buncher, a buncher, a part of beam transport vacuum system, and focusing coils have been fabricated.

The purpose of the JAERI FEL program is to prove the feasibility of FEL as a strong and tunable light source in an infrared region at the first stage(Phase I)[1]. In the succeeding stages, the shortening the wave length to visible light and upgrading the output light will be made. Overview of the system in Phase I is in the following.

In order to oscillate 10.6 μm infrared wave length, an electron beam of above 20 MeV is produced by a superconducting linac(508 MHz). The time structure of the beam is designed to be 4ns width and 10.6 MHz micropulse with an envelope 1 ms width and 10 pps macropulse. The electron gun is a thermionic cathode with a grid structure (Eimac Y646B), and an accelerating voltage 250 kV[2]. The cathode anode structures are so designed that the beam emittance is about 10 π mm mrad[3]. The beam is bunched by a sub-harmonic buncher (84.7 MHz, 1/6 of 508 MHz) and a buncher(508 MHz) in a rather long drift space[4], where a beam focusing is made by a series of focusing coils. The beam is accelerated by a superconducting pre-accelerator (508 MHz) to about 2 MeV. The superconducting main accelerator consists of 2 sets of structures where five 508 MHz cavities are united, and are contained in a 4.4 m long cryostat. By the 10 cavities acceleration of above 20 MeV will be expected in favorable cases. An RF power of 80 KW will be fed from two CW klystrons to accelerate the beam during the macropulse.

In this fiscal year, parts of injection system, the sub-harmonic buncher and the buncher have been fabricated by the Nihon Kousyuha Co., and the vacuum system for drift space, and the series of focusing coils have been fabricated by the Tokin Co. The above RF and vacuum components already fabricated are shown in Fig.1.

In the next fiscal year, parts of the accelerator system in the following items will be constructed and assembled.

1) A short pulsed(4ns) electron gun with 250 KV accelerating voltage. The timing control is made by a grid pulser triggered by a light pulses through an optical fiber.

2) A part of the beam transport system. The vacuum system, focusing coils, and a deflection magnet system are included.

3) An RF system. A standard source, frequency multipliers, phase and amplitude control systems for the RF cavities, and solid state high power RF amplifiers are included.

References

1) Ohkubo,M., Kawarasaki,Y., Shikazono,N.,Mashiko,K., Sugimoto,M., Sawamura,M., Yoshikawa,H. and Takabe,M.
A Linac for Free Electron Laser at JAERI, to be published in Proceedings of the 1988 LINAC Conference, Virginia, U.S.A.

2) Yoshikawa,H. and Mashiko,K.
An Electron Gun for JAERI-FEL
Proceedings of the 13th linear Accelerator Meeting in Japan, Electrotechnical Laboratory, Sept 7-9,1988, p115

3) Sugimoto,M.
Design of the electrode shape of the injection gun for the JAERI Free Electron Laser, Ibid. p118

4) Sawamura,M.
Design of the Injection System for JAERI FEL Linac, ibid p161

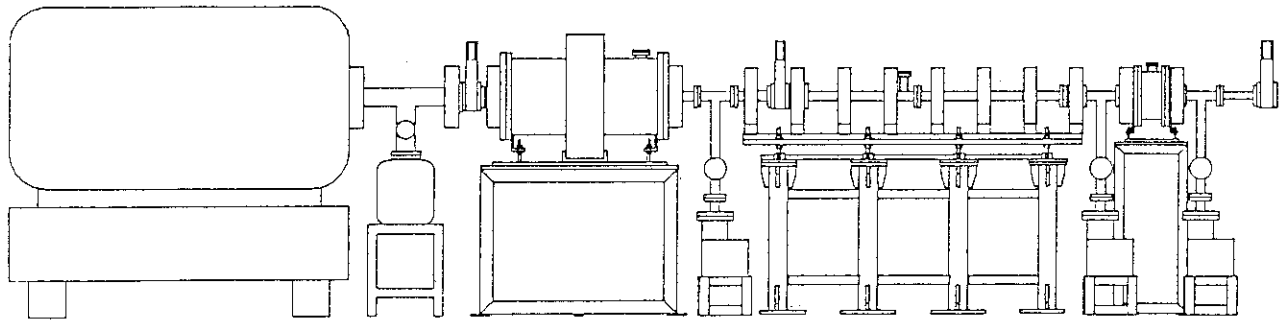

Fig.1 Injector of the JAERI FEL system. The electron gun, the subharmonic buncher, beam transport system with focus coils, and the buncher.

1.7 ESTIMATION ON FEL'S GAIN:Design Studies for the Total System in Phase-I

Masayuki TAKABE

Department of Physics, JAERI

The free-electron-laser(FEL) gains have been preliminarily estimated as one of the design studies for the superconducting RF-linac based FEL system in the phase-I. Typical gains calculated in small signal gain and homogeneous broadening regime are:

Energy	Wavelength	Gain	Undulator	Momentum Filter	Rise Time
25MeV	10.6μm	19%	new	not	10.4μs
2MeV	950μm	no	old	not	no
2MeV	950μm	0.8%	old	use	950μs

1. Introduction

The final aim of the FEL's R&D here at JAERI lies in the application of isotopeseparation for fuel-element production and group partitioning of waste-materials.

During the course of the FEL's R&D, however, novel tunable laser sources can be widely applied to the various basic research fields, together with the achievement of high quality electron beam being definitely required for the FEL oscillations.

This challenging FEL's R&D is scheduled in three stages:

Phase-I Infrared(10.6μm) wavelength operation

Phase-II Beam recirculation and visible wavelength operation

Phase-III Energy recovery

The superconducting RF-linac for the FEL's beam source is considered as one of the superior choice, because RF power loss is very small and high quality beam is easily attainable. The discussion on the problem above described led to the design of the RF-linac based FEL system. For the design of the FEL system, each parameter of the accelerator should be determined as having a high gain value. The gain is estimated, at the present time, using the latest data. For the calculation of the gain, we assumed that the system is under the small signal gain and the homogeneous broadening regime.

2. Main parameters

To realize the infrared(10.6μm) operation, the system is designed consisting of an electron gun with a grid-pulsed thermoionic cathoad, a sub-harmonic buncher, a buncher, a pre-accelerator, an α-magnet and a main accelerator.[1] The peak current is guessed to be more than 100mA at the exit of the gun, and 9.14A after the bunching process using the sub-harmonic buncher, the buncher and the pre-accelerator. At the exit of the gun, the emittance of the beam is estimated less than 10π mm·mr by using the SLAC electron trajectory program, E-gun[2]. At the final stage, the emittance is guessed 15π mm·mr. The beam energy amounts to 25MeV at the end of the main accelerator. Main parameters of our system are listed in table 1.

Table 1 Main parameters

Beam energy	25MeV
Normalized emittance	10π mm·mr
Energy spread	80keV
Micropulse(at Gun)	4ns(10.6MHz)
Macropulse	1ms(10Hz)
Peak current	9.14A
Bunch length	1.31cm

3. The calculation of the gain

The oscillation wave-length(λ) can be expressed[3] as,

$$\lambda=\frac{\lambda_q}{2\gamma^2}(1+K^2) \tag{1}$$

where λ_q is the undulator period, γ is the beam energy and K is the undulator parameter. When a planar undulator is used,

$$K=\frac{eB\lambda_q}{2\sqrt{2}\pi mc^2} \tag{2}$$

The gain(g) depends strongly on K value and can be written as,

$$g\propto\frac{K^2}{(1+K^2)^{3/2}}\left\{J_0\left[\frac{K^2}{2(1+K^2)}\right]-J_1\left[\frac{K^2}{2(1+K^2)}\right]\right\}^2 \tag{3}$$

where J_0 and J_1 are the Bessel function of order n. Eq.(3) leads to the maximum value of g at K=1.1. The value of K can then fix the undulator period and the magnetic field strength(B) under the condition of γ=49.9 (E=25MeV), λ=10.6μm, through eq.(1) and (2). The system is now assumed to work under the homogeneous broadening regime. The constraints between the parameters can be expressed as,

$$\sigma_E<\frac{\lambda_q}{4L}=\frac{1}{4N} \tag{4}$$

$$\gamma\varepsilon_y < \frac{1}{\sqrt{2|h|}} \frac{1+K^2}{2K} \frac{\lambda_q^2}{L} \tag{5}$$

where σ_E is the energy spread given by $\delta E/E$, L is the undulator length, N is the number of the undulator periods, $\gamma\varepsilon_y$ is the normalized emittance and h is a constant. At the end of the main accelerator the energy spread was estimated to be $\pm$80kV. Eq. (4) requires that N must be less than 78. In our case we chose N as 60. From eq. (5) $\gamma\varepsilon_y$ must be less than 63π mm·mr. The small signal gain[4] is given by,

$$g_0 = 32\sqrt{2}\pi^2 \lambda^{\frac{3}{2}} \lambda_q^{\frac{1}{2}} \frac{K^2}{(1+K^2)^{3/2}} \frac{I_p}{I_a} \frac{N^3}{\Sigma} f(x)F(K) \tag{6}$$

where Ip is the peak current and is estimated to be 9.14A, Ia is the Alfven current(17045A), Σ is the mean transverse area of the optical mode, f(x) and F(K) are given by next equations, respectively,

$$f(x) = \frac{1}{x^3}\left(\cos x - 1 + \frac{1}{2}x\sin x\right) \tag{7}$$

$$F(K) = \left\{ J_0\left[\frac{K^2}{2(1+K^2)}\right] - J_1\left[\frac{K^2}{2(1+K^2)}\right] \right\}^2 \tag{8}$$

The optimum value of Σ is provided as $L\lambda/\sqrt{3}$. Taking account of the fact that the maximum value of f(x) is 0.0675 for x=2.61 and F(K) is 0.715 for K=1.1, we obtain the gain as 55.9% from eq. (6).

Real beam has many factors to decrease the gain, that is, the energy spread(μ_E), the emittance(μ_y), the slippage(μ_z), etc. Taking those factors into account, we define the real gain that can roughly be expressed,

$$g = g_0 \frac{1}{(1+\frac{\mu_c}{3})(1+\mu_y^2)(1+1.7\mu_E^2)} \tag{9}$$

Here μ_E, μ_y, μ_c are given by next equations.

$$\mu_E = 4\sigma_E N \tag{10}$$

$$\mu_y = \frac{4K}{1+K^2} \frac{\gamma\varepsilon_y}{\lambda_q} N \tag{11}$$

$$\mu_c = \frac{\lambda N}{\sigma_z} \tag{12}$$

where σ_z is the bunch length and estimated as 1.31cm(8° at 508MHz). Substituting each value into the eq. (10), (11) and (12),

$\mu_E = 0.768$, $\mu_y = 0.229$, $\mu_z = 0.0485$

The gain was calculated as 26% from eq. (9). Furthermore, assuming that the optical cavity output coupling(ε) is 5% and the mirror loss(δ) is 2%, we obtained the final gain as 19%.

The laser pulse rise time is given by,

$$\tau=0.14\frac{L}{g-(\varepsilon+\delta)}, \tag{13}$$

In our case τ is calculated to be 10.4μs.

The estimation of the gain has been tried by using old undulator whose specification is listed in table 2 under the condition in which the beam has 2.00±0.08MeV. Through the same way and with the same parameters as described above, no gain can be estimated. However, if the beam that satisfies the conditions listed in table 3 is selected, the gain and the laser pulse rise time can be obtained to be +1.8% and 236μs, respectively. The operation of FEL in 950μm is possible.

Table 2 Old undulator parameter

Period length	3.0cm
Field strength	3670Gauss
K parameter	0.727
Number of period	16

Table 3 Beam condition

Beam energy	2MeV
Energy spread	35keV
Peak current	8A
Emittance	15π mm·mr

4. Conclusion

We obtained the gain to be expected at the FEL operation at JAERI as 19%. This value is enough for the FEL operation. Our estimation, however, takes no account of the space charge effects. More accurate estimation including the space charge effect is expected.

Reference

1) Y. Kawarasaki, et al., JAERI TANDEM, LINAC&V.D.G. Annual Report (1987) p23.
2) W. B. Herrmannsfeldt, SLAC 226(1979).
3) G. Dattoli and A. Renieri, "Experimental and Theoretical Aspects of the Free Electron Laser" in Laser Handbook Vol. IV (1985).
4) M. Castellano, "An Infrared Free Electron Laser on the Superconducting Linac LISA"-LNF-88/04(R).

1.8 INJECTOR GUN OF THE LINAC FOR A FEL OSCILLATOR

Hiroshi YOSHIKAWA* and Katsuo MASHIKO
Department of Physics, JAERI

Abstract

A structural design of the injector gun of the linac for a FEL oscillator was done. The electron beam from gun should have a low emissions (<10 micro mrad) and a micropulse sequence (4ns width and 80ns separation). The designed gun structure has the following specific features: 1) the position of the gun electrodes is centered at the HV-insulator vessel; 2) the shape of the electrodes forms the low perveance type Pierce gun.

Introduction

The most important parameter needed for FEL applications is the brightness of the beam, which should be as high as possible. And also the energy spread should be less than 1/2N, where N is the number of the undulator period. It is also required that the micropulse separation should match to the round-trip time of the light traveling in an optical cavity length.

The low-emittance beam may be produced from the injector gun using either a thermionic or a photoemissive cathode. The conventional thermionic cathode with a control grid is immediately available in commercial base and it can be used to form the required micropulse sequence.

The FEL scheme at JAERI and the R&D schedule are presented elsewhere[1)]

In the phase-1 R&D schedule, the injector consists of a grid-controlled thermoionic cathode gun, a sub-harmonic buncher, a buncher and two super-conducting cavities as pre-accelerator.

Design Consideration

However the micro- and macro-pulse sequence depends on the specification of the linac and the optical cavity, the micropulses with 4ns width and 80ns separation and the macropulses of 1ms duration and 1% duty are chosen as phase-1 parameters. Under this condition, the pulse transmis-

sion between the pulser and the grid should have extremely good frequency characteristics to achieve the fast timing response. The length of a lead wire must be as short as possible to reduce the unwanted stray capacitance. To avoid this difficulty, the position of the gun electrodes is moved to the center of the HV-insulator vessel in contrast to that of conventional structure, as shown in fig.1. This configuration will work if the electron beam extracted from the anode does not need an excessive focusing magnetic field. Practically, the grid-cathode assembly (e.g.,Eimac Y-646B) and the focusing electrode are mounted on a flat flange, while the anode is mounted on the top of the support with a hollowed cone shape. Such an ample space just adjacent to the cathode makes the design of the pulser and power-supply easy. And its maintenance of improvement also becomes easy.

The low-emittance beam can be produced using a small cathode, say, 2-5mm in diameter, but the commercially available grid-cathode assembly has a larger diameter, generally. In this design, the virtual area of the electron emission over the cathode is controlled by using the hole size of the focusing electrode, whose potential is kept negative to the cathode potential.

Another important point for the low-emittance gun design is the shape of the anode and cathode. If the current density from the cathode with the very small emissive area were enough, the best method for beam extraction would be that with the beam trajectory almost parallel to the axis accompanied by a slight electrostatic focusing to cancel the space-charge effect. The other choice which we employed is a low perveance configuration (week focus) with a relatively high voltage applied to cathode and the anode. The calculations of the beam trajectory under the various electrode shapes were done by M.Sugimoto[2].

Discussion

The design study on the injector gun is now in progress. Experimental tests are planned to prove the axial focusing properties of the beam exiting the anode and to tune up the associated electronics.

Reference

1) M.Ohkubo et al., PROCEEDINGS OF THE 13th LINEAR ACCELERATOR MEETING IN JAPAN 1988

2) M.Sugimoto, PROCEEDINGS OF THE 13th LINEAR ACCELERATOR MEETING IN JAPAN 1988

* On leave absence from Dept. of Elec., Waseda Univ.
Present address : SR-group, Dept. of Phys., JAERI

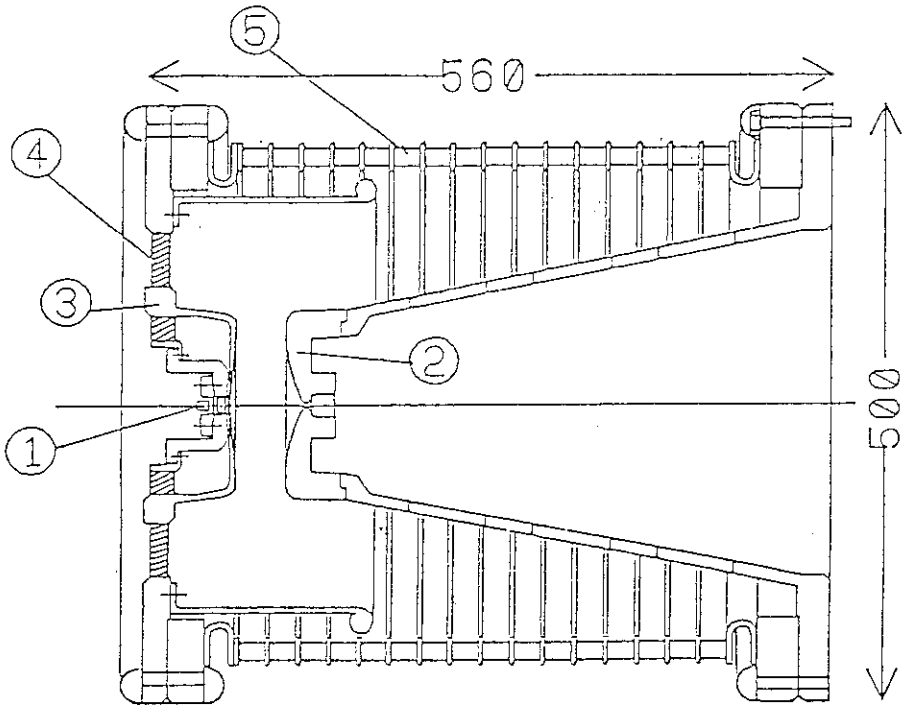

Fig.1(a) Cross sctional view of electron gun assembly.
The anode is mouted on the top of cone shape support which has vacuum openings. Cathode, Grid and Wehnelt are mounted on a flat flange. (1) Cathode Assembly, (2) Anode, (3) Wehnelt (4) Ceramic Insulator, (5) Ceramic Insulating Cylinder.

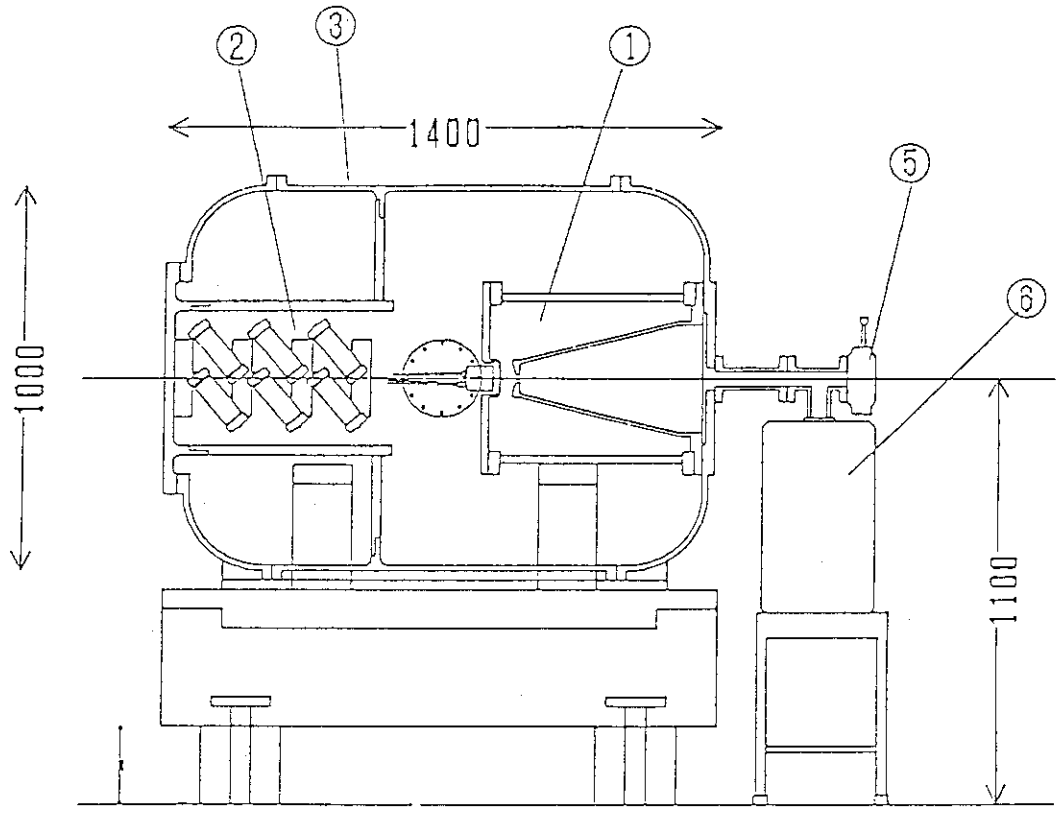

Fig.1(b) Side view of Gun tank (1) Electron Gun, (2) Cockcroft-Wolton, (3) Vessel, (5) Gate valve (6) Ion Pump

1.9 DESIGN OF THE ELECTRODE SHAPE OF THE INJECTION GUN FOR THE JAERI FREE ELECTRON LASER*

Masayoshi SUGIMOTO
Department of Physics, JAERI

The newly developed electron gun for JAERI free electron laser should have a good emittance, < 10 π mm-mr, with the moderately high peak current, ≈ 100 mA. To realize such a condition using the conventional thermionic cathode, we employed a special form of the electrodes and a small cathode. The focusing electrode is isolated to the cathode and the output beam compression can be controlled by changing its potential relative to the cathode potential.

Introduction

The essential requirement for the injectors used for the free electron laser is the high brightness, and under the condition of the limited peak current it means the low emittance, less than 10 π mm-mr for our purpose. There are some novel techniques to obtain a good quality beam[1]: photoemissive cathode using pulsed laser excitation and/or RF acceleration immediately after the cathode. However, it can be also realized by using the conventional thermionic emitter, as far as the current density is not too high , ≈ 10 A/cm or less. In our case, the peak current would be less than ≈ 100 mA and the beam diameter ≈ 1 mm, so we tried to design the shape of the electrodes for the injection gun, which satisfied the required condition.

Design study

The primary object of the design of the electrode shape is to realize the low emittance beam (≈ 10 π mm mradians) under the condition: energy 250 keV, peak current 100 mA, and beam diameter 1 mm. Firstly we made a decision to employ a low perveance type electrode shape to satisfy such a low emittance. Secondary we chose the beam envelope between the cathode and the anode. There are two types of beam extraction with low emittance: i) the beam is almost parallel to the axis of symmetry, and it has small diameter at the cathode area with the high current density. ii) the beam is focused into anode hole and it becomes almost parallel after extracted from the anode. The latter case would be preferable from the point of

view about the load for the cathode, but the former one is better when the high peak current is needed and the space charge effect is untolerable.

In any cases, the shape of the electrode must have the characteristics to reduce the unnecessary growth of the emittance between the beam extraction line: the radial component of the electric field formed by the electrodes is proportional to the radial coordinate[1]. If the beam is not extracted, such a condition is easily fulfilled by solving the Laplace equation, but actually the self-field of the beam makes difficult to solve the problem. The design was done by using the SLAC electron trajectory program[2] with some modifications about input data handling routines.

The calculations of the electron trajectory were carried out by changing the parameters: a) cathode radius, b) shape of the focusing electrode, c) distance between cathode and anode, d) shape of the anode. The calculations with different current density and the anode voltage were also done. And the possibility of the controlling the output beam size (or beam compression) is studied by changing the potential of the focusing electrode relative to the cathode potential[3].

Results

The optimal shape of the focusing electrode is fairly independent of the other parameters, and has a large focusing strength compared with that obtained from the solution of the Laplace equation for no beam case. But the focusing is much weaker than that for the usual Pierce type electrode. The anode shape gives relatively small effect to the final results but it must have a defocusing characteristics to avoid the over-focusing after the beam extraction.

The obtained emittance is exponentially decreased by decreasing the cathode diameter. To satisfy the beam diameter requirement after beam extraction, the cathode diameter should be less than 4 mm. The radial distribution of the extracted electrons has a peak at the edge, so it is like a hollow beam. This is caused by the space charge force inside the beam.

The increase of the emittance becomes linear about the decrease of the anode voltage between 200 and 300 keV, and the resulting unnormalized emittance is about 1.8 π mm-mr at 250 kV. If the anode voltage decreases to 150 kV, the emittance deteriorates to 2.7 π mm-mr.

The emittance increases, roughly speaking, linearly, as total current increases. So it becomes a very difficult task to maintain the beam size

small in the high current condition. The limit of the total current to preserve the good quality in the designed injection gun is about 200 mA.

By variation of the potential of the focusing electrode the extracted beam size can be changed, e.g. 5.8 mm radius becomes 5.5 mm when -50 V is applied. In Fig.1 the typical beam trajectory and equipotential lines are given. The horizontal axis is the symmetrical axis of the gun and the vertical axis shows the radial distance. The shape of the focusing electrode on the left hand side has a curve with small curvature whereas the shape of the anode side has a larger convex curvature. The filled area near the symmetrical axis shows the beam trajectory from the virtual cathode. In fig. 2a), the normalized current density at each radial point is plotted. A peak at the edge region can be found generally. Fig. 2b) shows the directions of each ray relative to the symmetrical axis at the exit of the problem region.

Conclusion

The electrode shape for the injection gun of the JAERI free electron laser is determined by using the electron trajectory calculation program. The required condition for the injection gun is satisfied if the small cathode is used. The higher anode voltage is preferred to get the smaller emittance at the exit. The maximum beam current available from the current geometry is less than 200 mA. The variation of the potential of focusing electrode can change the exit beam size.

References

1) J.S. Fraser, R.L. Sheffield and E.R. Gray, Nucl. Instr. and Methds A250 (1986) 71.

2) W.B. Herrmannsfeldt, SLAC 226 (1979).

3) R. Becker, Nucl. Instrum. & Methods 187 (1981) 255.

---

* This work is presented at the 13th Linear Accelerator Meeting in Japan (Sep. 7-9, 1989, Tsukuba).

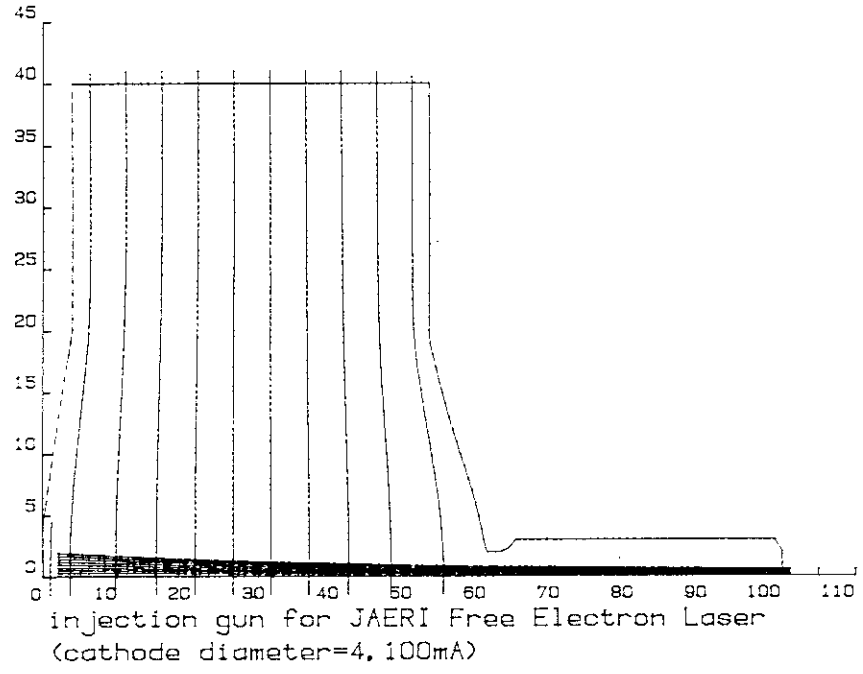

Fig. 1 Shape of the problem region boundary and the equi-potential lines for the cathode with 4mm diam and 100 mA peak current. The filled area near axis shows the beam trajectories from the virtual cathode. Unit is shown in mm.

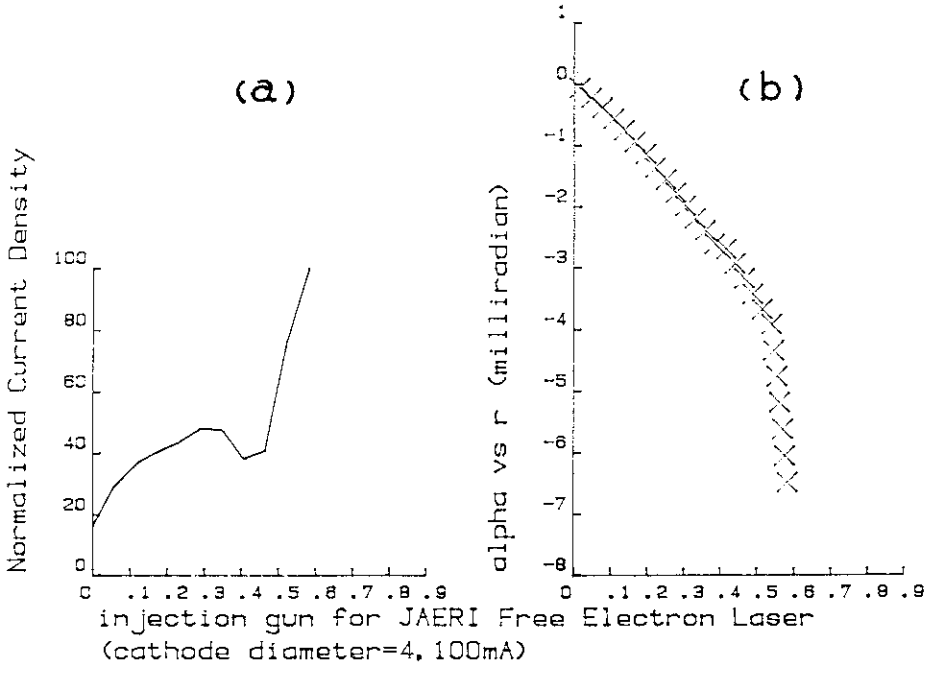

Fig. 2 a) Normalized current density as a function of radial point.
b) Tangential direction of each simulated trajectory. Unit of horizontal axes shown in mm.

1.10 SPACE CHARGE EFFECTS ON BUNCHED BEAM

Masaru SAWAMURA

Department of Physics, JAERI

Abstract

Beam dynamics calculation has been carried out on the bunched electron beam both in longitudinal and transverse direction through the injection system of the linac for the free electron laser. In order to get high beam quality for FEL oscillation, in case of high beam current, it is found that the energy selection is required before pre-accelerator.

Introduction

High beam quality, energy resolution and brightness, is definitely required for free electron laser (FEL) oscillation. It is necessary to make the phase spread narrow to get low energy spread through the RF linac. When we want to achieve high peak current, space charge effects are unavoidable. The space charge forces affect the beam emittance and phase spread badly. The longitudinal and transverse space charge effects are calculated.

Longitudinal bunching

The outline of JAERI FEL linac is described elsewhere.[1] The 84.7MHz-sub-harmonic buncher (SHB) and the 508MHz-buncher are located following the electron gun which emits the beam of 250keV and 4ns width. In case of no space charge effects it is possible to bunch the beam to less than a few tens-pico-seconds by stationing each element properly and by adjusting the RF phases and the amplitudes of the power. Table 1 shows the phase and energy spreads for several cases of the SHB voltage. As the SHB gap voltage increases, the drift length decreases while the energy spread increases. In order to bunch the beam, the velocity of the beam should be modulated, namely, the preceding beam is decelerated and the following beam are accelerated, and the velocity modulation causes the bunching after a certain drift length.

According to Table 1 the RF phase of the SHB corresponds to the bunching phase. On the other hand, the phase of the buncher corresponds to the debunching phase. This means that the buncher acts as a debuncher. The

sine curve of the SHB RF field can not linearly modulate the beam velocity. By adding the debunching effect of the buncher, almost linear velocity modulation can be achieved.

As the beam is being bunched, the current density becomes high and space charge forces affect each particle more strongly. These space charge forces cause the debunching effects of the beam, because the preceding part of the beam is accelerated and the following part of the beam is decelerated by the space charge forces. Fig.1 shows the bunch length aberrations from the bunch length of no space charge beam as a function of the drift length from the SHB. As the drift length becomes long, the interaction duration of the space charge forces becomes long and the bunch length aberration becomes large. According to Table 1 the long drift length (low SHB voltage) has the advantage of the low energy spread and has the disadvantage of large phase spread.

Fig.2 shows the bunch length aberration in the cases of the different position from the longitudinal center of the beam. As the particles are far from the center of the beam, the bunch length aberration becomes large and the beam spreads widely. In order to keep the energy spread minimum and not to spill the beam, the phase spread should be limited desirably less than about 9 degrees for the main accelerator frequency, so the energy selection is necessary to cut the tail of the beam and to get the small phase spread just before the pre-accelerator.

Transverse focusing

Solenoid coils are located along the beam line to focus the electron beam transversely. At just the downstream of the SHB the current is about 100mA and at just the upstream of the pre-accelerator it is about 10A. As the current density becomes high, the defocusing force by the space charge becomes strong. Strong focus strength is necessary to keep low transverse emittance.

A simple model of cylindrical beam are considered, where current density is assumed as reverse proportional to the bunch length and uniformly distributed in the volume. Fig.3(a) shows the beam radius as a function of the drift length through the uniform solenoid field. At the end of the drift space the bunch length is so short and the defocusing forces by the space charge forces are so high that the stronger focusing forces are necessary to keep low transverse emittance as shown in Fig.3(b).

Reference

1) M.Ohkubo et al.: in this Annual Report

Table 1 Achievable longitudinal phase space using SHB and buncher in the case of no space charge effects.

Longitudinal phase space (0mA)						
V_{SHB} (kV)	ϕ_{SHB} (deg)	$V_{buncher}$ (kV)	$\phi_{buncher}$ (deg)	$\Delta\phi$ (deg)	ΔW (keV)	Drift length (m)
40	-14.5	5.0	174.5	1.7	68.9	11.3
50	-16.7	6.5	175.6	2.2	85.0	8.9
60	-20.8	7.5	172.6	2.5	100.7	7.2

V_{GUN}=250kV Δt=4nsec

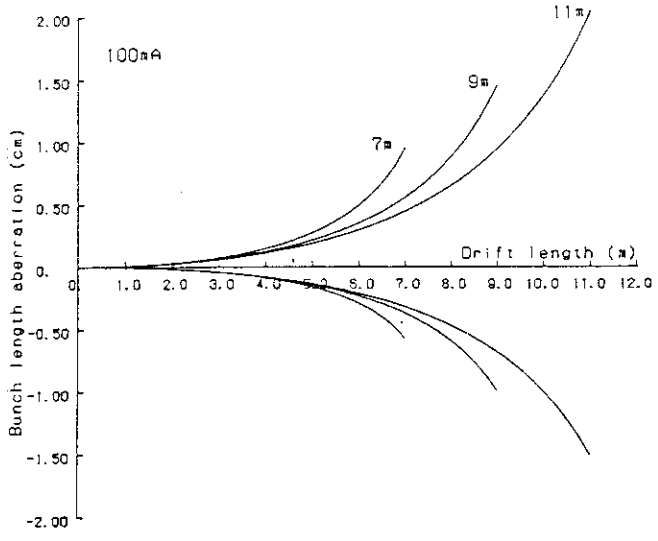

Fig.1 Bunch length aberration by space charge effects from bunch length with no space charge as a function of drift length in case of 7m, 9m and 11m bunching drift length.

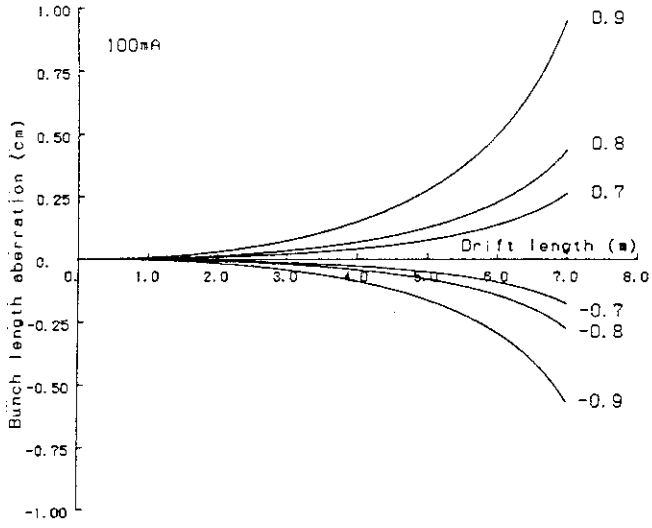

Fig.2 Bunch length aberration by space charge effects from bunch length with no space charge as a function of drift length in case of different positions from longitudinal center of beam.

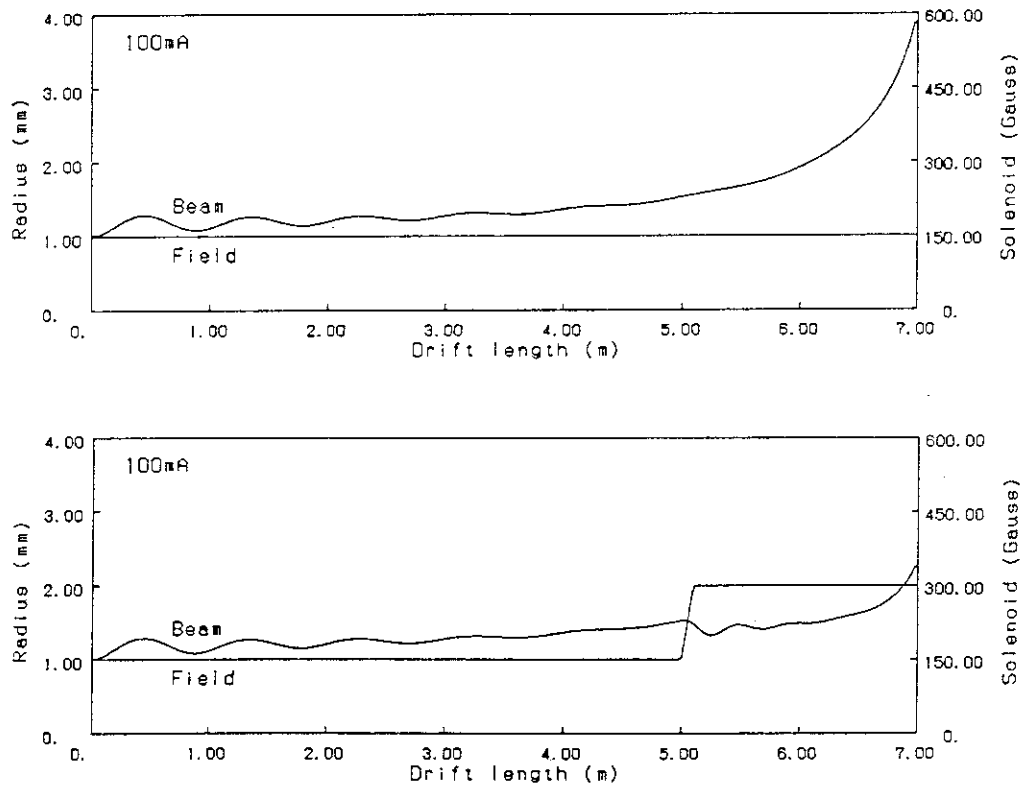

Fig.3 Beam radius through drift space in case of 7m focus length (a) with uniform solenoid field and (b) with strong solenoid field at the end of drift space.

1.11 HIGHER BRIGHTNESS INJECTOR:SURVEY ON PHOTOCATHODE INJECTOR DEVELOPMENT AND PRELIMINARY DESIGN CONSIDERATION

Jun SASABE*

Department of Physics, JAERI

Developmental status is surveyed on the higher brightness and higher energy resolution injectors with photocathodes for free–electron–laser (FEL) drivers. Design consideration is preliminarily undertaken for further improvement of the beam characteristics of the presently planned RF–linac (Phase–I) to the next stage of the FEL's R&D.

1. Introduction

An injector system and superconducting linear accelerators are now under construction in JAERI as the first stage (Phase–I) of the FEL' R&D.[1)]
At present stage, as an electron emitter of the injector system, a thermal cathode (dispenser cathode) with rather high voltage (300kV) is adopted.
In the second stage (Phase–II), an RF–or high voltage gun with photocathode is planned to get the high brightness and high energy resolution beam.
The optical gain of FEL is proportional to the brightness of the beam, so higher brightness injector is necessary. The brightness Bn can be expressed as following

$$Bn=I/<\epsilon n>^2 \quad [A/(m^2\cdot rad^2)]$$

Here I is peak current and ϵn is beam emittance.[2)]
In order to get the high brightness beam, the emmitter with high current density and low emittance are required.

As an electron cathode of the linac injector, thermionic cathode (e.g.,oxide–, dispenser–, and LaB_6–cathode, see Table 1) has been used for a long time. Thermionic cathodes are generally limited in the emission current density (typically, several ten A/cm^2). It is, therefore, necessary to compress (bunch) the beam longitudinally in use of the thermionic cathode for high brightness. For the purpose of the beam longitudinal bunching, sub–harmonic–bunchers and bunchers are required, associated long drift space causes the degeneration of emittance and energy spread of the beam (≈several tens keV) unavoidably , because of the space charge.

Photocathodes have been widely used in TV cameras or photo multipliers Their

development in these fields are not intended to use as high current electron emitter. The study of photocathodes for use of high current source has recently progressed, mainly in USA (e.g., LASER TRON). As high current density and high brightness, 600(A/cm^2) and 10^7($A/cm^2 \cdot rad^2$) have been achieved respectively by LANL group.[3] As electrons are emitted from the photocathode only during the laser pulse duration, no compression system is necessary, and then low emittance and low energy spread beam can be obtained.

2. Developmental Status of Photocathode Injectors

The developmental status of photocathode injectors for FELs in advancing laboratories are listed in Table 2. As the photocathode material, a semiconductor photoemitter Cs_3Sb has mainly chosen, because of it's capability of high current density.[2-3] Another semiconductor GaAs which has higher quantum efficiency is now being investigated, however, it has not demonstrated so high current density.
Table 3 shows the comparison of GaAs with Cs_3Sb. Because of the small optical absorption, the thickness of the GaAs layer has become thick to get enough current, so that it is difficult to get the short pulse beam. On the other hand, the transverse energy spread of GaAs is very low at the wavelength very close to the material threshold($\Delta E<0.1$(eV) is possible), so higher brightness beam can be obtained.[4] Further investigation of this material is expected.

Also another semiconductor or metal photoemitter is now being investigated. Recently, to get the higher quantum efficiency from the metallic cathode, France's group has proposed a method using two laser lights to lower the work function of the cathode.[5]

3. Preliminary Design Consideration

The specification of our photo cathode injector system is tentatively summilized in Table 4 and design schematics is shown in Fig 1.[6] The photo-emmited electrons are rapidly accelerated with high DC voltage (≈300kV) to keep the original emittance value. Higher voltage can well prevent emittance from growing.
The injector system consists of a preparation chamber of the cathode, a laser system (mode-locked YAG laser with KD^*P crystal), and a high voltage power supply.
In the preparation chamber, Cs and Sb in different vessels are vaporized and deposited on the surbstrate, monitoring the thickness of the depositing layer. The deposited surbstrate is then moved to the position in the hole of Wehnelt electrode. Since the vapor pressure of Cs is high, the thermal effect due to the high average laser power vaporizes Cs atoms on the cathode severely. A cooling system is necessary to avoid

this influence.[4)]

In the laser system, the mode-locked YAG Laser oscillates at 1064nm, and the fundamental is doubled in KD*P crystal to 532nm. Pulse-to-pulse duration time is controlled by optical delay system. Laser and RF system must be synchronized.
A vapor deposition experiment is firstly by monitoring the quantum efficiency and residual gas species. Secondly, the mesurement of current density and beam emittance and energy spread will be made.

The physics of photo materials is not solved entirely and the technology to gain enough current from the photo material has not been established yet. In order to get higher brightness beam and to use it practically, the key points are: "How can we lower the work function of the photo materials?" and "How can we improve the life time of the cathode?"

References

*On leave from Hamamatsu Photonics Inc.

1)M.Ohkubo et al., "LINAC FOR A FREE ELECTRON LASER OSCILLATOR" Proc. 1988 THE 13th LINEAR ACCELERATOR MEETING IN JAPAN

2)J.S.Fraser,R.L.Sheffield and E.R.Gray,"A HIGH-BRIGHTNESS ELECTRON INJECTOR FOR FREE-ELECTRON LASERS DRIVEN RFLINACS" Los Alamos National Laboratory, document LA_UR-85-3176

3)J.S.Fraser, R.L.Sheffield, E.R.Gray, P.M.Giles, R.W.Springer, and V.A.Loebs, Proc. 1987 Part.Accel.Conf., Washington,D.C., March 16-19,1987.

4)Peter.E.Oettinger, Ruth.E.Shefer, Dan.L.Birx and Michael.C.Green "PHOTOELECTRON SOURCES: SELECTION AND ANALYSIS" Proc. 1986. 8th FEL Conference

5)R.Dei-Cas et al., "PHOTO-INJECTOR,ACCELERATOR CHAIN AND WIGGLER DEVELOPMENT PROGRAMS FOR A HIGH PEAK RF-FREE ELECTRON LASER" Proc. 1988 10th FEL Conference

6)G.A.Lowe, R.H.Miller and C.K.Sinclair "THE SLAC LOW EMITTANCE ACCELERATOR TEST FACILITY", Proc. 1986 Linac Conference in USA.

Table 1 Summary of Typical Thermal Cathode Characteristics

Cathode	Peak J Area (A/cm^2) (cm^2)	Temprature (^oK)	Operational Pressure(torr)	Work Function(eV)
Oxide	20 <1000	800–1100	$<10^{-7}$	1.0–1.2
Dispenser	10 <500	1100–1400	$<3x10^{-7}$	1.8–2.0
LaB_6	40	1400–1800		2.7

Table 2 The Developmental Status of Photocathode Injectors

Laboratory	Emmiter	Current (A/cm^2)	Emittance (mm·mrad)	Energy (MeV)	Bunch (ps)
LANL(USA)	Cs_3Sb	600	5–10	1.0	60–70 (now 15)
SLAC(USA)	GaAs	180			1000
BNL(USA)	Yttrium or Cs_3Sb	100A	3–6	4.65	3–5
LBL(USA) (planned)	Cs_3Sb	760	0.56	4.1	15
Gesamthochzchule (planned)	Cs_3Sb	200A		2.0	5–10
CEA(FRN) (planned)	CS_3Sb	200–500		1.0–1.5	50–100

Table 3 The Comparison of GaAs and Cs_3Sb

	GaAs	Cs_3S
Quantum Efficiency	1–10%	1–3%
Thickness of Layer	thick ($\cong 1\mu m$)	thin (several hundred A)
Optical Absorption	small	large
Response	slow	fast
Operational Pressure	10^{-10}(torr)	$<10^{-8}$(torr)

Table 4 Specification

Photocathode material	Cs_3Sb
Photocathode gun voltage	300kV
Incident light	
wavelength	532nm
pulse width	10–30ps
Cathode Area	$1cm^2$
Current density	$200A/cm^2$
$\Delta E/E$(after gun)	0.5%

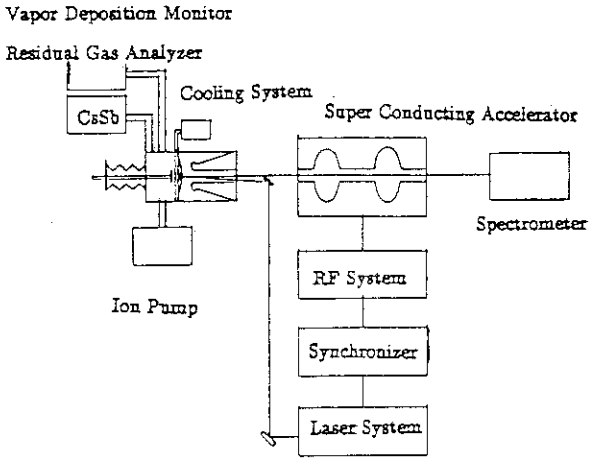

Fig.1 Design Schematics of Photocathode Injector

1.12 CONSTRUCTION OF A COMPACT ELECTRON STORAGE RING, JSR

SYNCHROTRON RADIATION RESEARCH LABORATORY and LINAC TEAM

Department of Physics , JAERI

Abstract

A compact electron storage ring (JSR) was completed in March, 1989 in order to study some accelerator technologies related to the R&D aiming at the high-brilliant synchrotron radiation facility(8GeV). The JSR lattice has a Chasman-Green lattice with three 1.5m long dispersion free straight sections. One of three straight sections is provided for the study of insertion device. The circumference of JSR is 20.546m. The electron beam are fed by the linac at 150MeV and their energy is ramped slowly up to 300MeV in the ring. The power supplies of all magnets and RF-system are controlled through optical fiber links by the real time computer system. The signals from beam monitors are stored in the same computer so as to simplify the procedures of diagnostics and controls.

We started the experiments of electron beam injection for JSR on May 25, 1989, and succeeded to observe the synchrotron radiation on May 31, 1989.

Table 1 Main Parameters of JSR.

Stored energy		300MeV
(Injection energy)		150MeV)
Circumference		20.546m
Average radius		3.27m
Revolution time		68.5nsec
Available straight section		1.45m
Number of bending magnets		6m
Strength of quadrupole field		$6.8m^{-2}$
		$4.1m^{-2}$
		$-5.6m^{-2}$
Natural emittance		$1.1x10^{-7}$mrad
Natural chromaticity	x	-1.81
	y	-4.54
Tune	x	2.25
	y	1.25
Damping time constant	x	58msec
	y	48msec
	s	22msec
Momentum compaction factor		0.044
Energy loss per turn		0.86keV/turn
RF frequency		116.7MHz
Harmonic number		8
Peak voltage		30kV
Synchronous phase		8.8degree
RF power		2kW
Natural bunch length		16mm
Touschek lifetime		2hours

1. INTRODUCTION

Three big projects of synchrotron radiation facility of the next generation in the world are almost simultaneously in progress: 8GeV in Japan, 7GeV APS ANL and 6GeV ESRF ILL. The design study on the big facility is effectively facilitated the technology accumulation thru the experiences of the construction and operation of the small storage rings JSR1),2). The aim of JSR is to study various kind of accelerator technologies as well as to examine the new ideas such

as the beam position control and the insertion device study.

2. CHARACTERISTICS OF JSR

The JSR lattice is Chasman-Green type. As shown in Fig.1, the lattice has three fold symmetry. One period of the lattice includes two bending magnets (deflection angle of 60 degree per each magnet) and five quadrupole magnets. The lattice parameters are summarized in Table 1. There are three straight sections in the ring, which are used for the spaces of the insertion device, RF-cavity and the beam injection magnets.

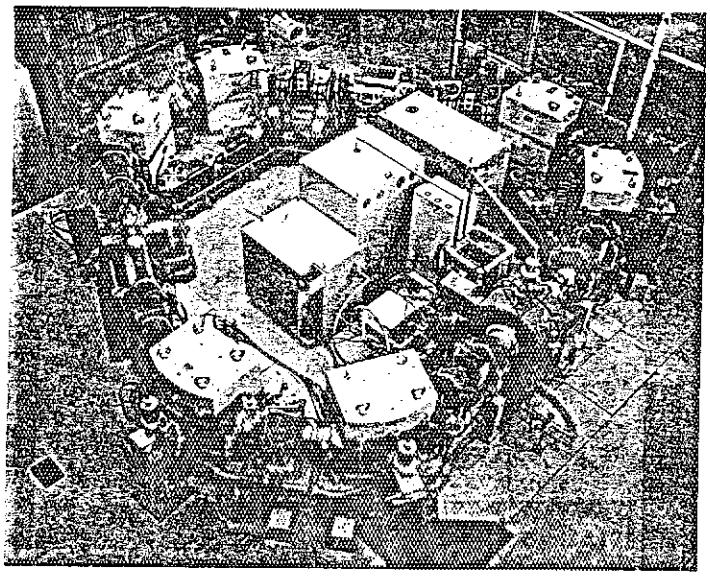

(a) Photograph of JSR.

BM1~6	BM ﾏｸﾞﾈｯﾄ
QDO	QDO ﾏｸﾞﾈｯﾄ
QD11, 12, 31, 32, 51, 52	QD ﾏｸﾞﾈｯﾄ
QFO	QF ﾏｸﾞﾈｯﾄ
QF11, 12, 31, 32, 51, 52	QF ﾏｸﾞﾈｯﾄ
QF2, 4, 6	QF ﾏｸﾞﾈｯﾄ
STM01	ST ﾏｸﾞﾈｯﾄ
STM02	ST ﾏｸﾞﾈｯﾄ
STM11~52	ST ﾏｸﾞﾈｯﾄ
BPM	ﾋﾞｰﾑﾓﾆﾀｰ
SPM	ｾﾝﾀﾘﾝｸﾞﾏｸﾞﾈｯﾄ
INF	ｲﾝﾌﾚｸﾀ
RF	RF ｷｬﾋﾞﾃｨ
BLP1~6	ﾋﾞｰﾑﾎﾟｰﾄ
PON1~8	ｷｯｶｰ電磁石電源ﾓﾆﾀ
PBNS0, 1	ｾﾌﾀﾑ電磁石ﾓﾆﾀ
DCCT	DCCT
FCT	Fast-CT
RFK	RF ﾉｯｸｱｳﾄ電極
IC	ｲｵﾝｸﾘｱﾘﾝｸﾞ電極
TGP0~10	ﾁﾀﾝｹﾞｯﾀﾎﾟﾝﾌﾟ
SIP1~6	ｽﾊﾟｯﾀｲｵﾝﾎﾟﾝﾌﾟ
GV	ｹﾞｰﾄﾊﾞﾙﾌﾞ
S1~6	直線部番号

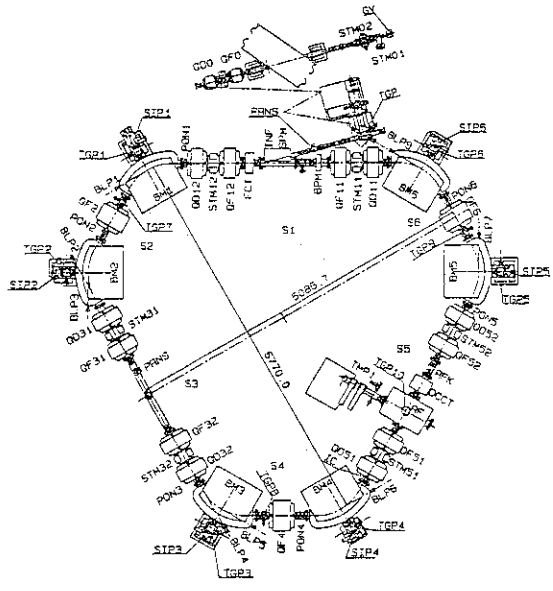

(b) JSR lattice.

Fig.1 Plane view of JSR.

The vacuum chamber is composed of the stainless steel SUS316L and SUS316 of 3mm thickness. The several vacuum pumps with the total pumping speed of more than 5000 *l*/sec are installed in the ring and the pressure is between 5×10^{-9} Torr and 5×10^{-10} Torr at pump heads.

The injection system is composed of a septum magnet and a kicker magnet which are located at the same straight section. A kicker magnet generates the pulse dipole field about 0.04T with the pulse width of 0.6μsec which gives 6mrad kick for electron beam. A septum magnet deflects the injection beam by 15.172degree with the field of 0.89T and the length of 148mm. An electron beam is supplied by the linac with the energy of 150MeV. The injection from the linac are repeated every 1 sec to accumulate electrons in the ring. After the

accumulation of electrons at 150MeV, the electron energy is gradually increased up to 300 MeV.

The brightness of synchrotron radiation from the bending magnet is shown in Fig.2. The main part of radiation is in the soft X-ray and VUV region. The critical wavelength is 17.3nm at the electron energy of 300MeV. A test undulator is planned to be installed in one of the straight sections for the studies of undulator and electron beam dynamics.

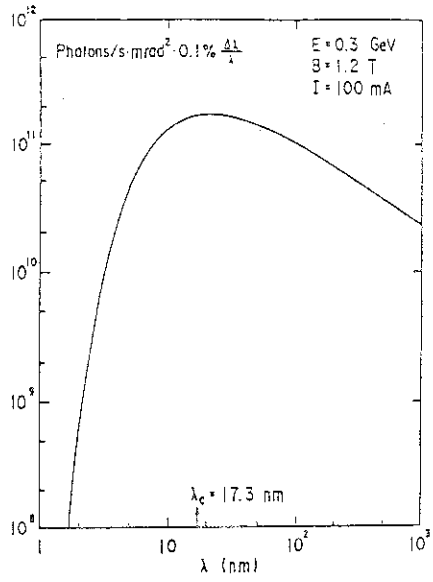

Fig.2 Brightness of the synchrotron radiation from the bending magnet.

3. BEAM MONITORS

The beam intensity is monitored by two current transformers(DCCT and Fast-CT). Six position monitors are welded in the vacuum chamber at the entrance of each bending magnet. Their signals(6 positions times 4 electrodes) are sequentially archived into the control computer within the time of 0.24sec. A tune is measured by RF-knock out electrodes which are composed of four wires with the length of 150mm and the diameter of 1mm. One pair of electrodes is installed for the purpose of the ion clearing. The maximum voltage of 500V is able to be supplied to each electrode. If necessary some electrodes of the position monitors will be used for the ion clearing. The injection beam is monitored by two profile monitors composed of screen targets.

Six photodetectors are installed to measure the locations of the synchrotron radiation from the bending magnets.

4. CONTROL SYSTEM

JSR is controlled by one control computer(real time computer) as shown in Fig.3. The control computer is selected a 32 bit CPU(rt VAX 1000). It takes roles of controlling the devices, observing the status and alarms of each devices and also representing the operation mode and the informations of the beam monitors. Many devices are connected with the computer through the universal device controller(UDC) and the optical fibers. Presently all power supplies for the magnets and RF-system are connected with the control computer.

This control system is ready for studying procedures of the feedback control of the electron beam position.

The upper level computer, which is connected with the control computer through DECnet(Thin Wire Ethernet), is for the purpose of the data storage and the development of the control program.

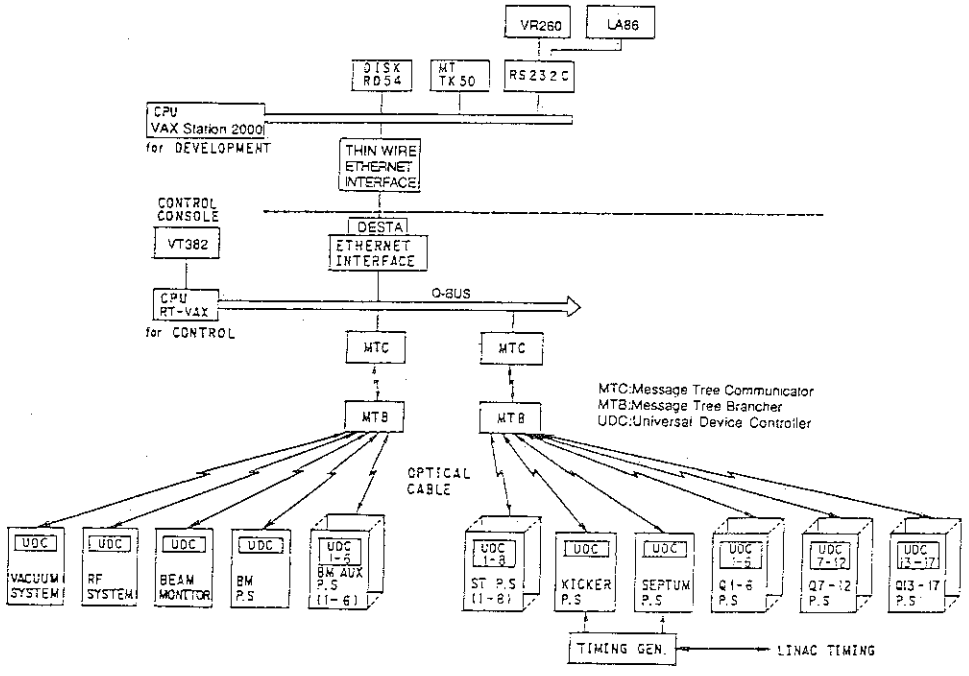

Fig.3 Computer system of JSR.

5. CONCLUDING REMARKS

JSR is a test ring aiming at the next generation synchrotron radiation facility so that it has been designed to be flexible to study the control procedures and to install the insertion device. Design study of the lattice was carried out from January to June in 1988, and all devices were manufactured at the end of 1988. The installation in the linac building was started in November 1988. An initial beam was injected into JSR and an electron beam revolved one turn in JSR on May 25, 1989. We succeeded in taking a photograph of synchrotron radiation light on May 31, 1989.

REFERENCE

(1) H.YOKOMIZO, et al.:"CONSTRUCTION OF A COMPACT ELECTRON STORAGE RING JSR",to be published in Rev. Sci. Instrum., 1989.

(2) H.YOKOMIZO, et al.:"DESIGN OF A SMALL STORAGE RING IN JAERI",in Proc. of the European Particle Accelerator Conference, Rome Italy, 1989.

1.13 FABRICATION AND RF PROPERTIES OF THE S-BAND TM010 MICROWAVE CAVITY MADE OF $YBa_2Cu_3O_{7-\delta}$

Eisuke MINEHARA, Ryoji NAGAI[+],
and Manabu TAKEUCHI[+]

Department of Physics, JAERI
[+]Faculty of Engineering, Ibaraki Univ.

After the discovery[1] in late 1986 and the confirmation of the newly-developed metal oxide superconductors with higher transition temperatures raised the possibility of a new class of superconducting microwave devices operating at temperatures well above the liquid He and near the liquid hydrogen, neon and nitrogen, the feasibility study for the superconductor devices at microwave, and millimeter-wave frequencies, i.e., cavity resonator, transmission lines, waveguide, and antenna, was started at JAERI,Tokai in April 1987.

In order to examine the feasibility of such devices, and to investigate the nature of superconductivity in these new superconductors, we have studied the microwave response of the oxide superconductors over a wide temperature range[2]. In addition, we have also studied the fabrication, and microwave properties of these actual devices using the new superconductors.

The successful fabrication and microwave properties of the superconducting TM_{010} cavity[4] were previously reported to be resonant at 7 GHz with the quality (Q) factor of 10^4-10^5. In the present work, it would be reported that the new bonding method utilizing low- and high-temperature brazing agents could be successfully applied to make the s-band cavities larger than the previous ones, and microwave properties of the cavities were much improved to have the quality factor of 10^5 - several x 10^6. The body of the cavity was made out of the single-phased and bulk $YBa_2Cu_3O_{7-\delta}$ material with a transition temperature of about 92 °K. The Q factor of the cavity was measured as a function of temperature from 300 °K to 30 °K. Starting from a value of Q=~ a thousand from 300 °K to about 100 °K, the Q increased by a

factor of thousands to Q=>10^6 at 15° - 30°K and upon further conditioning of the cavity and the RF coupler, to several x 10^6 at the same temperature. The temperature dependence of the Q factor was observed to be very similar with independent measurements of the ac Meissner effect and the surface resistance for the $YBa_2Cu_3O_{7-\delta}$ samples[2,3], and the Q factor of the 7 GHz cavity resonator[4].

A high Tc superconducting microwave cavity may be considered as a fundamental device whose microwave characteristics define the performance of the bulk microwave structures. Other kinds of the microwave devices utilizing a wave guide, coaxial cable, normal-conducting and classic superconducting cavities were recently designed and made to measure microwave responses for the high Tc superconducting samples. Except for the classic superconducting cavity devices, their sensitivities for measuring microwave characteristics of the high Tc material are several orders of magnitude lower than the high Tc superconducting cavity device. The fabrication technology utilized in the cavities have potential applications for any kinds of passive microwave elements, i.e., particle accelerators[3], resonant filters[5], ultrastable clocks[6], transmission lines and so on.

High-purity Y-, Ba-, and Cu- oxides were mixed as fine powdered materials, and reacted at 900 °C for about 5 hours. The Cu-oxide powder used here was specially prepared to have the powder particle diameter of 400 angstrom in average. The mixture was repeatedly pulverized, reground, and sintered at 900 °C for about 10 hours. The resultant black powder was then cold-pressed into solid and disc forms, using an isostatic press at pressure of 300-400 kg/cm^2, and then mechanically machined into flat disc and ring forms. Before and after the final machining and polishing, the ring and discs were sintered at 920 °C in dry air for about 7 hours.

Characterization of the samples by four-point dc resistance, ac Meissner measurements and the others indicated a Tc onset of 92 °K with a transition width of less than 2 °K, and the density was measured to be about 75 % - 95 % of the

theoretical value. X ray diffraction patterns taken in each process step showed that the final discs and rings had the single-phased , the slightly ab-plane aligned structure parallel to the surface, no other structures than the $YBa_2Cu_3O_{7-\delta}$ and no impurities within the statistical error.

The high Tc superconducting cavities were designed and made to be resonant in the TM_{010} mode at 2.856GHz. Because of the immature bonding technique at the first assembling of the cavity, the resonant frequency for the assembled cavities was shifted to be 2.43 GHz. Because the technique was improved after measurement of the first cavity, the second cavity could be successfully assembled and measured to be exactly resonant at the designed frequency of 2.856GHz. The resonances of the other TM_{0n0} modes with n=2,3,4 and 5 were observed at the calculated resonance frequencies from the fundamental frequency of the TM_{010} mode.

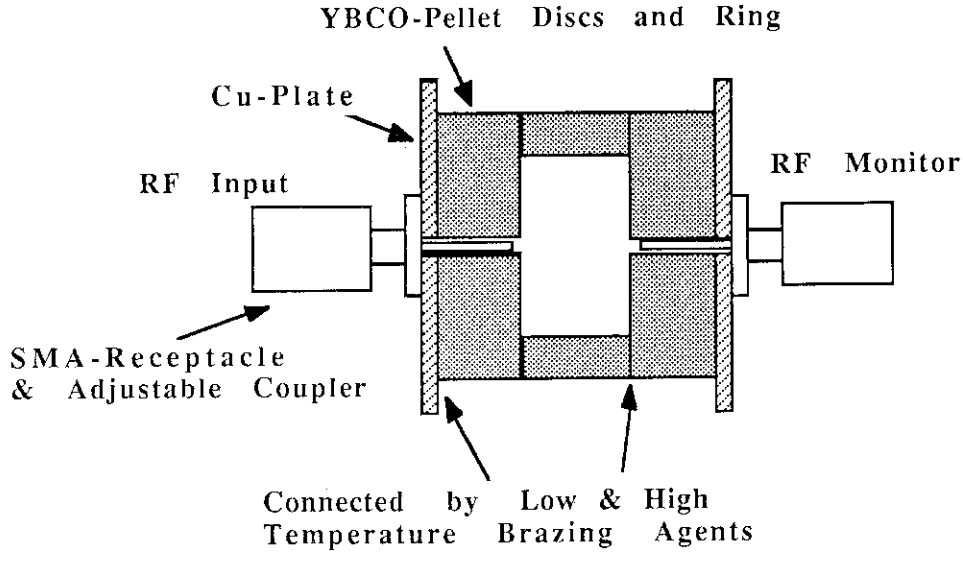

Fig. 1 Schematic of the $YBa_2Cu_3O_{7-\delta}$ cavity.

The cavities were made from the two identical $YBa_2Cu_3O_{7-\delta}$ discs, and the ring as shown in fig.1. Each of the discs has dimensions of 110 mm outer diameter x 8 mm thickness which

contains a coupling hole of diameter 4 mm at the center. The ring has dimensions of 110 mm outer diameter, 80 mm inner diameter x 5 mm and 8 mm thicknesses. The cold-pressed disc could be machined smoothly without any special care to avoid some damage to the disc. No coolant or lubricant was used to avoid contamination during machining. These two discs and the ring were sintered in dry air, and were assembled in the form of a cavity by welding mainly with a low-temperature indium-based brazing agent and a high-temperature silver-based brazing agent.

We tried several kinds of soft metal wire (gold, silver, aluminum and indium) O rings as a seal between the bulk discs and the rings before the welding technique was applied to fabricate the cavities. Concerning the metal-wire sealed cavities, we found very frequent and irreversible irregularities, and deterioration of the measured Q values during the cooling down and warming up. Except for the early stage of the present work, we did not try to apply the metal O ring to fabricate them.

The resonant frequency measured for the first cavity with TM_{010} mode was around 2.43 GHz between 300 °K and 30°K. The lower resonance frequency measured in the cavity than the calculated showed that the cavity should have the inner diameter larger than the ring's one effectively. The lower resonance frequency than the expected one mainly came from the bad contact between the ring and discs, and imperfect diffusion of the brazing agents, and roughness of the bonding surface around the inner edge of the ring.

As shown in fig.2, experimental set up used in the present work consists of a large cryostat, a He-gas closed loop refrigerator, a magnetic-suspended turbomolecular pumping system, and the vector network analyzer system. Q_{loaded} was measured with RF couplers critically adjusted at each temperature. $Q_{unloaded}$ was found to be dependent on input RF power to a small extent. $Q_{unloaded}$ is small and weakly temperature dependent between 300 °K and 100 °K, attaining a value of about a thousand at 100 °K. A sharp increase is observed as the cavity is cooled down below 92 °K. Q_{loaded}

increases steadily attaining a value of about 10^5 around 70 °K. The Qloaded increase appears to slow down at lower temperatures, below 70 °K. The Qloaded reached well over

Experimental Setup

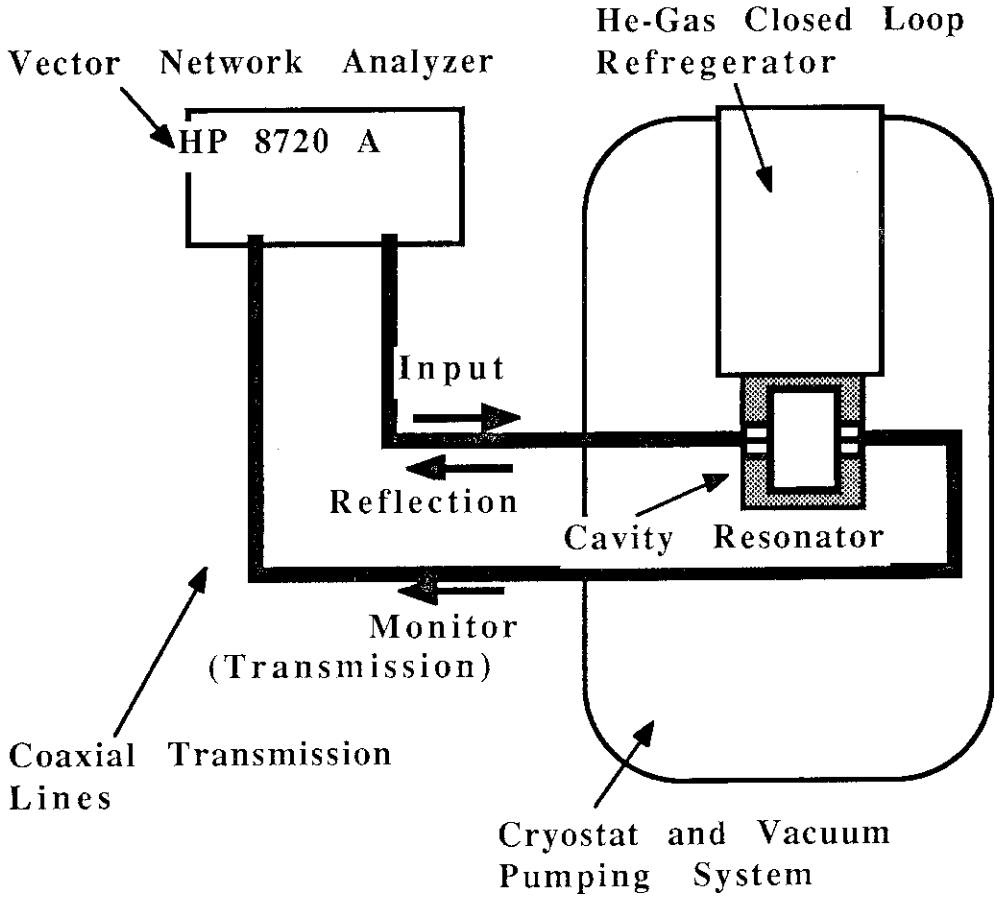

Fig. 2 Experimental set up.

10^6 at 15 °K - 30 °K. Typical frequency scan of the network analyzer at 30 °K shows a quite symmetric Lorentizan pattern with the resonance frequency of 2.856 GHz and Q~>several x 10^6 after some optimization and conditioning of the cavity resonator.

RF measurements for single crystal $YBa_2Cu_3O_{7-\delta}$ samples[3] showed that the surface resistances were nearly the same as the Nb ones. Although we should expect a Q factor of 10^{10} or even

more from the theoretical consideration applying a conventional BCS theory, the Q factors for the single-phased and bulk $YBa_2Cu_3O_{7-\delta}$ cavity of the several orders of magnitude less than the expected theoretically could be obtained in the present work. The lesser Q factors than the theoretical consideration are thought to have some origins in the weak links of the grain boundary, surface roughness, impurities and so on. However, the detailed mechanism is not clear at the present because there is no standard theory for the high Tc superconductors. And, we could not point out here what the major origins are for the large Q factor difference. The Q factor of the cavity may be improved by materials processing because the lesser Q factor is not inherent in $YBa_2Cu_3O_{7-\delta}$ materials[3].

References

1) J. G. Bednorz and K. A. Muller : Z. Phys. B64(1986)189.

2) E. Minehara : Proc. 6th Symp. on Accelerator Science and Technology, Tokyo(IONICS Publishing Co. Ltd., Tokyo (1987)p.178.

3) H. Padamsee, K. Green, J. Gruschus, J. Kirchgessner, D. Moffat, D. L.Rubin, J. Sears, Q. S. Shu, R. Buhman, D. Lathrop, T. W. Noh, S.Russek, and A. Sievers: CLNS 88/835 (Cornel University, Ithaca, 1988), and also Proc.Conference on Superconductivity and Applications, Buffalo, NY 14620, April 18-20, 1988, (to be published).

4) E. Minehara, R. Nagai, and M. Takeuchi : Jpn. J. Appl. Phys. Vol.28,No.1, January, 1989, pp. L100-L101.

5) J. J. Bautista and S. M. Petty: IEEE Trans. Magn. MAGN-21(1985)640.

6) S. Thakur, D. M. Strayer, G. J. Dick, and J. E. Mercereau: J. Appl. Phys.59(1986)854.

Title of Contents

Fabrication and RF Properties of the S-band TM010 Microwave Cavity Made of $YBa_2Cu_3O_{7-\delta}$

Publication List

Journal/Proceedings

Minehara,E.

RF Properties of High Tc Superconductor Prepared by Plasma-Spray Painting Method.

Extended Abstracts of 5th International Workshop on Future Electron Devices/Topical Meeting on High Temperature Superconducting Electron Devices.

June 2-4th,1988,Miyagi-Zao,Japan

Minehara,E., Nagai,R., and Takeuchi,M.

Plasma Spray Painting for Metal Oxide High Tc Superconductors,

Proceeding of Surface Engineering International Conference,

Oct.18-Oct.22, 1988, Tokyo, Japan.

Minehara,E., Nagai,R., and Takeuchi,M.

The TM_{010} Microwave Cavity Made of $YBa_2Cu_3O_{7-\delta}$

Jpn. J. Appl. Phys.Vol.28,No.1, January, 1989, pp. L100-L101.

Minehara,E., Nagai,R., and Takeuchi,M.

RF Properties of High Tc Superconducting Microwave Elements Fabricated by Plasma-Spray Painting, and Bulk-Material Machining Methods

J.Electrochem.Soc.,Vol.136,No.4, p.239C April 1989,

Minehara,E., Nagai,R., and Takeuchi,M.

Quality Factor Performance for the S-band TM_{010} Microwave Cavity Made of $YBa_2Cu_3O_{7-\delta}$.

to be published.

Scientific Meetings

Spring Meeting of the Japan Physical Society

Minehara,E., Nagai,R., and Takeuchi,M.

Fabrication and RF Properties for High Tc Superconducting Waveguide,Coaxial Cable, and Cavity Resonator made of $YBa_2Cu_3O_{7-\delta}$.(Mar.28-31,1989,Hiratsuka)

Autumn Meeting of the Japan Physical Society

Minehara,E., Nagai,R., and Takeuchi,M.

High Tc Superconducting Magnetic Shield for Nb Superconducting Cavity Resonator.(Oct.3-6,1988, Matsuyama)

Spring Meeting of the Japan Society of Applied Physics and Related Societies

Minehara,E.,Obana,H., Nagai,R., and Takeuchi,M.

Fabrication of High Tc Superconductor utilizing Oxygen Gas Plasma Spray Painting with Aqueous Spraying Materials.(Apr.1-4,1989,Chiba)

Autumn Meeting of the Japan Society of Applied Physics and Related Societies

Nagai,R., Shimoizumi,M., Takeuchi,M., and Minehara,E.

Fabrication of High Tc Superconductor utilizing Oxygen Gas Plasma Spray Painting Method.(Oct.4-7,1988, Toyama)

The 13th Linear Accelerator Meeting in Japan

Minehara,E., Nagai,R., and Takeuchi,M.

Possible Application of High Tc Superconductors to Accelerator Components.(Sep.7-9th,1988, Tsukuba)

1.14 DATA ORIENTED PROGRAMMING USING LSSOLVER

Masayoshi SUGIMOTO

Department of Physics, JAERI

The LSSolver program for PC was originally developed to support nuclear data evaluation study and was designed to allow users to employ the Data Oriented programming style for solving the least squares fitting problems. Now it is extended to handle more general problems including the design study of the free electron laser.

Introduction

The LSSolver program[1] written in Pascal was originally developed by the author as a support tool of the nuclear data evaluation study using IBM-PC, which has a spreadsheet-like user interface and a capability of representing the results graphically without programming. The specific feature of the LSSolver is the full adaptation of the data and the parameter covariances in the least squares fitting procedure, which was formulated by Smith[2]. Recently, the LSSolver is totally rewritten to include a lot of functions and is implemented to NEC-PC9800 series, too. The LSSolver has an interpreter to parse the input stream and to execute the meaningful sentence. This sounds like as BASIC, but its uniqueness is in the "Data Oriented" programming style. The Data Oriented programming means that users define the source data first and process them to produce new data, step by step, by applying a series of operations. Since these operations are embedded as the formula to define the data (or equivalently saying, the message passed to the data) and they do not appear explicitly, only the resulting data take the main role in the programming process.

The spreadsheet-like user interface lets users to modify any data in the cells of the spreadsheet and recalculate the whole data, easily. Such trials confirm the correctness of the data processing method and give us the inspection for sensitivity of the parametric data. The new program, LSSolver ver.2, is based on the same philosophy as LSSolver ver.1, but it has much more functions than ver. 1, explained below. It is intended to be used as a general purpose application program. Currently, it is used as a support tool of the design study of the free electron laser, and such

an application is described as an example of usage.

Features

(1) User interface: A spreadsheet contains cells in a matrix of 100 columns by 100 rows, however the dimensional size can be changed according to the system memory size. Any data in each cell is entered from the keyboard or from the disk files. A command to edit a cell or to insert/delete/copy/move column or row, etc..., is invoked by pressing '/' key and selecting a highlighted character in a main menu line. Some commands have sub menus and users can select a highlighted command character in a sub menu.

(2) Data types: Each cell has an attribute corresponds to one of the data types: text, value, formula, vector, matrix and macro. The text data can contain a text string up to 255 characters. The value data represents a real number. The formula data contains the formula to define the cell value and the calculated value. The vector and matrix data represent the vector and matrix of real numbers, respectively, and can also contain the formula to calculate the elements, optionally. The macro data has a string that contains commands and their arguments to perform a series of operations to the spreadsheet and cells, just like as the command string input from the keyboard.

(3) Formula: Users can use conventional arithmetic operators (+,-,*,/,^), arithmetic functions (exp,log,sin,cos,arcsin,sinh,Legendre/Bessel functions,random number generators,...) and vector/matrix operations (multiply,transpose,inverse,...) in a formula to define data. The least squares fitting, numerical differentiation / integration and interpolation are implemented as a special function. If the data cell is given by the formula, such a cell will be recalculated when some other cell values are changed. The recalculation of each cell can be controlled by setting the dependency flag assigned to cell by cell.

(4) Graphics: The vector or matrix data can be displayed graphically as many styles of plots: histogram, X-Y plot, two-dimensional surface, contour, three-dimensional histogram and scattered plot.

(5) Subprocess: There are two paths to execute other programs from the LSSolver: one is the creation of the subprocess without destroying the current memory status used by the LSSolver, and the other is the chaining of the batch processes which execute LSSolver and other program in turn.

Using either method, an arbitrary program which accepts the input data in the spreadsheet and returns some data to a cell of the spreadsheet, can be done externally.

Application to FEL gain calculation

Fig.1 shows the example of the listing of the spreadsheet, which calculates the gain parameters of free electron laser. The cells from A2 to A5 defines the parameters of the undulator magnet, and A6 is the K parameter of the linear undulator constructed from permanent magnets, whereas A7 is calculated by assuming the electromagnetic undulator. Cells between A8 and A12 define the beam condition. A14 and A15 are the fundamental resonant wavelength, λ_0, and it is 9.95 μm in this parameter setting. The criterion value shown at the cell D17 is much less than one, so in this case the free electron laser is operated in the low gain Compton regime, and the small-signal gain formula can be applied. Cells from A20 to A24 calculate the gain, which depends on the detuning parameter, ν.

Fig.2 is the X-Y plot of the detuning parameter(cell A21) vs the calculated gain(cell A24). Positive detuning means smaller angular frequency (or larger wavelength) than resonant frequency, ω_0, so the figure shows the well-known fact that the maximum small-signal gain can be achieved at ν = 2.6.

Summary

The new programming style, Data Oriented programming, using the LSSolver program is proposed to get the solution of the least squares fitting and other problems and to inspect the sensitivity of the calculated results to many driving parameters, quickly and easily. Though this method has been applied to the design study of the free electron laser successfully, it could be also used in the other fields widely.

References

1) M. Sugimoto, "LSSOLVER" ver.1 manual, unpublished.
2) D.L. Smith, Argonne National Laboratory, personal communication.

```
      A          B          C          D          E          F          G
 1  undulator definitions << cgs unit >>              0.51= rest mass of elect
 2        3.56= period(cm)      0.50= drift part 3.0E+0010= c , light speed(cm
 3       75.00= no of periods                    7.3E-0003= fine structure con
 4      267.00= total length(cm)                 2.8E-0013= classical electron
 5        2.67= Mag.fld(kG      1.34=avg mag fld 1.6E-0019= charge of electron
 6        0.63= K , undulator parameter (permanent magnet)
 7        0.57= K , undulator parameter (electromagnet)
 8       25.00= E , electron energy (MeV)          49.93   = gamma     42.29
 9       15.00= I , beam current (Ampere)       2.5E+0010= number density of
10        0.13= beam cross section (cm**2)
11        0.13= radiation cross section (cm**2)
12        0.97= filling factor = (beam c.s.)/(radiation c.s.)
13  fundamental wavelength     freq.            wavenumber
14    99537.74  (angstrom) 1.9E+0014   (rad/sec)   6312.36= k (1/cm)
15        9.95   (micro m)      1.33(% line width)
16   8.9E+0009= beam plasma frequency(rad/sec)   8.8E-0004= Budker's 1.8E-0005
17   2.0E-0004= k beam (1/cm)        2.928E-0003= ((k beam)*(total length))^2
18                                   low gain Compton regime when above value
19  Low Gain Compton Regime --- gain calculation
20   2.4E-0007= gain(factor)         5.940E-0008          7.1E-0003=amplitude
21  [100]=(#-5= detuning param      [100]=(1-A21= ang.freq 5.4E-0009=(Pierce p
22  [100]=SQR(= (sin(nu/2)/(nu/2))^2                              1.14=Gmax(Krin
23  [100]=DIFF=d( above ) / d(nu)   [100]=DIFF3([100]=DIFF= d^3( above ) / d(n
24  [100]=-A20= gain (Datt[100]=-A20[100]=A24+C2= gain (Sprangle)
25
```

Fig.1 An example of the listing of the spreadsheet calculating the gain of the free electron laser.

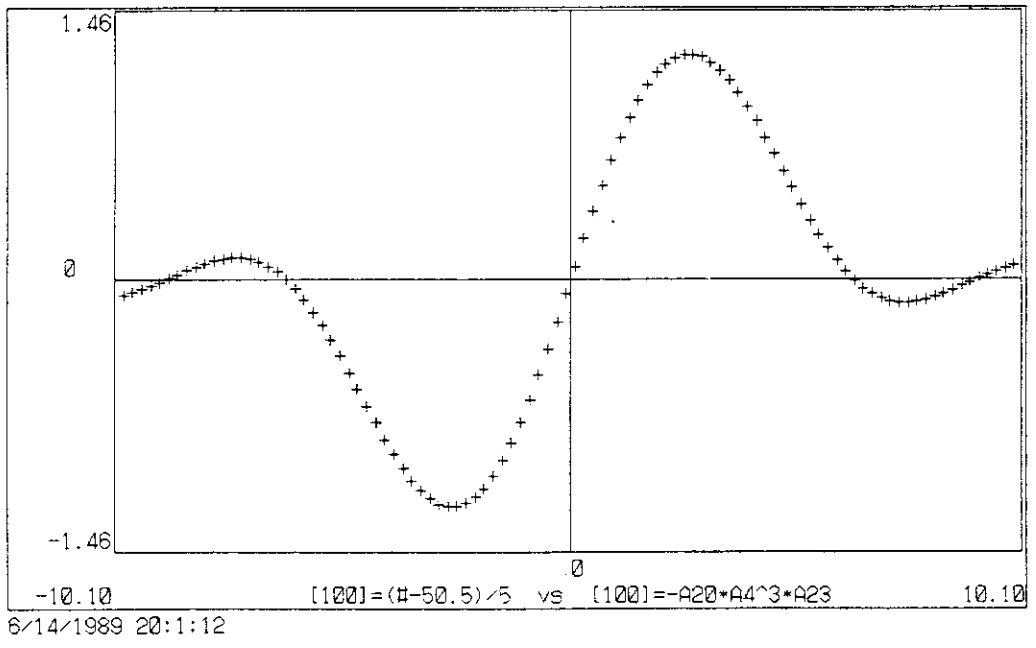

Fig.2 Graphical plot of the detuning paramter vs small-signal gain calculated in the spreadsheet shown in Fig.1.

1.15 FORTH-NODAL PREPARATIVE: IMPLEMENTATION OF A FORTH MONITOR NUCLEUS INTO A 16-BIT PC

Yuuki KAWARASAKI

Department of Physics, JAERI

A Forth monitor nucleus has been transported into a 16-bit personal computer(PC) from an original 8-bit PC's by rewriting primitive words only, for aiming at the construction of an interactive and distributed multi-computer control system.

A typical test example of execution speed is demonstrated, yielding in an encouraging result.

Further expansion, including real-number arithmetics, multi-segment programming and network configuration is briefly discussed.

Introduction

There are many ways how to construct computer-based control and/or data-logging systems: in hardware configurations and in sorts of software implemented herein. In these applications, a somewhat different feature may reasonably be adequate from ordinary environments, from the viewpoints of high-speed execution and programming flexibility which includes the system expandability.

A distributed multi-computer system, typically like NODAL systems/1/, has already been proven the effectiveness. A PC-and-intelligent CAMC system/2/ or a linked single-board-computer (SBCs) system/3/ eventually formed themselves a simplest distributed system.

An interactive programming environment can be provided by use of an interpreter language instead of compiler languages: in NODAL, the BASIC-like interpreter is used. However, the execution speed of the task written in the above is not sufficient. FORTH /4,5/ is then expected to overcome the deficiency of the speed, keeping other kinds of distinctive characteristics; self-producing, as a Forth system can be

described in Forth itself, (high expandability) and both in low level like an assembler and in high level (high productivity).

In addition, a Forth system is simple and then it can rather easily be assembled. This situation allows births of many dialects of Forth, just like LISP. NEON used in well known APPLE's MacIntoshs and STOIC in rumor in EPSON's are also one of the dialects.

Forth Monitor

The structure of the monitor is basically the same as the 8-bit PC's, whose MPU is Z-80/2,3/. The transportation into the 16-bit PC's, whose MPU is 8086 or equivalent, has been performed by rewriting only the kernel, in which several tens primitive words have been assembled. A 8086 has been naturally developed from a 8085, similar to a Z-80. A 32-bit 80386 is then similarily developed from a 8068. Some words in the 8086's can be assembled more compact than in the Z-80's. Newly prepared words are due to the differences between the hardwares.

Speed Test Example

At present, only integer arithmetics is available in the developing Forth system. A heart of a sample program written in BASIC is then chosen as/6/:

```
250 FOR N=1 TO 399
260 Y(0)=(X(0)+X(399)) MOD 2
270 PSET(0,N),Y(0)
280 FOR I=1 TO 399
290 Y(I)=(X(I)+X(I-1)) MOD 2
300 PSET(1,N),Y(1)
310 NEXT I
320 FOR I=0 TO 399
330 X(I)=Y(I)
340 NEXT I
350 NEXT N
```

The program cited is a kind of cellar automaton; a model of self-producing machines.

The above BASIC program can be converted in Forth program:

```
( Y-X      B400H B000H 400H MOVE )
( AUTOS    400 1 do i B* B000H + DUP @ SWAP B- @ + 2 /
           DROP DUP i B* B400H + ! B800H @ i PSET loop )
( AUTO     B002H SET1 , 400 1 do B000H @ B31EH @ + 2 /
           DROP DUP B400H ! i DUP B800H ! 0 PSET AUTOS Y-X loop )
```

where Y-X corresponds to lines 320-340 in BASIC'S, AUTOS to lines 280-310 and AUTO to 250-350, including AUTOS and Y-X, respectively.

In Forth, each sentenc, newly compiled task, is immediately executable and able to be, in its characteristic, sub-routinized in proceeding sentnce compilation; X-Y, AUTOS and AUTO can run quite independently. B400H and B000H are variable areas for X(I) and Y(I) in BASIC's, respectively, being represented directly in the absolute addresses in a hexadecimal expression.

The following lists the execution times in three kinds of programming language on NEC PC-9801 vm (10 MHz).

1.	BASIC	N88-original	17:21. (min:sec.XX)
2.	BASIC	on MS-DOS	18:38.
3.	BASIC	MS'-compiled	6:22.
4.	MS-Fortran		1:22.
5.	FORTH	listed	1:05.
6.	FORTH	tuned-up(1)	0:48.3
7.	FORTH	tuned-up(2)	0:28.6

In the tuned-up(1), separate primitive words are concatenated together, compound primitive words; "i B*" to "iB*", " + DUP @ SWAP B- @ +" to " +D+ " and " 2 / DROP DUP" to "MOD2D", respectivrly. In the tuned-up(2), PSET in the BASIC's original subroutines is replaced by newly prepared one.

Discussion and Conclusion

The table can be interpreted as:

1) Even the same program runs in a different speed: the OSs can not always offer the environment where a task can run fast, while the BASIC monitor can do.

2) A compiled task of BASIC can run faster only by three time.

3) A fortran compiled task, faster than BASIC's roughly by 10 time.

4) Forth one of the case, faster than the Fortran's.

5) Tuning-up technique, a kind of prototyping/7/, is proved as effective one.

For real-number arithmetic, a numeric data processor, NDP, e.g., 8087/8/ for 8086, can effectively be incorporated in the system. The NDP has the architecture of 8 80-bit stack registers, which is thus the most suited to Forth's function, because Forth functionally operates through the stack; popping data up and pushing data down. New primitive words for NDP's operation can, therefore, be prepared more directly than for MPU's.

The directly addressing range of 8086's is intrinsically limited to 64 kilo-bytes; this leads to the introduction of the segment. Thus the multi-segment programming will in its structure become resemble to that of multi-computer's, as in NODAL.

For a distributed control system, a star-like network may be better than a loop's, because the system has, a priori, to be in a definite hierarchy.

The author thanks M.Mizumoto for his collaboration of the measurement of the execution speed in the cases of 2., 3. and 4.

References

1) M.C.Crowley-Milling and G.C.Shering: CERN 78-07

2) Y.Kawarasaki: JAERI-M 86-112, p25

3) Y.Kawarasaki: Proc. 10-th LINAC MEETING, p.19

4) Trademark of FORTH Inc.,

5) Y.Kawarasaki: Proc. 1-st Workshop on Control Systems, KEK Report 87-25, p.106

6) H. Takayasu:"Fractal",p.110, Asakura Publishing Co.

7) M. Arisawa:"Software Prototyping", Kindai-Kagaku Sha.

8) J.F.Palmer and S.P.Morse:"The 8087 Primer",John Wiley & Sons, Inc., New York

Ⅱ ATOMIC PHYSICS AND CHEMISTRY

2.1 HIGH-RESOLUTION ZERO-DEGREE ELECTRON SPECTROSCOPY (I)

Kiyoshi KAWATSURA, Masao SATAKA, Hiroshi NARAMOTO, Yohta NAKAI, Yasunori YAMAZAKI[*], Ken-ichiro KOMAKI[*], Kenro KUROKI[*], Fuminori FUJIMOTO[**], Yasuyuki KANAI[***], Tadashi KAMBARA[***], Yohko AWAYA[***] and Nikolaus STOLTERFOHT[****]

Department of Physics, JAERI, [*]College of Arts and Sciences, University of Tokyo, [**]The Institute of Scientific and Industrial Research, Osaka University, [***]The Institute of Physical and Chemical Research, [****]Hahn-Meitner Institute, Berlin, Federal Republic of Germany

Introduction

A great deal of attention has been paid to measurements of secondary and Auger electrons ejected in ion-atom collisions. High resolution studies have primarily been devoted to Auger electrons emitted from the target atom. Zero-degree electron spectroscopy was used to measure convoy or cusp electrons emitted during ion-atom interactions.

Recently, the method of zero-degree spectroscopy was applied to projectile Auger electrons reducing the kinematic broadening effects.[1] At zero-degree observation angle of the electrons, the broadening effects cancel in first order.

In this work, we applied the method of zero-degree electron spectroscopy for fast ion-atom collisions. We measured high-resolution L-Auger spectra of S^{5+} excited in collisions with He at an incident energy of 64 MeV. This method is well suited to avoid Doppler broadening effects normally causing problems in fast ion spectroscopy. The light target atom He and the relatively high energy projectile were chosen to establish the conditions for "needle excitation" i.e. the excitation of the inner-shell electron without disturbing the outer shell electron.[2]

Experiment

The experiments to measure Auger electrons in ion-atom collisions were performed using electrostatic spectrometer inside a high vacuum scattering chamber at H2-2 beam line. The experimental setup is shown schematically

in Fig. 1. Projectiles of 64-MeV S^{5+} were provided by the tandem accelerator facility at JAERI in Tokai. A beam of ions is carefully collimated to about 1.5 mm in diameter to avoid edge scattering, and directed into the scattering chamber and the target gas cell. The typical beam currents of 100 nA were collected in the Faraday cup, which was used for normalization of spectra.

Auger electrons were measured by a tandem-type electron spectrometer which was composed of two consecutive 45^0 parallel-plate electrostatic analyzers.[1] The first device was used as a deflector to steer the electrons out of the ion beam, and the second as an analyzer to determine the electron energy with high resolution. To improve the electron energy-resolution, the deflected electrons were decelerated in the region between two grids in front of the analyzer to 50 eV by a retarding electric field. In the experiments, a typical resolution achieved was $\Delta E/E = 10^{-3}$ full width at half maximum (FWHM). This resolution was sufficient to resolve individual Auger lines.

Results and discussion

In Fig. 2 an example is shown for a low-resolution secondary electron spectrum observed at zero degree. The spectrum is obtained using 64 MeV S^{5+} projectiles incident on a He-gas target. The dominating peak at 1.08 keV (cusp) is due to electron loss to the continuum (ELC), whereas the low- and high-energy peaks in the vicinity of the cusp originate from the ejection of projectile Auger electrons emitted at 180^0 and 0^0 in the projectile frame, respectively.

In the experiments, the velocity of the projectiles is greater than that of the Auger electrons in the projectile frame. Therefore, electrons emitted with an energy E' in the projectile frame are observed at 0^0 in the laboratory frame at two different energies

$$E_{H,L} = (t_p^{1/2} \pm E'^{1/2})^2, \qquad (1)$$

where the signs + and - correspond to emission angles of 0^0 and 180^0 in the projectile rest frame, respectively. The quantity $t_p = T_p m/M$ is the projectile energy T_p scaled by the electron to projectile mass ratio. The Auger electron spectra observed in the laboratory frame were transformed to the projectile rest frame by using the following relation for the doubly

differential cross section,

$$\frac{d\sigma'}{dE'd\Omega'} = \left(\frac{E'}{E}\right)^{1/2} \frac{d\sigma}{dEd\Omega} .$$

A part of high-resolution Auger spectrum is given in Fig. 3. This spectrum corresponds to the high-energy (E_H) Auger electrons, which were ejected to the angle of 0^0 in the projectile rest frame. The spectrum shows lines groups attributed to configuration $1s^2 2s^2 2p^5 3s3l$ where l=0,1 and 2. As expected the most intense group is attributed to the configuration $1s^2 2s^2 2p^5 3s3d$ due to the dipole transition 2p → 3d. The group due to the quadrupole transition 2p → 3p is also found to be rather significant. The peak group at lowest energy clearly shows that the two lines were produced by the $2p_{1/2}$- $2p_{3/2}$ fine-structure splitting. However, it is seen that each group of the whole spectrum exhibits individual lines whose identification requires further theoretical work involving atomic structure calculations.

References

1) A. Itoh, T. Schneider, G. Schiwietz, Z. Roller, H. Platten, G. Nolte, D. Schneider and N. Stolterfoht: J. Phys. B 16 (1983) 3965.

2) N. Stolterfoht: Phys. Reports 146 (1987) 315.

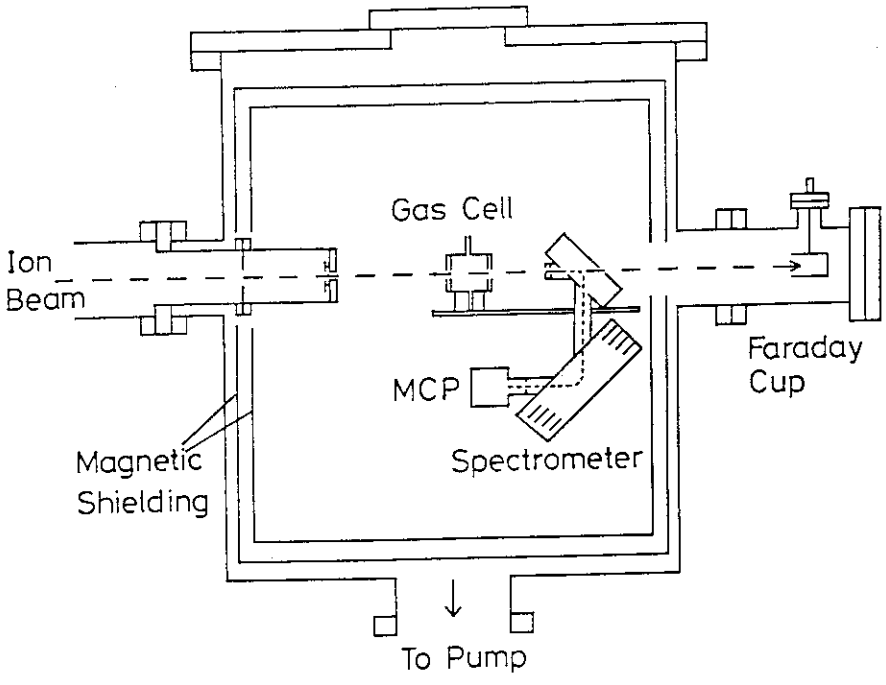

Fig.1 Experimental setup showing the target-gas cell and tandem-type electron spectrometer.

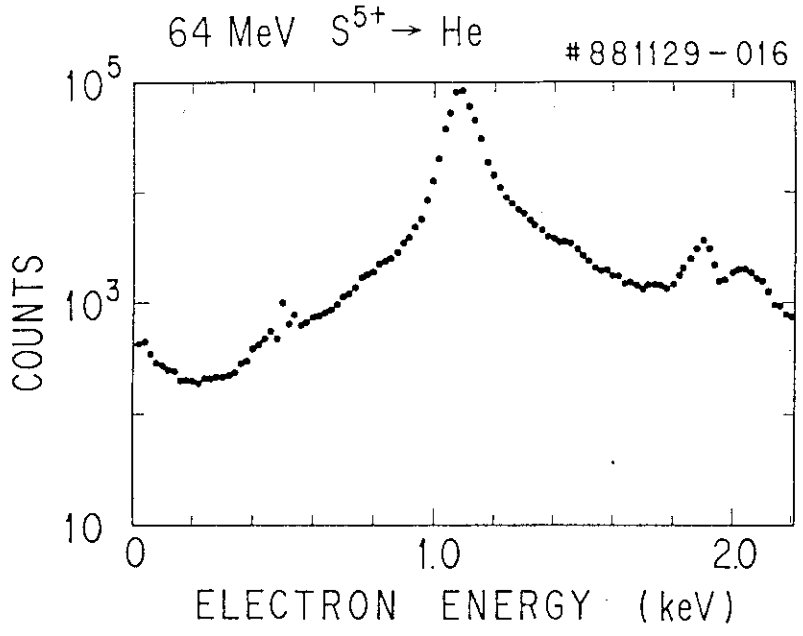

Fig.2 Low-resolution electron spectrum from 64-MeV S^{5+} + He collisions.

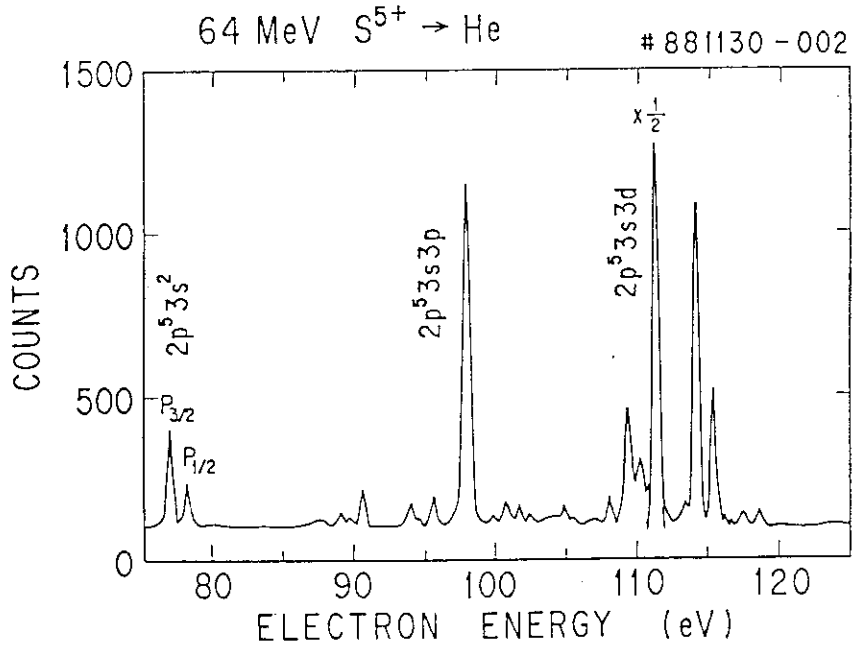

Fig.3 High-resolution L-Auger spectrum.

2.2 ION CHANNELING SPECTROSCOPY OF SINGLE CRYSTAL AUSTENITIC STAINLESS STEEL

Tohru MITAMURA*, Kiyoshi KAWATSURA, Keiji KOTERAZAWA*,
Hajime IWASAKI*, Yohta NAKAI and Mititaka TERASAWA*

Department of Physics, JAERI
*Faculty of Engeneering, Himeji Institute of Technology

Radiation effect on lattice structure of single crystal austenitic stainless steel SUS310S under He^+ ion bombardment was studied by a method of ion channeling spectroscopy. K X-rays of the constituent elements induced by the He^+ ions as well as Rutherford back-scattered He^+ ions were measured. From the analysis of the K X-ray spectra obtained, the lattice position of the alloying and impurity atoms and their disordering caused by the He^+ irradiation were investigated. It was found that the impurity atom P is situated at the octahedral site of the fcc crystal and it tends to displace from the site under the irradiations of the energetic He^+ ion beams.

1. Introduction

Radiation damage in the materials caused by energetic neutron bombardments is one of the most important items to be fully understood in nuclear reactor material development. It has been known that, during irradiation of energetic electrons or neutrons, the impurity or alloying atoms such as P or Si of the austenitic stainless steels move and concentrate to the sites of grain boundaries and that this phenomenon of so-called radiation induced segregation never ocurrs under only thermal condition.[1,2)]

The present investigation was intended to make clear the fundamental process of radiation damage by means of ion beam analysis method. Single crystal austenitic stainless steel SUS310S was chosen as a specimen. Location of the impurity or alloying atoms in the fcc lattice structure of the single crystal was studied as well as the mechanism and process of their displacements through the crystal lattice under energetic He^+ ion beam irradiations. The He^+ ion induced characteristic X-rays of alloying and impurity elements were measured as a function of angle around the

<110>, <100> or <111> crystal axis and analyzed.

2.Experimental method

A single crystal rod of austenitic stainless steel SUS310S was prepared by the Bridgeman method. The specimens with the surface plane to be normal to the <110>, <100> and <111> crystal axis, respectively, were cut out from the rod.

He^+ ions with an energy of 1.7 MeV accelerated by the 2 MV Van de Graaff accelerator of JAERI were bombarded at room temperature to a specimen, which was mounted on a three-axis goniometer and tilted for varying crystal orientation. The yields of He^+ ion induced characteristic X-rays emitted from the specimen were measured as a function of the tilted angle through a crystal axis. A 30 mm^2 x 3 mm thick Si(Li) detector with 15 μm thick beryllium window was used for the X-ray detection. After about 10 hours irradiation of 1.7 MeV and 0.8 MeV He^+ ions, the irradiation effect on the crystal structure was evaluated. Rutherford backscattering (RBS) measurement was supplementally performed with a solid state detector.

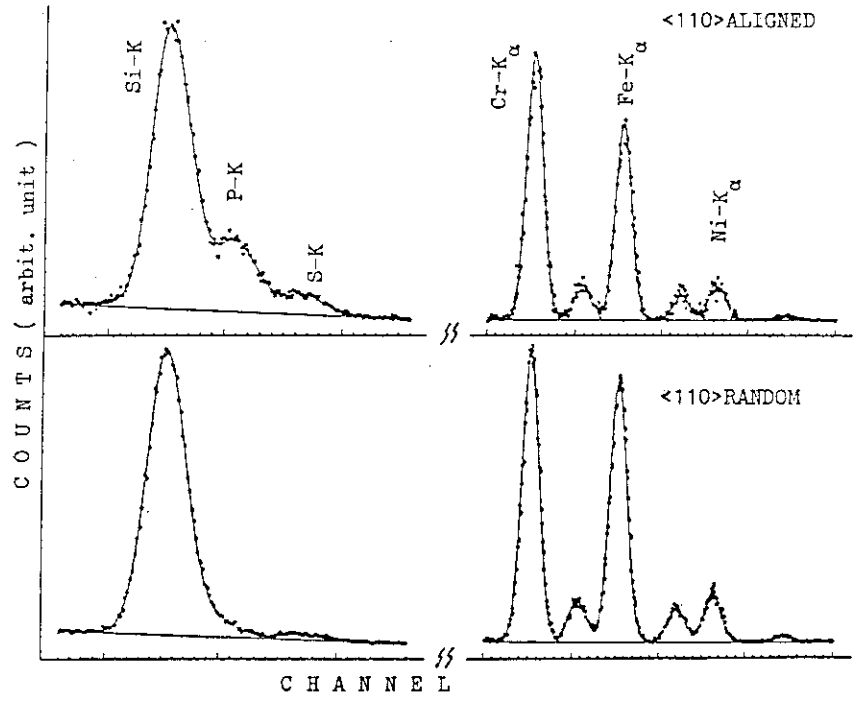

Fig.1 Aligned(<110>) and random spectra characteristic X-rays induced by 1.7 MeV He^+ ion irradiations.

3. Results

Fig.1 shows examples of the X-ray spectra obtained in the observation of the virgin specimen with <110> axis. The upper one was in the case that the He^+ ion beams was incident to the surface place in alignment with <110> crystal axis, while the lower one in the case that the He^+ ion beam was incident at an angle of 2.2 off the aligned direction. K X-ray peak of P atom is clearly seen in the "aligned" spectrum. No visible peak could found in aligned spectra of <100> and <111> specimens. By computer spectral analysis, it is found that, only in the <110> specimen, the K X-ray yields curve (dip curve) of P atom has a rise when the ion beams align with the crystal axis.

In order to see the degree of radiation damages, the specimen was bombarded by 1.7 MeV He^+ ions in random direction up to a fluence of 1.27×10^{18} ion/cm^2 and, then, 0.8 MeV He^+ ions up to 2.0×10^{16} ion/cm^2. Fig.2 shows the variations of K X-ray yield for each element as a function of He^+ ion fluence. The K X-ray yield of the impurity atom, P, decreases with He^+ ion fluence and those of other elements increase. The Ni and Si X-ray yields are larger than other X-rays.

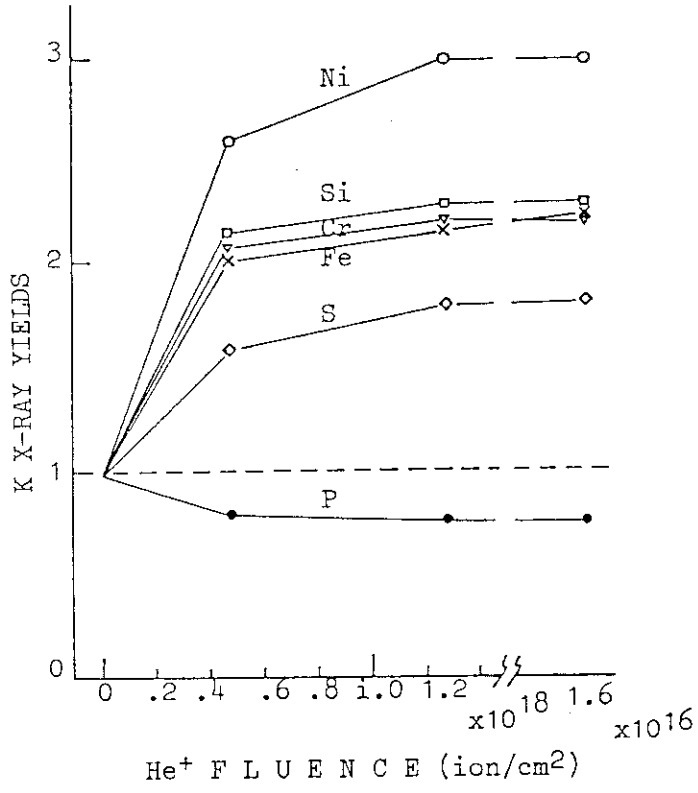

Fig.2 K X-ray yields as a function of the He^+ ion fluence.

Changes of full width at half maximum, 2Ψ, and minimum yield, χ_{min}, of the dip curve were analized as a function of He^+ ion fluence. Value of 2Ψ in the case of major alloying elements, Ni+Fe+Cr, gradually decreased from 1.3 to 0.9 with increasing 1.7 MeV He^+ fluence and sharply decreased to 0.4 after 0.8MeV He^+ ion bonbardment. The χ_{min} value increased from 0.2 to 0.4. In the Si dip curve, similar tendensies were observed.

4.Discussions

Assuming that the P atom locates at the octahedral site of the fcc structure, the K X-ray yield from the P atoms will be prominent in the case of <110> axis channeling, and, in both cases of <100> and <111> axis channeling, P atoms will be shadowed by lattice elements and hence K X-ray yields will not be expected. And K X-ray yield in <110> axis channeling will be decrease. The present observation might be an evidence of this speculation. As He^+ bombardments, P atoms move through the crystal lattice

According to the theoretical calculation for the 1.7 MeV He^+ ion irradiation of total amount of 1.27×10^{18} ion/cm^2, the dpa at the surface is 0.91 and the maximum dpa is 35 at a depth of 2.6 μm (near He range). In the 0.8 MeV He^+ ion irradiation of the amount of 2.0×10^{16} ion/cm^2, the surface dpa is 0.02 and the maximum dpa is 0.47 at a depth of 1.3 μm [3]. As an X-ray excitation cross section strongly depends on the He^+ ion energy, the 1.7 MeV He^+ ion induced X-ray yields will be insensitive to damages at a depth of 2.6 μm where the dpa value is very high. The larger decrease of 2ψ value after 0.8MeV He^+ ion iradiation may be due to damages produced by the He irradiation at a depth of 1.3 μm.

It should be noticed that the X-ray yields increase especially in Ni and Si which have been pointed out to be the atoms which tend to show radiation induced segregation. Decrease of K X-ray yield of P atoms suggests that P atoms displace from initial lattice location site.

Acknowlegements

The authors would like to thank to Dr.T.Aruga for providing dpa calculation data obtained using his revised computer program code prior to publication.

References

1)K.Fukuya, S.Nakahigashi and M.Terasawa,Scripta Metal.,19(1985)959.

2)K.Fukuya, S.Nakahigashi, S.Ozaki, M.Terasawa and S.Shima: Enviromental Degradation of Materials in Nuclear Power Systems Water Reactors, ed. by G.J.Theus and J.R.Weeks (The Metallurgical Society,1988) P.665.

3)T.Aruga, private communication.

2.3 PERTURBED ANGULAR CORRELATION MEASUREMENT USING Pd-100/Rh-100 NUCLEAR PROBES

Hiroshi NARAMOTO, Yukio KAZUMATA, Masumi OHSHIMA, Masao SATAKA, Kiyoshi KAWATSURA, Yohta NAKAI, Sadae YAMAGUCHI*, Shinji NAGATA* and Yutaka FUJINO**

Department of Physics, JAERI, *Institute for Materials Research, Tohoku University, **Faculty of Engineering, Tohoku University

1. Introduction

In the course of materials analysis, the interaction of energetic ions with atoms in solids gives us fruitful information about the microstructure of atomic arrangement. The ion beam analysis[1] using such as Rutherford backscattering, nuclear reactions and inner-shell excitation combined with channeling can locate the the relevant atoms in the real space, crystallographically. The information obtained is direct and the elaborate process for data-handling is not necessary. But the results are the averaged ones in their nature, and it is difficult to extract the information about the distribution of the occupation of the relevant atoms. The specroscopic analysis is the counter part of the ion beam analysis mentioned above.

Since the finding of the alloy-effect on the lattice location of deuterium atoms in the bcc niobium crystal lattice using the ion beam analysis [2], we have developed the measurement system for the spectroscopic analysis like Mössbauer spectroscopy and time differrential perturbed angular correlation measurement(TDPAC). For the study about the alloy effect, are chosen the two kinds of unstable nuclear probes such as Pd-100/Rh-100 and In-111/Cd-111 which are expected to be smaller and larger in the atomic radii compared with niobium atoms, respectively. Here in this report, the recent development of the system for TDPAC measurement is described.

2. Recoil implantation procedure

In this study, we started with the TDPAC measurement using Pd-100/Rh-100 nuclei. These nuclei were introduced into various kinds of samples through recoil implantation after nuclear fusion reaction between incident 100 MeV C-12 ions and Nb-93 atoms in the thin foil target. Judging from the excitation function and the recoil energy, Nb foils with 4 micron thickness

were prepared and the best efficiency of recoil implantation was assured. Nb samples implanted at high and low temperature were prepared for a comparison of irradiation-induced effect. We used 0.5∿1.0 μA of 100 MeV C^{6+} ion beam, and the ion beam was scanned two-dimensionally in the case of recoil implantation into the specimens with low melting point even if the substrate of specimens was cooled down to about 120 K. The reasonable radioactivity of probe nuclei was obtained after 12 hour irradiation. During the irradiation, the two-dimensional temperature distribution was measured under the in-beam condition using the detecting system of infrared light emission.

3.Experimental procedure and results

The 84-75 keV(gamma-gamma)casdade in Rh-100 is ones of the favourable examples for TDPAC measurement. The intermediate state at 75 keV, with a half life of 215 nsec, magnetic moment(u)=+4.324(8)[3] and the quadrupole moment(Q)=0.076(20)b[4] make Rh-100 an excellent probe for the study of magnectic and electric quadrupole interactions even in the materials system such as metal hydrides and oxide superconductors. TDPAC measurement is performed using four NaI detectors arranged perpendicularly with each other, where the coincidence procedure is controled by a personal computer, and the gated spectra are obtained directly. 6 gated time spectra are recorded simultaneously, and about 30 hour measurement is necessary for the good statistics.

In the induced gamma-ray spectrum from Nb foil irradiated with 100 MeV C-12 ions, most of the photo peaks can be attributed to only the decay of Pd-100/Rh-100 probe nuclei, and no interference effect is found in the spectrum. Fig. 1 shows the induced gamma-ray spectrum measured with germanium detector. In the case of recoil implantation into yttrium oxide superconductors, the radioactive nuclei induced through the nuclear reactions of component nuclei with incident carbon ions form the photo peaks around the 75-84 gamma-ray cascade, and this technique is not applicable to such multi-component system with larger atomic number.

Fig. 2 shows the R(t) spectrum obtained from the Nb sample irradiated at high temperature(estimated to be more than 800 K). R(t) is calculated through the relation of $((n(\pi,t)-n(\pi/2,t))/(n(\pi,t)+n(\pi/2,t)))$ to eliminate the component of exponential decay where $(n(\pi,t)$ and $n(\pi/2,t)$ are gamma-ray time spectra taken at π and $\pi/2$ arrangement, respectively. In this figure, the existence of any pertubed effect is not observed. This result assures

the substitutional replacement of probe nuclei in bcc Nb crystal lattice after annealing the irradiation-induced defects. Some perturbations are observed in the sampleswhich were irradiated with He and H ions after the introduction of probe nuclei.

If we employ a sample with smaller atomic number, the recoil implantation is successful. Fig.3 shows the precession spectrum from recoil implanted Be foil. Huge oscillation is observed with the cycle of about 3.2 MHz. This large pertubation can be attributed to the probe nuclei embed in the non-cubic hexagonal crystal lattice of Be sample.

References

1)For example: J. W. Mayer and E. Rimini ed.: Ion Beam Handbook for Material Analysis(Academic Press, Inc., New York, San Francisco, London, 1977).

2)H. Naramoto, K. Kawatsura, M. Sataka, Y. Sugizaki, Y. Nakai, K. Ozawa, S. Yamaguchi, Y. Fujino and M. Aoki, Nucl. Inst. and Meth. B33 (1988) 595.

3)E. Matthias and D. A. Shirley, Nucl. Instr. and Meth. 45 (1966) 309.

4)R. Vianden, E. N. Kaufmann, R. A. Naumann and G. Schmidt, Hyperfine Interactions 7 (1979) 247.

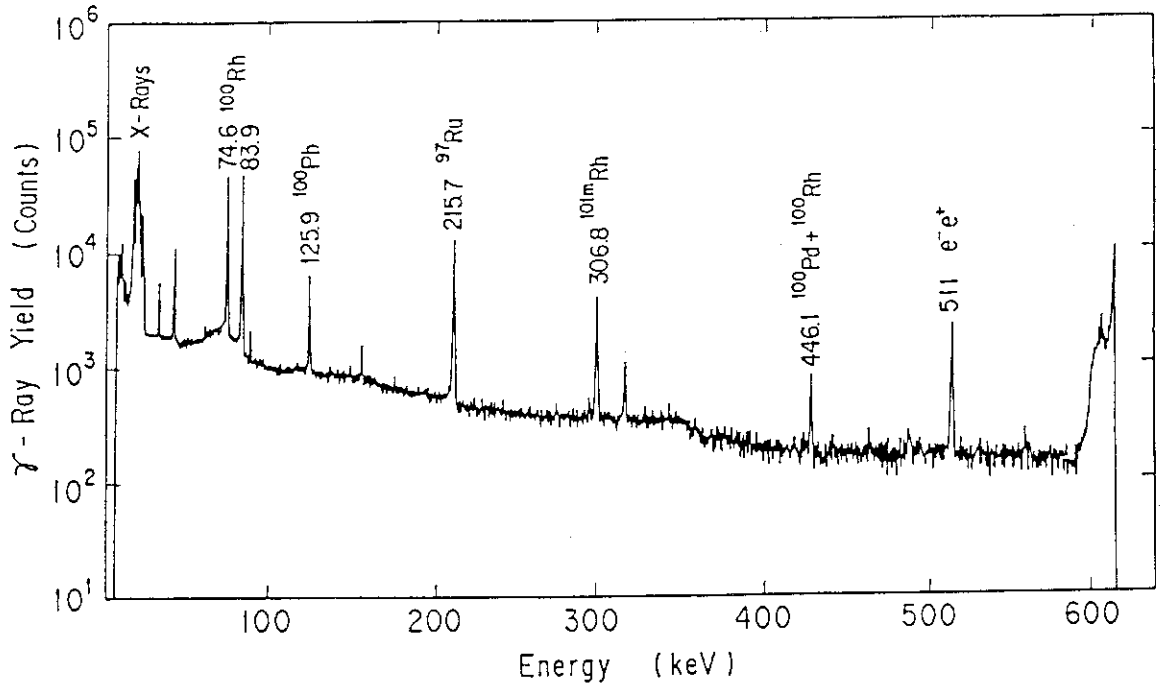

Fig. 1 Induced gamma-ray spectrum from Nb target foil when bombarded with 100 MeV C-12 ions.

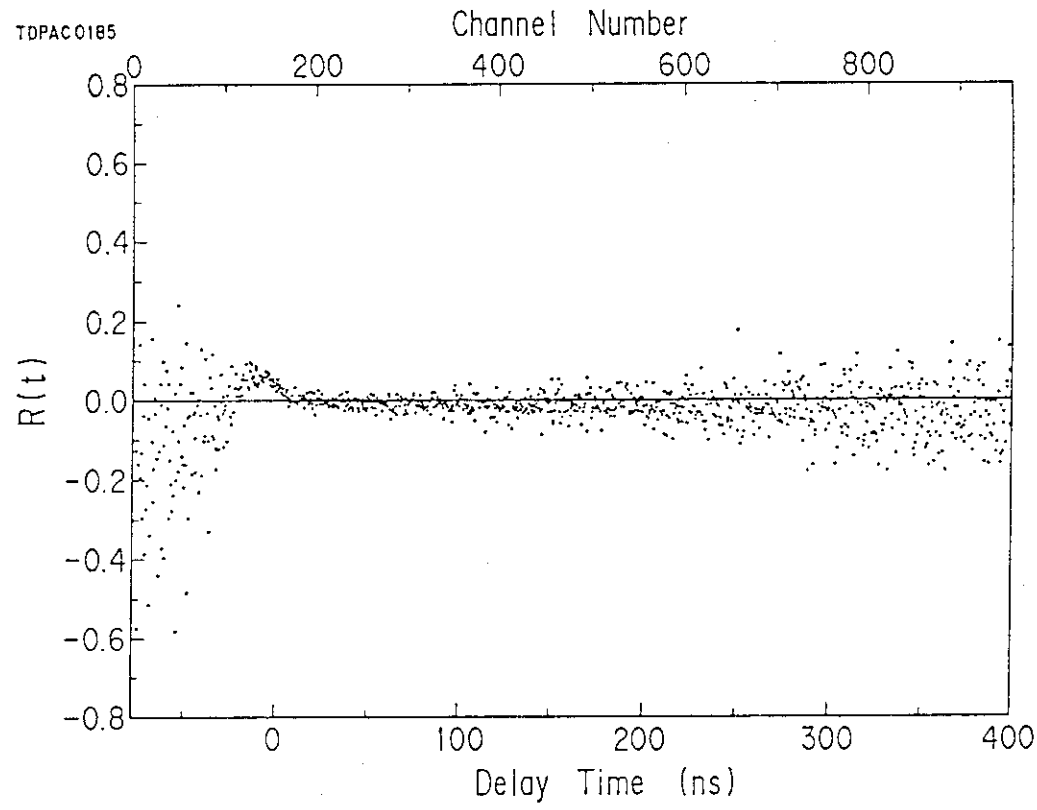

Fig. 2 R(t) spectrum in as-prepared Nb foil when bombarded with 100 MeV C-12 ions at higher temperature.

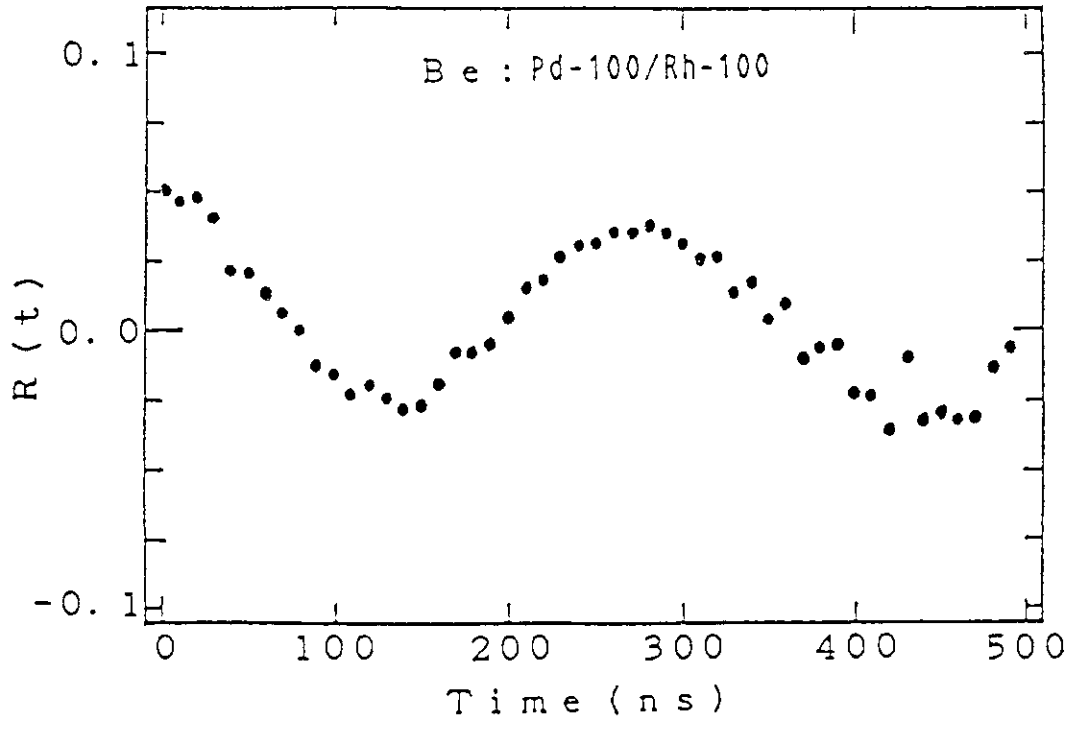

Fig. 3 R(t) spectrum of Pd-100/Rh-100 probe nuclei in recoil implanted Be foil sample.

2.4 IONIZATION MEASUREMENT IN A GAS TRAVERSED BY A BEAM OF HIGH-ENERGY HEAVY ION

Katsutoshi FURUKAWA, Shin-ichi OHNO,
Yoshihide KOMAKI, Hideki NAMBA*, Yasushi AOKI*,
Yohta NAKAI**

Department of Chemistry, *Department of
Research, **Department of Physics, JAERI

1. Introduction

Information on the track structure of high-energy heavy ion is needed to understand the relation between physical quantities and observed radiation effects on matter[1]. The initial energy deposited is composed of two parts: a "core" which is formed along the incident ion track and a much more diffuse "penumbra" which is the results of many secondary electrons emitted by the incident ion. Here, we aim at experimental measurements of the W-value of Ar gas for heavy-ion of the energy range 100-150 MeV from the JAERI Tandem accelerator.

The method employs a large cylindrical ionization chamber filled with a gas at variable low pressure. A collimated beam of the incident heavy ion is introduced into the ionization chamber, and from the resulting ionization current in the chamber, we may get information on the energy deposit around the incident ion track. The method is based in principle on the work reported by Wingate and Baum[2].

2. Experimental

A schematic view of the ionization chamber used in the present work is shown in Fig. 1. It is placed inside the vacuum vessel into which the collimated beam of high-energy heavy ion from the Tandem accelerator is introduced through a set of apertures (0.1 and 0.5 mm diameters). These apertures also serve as a differentially evacuating system for the beam transport tube (10^{-7} Torr) while the chamber contains a gas at atmospheric pressure. The position of the two apertures are adjustable in three dimensions by the remote controlling system. The sample gas is admitted into the vessel through an automatically controlled leak valve (MKS 248A) so that the pressure of the sample gas in the chamber may be kept constant within the range from 10^{-4} to 10^{2} Torr. The pressure is measured

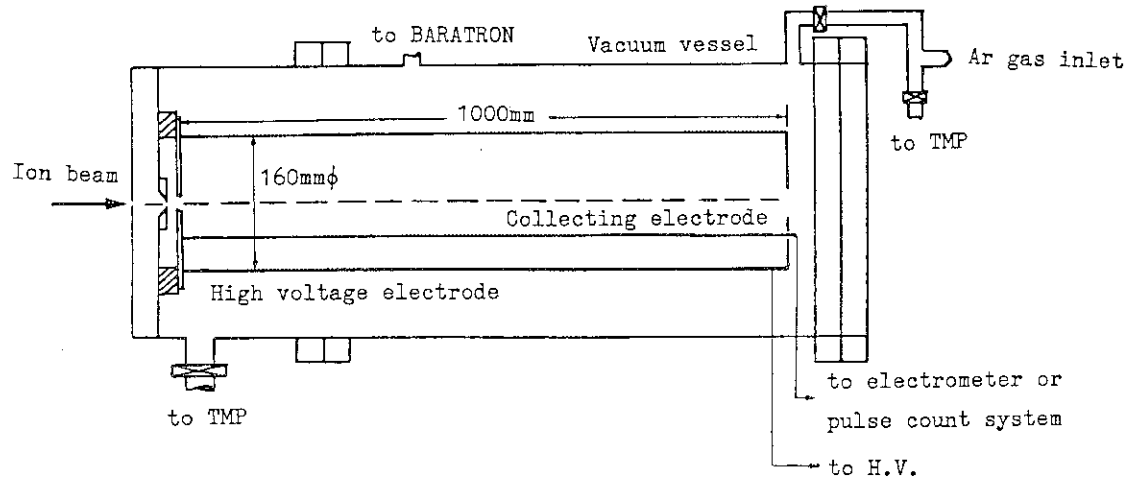

Fig. 1 Schematic diagram of the ionization chamber

with a Baratron capacitance manometer (310CA).

The intensity and energy of the ion beam from the accelerator was adjusted in some measurements by using Al foils of various thickness placed in front of the aperture system. The energy of the ion is decreased by letting the ion-beam transmitted the Al foil by an amount which can be estimated from data on stopping cross sections. The number of the high-energy ion incident into the ionization chamber was determined by counting electric pulses. Either the electrons or ions produced by an incident high-energy ion are collected without any amplification with the aid of an appropriate applied electric field, forming an electric pulse on the collecting electrode in the chamber.

The typical shape of the pulse is shown in Fig. 2. The pulse width is nearly 2 usec. The number of the incident ions entering the cylindrical chamber was kept less than 10^5 particles per second to avoid a "pileup". The ionization currents were measured with an electrometer(ADVANTEST 8652).

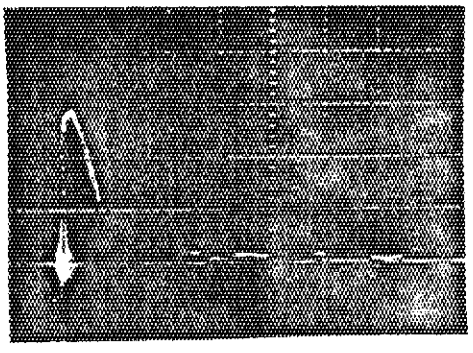

Fig. 2 An electric pulse formed by an incident ion (120MeV I^{7+}) in the ionization chamber filled with an Ar gas (10 Torr)

3. Results and discussion

1) Saturation charactristics

The saturation curves for the 165 MeV S^{10+} ions entering the chamber containing Ar gas at various pressures are shown in Fig. 3. The saturation currents obtained at the gas pressure of 50 and 100 Torr are nearly the

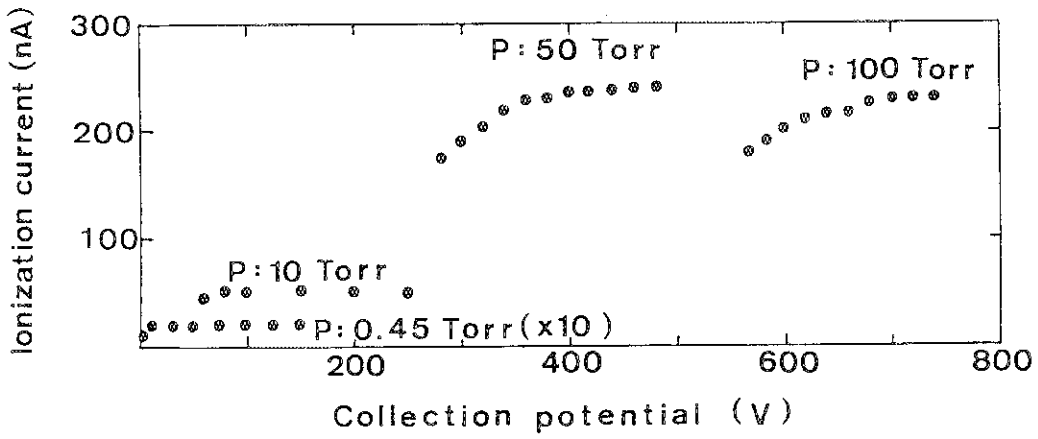

Fig. 3 Saturation curve obtained with 165 MeV S^{10+} in Ar gas

same value, indicating that the incident ions from the accelerator are completely stopped within the ionization chamber. This has been confirmed by the expected ion ranges calculated from mean ion depth data[3].

2) W-value

W-value is the mean energy required to create an ion-electron pair when an incident ion is stopped in the gas. Thus, if N ions of energy E lose all their energy in the gas and produce ionization current I then W is given by

$$W = E N e / I \qquad (1)$$

where e is the electronic charge.

W-value which have been determined in the present experiment using equation (1) are listed in the Table 1.

Table 1 W-value determined in the present experiment

Ion	Energy MeV	Rate of incident ions /s	Ionization current nA	Ion pair yield 10^6	W-value
S^{10+}	23.1	110	0.016	0.91	25.4
S^{10+}	86.7	1.5×10^4	8.64	3.6	24.1

The intensity and energy of S^{10+} ion beam was adjusted by using an Al foil of 25 um or 41 um thickness. The resulting energy of the ion passing through the foil was calculated from data on stopping cross section[4].

The W-values for Ar gas thus obtained and including the previously reported ones are shown in Fig. 4 as a function of the incident ion energy. The results indicate that W-value is clearly dependent on the energy of the incident ion.

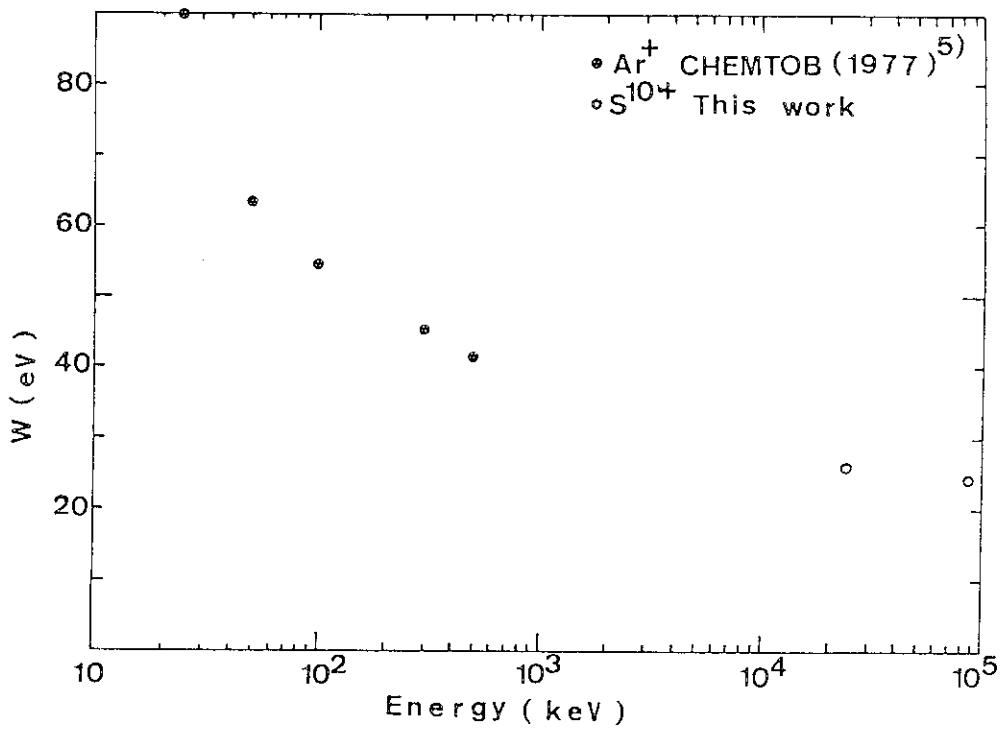

Fig. 4 W-values for incident ions in Ar gas

It is generally considered that, for the heavy incident ion, the fraction of the energy transferred to kinetic energy of gas atom due to nuclear collision becomes rather large at low energies, producing a corresponding increase in W-value.

Our present results will show that W-value for the heavy ion such as S^{10+} up to several tens MeV is still dependent on the energy.

We thank Mr. T. Yoshida for his technical advice in constructing the differential pumping system.

Reference

1) A. Chatterjee and J. L. Magee, "6th Symposium on Microdosimetry," J. Booz and H. G. Ebert, Eds (1978).
2) C. L. Wingate and J. W. Baum: Radiat. Res., 65, 1 (1976).
3) U. Littmark and J. F. Ziegler: "Handbook of Range Distributions for Energetic Ions in All Elements," Pergamon Press, N. Y., (1980).
4) J. F. Ziegler: "Handbook of Stopping Cross-Sections for Energetic Ions in All Elements," Pergamon Press, N. Y., (1979).
5) M. Chemtob, B. Lavigne, J. Chary, V. D. Nguyen, N. Parmentier, J. P. Noel and C. Fiche: Phys. Med. Biol., 22, 208 (1977).
6) "Average Energy Required to Produce an Ion Pair," ICRU Report 31 (1979)

2.5 HEAVY ION IRRADIATION INDUCED RADICALS IN POLYVINYLIDENE FLUORIDE

Yoshihide KOMAKI*, Niro ISHIKAWA*, Tsutomu SAKURAI*, Norio MORISHITA**, Naohiro HAYAKAWA**, and Saburo TAKAMURA***

*Department of Chemistry, **Takasaki Radiation Research Establishment, and ***Department of Physics, JAERI

1. Introduction

In this paper, are presented the measurement of radicals and the examination of the kinds of radicals when polyvinylidene fluoride(PVDF) were irradiated by the heavy ions, and the influence for emergence of etched tracks in relation to the radicals induced.

Hitherto many workers have studied the radiation damage of polyethylene, polypropylene, polyvinyl chloride, and PVDF subjected to γ-ray and electron irradiations by means of various analytical techniques. There have been only a few works on ESR spectroscopy of heavy ion irradiated polymers, besides for γ-ray and electron irradiation[1].

Authors[2] have prepared the microfilter of PVDF by heavy ion bombardment and chemical etching, and indicated that track holes were not necessarily formed by any etchants. The dependency of energy and mass of ion for the etching development of tracks leads to the examination of radiation induced radicals in a polymer.

We here present the ESR spectra of PVDF films subjected to bombardment of several ions at high energy using Takamura's cryostat and discuss the relation to the track revelation.

2. Experimental

The biaxially stretched and the monoaxially stretched PVDF films were irradiated separately with $^{12}C^{5+}$(90 MeV), $^{35}Cl^{6+}$(70 MeV), $^{35}Cl^{9+}$(150 MeV), and $^{79}Br^{11+}$(160 MeV) at JAERI tandem accelerator. The several pieces of sample(2.5mmx35mm)were cooled at 5.7K indirectly and exposed to the homogeneously spread beam of ions in a constant current of 2 nA up to accumulate totally 10^{9}-10^{12}ions/cm^2. The doses for ions were calculated on the stopping powers which were obtained from Northcliffe and Schilling's table and the ion fluence, and the doses for γ-ray from Alanin dosimeter. JES-FE3X spectrometer was used for ESR spectroscopy at 77K to 293K.

3. Results and discussion

(1) Effect of ions

Three kinds of ESR spectra of PVDF obtained by $^{79}Br^{11+}$(A), $^{35}Cl^{9+}$(B), $^{12}C^{5+}$(C) show no intrinsic difference between them as shown in Fig. 1. The tracks by the former two ions were etched to develop but the ones by the latter ion not etched.

(2) Effcet of dose

The dose ranging from 10^9 to 10^{11}ions/cm^2 was best suitable for the measurement of PVDF by ESR spectroscopy, when the overlapping split signals having large wings were symmetrically observed. The higher dose yields only a singlet which is assigned to the polyenyl radical.

(3) Effect of elapsed time and increasing temperature

The radical shows no changes with the elapsed time at low temperature, but changes with the increasing temperature. The radicals produced by ion irradiation decay quickly in a short time. They decay to a level of 50% or less within a few minutes and thereafter rather slowly. After 50 hr at room temperature these radicals remain only a central peak, as shown in B of Fig. 2. Such a singlet changes to the peroxy radical which shows asymmetrical signals in ESR spectrum. The residual radicals induced by $^{12}C^{5+}$ faded after only 30 min as shown in B of Fig. 3, of which the decay rate is faster than the ones by $^{79}Br^{11+}$ and $^{35}Cl^{9+}$. The difference of such a decay behavior between them may be related to track etchability.

(4) Kinds of radicals:

In Fig. 4 A-1 to A-3 are ESR spectra of PVDF irradiated by $^{35}Cl^{9+}$ and measured in paralell to magnetic field ,and B-1 and B-2 are those measured rectangurly. In order to know the changes of radicals with the increasing temperature, monoaxially stretched PVDF films were used. The split peaks to sextet or more are detected in A-2 and B-1 of Fig. 4 after over 30 min. at room temperature. From the distinct anisotropy and the formation of peroxy radicals shown in A-3 amd B-2 of Fig. 4, it seems most reasonable to consider the existence of alkyl radicals. Moël et al.[3] proposed an allyl radical for such a complex split signal. The complex split signals of short-life change into a singlet at the center of spectrum. This is also assigned to the polyenyl radical of conjugated double bonds. The radicals finally change into the peroxy radicals.

(5) Amount of radical

Table 1 shows the amounts of radicals produced by the C, the Cl, and

the Br ion irradiations under some different circumstances. The radicals yield in proportion to the fluence of ions. Bombarding ions with the same mass, $^{35}Cl^{9+}$ produced more radicals than $^{35}Cl^{6+}$. $^{79}Br^{11+}$ with the highest mass yielded the most radicals . $^{35}Cl^{9+}$ gave 4.6 times more radicals per fluence of ions than $^{12}C^{5+}$. $^{12}C^{5+}$ did not achieved any etched tracks, although $^{12}C^{5+}$ with almost same charge as $^{35}Cl^{6+}$ yields more radicals than $^{35}Cl^{6+}$. These facts suggest that the track etchability in a polymer may be controlled by changing the mass and the charge state of ion.

References

1) T. Seguchi,K. Makuuchi,T. Suwa,T. Abe,N. Tamura and M. Takehisa., Nippon Kagaku Kaishi (1974)1309.
2) Y. Komaki,N. Ishikawa,T. Sakurai,N. Morishita and M. Iwasaki., Nucl.Instru & Meth.B34(1988)332.
3) A.Le Moël,J.P. Duraud,C. Lecomte,M.T. Valin,M. Henriot,C. Legressus, C. Darnez,E. Balanzat and C.M. Demanet.,Nucl.Instru & Meth.B34(1988)115.

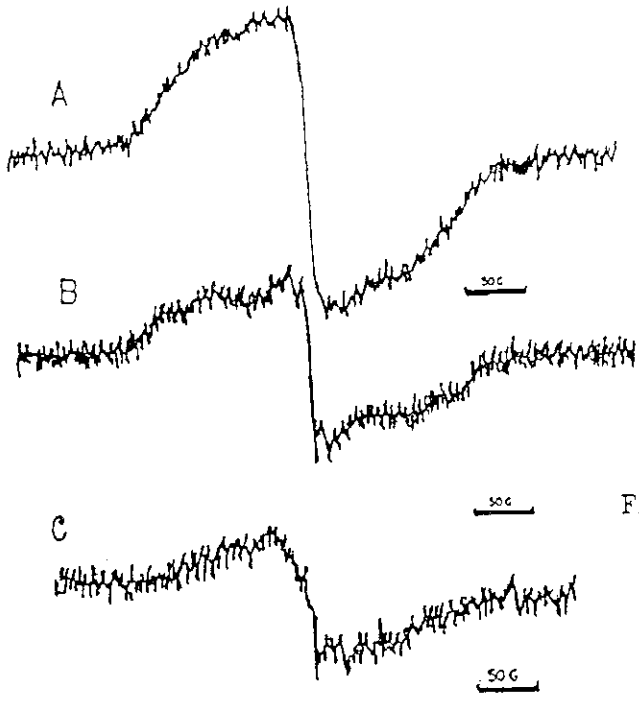

Fig. 1 ESR spectra of PVDF irradiated by $^{79}Br^{11+}$, $^{35}Cl^{9+}$ and $^{12}C^{5+}$ at 5.7K and measured at 77K. Ions; $10^{10}/cm^2$

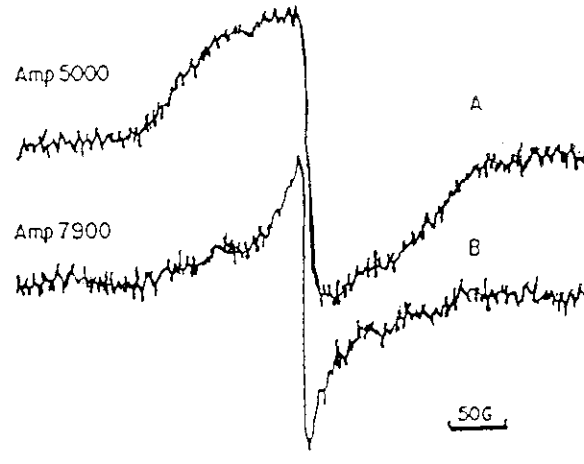

Fig. 2 Decay after breaking vacuum of radicals in PVDF irradiated by $^{79}Br^{11+}$ at 5.7K and measured after 50h (B). Ions; $10^{10}/cm^2$

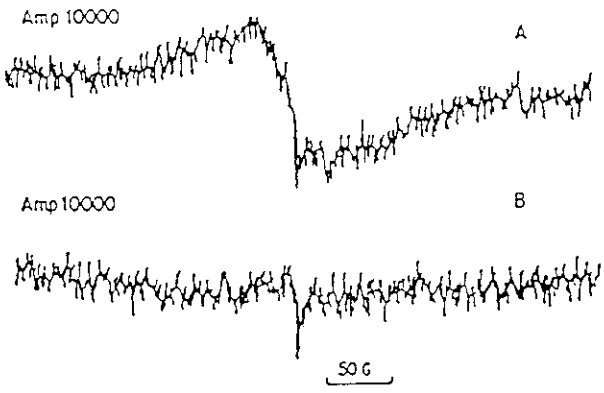

Fig. 3 Decay after breaking vacuum of radicals in PVDF irradiated by $^{12}C^{5+}$ at 5.7K and measured at 77K after 30 min(B).

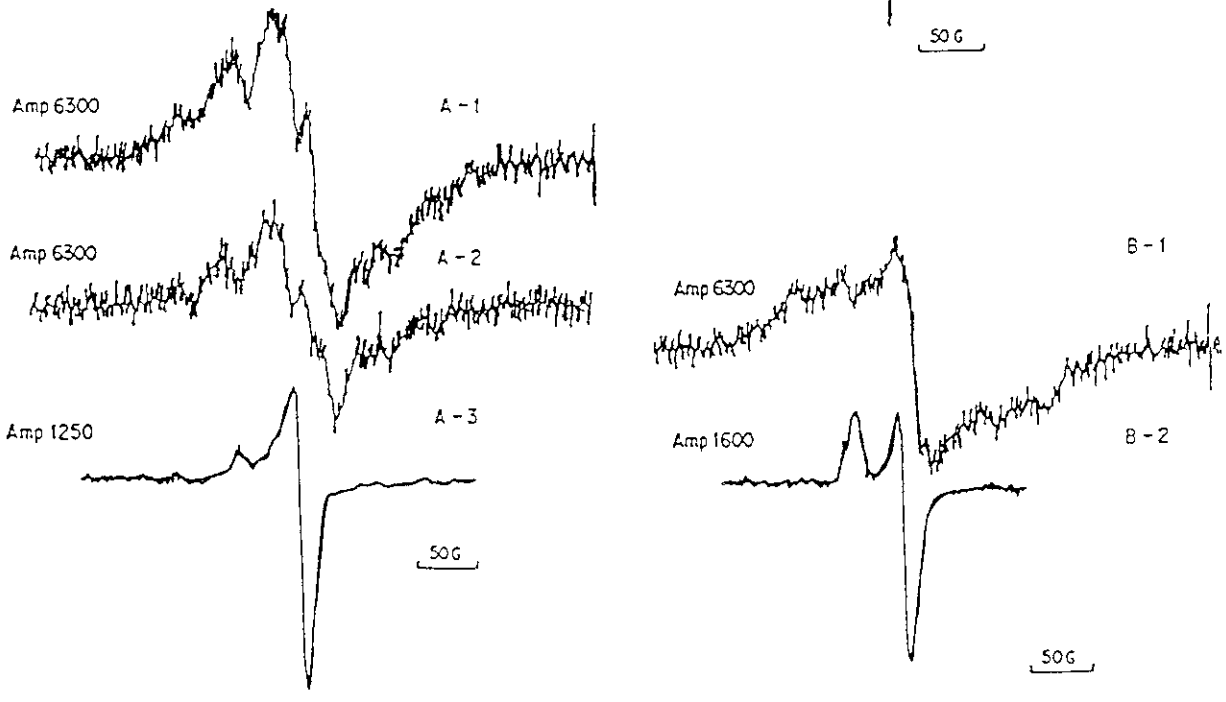

Fig. 4 ESR spectra of monoaxially stretched PVDF irradiated by $^{35}Cl^{9+}$ at 5.7K and measured at 77K(A-1;paralell, B-1;rectangular).
A-2; after 30 min in vacuum at room temperature.,
A-3,B-2; after 30 min in air at room temperature.

Table 1 Amounts of Radicals.

		Ions					
		$^{35}Cl^{9+}$		$^{35}Cl^{6+}$	$^{12}C^{5+}$		$^{79}Br^{11+}$
flux of ions	ions/cm^2	4.2×10^{10}	1.1×10^{11}	5.7×10^{11}	9.7×10^{10}	2.3×10^{11}	7.4×10^{10}
energy	MeV	150		70	90		160
dE/dx	MeV/(mg/cm^2)	16		22	1.9		50
total radicals	spins/g	3.7×10^{18}	5.7×10^{18}	5.4×10^{18}	1.4×10^{18}	3.7×10^{18}	8.9×10^{18}
radicals/ion	spins / ion	4.4×10^5	7.5×10^5	8.1×10^4	1.2×10^5	1.4×10^5	2.0×10^6
		mean: 6.0×10^5			mean: 1.3×10^5		

Ⅲ SOLID STATE PHYSICS AND RADIATION EFFECTS IN MATERIALS

3.1 ION CONDUCTIVITY OF LITHIUM OXIDE IRRADIATED WITH OXYGEN AND LITHIUM IONS

Kenji NODA, Yoshinobu ISHII, Hisayuki MATSUI*, Mikio HORIKI*, Kenji Nakaya*, Kouji Nezaki*, Naomi OBATA* and Hitoshi WATANABE

Department of Fuels and Materials Research, JAERI, *Faculty of Engineering, Nagoya University

1. Introduction

Lithium oxide (Li_2O) as a solid breeder material for fusion reactors will be subjected to severe neutron irradiation. During the irradiation a large number of irradiation defects will be introduced. Such defects induce not only degradation of dimension stability (for instance; swelling and cracking) but also change of various properties such as diffusion.

Ion conductivity of Li_2O is controlled by lattice defects including irradiation defects and impurities, and reflects diffusion of lithium ions. Furthermore, the conductivity would be related to the tritium diffusion behavior through lithium ion diffusion, since the rate determinant for the mechanism of tritium diffusion is considered to be the same as that of lithium ion diffusion[1,2].

In the present study, irradiation effects on ion conductivity of Li_2O were investigated by in-situ experiments using oxygen or lithium ion irradiation, in order to obtain information of irradiation defects and irradiation effects on transport phenomena of lithium and tritium.

2. Experimental

The specimens used were thin plates of Li_2O single crystals (7 to 9 mm in length, 8 to 9 mm in width, 0.36 to 0.38 mm in thickness). The specimens were irradiated at each prescribed temperature (in the range 393 to 593 K) for each irradiation series in an irradiation vacuum chamber attached to a tandem accelerator at JAERI with 120 MeV oxygen ions, 24 MeV lithium ions and 60 MeV lithium ions. Measurements of ion conductivity of the specimens along the direction perpendicular to the thickness were carried out "in-situ" at the temperatures same as the irradiation temperature for each irradiation series in the chamber with the two terminal AC

method using a HP 4194 A impedance analyzer after interruption the irradiation.

3. Results and Discussion

Figures 1, 2 and 3 show relationships between the ion conductivity after interrupting the irradiation and oxygen or lithium ion fluence at various temperatures for 120 MeV oxygen ion irradiation, 24 MeV lithium ion irradiation and 60 Mev lithium ion irradiation, respectively. For the 120 MeV oxygen ion irradiation, the conductivity increased with the fluence at 393 K and 413 K, while the conductivity decreased at 453 K and 493 K. (Fig. 1) In case of the 24 MeV lithium ion irradiation, the conductivity increased with the fluence at 413 K and decreased in the range from 453 K to 573 K. (Fig. 2) For the 60 MeV lithium ion irradiation, the conductivity decreased with the fluence in the range from 443 K to 543 K and increased at 593 K. (Fig. 3)

From these, the irradiation effects on the ion conductivity of Li_2O in the present results are seen to be as follows. 1) The irradiation effects due to the lithium ion irradiation were essentially the same as those due to the oxygen ion irradiation. 2) The conductivity in the range from 393 K to 413 K increased with the fluence, while it decreased in the range from 443 K to 573 K. 3) At 593 K the conductivity increased with the fluence again.

The ion conductivity of Li_2O irradiated at an ambient temperature in the irradiation chamber with 120 MeV oxygen ions has been measured around 440 K and 490 K after interruption the irradiation[2,3]. In the studies, the conductivity around 440 K increased with the fluence and decreased around 490 K. From the thermal recovery behavior of the conductivity, the decrease around 490 K was attributed to F^+ centers which were almost recovered above 573 K[3,4]. On the other hand, the increase around 440 K was referred to irradiation defects, which were recovered in the range from 443 K to 498 K and were assumed to increase concentration of lithium ion vacancies[2].

The fluence dependence of the ion conductivity in the present study is somewhat different from the results of the above mentioned studies in respect of the temperature range. However, the irradiation effects on the conductivity in the present study can be considered to be consistent with those in the above mentioned studies by taking temperature rise in the ir-

radiated region due to the ion beam heating during the irradiation in the present study, except the 24 MeV lithium ion irradiation. (In case of the 24 MeV lithium ion irradiation the beam current was very small.) The increase at 443 K in the 60 MeV lithium ion irradiation is considered to arise from recovery of the defects, which are assumed to increase concentration of lithium ion vacancies, by the beam heating. In contrast with this, the F^+ centers were hardly recovered even at 573 K in case of the 24 MeV lithium ion irradiation, since the temperature rise due to the beam heating was negligibly small.

Thus, the irradiation effects on ion conductivity of Li_2O are considered to be as follows. 1) The conductivity in the range from 393 K to 440 K is increased with the fluence by the irradiation defects which are assumed to increase concentration of the lithium ion vacancies. 2) The conductivity in the range from 453 K to 573 K is decreased by the F^+ centers. 3) The increase of conductivity which is attributed to recovery of the F^+ centers is observed above 573 K.

The ion conductivity of Li_2O reflects lithium ion diffusion and is controlled by mobility and concentration of lithium ion vacancies in the examined temperature range[2]. Furthermore, the conductivity can be supposed to be related to tritium diffusion, since the rate determinant of tritium diffusion seems to be the same as that of lithium ion diffusion[1,2]. Consequently, it is considered that the lithium ion and tritium diffusion in the range from 393 K to 440 K are increased by the defects which are assumed to increase concentration of lithium ion vacancies, and that they in the range from 453 K to 573 K are decreased by the F^+ centers.

References

1) H. Ohno, S. Konishi, T. Nagasaki, T. Kurasawa, H. Katsuta and H. Watanabe: J. Nucl. Mater. 133-134 (1985) 1881.

2) K. Noda, Y. Ishii, H. Matsui, H. Ohno and H. Watanabe: Fusion Engineering and Design 8-10 (1989) in press.

3) K. Noda, Y. Ishii, H. Matsui, H. Ohno, S. Hirano and H. Watanabe: J. Nucl. Mater. 155-157 (1988) 568.

4) K. Noda, K. Uchida, T. Tanifuji and S. Nasu: Phys. Rev. B 24 (1981) 3736.

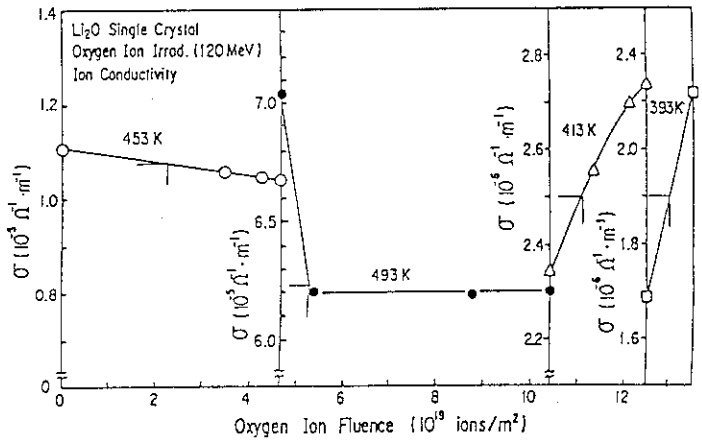

Fig.1 Relationships between the ion conductivity after interrupting the irradiation and the fluence at various temperatures in 120 MeV oxygen ion irradiation.

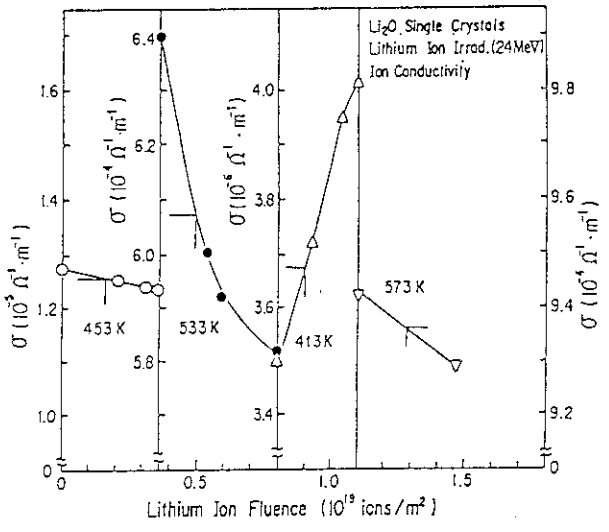

Fig.2 Relationships between the ion conductivity after interrupting the irradiation and the fluence at various temperatures in 24 MeV lithium ion irradiation.

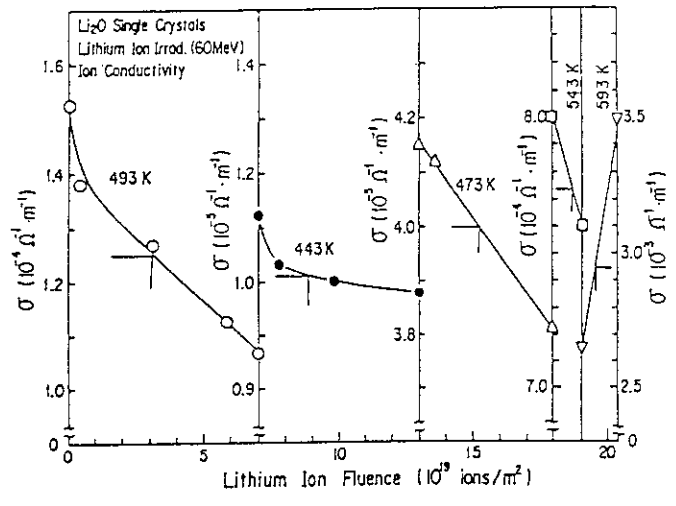

Fig.3 Relationships between the ion conductivity after interrupting the irradiation and the fluence at various temperatures in 60 MeV lithium ion irradiation.

3.2 SWELLING OF LITHIUM OXIDE IRRADIATED WITH HIGH ENERGETIC LITHIUM IONS

Yoshinobu ISHII, Kenji NODA and Hitoshi WATANABE

Department of Fuels and Materials Research, JAERI

1. Introduction

Lithium oxide (Li_2O) is a prime candidate material of the blanket for a fusion reactor, because of excellence for a tritium breeding. During operation of the fusion reactor, a lot of defects will be introduced in the lithium oxide by the energetic particles (neutrons, tritons and helium ions) and then will induce swelling and cracking. These phenomena are very important for the integrity of lithium oxide. Ion irradiations have been used as a means of simulating the irradiation effects for the fusion reactor materials, because many defects can be introduced in the material for a short time. The swelling of Li_2O sintered pellets was measured after high dose irradiation at high temperature and it was concluded to be mainly associated with helium bubbles[1]. The lattice parameter measurement of Li_2O sintered pellets irradiated to thermal neutrons was reported[2]. At a fluence of 2×10^{23} thermal neutron/m^2 the lattice was expanded by 0.15%. This lattice expansion was concluded to be mainly associated with irradiation defects. To get the information for the swelling associated with only displacement damages except helium bubbles, volume change of Li_2O irradiated with high energetic lithium ions was measured by using a photoelastic technique.

2. Experimental

The specimens used were thin rectangular plate of Li_2O single crystals. The dimensions and the orientations of the specimen are shown in Fig.1(a). The specimens were annealed at about 1300 K in high vacuum (1×10^{-3} Pa) for about ten hours to remove the surface damages due to the cutting and decompose the LiOH on the surface. After these treatment, the specimen was mounted on a circular polarimeter which was equipped in a high vacuum chamber. One half of the specimen was irradiated with

lithium ions (60MeV) along z axis by using a tandem accelerator at JAERI. By such irradiation the irradiated part of the specimen expands, but unirradiated part remains unchanged. Then a strain field is induced in the specimen. The profile of the strain is schematically illustrated in Fig.1(b) as a function of the distance from the boundary between an irradiated and unirradiated part. From the photoelastic measurement of this strain, the volume change of irradiated Li_2O can be determined. The detail for the photoelastic measurement of the induced strain has been described elsewhere[3].

The measurement of the volume expansion of a specimen was intermittently carried out after interrupting the irradiation. All measurements of the volume expansion were done at room temperature. After the irradiation, the specimen was isochronally annealed in the temperature range from 300 to 870K by holding 30 min. at each temperature.

3. Results and discussion

The penetration depth of Li ions (60 MeV) for the Li_2O was calculated by using E-DEP-1 computer code and it is about 400 um. Because the thickness of the specimen is very thin, the bombarded ions (Li ion) completely pass through the specimen and induce the defects uniformly along z axis in the irradiated part. The typical strain profile of the Li_2O irradiated with Li ions at 2.1×10^{19} ions/m^2 shows in Fig.2 as a function of the distance from the boundary between the irradiated and unirradiated part. Longitudinal axis indicates the rotation angle which is directly proportional to the induced strain. The broken lines in Fig.2 indicate the edges of the specimen. The profile of the induced strain in the specimen is good agreement with the theoretical curve (Fig.1 (b)). The fractional volume change was calculated with the same manner as described in previous report[3].

A fluence dependency of the fractional volume of irradiated Li_2O are shown in Fig.3. The longitudinal axis and the transverse axis show the fractional volume and the ion fluence, respectively. The fractional volume increases rapidly with the ion fluence up to 3×10^{19}. The value of fractional volume of about 7.6×10^{-4} is attained at the ion fluence of 1.3×10^{20} ions/m^2. A broken line in Fig.3 shows increasing rate of the fractional volume at the fluence of zero. The experimental curve

deviates from this line with increasing of ion fluence. It is seen that induced defects are segregated to form the clusters and annihilated by recombination between interstitials and vacancies.

The recovery of induced volume of the specimen irradiated to 1.34×10^{20} ions/m^2 during isochronal annealing is shown in Fig.4. The two recovery stages are observed in this figure. The first and the second stage take the temperature range from 350 to 600K and from 650 to 870K, respectively. At the first stage, the beginning temperature of recovering is lower than that of recovering of the F^+-centers determined by the ESR and optical absorption experiments[4]. Therefore, recovery in this stage is associated with not only F+centers but also an another kind of defect i.e. "unspecified defect". This fact is supported by the annealing experiments of the irradiated Li_2O by electrical conductivity measurements[5]. An amount of 20% of the induced volume change still remain even at the annealing temperature of 870K.

To clarify the mechanism and the fluence dependency of swelling for the irradiated Li_2O, the fundamental constants such as the displacement cross section, the recombination volume are required. To get informations about the concentration of F^+-center and Li metal colloid and the volume change due to each of them, The optical absorption measurements of the irradiated Li_2O are currently carried out.

Acknowledgments

The authors thank to Dr. T.Aruga for the computation of penetration depth by using computer code.

References

(1) G. W. Hollenberg : J. Nucl. Mater. 122/123 (1984) 896

(2) N. Masaki, S. Nasu, T. Tanifuji, K. Uchida, K. Noda, H. Takeshita, T. Kurasawa and H. Watanabe :J. Nucl. Mater. 116 (1983) 345

(3) Y. Ishii, K. Noda and H. Watanabe : JAERI-M 88-181 (1988) 68

(4) K. Noda, Y. Ishii, H. Matsui, H. Ohno and H. Watanabe : Fusion Engineering and Design 8-9 (1989) in press

(5) K.Noda, Y.Ishii, H.Matsui and H.Watanabe: Radiat. Eff. 97 (1986) 297

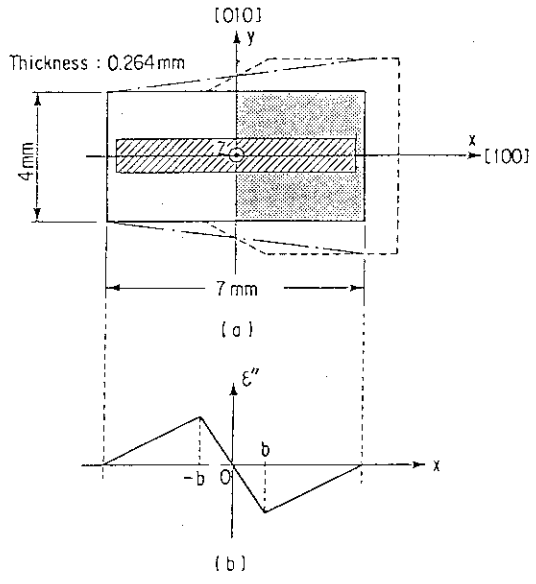

Fig.1 Schematic illustration of an irradiated specimen. A dotted area show irradiated part. (b) the induced strain.

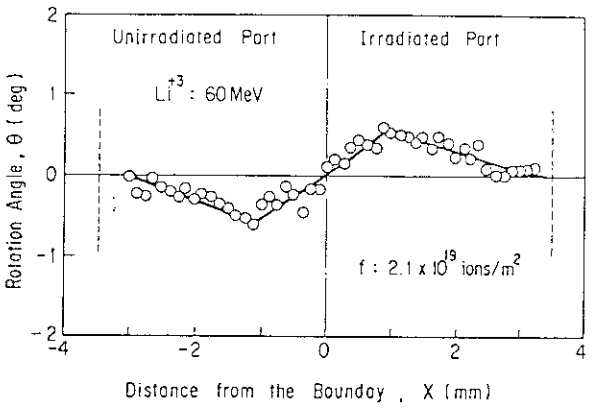

Fig.2 The profile of strain field of Li_2O irradiated to 2.1×10^{19} ions/m^2.

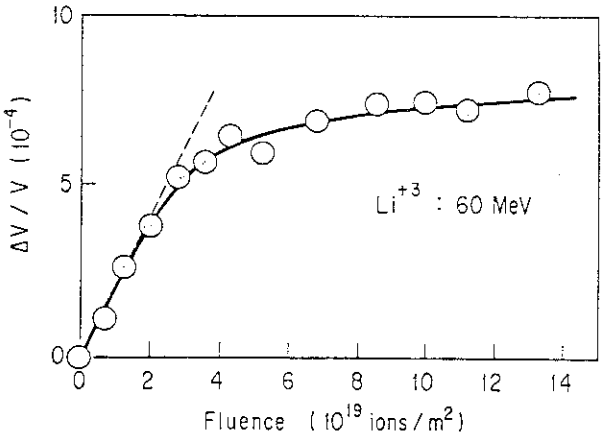

Fig.3 Fluence dependency of the fractional volume of irradiated Li_2O

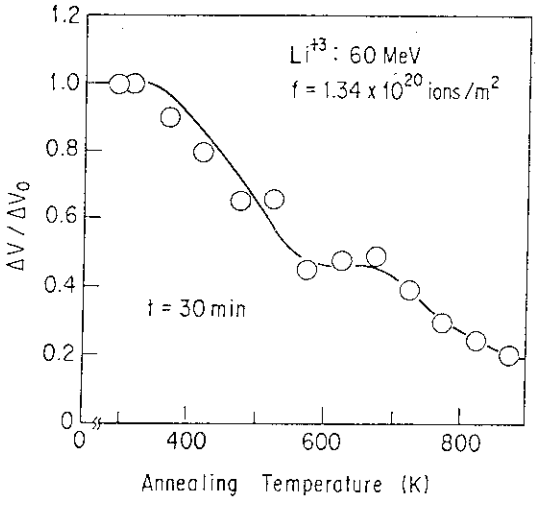

Fig.4 Annealing behavior of Li_2O irradiated to 1.3×10^{20} ions/m^2. Annealing time is 30 min. at each annealing temperature.

3.3 DAMAGE STRUCTURE OBTAINED BY CROSS-SECTIONAL OBSERVATION IN He-ION IRRADIATED SiC

Yoshio KATANO, Shigeki KASAHARA*, Kiyotomo NAKATA* and Hideo OHNO

Department of Fuels and Materials Research, JAERI,
* Hitachi Research Laboratory, Hitachi Ltd.

1. Introduction

Silicon carbide, SiC, is one of the candidate materials for near-first wall structural applications in fusion reactors[1)2)]. When ceramics are irradiated with 14 MeV neutrons, a large amount of transmutation-induced gas such as He and H are produced in the materials, and the gas atoms worsen radiation damage effects[3)].

In this work, the damage structure after He ion-irradiation in a hot-pressed SiC is studied by cross-sectional observation to clarify the effects of He atoms in radiation damage.

2. Experimental procedure

A material used in this study was hot-pressed SiC with addition of 2 wt% BeO as binder; grain size was 3-5 μm in diamater. Samples of about $5\times8\times0.2$ mm^3 were annealed in air at about 1273 K for 1 h prior to ion-irradiations. The He-ion irradiation was carried out by using a W-2 beam line in the 2 MV Van de Graaff ion accelerator facility; schematic diagram of the beam line is shown in Fig. 1. The surfaces of several samples were set exactly in perpendicular to the ion beam by using the sample holder in the target chamber,and irradiated with 400 keV He ions up to a dose of 1×10^{20} ions/m^2 at temperatures of 300 and 1023 K. The arrangement of samples is illustrated in Fig. 2. The irradiation temperature was measured with a thermo-couple attached to a side of the sample.

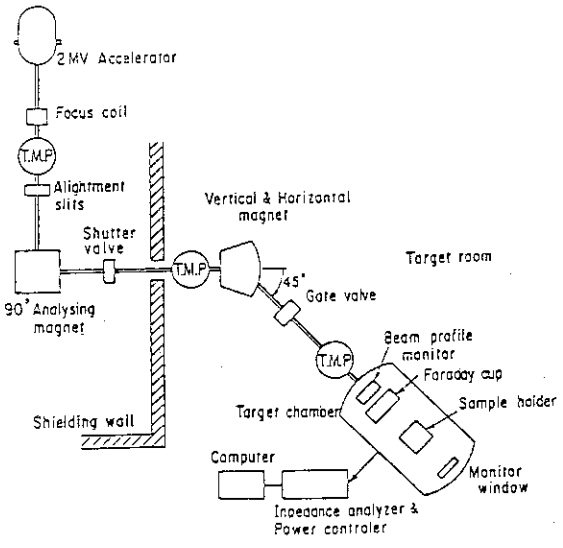

Fig.1 W-2 beam line in the 2 MV Van de Graaff ion accelerator facility.

After irradiation, ion-irradiated surfaces of two samples were pasted together, and then, the area

containing damaged regions was cut into a disk,3 mm in diameter,as also shown in Fig. 2. Foils for observation in a 200 keV transmission electron microscope(TEM) were made from the disks by a ball-milling and ion-sputtering with 3 keV Ar ions at room temperature.

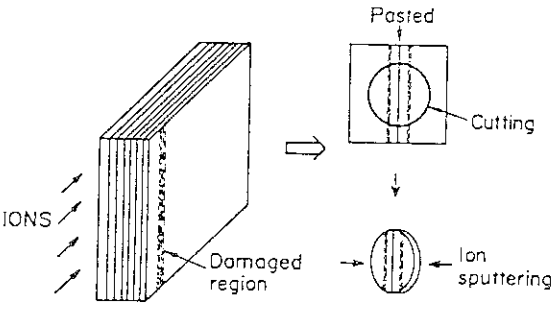

Fig.2 Arrangement of the samples and TEM disk preparation procedure.

3. Results and discussion

The damage and the injected He-ion profile calculated using a modified EDEP-1 (EDEP-81) code [4] are shown in Fig. 3 for the irradiation condition in this study. The damage has a steep distribution in depth with a maximum; the damge peak and straggling are 1.18 μm in depth and 0.28 μm, respectively. The distribution of injected He ions is maximized at 1.25 μm in depth.

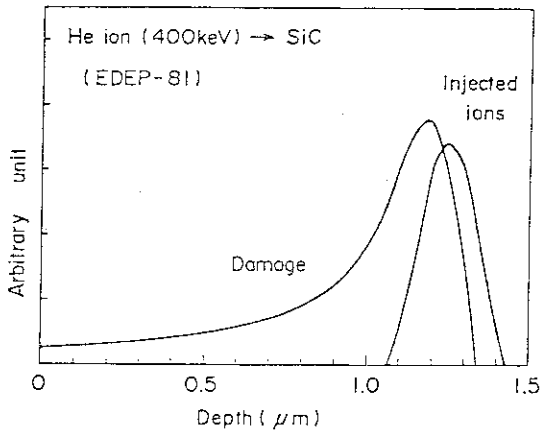

Fig.3 Calculated damage and injected ion depth profile .

The damage structure, observed in the direction of depth from the ion-bombarded surface, is shown in Fig. 4 for the sample He-irradiated

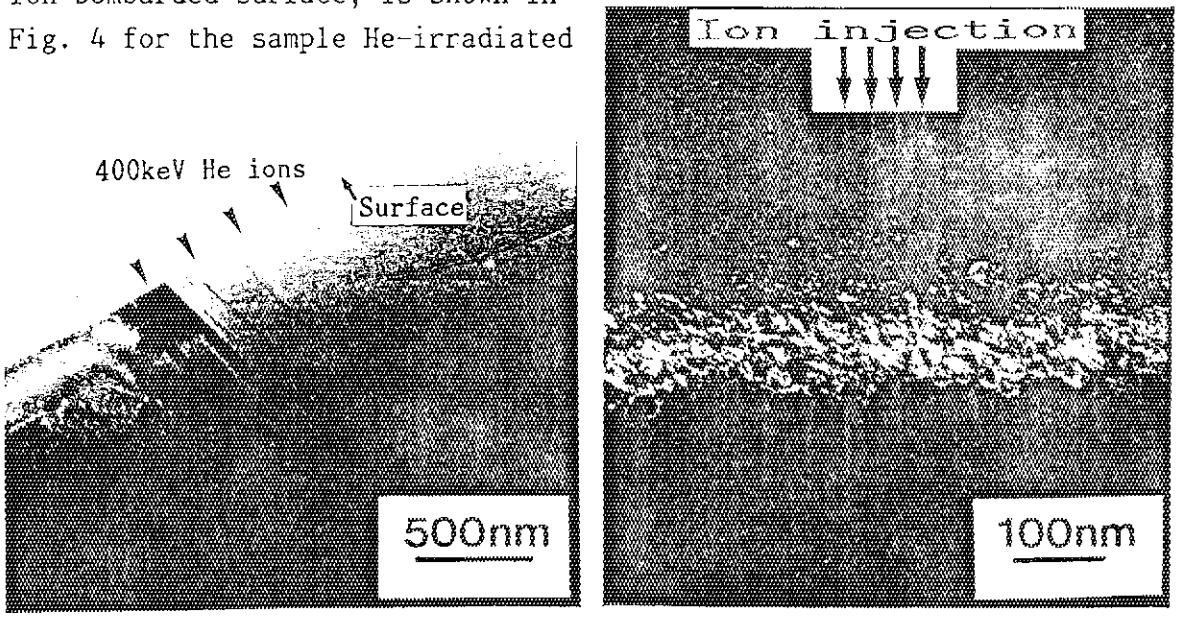

Fig.4 Damage structure in the direction of depth from the ion-bombared surface after the irradiation to 1×10^{20} ions/m² at 1023 K. Dark-field micrograph of high damaged region(right).

to 1×10^{20} ions/m^2 at 1023 K. The damaged region with fairly large strain field can be seen as a band, which is located between about 0.95 and 1.15 μm in depth from the ion-bombarded surface. Both loop-shaped and small dot defects are found in the damaged region. The damage distribution analyzed from the micrograph has a peak at 1.15 μm in depth, and a half-value width of distribution is about 0.1 μm. The experimental damage peak depth is in a good agreement with the calculated one, but the half-value width obtained from the experiment is narrower than that predicted from the calculation.

A lot of cavities with less than 2 nm in diameter are also found in the damaged region, and most of the cavities are formed in straight and curved lines shown in Fig.5. The density of cavities increases with depth to 1.15 μm, while the size is independent of depth from 0.95 to 1.15 μm. Preferential arrays of He bubbles in the c planes have been found in SiC irradiated with 10 keV He ions at 1273 K[5,6]. From the result, the cavities found in this study are considered to be bubbles

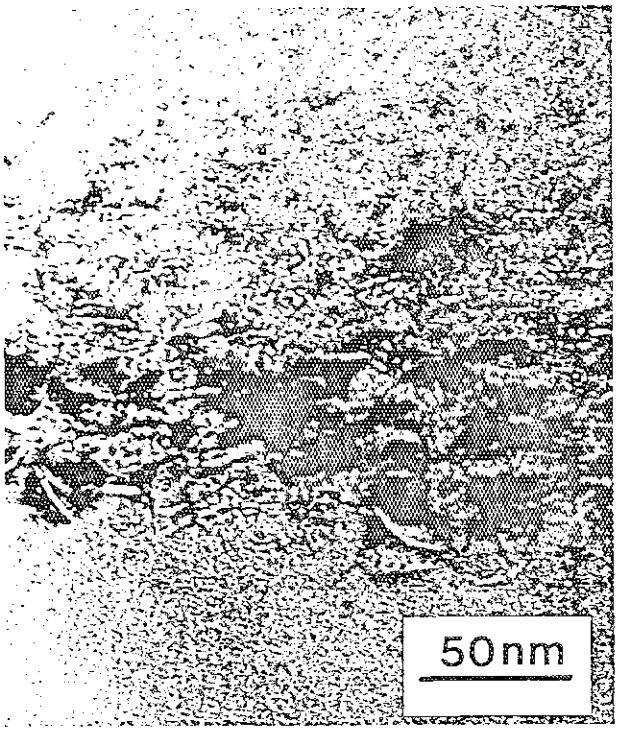

Fig.5 Alined cavities in SiC He-irradiated to 1×10^{20} ions/m^2 at 1023 K.

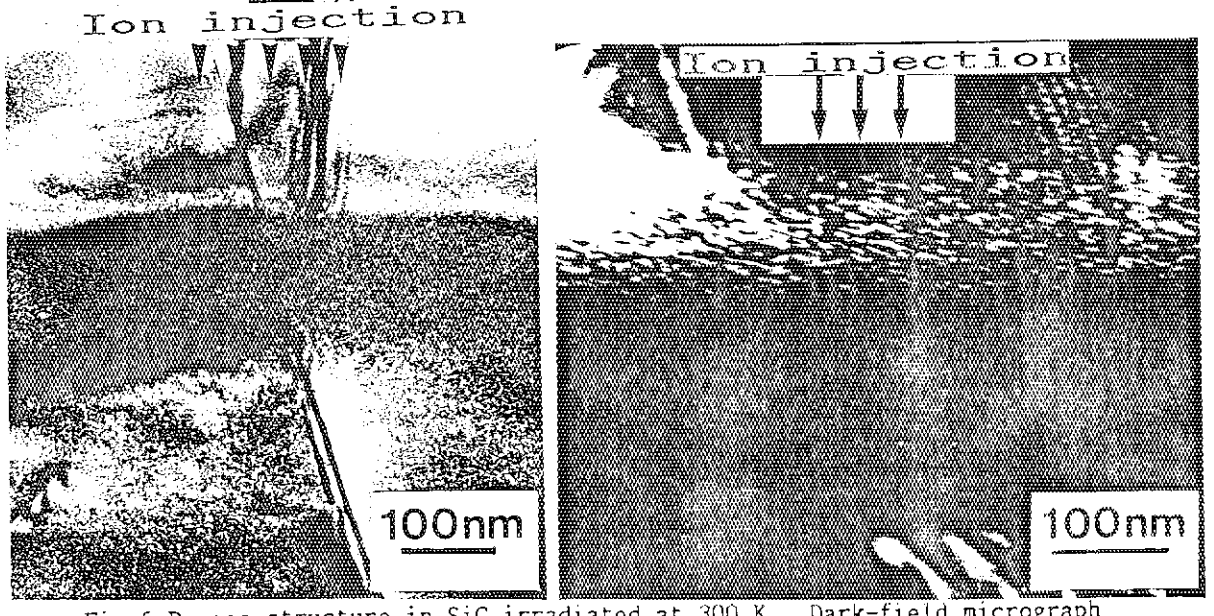

Fig.6 Damage structure in SiC irradiated at 300 K. Dark-field micrograph of high damaged region(right).

with a high density of He atoms, and the alined bubbles seem to be formed on the c planes and along radiation-induced dislocations.

In the sample irradiated at 300 K, three well defined layers appear in the direction of depth from the ion-bombarded surface as shown in Fig. 6. Small defect clusters are observed as black dots in the layer from surface to 1.1 μm in depth; the density of defect clusters increases extremely over about 1.0 μm in depth. The second layer between 1.1 and 1.25 μm is considered to be amorphous from the result of electron diffraction analysis, and neither grain boundary and stacking fault existed before irradiation nor radiation-induced defects can be seen in the layer. In the thin layer behind the amorphous zone, the defect clusters are also observed. No cavities can be found in the layers. Since the amorphous zone is found in the region with a higher concentration of He atoms slightly behind the damage peak depth, the injected He atoms seem to play an important role in the amorphization of SiC crystal.

4. Summary

The microstructural change due to 400 keV He ion-irradiation at temperatures of 300 and 1023 K has been investigated by cross-sectional observation in SiC.

(1) The experimental damage peak depth from the ion bombarded surface is in a good agreement with the calculated one.

(2) In the case of 1023 K irradiation up to 1×10^{20} ions/m^2, alined He bubbles are formed on the c planes and along radiation-induced dislocations.

(3) In the 300 K irradiation, the amorphous zone is formed slightly behind the region of defect clusters produced.

References

1) For example; L. H. Rovner and G. R. Hopkins: Nucl. Tech. 29 (1976) 274.
2) F. W. Clinard,Jr., G. F. Hurley and R. W. Klaffky: Res. Mechanica, 8 (1983) 207.
3) F. W. Clinard,Jr. and L. W. Hobbs: Physics of Radiation Effects in Crystals, eds. R. A. Johnson and A. N. Orlov (North-Holland, Amsterdam, 1986) pp. 387.
4) T. Aruga: JAERI M 83-226 (1984) pp. 1; K. Nakata, S. Takamura, T. Aruga and M. Kobiyama: J. Nucl. Mater. 151 (1988) 301.
5) K. Hojou, S. Furuno, H. Otsu, K. Izui and T. Tsukamoto: J. Nucl. Mater. 155-157 (1988) 298.
6) K. Hojou and K. Izui: J. Nucl. Mater. 160 (1988) 147.

3.4 ELECTRON MICROSCOPIC OBSERVATION OF LITHIUM ALUMINATE IRRADIATED WITH OXYGEN IONS

Kenji NODA, Yoshinobu ISHII, Kotaro KURODA*,
Masakatsu SASAKI*, Hiroyasu SAKA* and Hitoshi WATANABE

Department of Fuels and Materials Research, JAERI, *Faculty of Engineering, Nagoya University

Ceramic materials for nuclear energy application are subjected to radiation such as neutrons etc. The radiation induces degradation of the dimensional stability and the functional performance. Researches of radiation-resistance ceramic materials are very important to develop new nuclear energy systems including fusion reactors and to improve the performance and reliability of current fission reactors.

In the present study irradiation damage of lithium aluminate ($LiAlO_2$) which is one of lithium ceramic materials for breeder blanket of D-T fusion reactors was investigated using oxygen ion irradiation.

$LiAlO_2$ thin disks were obtained by cutting and lapping the sintered pellets (bulk density; about 100 %)[1] with a diamond cutter and emery papers, respectively. The disks were thinned by ion-beam milling, to make specimens for transmission electron microscopic observation. The $LiAlO_2$ specimens were irradiated by oxygen ions with an energy of 400 KeV using 2 MV VDG (Van de Graaff accelerator) at JAERI. Microstructures of unirradiated and irradiated specimens were observed with a 200 KV transmission electron microscope.

An electron micrograph of dark field image and an electron diffraction pattern of an unirradiated $LiAlO_2$ specimen are shown in Fig. 1. As seen in the electron micrograph, the unirradiated specimen consisted of relatively large grain (grain size; larger than several μ). The electron diffraction pattern with clear Kikuchi lines suggests that the crystallinity of the grain was fairly good.

Fig. 2 shows an electron micrograph of bright field image and an electron diffraction pattern of $LiAlO_2$ specimens irradiated to 1.3×10^{21} ions/m^2 by oxygen ions with an energy of 400 KeV. Remarkable change due to the irradiation could not be found in the electron micrograph. It is, however, observed in the electron diffraction pattern that diffused inten-

sity maxima were superimposed on diffraction spots due to $LiAlO_2$ crystal. This may suggest that small amounts of another phase such as $LiAl_5O_8$ were formed or amorphization occurred very slightly. In contrast with this, complete amorphization due to the irradiation was observed for SiC and $YBa_2Cu_3O_{7-x}$ irradiated to $1.4X10^{21}$ ions $/m^2$ by nitrogen (400 KeV) or oxygen (1 MeV) ions[2]. In an optical absorption spectroscopic study of $LiAlO_2$, no prominent absorption band due to irradiation defects was found for the sintered specimens irradiated to $1.4X10^{21}$ ions $/m^2$ by oxygen ions with an energy of 1 MeV[3]. From these, $LiAlO_2$ seems to be have considerably high resistivity to irradiation damage.

References

1) S. Hirano, T. Hayashi and T. Kageyama: J. Am. Ceram. Soc. 70 (1987) 171.

2) K. Noda, Y. Ishii, K. Kuroda, M. Sasaki, M. Suginoshita, T. Imura, H. Saka and H. Watanabe: JAERI-M 88-181 (1988) p.76-79.

3) K. Noda, Y. Ishii, H. Matsui, H. Ohno, S. Hirano and H. Watanabe: J. Nucl. Mater. 155-157 (1988) 568.

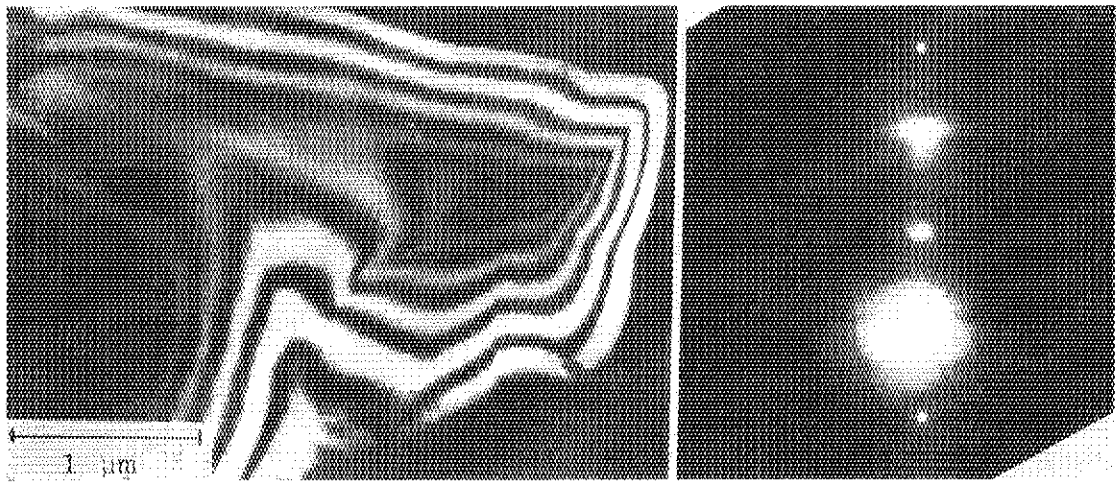

Fig.1 An electron micrograph and an electron diffraction pattern of unirradiated $LiAlO_2$.

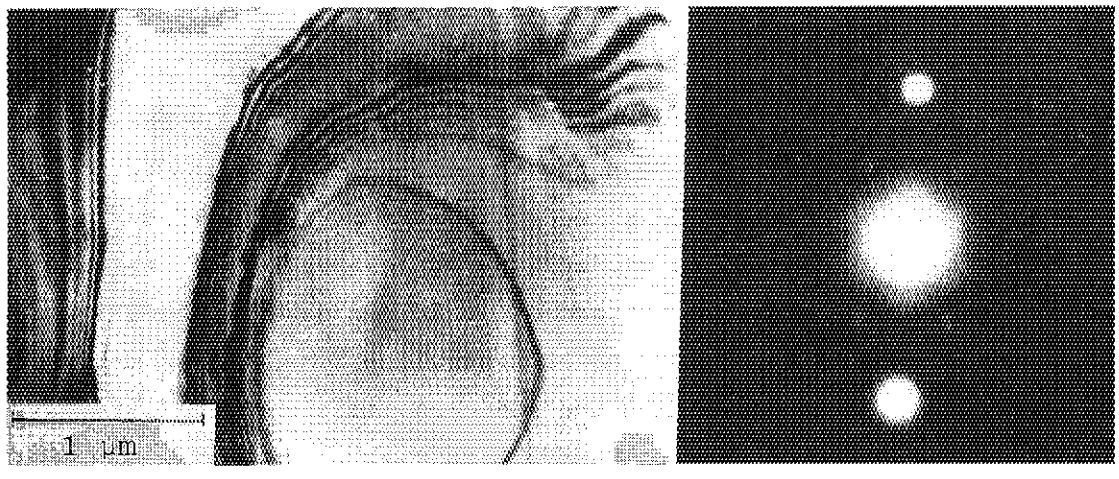

Fig.2 An electron micrograph and an electron diffraction pattern of $LiAlO_2$ irradiated to 1.3×10^{21} ions/m^2 by oxygen ions with an energy of 400 KeV.

3.5 Defect Production by Electron Excitation in FCC Metals Irradiated with High Energy Heavy Ions

Akihiro IWASE, Tadao IWATA, Takeshi Nihira* and Shigemi Sasaki

Department of Physics, JAERI, *Faculty of Engineering, Ibaraki University

In previous papers[1-3], we pointed out that the electron excitation by high energy heavy ions could cause the radiation annealing (defect annihilation during irradiation) in FCC metals with a strong electron-phonon interaction. In this paper, we present the possibility of defect production by electron excitation in Ni and Cu. The experiment was performed as follows; the thin foils of Ni and Cu about 0.2-0.25μm thick were irradiated with 84-126 MeV heavy ions. During the irradiations the electrical resistivity change $\Delta\rho$ was measured as a function of ion fluence. The temperature of the specimens was held below 10 K during the irradiations and resistivity measurements. The experimental results were analyzed using a new model which describes the defect production and radiation annealing of several types of defects, where the respective defect concentration is expressed as a function of ion fluence. The detail of the analysis will be published elsewhere[3]. Figures 1 and 2 show the examples of damage production rate curves, where the damage production rates in Ni and Cu are plotted on a log scale as a function of ion fluence. The figures show that the damage production rate curves can be expressed as the sum of 2 or 3 exponential functions of ion fluence. From the gradient and the extrapolated value to $\Phi=0$ of each straight line, we can determine the defect production cross section and the cross section of radiation annealing for each type of defects, and the initial value of damage production rate ($dC/d\Phi$ at $\Phi=0$) gives the total defect production cross section σ_d^{exp}. Figure 3 shows the damage efficiency, which is defined by the ratio of experimental defect production cross section σ_d^{exp} to the calculated one, is plotted as a function of PKA median energy $T_{1/2}$, for Ni and Cu irradiated with ∿100 MeV ions. For comparison, the results for ∿1

MeV ion irradiations are also plotted. In the case of ∿1 MeV ion irradiations, the dependence of the damage efficiency on $T_{1/2}$ is about the same in Ni and Cu. This means that, for ∿1 MeV ion irradiations, the elastic collisions dominate the defect production and radiation annealing in Ni and Cu. On the other hand, the damage efficiency for ∿100 MeV ion irradiated Cu is much larger than for ∿1 MeV ion irradiation. This result suggests that the high density electron excitation by ∿100 MeV ions can produce the lattice defects in Cu. The defect production by electron excitation is expected also in Ni irradiated with ∿100 MeV ions. The radiation annealing by electron excitation is, however, much larger in Ni than in Cu[3]. Therefore, We can hardly observe the enhancement of defect production in Ni, and the effective damage efficiency for ∿100 MeV ion irradiated Ni is smaller than for Cu as can be seen in Fig. 3.

References

1) A. Iwase, S. Sasaki, T. Iwata and T. Nihira, Phys. Rev. Lett. 58 (1987) 2450.
2) T. Iwata and A. Iwase, Rad. Eff. in press.
3) A. Iwase, T. Iwata, S. Sasaki and T. Nihira, Phys. Rev. B to be published.

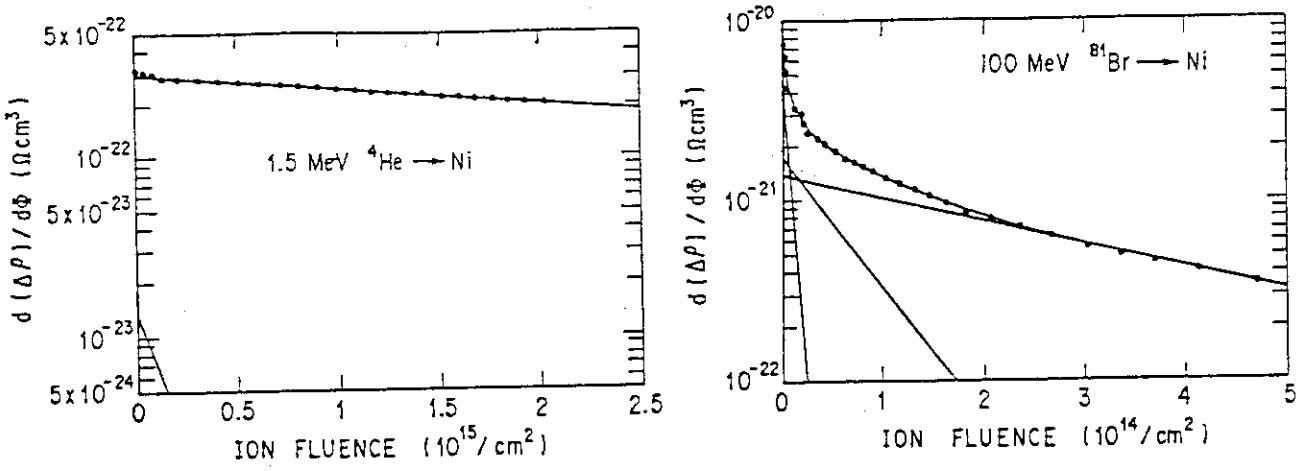

Fig. 1 Analysis of damage production rates as a function of ion fluence in ion-irradiated Ni. Experimental data (solid circles) can be reproduced by the sum of 2 or 3 exponential functions.

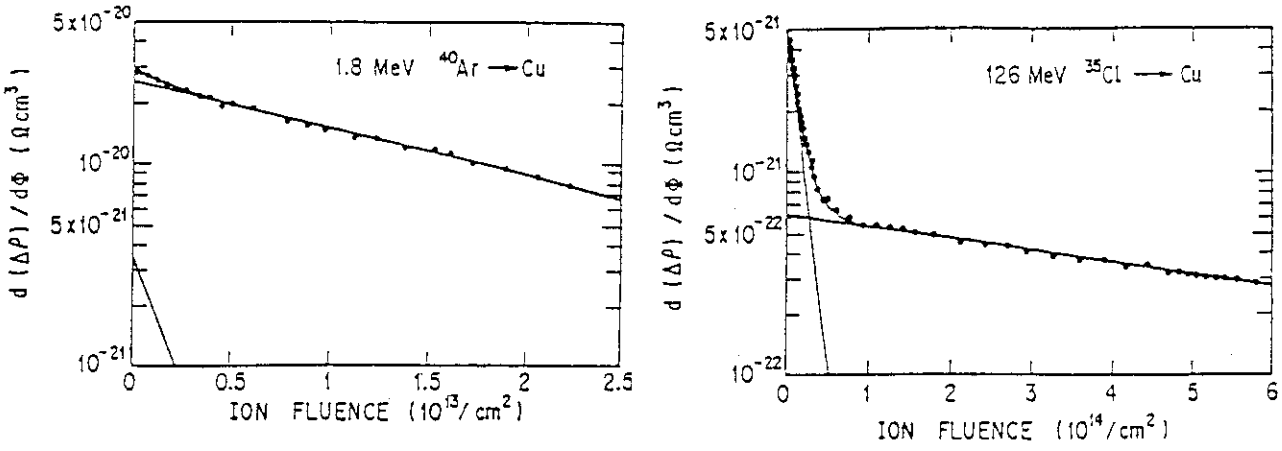

Fig. 2 Same as FIG.1 except in Cu.

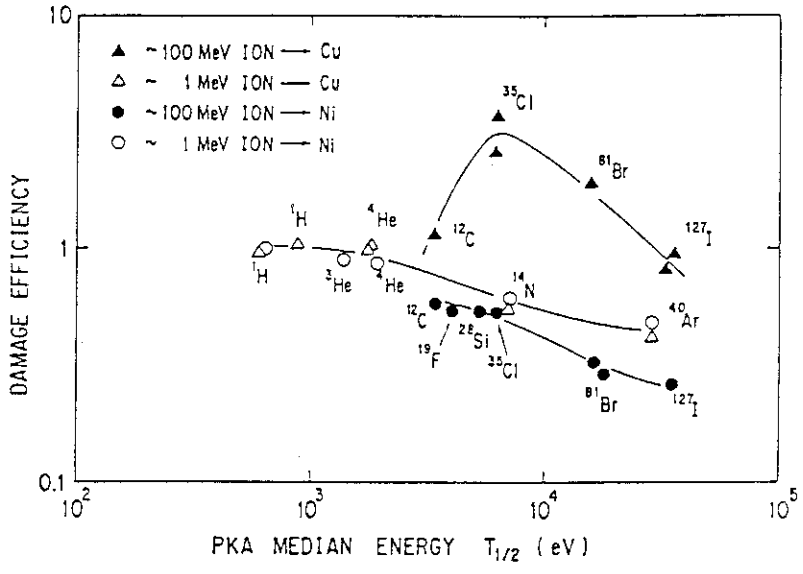

Fig. 3 Damage efficiency vs. PKA median energy in Ni and Cu irradiated with ∿1 MeV and ∿100 MeV ions. Scale of the ordinate is logarithmic.

3.6 A STUDY OF X-RAY DIFFRACTION ON ION IRRADIATED GaAs CRYSTALS

Hiroshi MAETA, Katsuji HARUNA*, Kazutosi OHASHI*, Takuro KOIKE* and Fumihisa ONO**

Department of Physics, JAERI, *Faculty of Engineering, Tamagawa University, **College of Liberal Arts and Sciences, Okayama University

1. Introduction

Irradiation of materials with energetic ions produces displacement cascade containing high local concentrations of vacancy-interstitial pairs, and at an elevated temperature these vacancies and interstitials aggregate to form clusters such as dislocation loops, stacking fault, tetrahedra, or voids. Investigations of these cascades and their thermal annealing process by transmission electron microscopy and field ion microscopy have provided a considerable amount of information . However, additional quantitative information regarding cascade sizes, morphologies, internal defect densities, and thermal evolution is need for further understanding of the physics of defect production and defect interaction. Usually, the energetic ion irradiation makes an inhomogeneous damaged region within the penetration range. This effect makes it difficult to analyze the data so far obtained by various experiments. Therefore, it is needed to develop the ion irradiation technique to get an uniformly damaged region[1,2].

In this work, we have explored an irradiation technique to make an uniformly damaged region varying the ion energy. The damaged area in a GaAs specimen was investigated by X-ray diffraction measurements, and the applicability of this technique for study of radiation effects is discussed.

2. Experimental Procedures

GaAs single crystals with <111> orientation were irradiated at liquid nitrogen temperature with He ion using 2MV VdG Accelerator. The specimens were irradiated in non channeling direction with ions of energy from 0.25 to 1.5 MeV. The fluences at the various energies were chosen by fitting

EDEP1 damage energy calculations to obtain a constant number of the defects produced by the He ion as a function of depth in the crystal. Fig. 1 shows the calculated number of the defect to be dpa = 0.001 for the He ion irradiation using 14 energy steps of ions (0.25, 0.3, 0.4, 0.5, 0.6, 0.7, 0.8, 0.9, 1.1, 1.2, 1.3, 1.4, 1.5 MeV). Total dose is correspond to 5×10^{14} ions/cm^2. After the irradiation the specimens were warmed up to room temperature. Then, x-ray measurements were carried out. By using a CuK_α beam through a fine slit of 0.2 mm in width, the measurements of the lattice parameter were carried out by the Bond method in which two counters were placed symmetrically.

3. Results and Discussion

Remarkable changes of diffraction profiles have been in the irradiated GaAs specimen. An extra peak appeared after He ion irradiation, as seen in Fig. 2. The additional peak is located on the lower angle side of the Bragg peaks . This peak comes from the irradiated region. It is due to the volume expansion in the irradiated region where the defects would cause increase in the lattice parameter.

The lattice parameters by the Bond method are presented in table 1 together with the values of the lattice parameters in the opposite side of

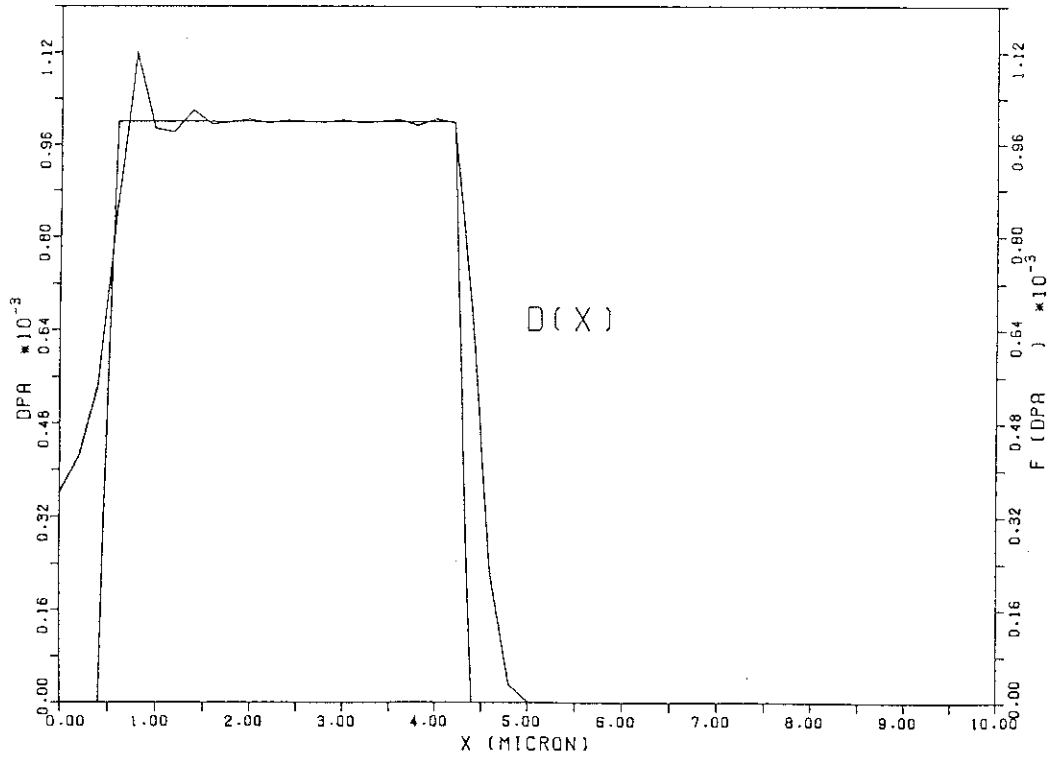

Fig 1. Damage profile for the He-ion irradiation of GaAs.

the irradiated specimen and the unirradiated specimen. The fractional change in the lattice parameter is found to be $\Delta a/a_0 = 3.4 \times 10^{-4}$ for the damaged region. The values of the lattice parameters for the peak 1 which come from the unirradiated region are in good agreement with that in the opposite side of the irradiated specimen and nonirradiated specimens. From this fact it is concluded that the slightly larger lattice parameter of the peak 2 is due to the the defects induced by ion-irradiation. We have also measured the lattice parameter of the irradiated specimen at the (333) reflection . No splitting has been seen in this peak as shown in fig 2. We did obtain the value of the lattice parameter to be 5.6550 A which is in very good agreement with the value of the lattice parameter in the irradiated region of the (444) reflection. This means that the Bragg peak is reflected only on the irradiated region at the (333) reflection.

On the other hand, in LiF specimens which were bombarded with 165 MeV Cl^{+10} ion to 10^{13} ion/cm^2 at room temperature, we found the Bragg peaks together with two peaks on lower side of the main Bragg peak. The lattice parameters in the irradiated region were an expansion $\Delta a/a_0 = 8 \times 10^{-4}$ for the region near the surface and $\Delta a/a_0 = 2.4 \times 10^{-3}$ for the heavily damaged region[3]. These two peaks come from the normally irradiated region and the more heavily irradiated area where the defects were not produced uniformly and profile of the reflection appeared as two peaks associated with the main Bragg peak.

From the present experiment it is shown that the controlled ion energy irradiation produces an uniformly irradiated region in near surface of the specimen. This method is useful for the study of radiation damage experiments.

A more detailed analysis of the present results and measurement of the diffuse scattering are currently in progress.

References

[1] B.C. Larson, T.S. Noggle and J.E. Barhorst ; MRS Symposia Proceedings Volume 41 " Advanced Photon and Particle Techniques for the characterization of Defects in Solids ed. J.B. Roberto et al. p25('85).

[2] H. Maeta, B.C. Larson, T.P. Sjoreen, O.S. Oen and J.D. Lewis ; to be published in MRS Symposia Proceedings Vol. 138 (1989).

[3] H. Maeta, K. Haruna, K. Ohashi, T. Koike and F. Ono ; JAERI TANDEM, LINAC & V.D.G. Annual Report 1986, p 65.

Table 1

The lattice parameters of GaAs single crystal irradiated and unirradiated regions and opposite side regions of the irradiated specimen by the He ion at liquid nitrogen temperature.

	Peak 2 damaged region	Peak 1 undamaged region	Opposite side region of the irrad. specimen	Nonirradiated specimen
lattice parameter (A)	5.6551	5.6535	5.6532	5.6533

$\Delta a/a_0 = 0.034$ %

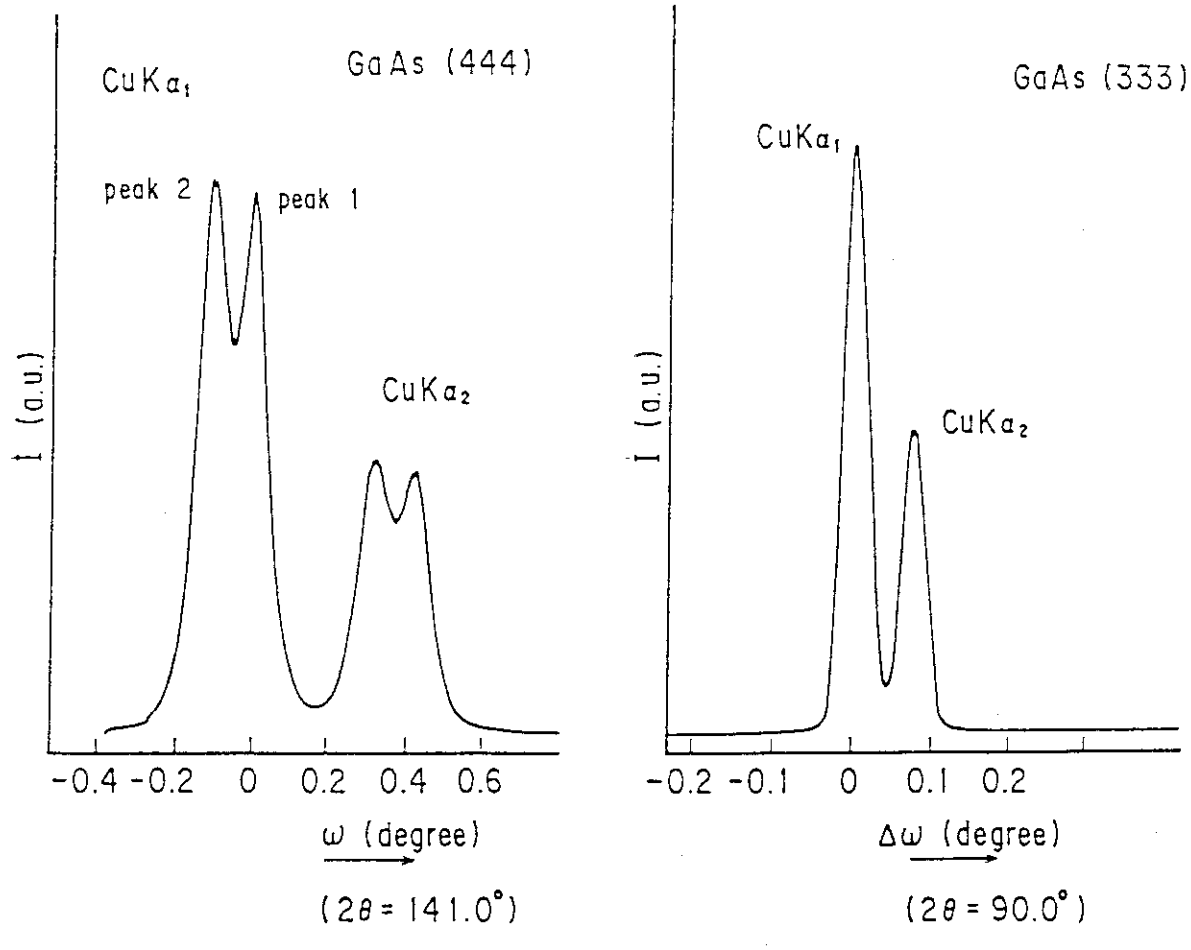

Fig. 2 X-ray profile of GaAs crystal after the irradiation with the He ion irradiation .

3.7 PRECISE X-RAY OBSERVATION OF Si SINGLE CRYSTALS IRRADIATED WITH ENERGETIC HEAVY IONS (7)

Hiroshi TOMIMITSU

Department of Physics, JAERI

1.Introduction

From the conventional X-ray diffraction topographic observation on more than 50 pieces of the Si single crystals irradiated with energetic heavy ions, the present author has reported the following conclusions[1,2]:

1) In more than 50% of the specimen examined, macroscopic deformation through the crystal due to the ion-irradiation was recognized.
2) Almost all the specimens examined sustained heavy lattice-strains which concentrated at the boundaries between the irradiated- and non-irradiated areas.
3) Regularly arrayed systematic fringes were observed within the irradiated area in more than 70% of the specimen. The origin of such interference fringes seems to be caused by the inhomogeneous distribution of the projectile ions, just as assumed by Bonse, Hart and Schwuttke[3,4]. It would be emphasized, however, that several of the specimens are not applied in the case, and the results observed apparently contradict with their assumption.
4) In more than 60% of the specimens examined, irregular contrasts were observed within the irradiated ares, and they seemed to indicate the disordered lattice caused by the ion-irradiation.

In order to reveil the origin of the interference fringes mentioned above (3), so-called a double crystal X-ray diffraction method was applied to those specimens, and preliminary results will be reported in the present article.

2.Experimental Procedure

The preparation of the Si wafers used in this experiment and the procedures of the ion-irradiation of the wafers are reported in the Ref.4.

The experimental set-up of the X-ray double crystal diffraction method is shown in Fig.1. Here, the monochromator crystal(M) is as perfect as the

specimen crystal(S) before the ion-irradiation, when both of the reflecting planes of M and S are the same to each other, the FWHM of the rocking curve is very small, as shown in Fig.2-a, as an example. Therefore, one can observe the crystal-imperfections with the angular resolution of about 0.5", which corresponds to the relative deviation of the crystal lattice constant of about 10^{-6}.

3.Results

As the measurement has been just started, only very preliminary results can be briefly reported;

1) The lattice constant is measured by the present double crystal diffraction set-up. Fig.3 shows the example of the 333 peaks with +,+ reflection and +,- reflection, respectively. The lattice constant thus measured agreed well with the known value,which showed the credibility of the present method.

2) As for the specimen irradiated with $^{12}C^{+6}$ (100MeV) ion with the dose of around 3×10^{15}ions/cm^2, an example of the rocking curve of 333 reflection in the transmittion case is shown in Fig.2-b, which shows much complicated profile, compared with the original Si wafer without ion-irradiation(Fig.2-a).

Further investigations are now in progress.

The author is much indebted to Drs. Abe and Masui of Shinetsu-Handotai Co. for their kind offering him the Si wafers used in this experiment.

References

1) H.Tomimitsu: Jpn.J.Appl.Phys. **22** (1983) L674.
2) H.Tomimitsu: JAERI-M Report No.88-181(1988) pp84-87.
3) G.H.Schwuttke, K.Brack, E.E.Gardner and H.M.DeAngelis: Proc. Santa Fe Conf.Radiation Effects in Semiconductors, ed. F.Vook,(Plenum Press,N.Y., 1968) pp.406.
4) U.Bonse, M.Hart and G.H.Schwuttke: Phys.Stat.Solidi **33** (1969) 361.

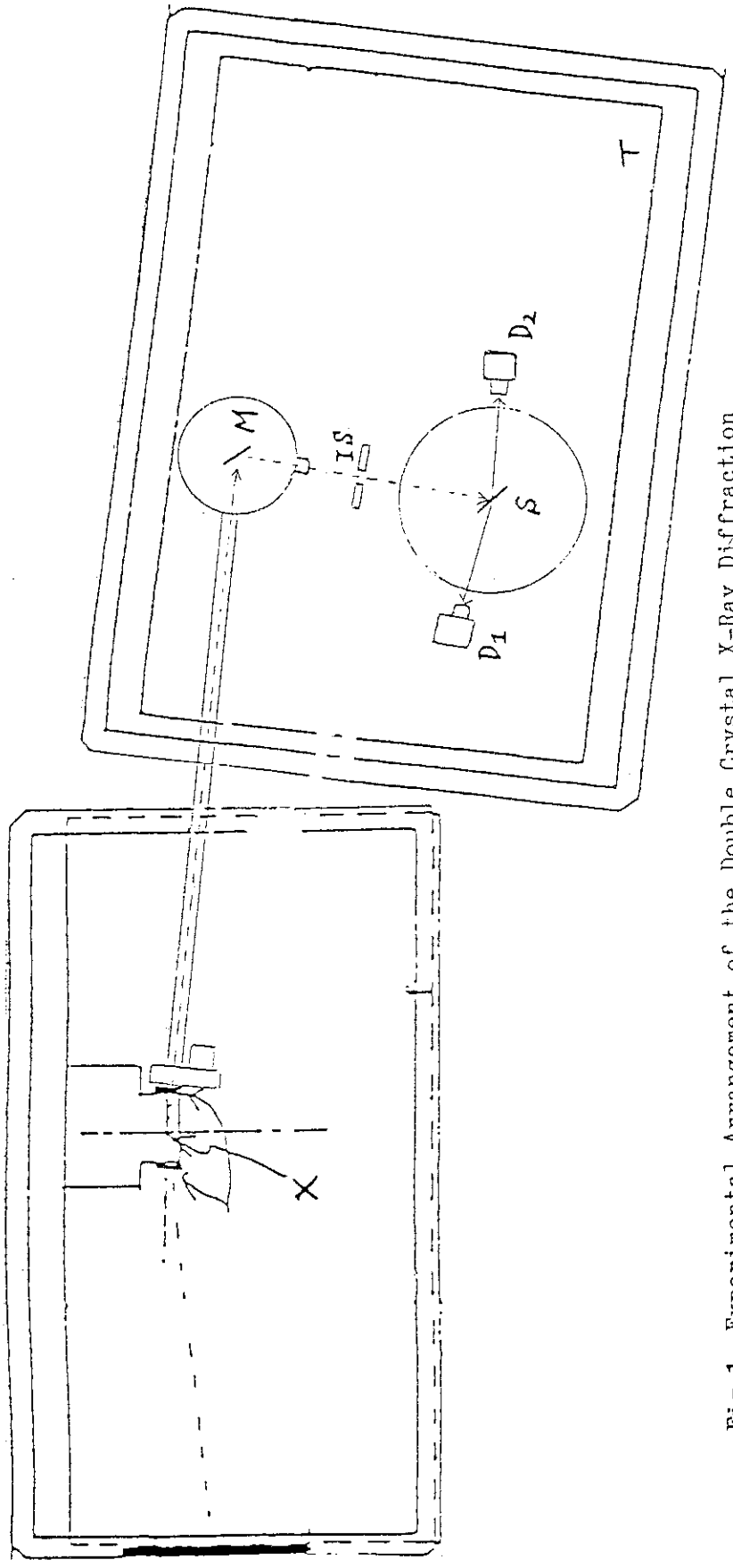

Fig.1 Experimental Arrangement of the Double Crystal X-Ray Diffraction

X: X-Ray Focus (Cu-Target, Effective Size:1x1mm2, Power:55kVx250mA)

M: Monochromator Crystal in a Radiation-Shielding on a Single-Axis Goniometer

IS: Incidence Slit with Variable Cross-Section

S: Specimen Crystal on a High Anguler-Resolution Goniometer

D1, D2: Detectors for (+,+) and (+,-) Reflections, respectively

T: Vibration-Free Table in the Temperature Regulated Atomosphere

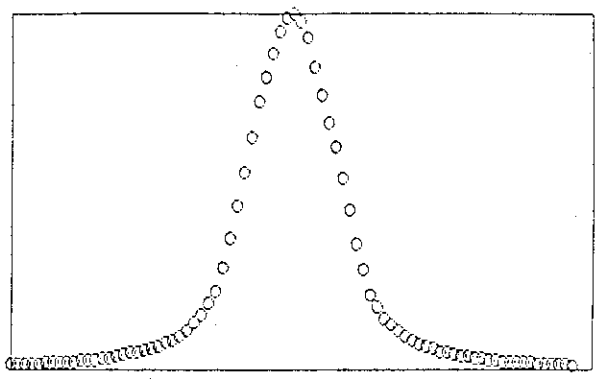

Fig.2-a Rocking Curve of the Standard Si Wafer without Ion-Irradiation, the FWHM being about 2.6", by 333 Refletion in Bragg-case with the 333 monochromator reflection.

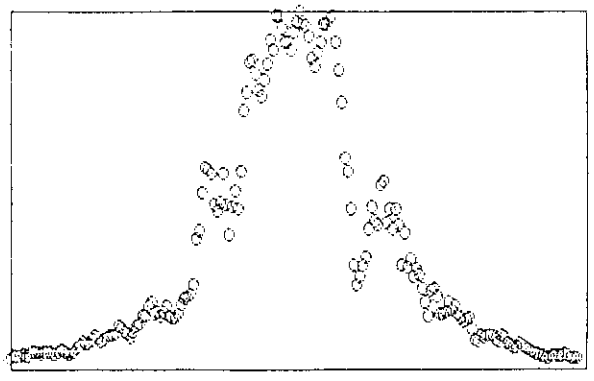

Fig.2-b An Example of the Rocking Curve of a C-Irradiated Si Wafer, by 333 Reflection in Bragg case.

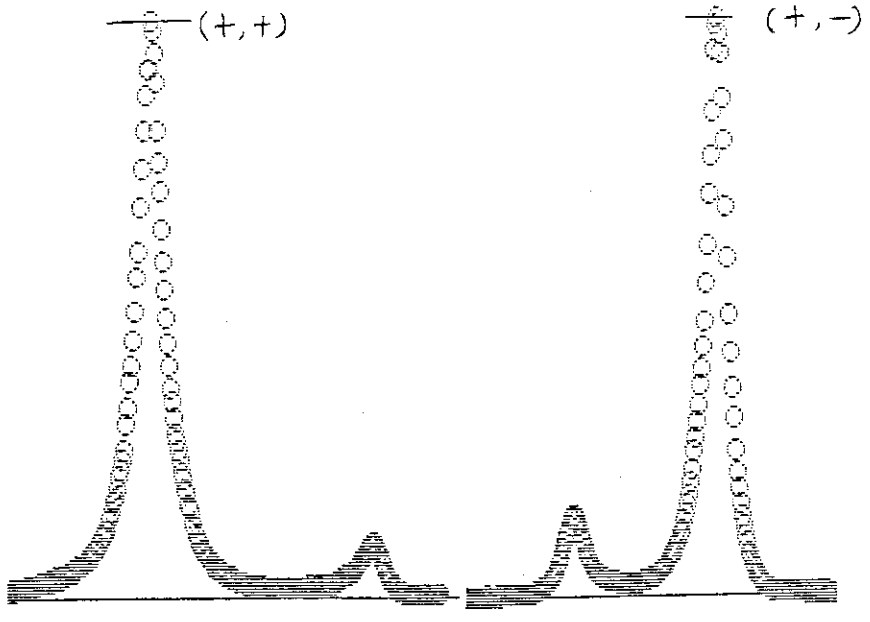

Fig.3 Profile with Very Wide Range Angular Scanning, Showing 2 Main Peaks by Cu-$K_{\alpha 1}$ Radiation and 2 Smaller Peaks by $K_{\alpha 2}$, Giving the Lattice Constan of Well-Known Value. 333 Reflections were used.

3.8 Effect of 120 MeV ^{16}O Ion Irradiation on Electronic Properties of La_2CuO_4

Akihiro IWASE, Norio MASAKI, Tadao IWATA and Takeshi NIHIRA*

Department of Physics, JAERI, *Faculty of Engineering, Ibaraki University

Recently, there has been great interest in La_2CuO_4 because this material is the parent compound of the doped high-temperature superconductors $La_{2-x}(Sr/Ba)_xCuO$, and exhibits both filamentary superconductivity and antiferromagnetic transition. Concerning the irradiation effect on the properties of La_2CuO_4, Yoshida and Atobe reported that the superconducting transition was induced by neutron irradiation in the insulating La_2CuO_4[1], and Groult et. al. reported that 2.9 GeV Kr ion irradiation increased the transition temperature in La_2CuO_4 which showed the filamentary superconductivity.[2]

In this paper, we present the effect of 120 MeV ^{16}O ion irradiation on the electronic properties of La_2CuO_4. The samples used in the present experiment were carefully prepared by the following two different methods from aqueous solution of La- and Cu-nitrate in the appropriate ratio. Method (A); the solutions were dried with an infrared lamp heater and were washed with ethanol several times to remove completely all traces of water. The well-mixed materials were calcined at 400^0 C for 2 hours in air . Method (B) (precipitation method); by adding an aqueous solution of oxalic acid to the solutions, an intimate mixture of the corresponding oxalate was formed. The resulting precipitated mixture was filtered and then the precipitate was heated at 1000^0 C for 15 hours in air.
Electrical resistance measurements by four probe method were performed using 1mmx1.2mmx0.1mm La_2CuO_4 ceramics which were prepared by sintering the pressed powder at 950^0 C for 15 hours. Hereafter, the sample prepared by method (A) is called sample (1) and those prepared by method (B) are called sample (2) and (3).

Figures 1 and 2 show the temperature dependence of the electrical resistance for samples (1) and (3), respectively. The result for sample (2) is about the same as for sample (3). At high temperature, the resistance of every sample increases slowly with decreasing temperature and there is an anomaly around 250 K which is caused by an antiferromagnetic transition. At lower temperature, the resistance for sample (1) decreases steeply below ∿40 K with decreasing temperature. On the other hand, for samples (2) and (3), though a small anomaly appears at ∿40 K, the resistance increases with decreasing temperature even below ∿40 K. This difference at low temperature will be due to the difference in the oxygen-defect concentration[3] which depends on the method of sample preparation. Samples (1), (2) and (3) were irradiated with 120 MeV ^{16}O ions at 8 K, 77 K and room temperature, respectively. During the irradiations the change in the electrical resistance was measured as a function of ion fluence. As can be seen in Figs. 3 and 4, for samples (2) and (3) the resistance increment by irradiation tends to saturate at higher ion fluence. On the other hand, for sample (1) which was irradiated at 8 K the resistance increases exponentially with increasing the ion fluence.(See Figs. 5 and 6.)

After the irradiations the electrical resistance were measured as a function of temperature from 4.2 K to 300 K. The results are shown in Figs. 1 and 2 for sample (1) and (3), respectively. The result for sample (2) is about the same as for sample (3). The effect of O ion irradiation on the temperature dependence of the electrical resistance is as follows; the anomaly around 250 K, which is due to the antiferromagnetic transition, disappears after the irradiation, and the small anomaly at ∿40 K also disappears in samples (2) and (3) after irradiation. Irradiation induced superconducting transition, which has been reported previously[1-2], was not observed in the present experiment.

References

1) H. Yoshida and K. Atobe, Physica C 153-155 (1988) 337.

2) D. Groult, J. Provost, B. Raveau, F. Studer, S. Bouffard, J. C. Jousset, S. J. Lewandowski, M. Toulemonde and F. Rullier-Albenque, Europhys. Lett., 6 (1988) 151.

3) For example, D. C. Johnston, J. P. Stokes, D. P. Goshorn, and J. T. Lewandowski, Phys. Rev. B, 36 (1987) 4007.

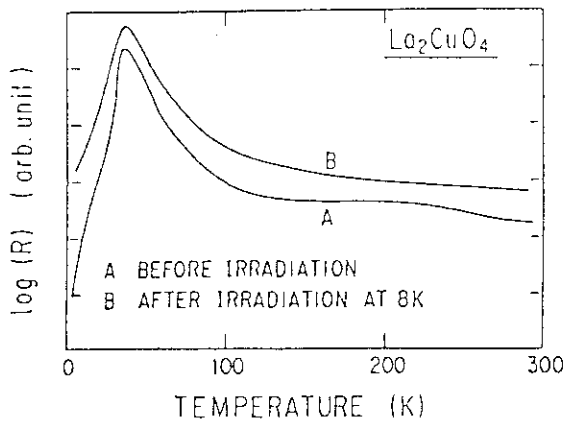

Fig. 1 Electrical resistance R vs. temperature for sample (1) before and after 120 MeV O ion irradiation.

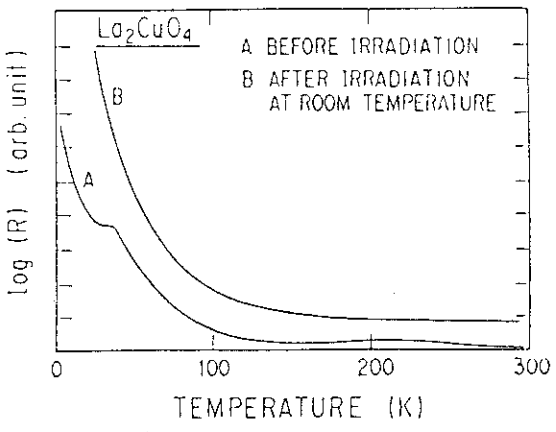

Fig. 2 Electrical resistance R vs. temperature for sample (3) before and after 120 MeV O ion irradiation.

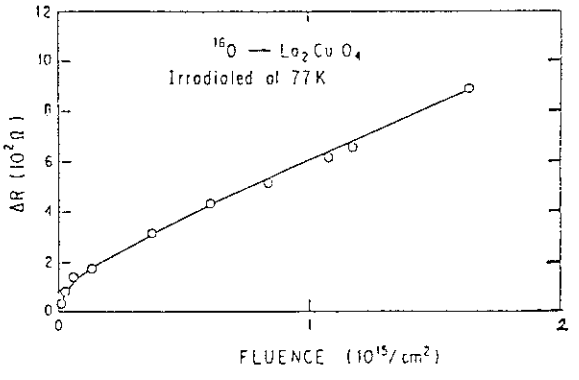

Fig. 3 Change in electrical resistance ΔR as a function of O ion fluence for La_2CuO_4 irradiated at 77 K (sample (2)).

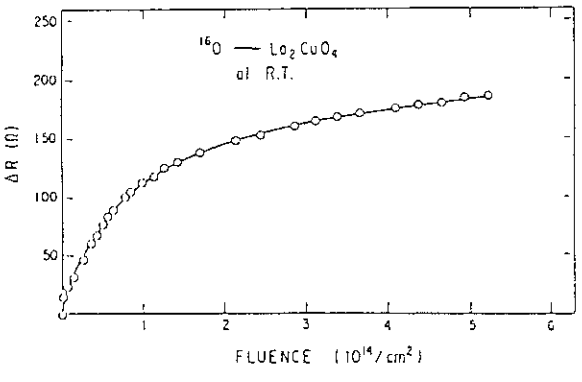

Fig. 4 Change in electrical resistance ΔR as a function of O ion fluence for La_2CuO_4 irradiated at room temperature (sample (3)).

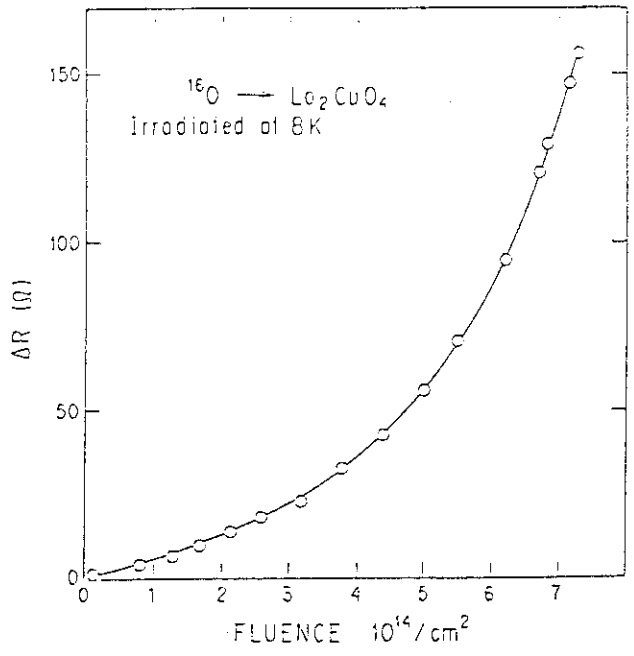

Fig. 5 Change in electrical resistance ΔR as a function of O ion fluence for La_2CuO_4 irradiated at 8 K (sample (1)).

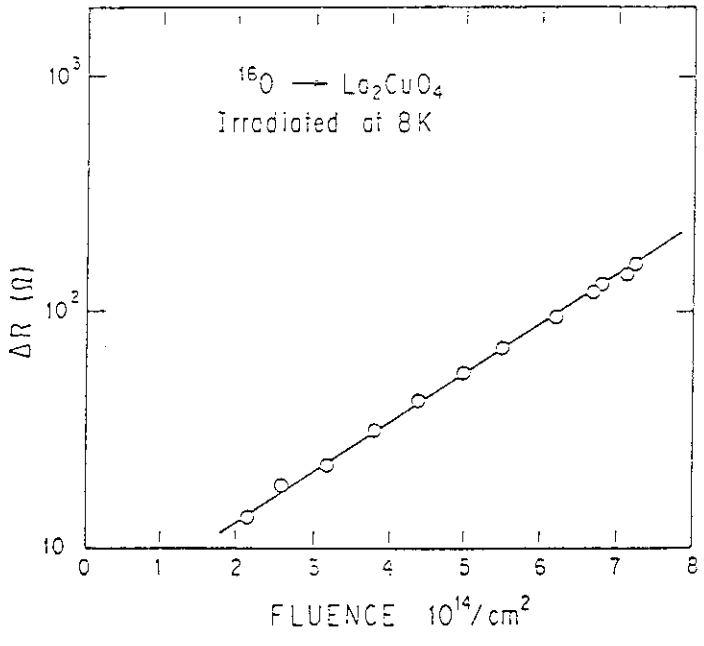

Fig. 6 Same as FIG. 5 except that ΔR is plotted on a log scale.

3.9 EFFECTS OF He ION IRRADIATION ON SUPERCONDUCTIVITY OF Bi-Sr-Ca-Cu-O FILMS

Takeo ARUGA, Saburo TAKAMURA*, Taiji HOSHIYA**
and Mamoru KOBIYAMA***

Department of Fuels and Materials Research, *Department of Physics, **Oarai Research Establishment, JAERI, ***Faculty of Engineering, Ibaraki University

Since the discovery of high temperature superconductivity in a La-Ba-Cu-O system[1], many studies of radiation effects on superconducting properties of the La-Ba-Cu-O and Y-Ba-Cu-O systems have been made. However, there have been few experiments studying the radiation effects on a Bi-Sr-Ca-Cu-O system. Matsui et al.[2] observed a decrease in transition temperature Tc(R=0) and an increase in normal state resistivity in Bi-Sr-Ca-Cu-O films implanted with 200 keV Ne ions at room temperature. In this report, we describe the effects of helium ion irradiation on the electrical superconducting behaviors in Bi-Sr-Ca-Cu-O films at room temperature and low temperature[3].

Thin films of a Bi-Sr-Ca-Cu-O system were prepared by magnetron sputtering on MgO substrates. The films were subsequently heated at 1163 K. The thickness of the films were about 0.2 μm. Electrical resistivity measurements were performed by the standard four-probe method. The samples were irradiated with 400 keV He ions accelerated by a Van de Graaf in JAERI in a vacuum chamber at a low current density of 1 mA/m^2. The sample holder was cooled by liquid nitrogen. The temperatures of the sample during irradiation were either room temperature or 85 K. Resistance-temperature (R-T) measurements down to 4.2 K were carried out in a helium atmosphere after removing the sample from the holder. Since the ion range of 400 keV He ions in the sample was predicted to be 1.1 μm, which is five times larger than the film thickness, no He atoms remained in the sample.

The R-T characteristics are shown in Fig. 1 for the sample which was sequentially irradiated by He ion fluences from 0 (no irradiation) to $1.9\times10^{19}/m^2$, as a maximum, at room temperature. The Tc(onset), defined here as an intersection point of the two straight lines around the

transition region, changed little from a fluence of 0 to $1.1 \times 10^{19}/m^2$. The Tc(R=0), Tc(midpoint) and Tc(onset) are plotted in Fig. 2 as a function of the fluence, along with the resistivity at 130 K in the normal state resistance region. As shown in the figure, both the Tc(R=0) and the resistivity change, apart from the linear change, with increasing the fluence. The fact indicates that the radiation-induced defects, which would be accumulated by the sequential irradiations, begin to interfere with each other so as to accelerate the deterioration of the superconductivity for the fluences in the present study. The deviations from the linear change of Tc(R=0) or resistivity were reported for Y-Ba-Cu-O films irradiated at room temperature with various kinds of ions[4].

Another sample was sequentially irradiated at 85 K with He ions and the R-T characteristics is shown in Fig. 3. The resistivities at 130 K are shown in Fig. 2 as a function of the fluence. The irradiation up to $2 \times 10^{18}/m^2$ induces a 70 % increase in the electrical resistance at 130 K, and the resistances no longer increase with raising temperatures to 300 K. We observe that heating to 160 K when measuring resistances induces fractional reduction of the resistances, as shown by the differences between the solid curve (3) and dashed curve (4), below 160 K, in Fig. 3. Further annealing to 300 K during measurement of curve (4) results in about 50 % reduction of the increased resistance at 130 K, as shown by the differences between curves (4) and (5). Moreover, the Tc(R=0) is found to be depressed to 73 K, which is comparable to that observed after the irradiation at the higher dose of $1.1 \times 10^{19}/m^2$ at room temperature (Fig. 1). After prolonged irradiation from 2 to 9 ($\times 10^{18}/m^2$) and subsequent heating to 320 K, the reduction of resistance is observed, as shown in the two R-T curves of (6) and (7) in the figure. The fractional reduction of the resistance at 130 K is 35 % of the resistance increase, which is increased by the prolonged irradiation; it is noted that the fraction is smaller than that observed at the first annealing to 300 K after the irradiation to $2 \times 10^{18}/m^2$. Furthermore, the superconducting behavior disappears down to 4.2 K after irradiation to $9 \times 10^{18}/m^2$ at 85 K and subsequent annealing to 320 K. This fluence is less than a half of the maximum fluence at room temperature irradiation, where Tc(R=0) remains at 15 K. The lower temperature irradiation has already been shown to require less ion fluence to destroy

superconductivity than that at room temperature[4], which is also exhibited in the present study.

Irradiation-induced changes in Tc(R=0) and resistivity above transition are considered to depend on the displacement damage. The present 400 keV He ion irradiation to $1x10^{19}/m^2$ is calculated to correspond to 0.003 dpa of displacement damage, using an extended E-DEP-1 computer code[5], assuming the displacement threshold energy of 25 eV. The fluence at the room temperature irradiation induces the reduction of 30 K for Tc (R=0) and 13 K for Tc(midpoint) (Fig. 1, 2). Then, the decrease rate of Tc, if expressed as an average displacement damage necessary to reduce 1 K of the Tc, is calculated to be $1x10^{-4}$dpa for Tc(R=0) and $2.3x10^{-4}$dpa for Tc(midpoint). Hereafter, the rate is depicted as $1K/1x10^{-4}$dpa. This value agrees with $1K/2x10^{-4}$dpa obtained based on the reported result[2] of a 22 K decrease in Tc(R=0) for a Bi-Sr-Ca-Cu-O film implanted uniformly by 200 keV Ne ions to $9x10^{16}/m^2$. However, if compared with the Tc decrease rates in irradiated Y-Ba-Cu-O systems, the Bi-Sr-Ca-Cu-O system is more sensitive to radiation damages, e.g. less nuclear energy depositions induce Tc decrease of 1 K; for example, in a Y-Ba-Cu-O system, $1K/(6-8)x10^{-4}$dpa by Ar or Ne ion irradiations at room temperature[4]. As for a displacement damage necessary to destroy the superconductivity below 4.2 K, the present fluence for the 85 K irradiation corresponds to $2.5x10^{-3}$ dpa, which is smaller by about one order than $4.4x10^{-2}$ dpa calculated for the Bi-Sr-Ca-Cu-O film [2] cited above, or $3.5x10^{-2}$ dpa for a Y-Ba-Cu-O film irradiated with Ne ions at room temperature[4].

References

1) J. G. Bednorz and K. A. Müller: Z. Phys. B64 (1986) 189.
2) S. Matsui, H. Matsutera, T. Yoshitake, and T. Satoh: Appl. Phys. Lett. 53 (1988) 2096.
3) T. Aruga, S. Takamura, T. Hoshiya and M. Kobiyama, Jpn. J. Appl. Phys. 28 (1989), in press.
4) A. E. White, K. T. Short, D. C. Jacobson, J. M. Poate, R. C. Dynes, P. M. Mankiewich, W. J. Skocpol, R. E. Howard, M. Anzlowar, K. W. Baldwin, A. F. J. Levi, J. R. Kwo, T. Hsieh, and M. Hong: Phys. Rev. B37 (1988) 3755.
5) T. Aruga, K. Nakata and S. Takamura: Nucl. Instrum. & Methods

B33 (1988) 748.

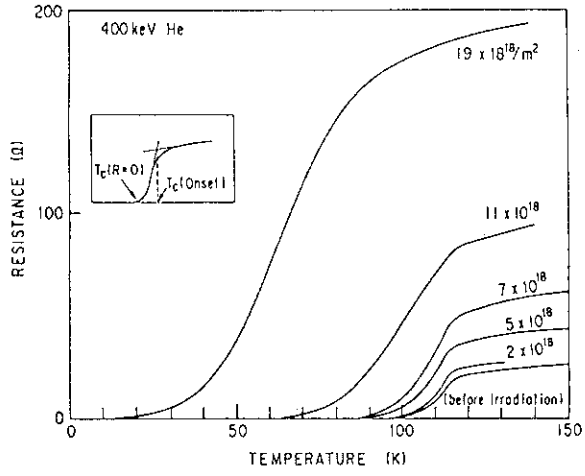

Fig. 1 Resistance versus temperature of Bi-Sr-Ca-Cu-O film irradiated with 400 KeV He ions at room temperature. Irradiation fluences are 0 (no irradiation), 2, 5, 7, 11 and 19 ($10^{18}/m^2$).

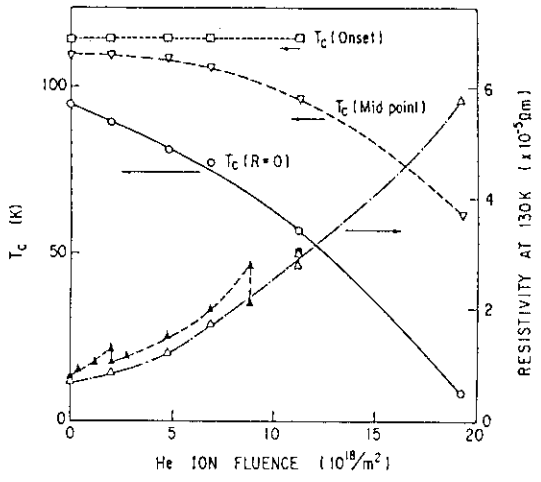

Fig. 2 Tc(onset), Tc(midpoint) and Tc(R=0), and resistiviies at 130 K versus He ion fluences for Bi-Sr-Ca-Cu-O film irradiated with 400 keV He ions at room temperature. Solid triangles represent 85 K irradiation.

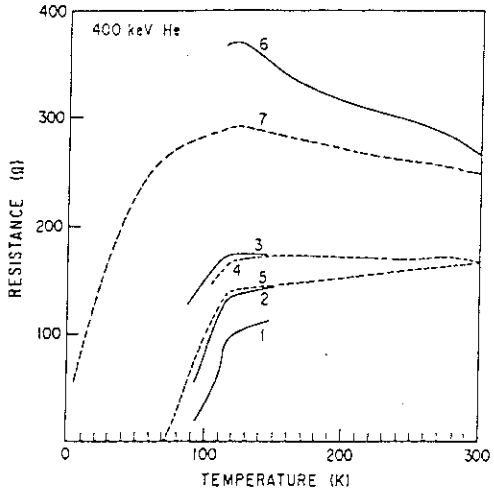

Fig. 3 Resistance versus temperature of Bi-Sr-Ca-Cu-O film irradiated with 400 KeV He ions at 85 K. Irradiation fluences in 10^{18} m^2 are 0 (no irradiation) for curve (1), 1.2 for (2), 2 for (3) and 9 for (6). Dashed curve (4) is obtained after the measurement of (3) up to 160 K. Curve (5) is obtained after annealing to 300 K in the measurement of (4) up to 300 K. Curve (7) is obtained after the measurement of (6) up to 320 K. Each measurement is taken during heating.

Ⅳ NUCLEAR CHEMISTRY

4.1 COMPLEX FRAGMENT EMISSION IN THE REACTION $^{37}Cl + ^{68}Zn$

Yuichiro NAGAME, Hiroshi IKEZOE*, Tsutomu OHTSUKI**,
Sumiko BABA, Kentaro HATA, Toshiaki SEKINE and
Kazumi IDENO*

Department of Radioisotopes, *Department of Physics, JAERI,
**Department of Chemistry, Tokyo Metropolitan University

Statistical emissions of complex fragments produced in the reaction $^{37}Cl + ^{68}Zn$ have been studied. In this report, we present the experimental results on the measurement of kinetic energy, angular and charge distributions of complex fragments. The experimental cross sections for the complex fragment formation are compared with those calculated from a statistical model which takes into account the potential energy associated with mass asymmetry and angular momentum [1]. The width of the charge (mass) distribution for the symmetric mass division is discussed as a function of angular momentum ℓ.

Beams of ^{37}Cl with energies of 156, 166 and 177 MeV obtained from the JAERI tandem accelerator were used to bombard a self-supporting target of ^{68}Zn (755 $\mu g/cm^2$). The reaction products were measured with a ΔE-E counter telescope.

Complex fragments with $5 \leq Z \leq 29$ have been detected. The characteristics of the fragments corresponding to the $1/\sin\theta_{cm}$ angular distribution were consistent with those of the fully equilibrated compound nucleus. For the above component, angle-integrated cross sections were obtained from the averaged value of $d\sigma/d\theta_{cm}$.

Figure 1 shows the integrated cross section of each fragment Z for the three values of bombarding energy. No signifficant bombarding energy dependence of the charge distribution was observed. The results of the statistical model calculation [1,2] are also shown in Fig.1 in comparison with the experimental data. The substantial agreement between experiment and calculation is obtained. This suggests that the fragment production results from the statistical binary decay of the compound nucleus.

Assuming that the symmetric mass distribution is represented by a Gaussian function, we have obtained a variance σ_A of the fragment mass distribution. In Fig.2, the variance σ_A^2 are plotted as a function of $\sqrt{<\ell^2>}$ together with the data obtained from refs. 3-7), where $<\ell^2>$ is the average angular momentum for fusion. As shown in Fig.2, th observed σ_A^2 strongly depends on $\sqrt{<\ell^2>}$. If the mass distribution is determined substantially by the static potential energy surface [1], the width of the corresponding mass distribution is expected to become narrow as the angular momentum increases. The broad widths at large angular momentum are inconsistent with this consideration. Meanwhile, it has been predicted by Faber [8] that the stiffness of the potential energy associated with the mass asymmetry degree of freedom at the saddle-point is expected

to decrease with increasing angular momentum. The mass distribution, therefore, would become wider with the increase of angular momentum. Although the effect of angular momentum has not yet been fully accounted for in a quantitative manner, the trend of the mass distribution observed in the systems around $A \sim 100$ can be qualitatively explained by the Faber's model [8].

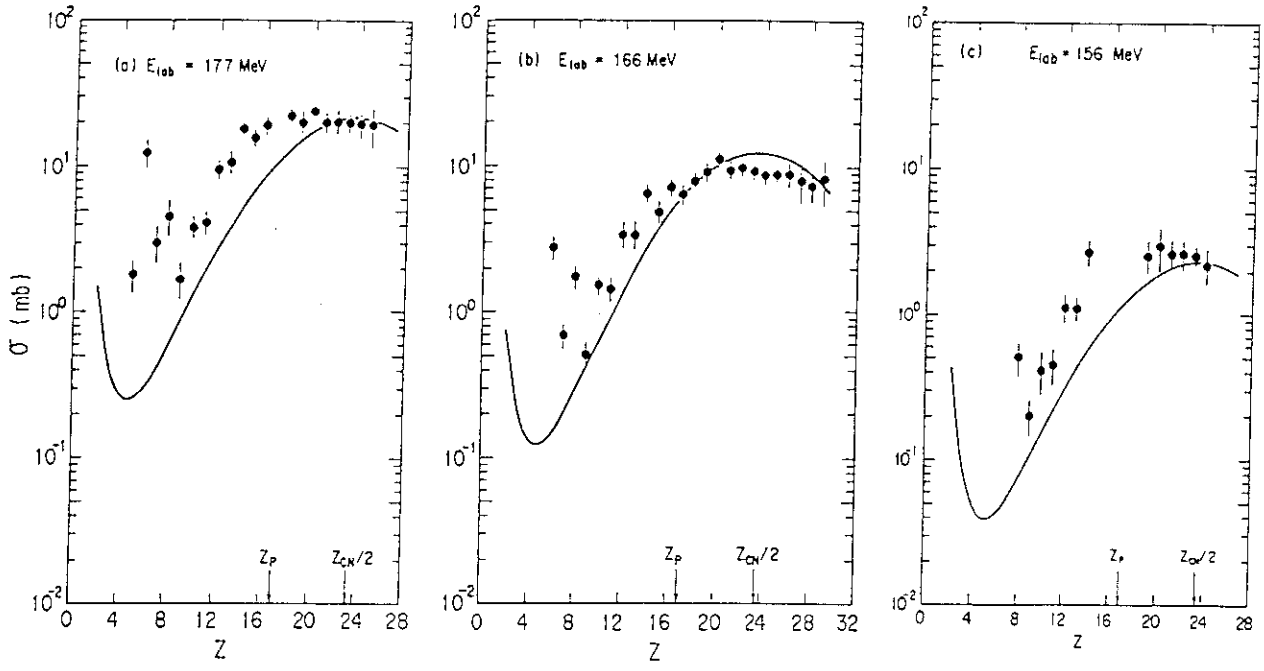

Fig.1. Integrated cross sections over the flat region in the angular distribution: E_{lab} = (a) 177 MeV, (b) 166 MeV and (c) 156 MeV. The atomic numbers of projectile and compound nucleus are indicated with Z_P and Z_{CN}, respectively. The solid lines are the results of the statistical model calculation.

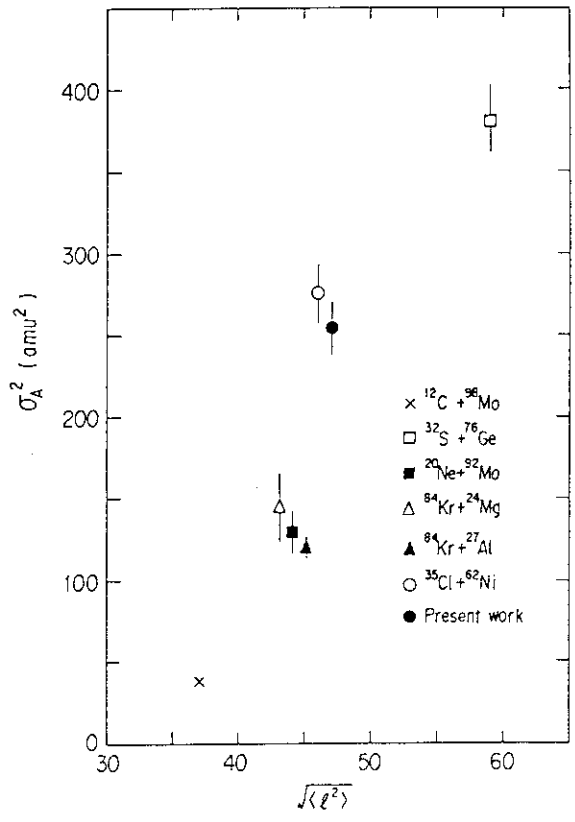

Fig.2. Variance σ_A^2 of the symmetric mass distribution as a function of $\sqrt{<\ell^2>}$. The internal excitation energy of the fissioning system is normalized to an excitation energy corresponding to T = 1.6 MeV.

References

1) L.G. Moretto, Nucl. Phys. A 247 (1975) 211.
2) W.J. Swiatecki, Aust. J. Phys. 36 (1983) 641.
3) J. Bisplinghoff et al. Phys. Rev. C 17 (1978) 177.
4) G. Guillaume et al. Phys. Rev. C 26 (1982) 2458.
5) J.B. Natowitz et al. Phys. Rev. C 13 (1976) 171.
6) Y. Nagame et al. Z. Phys. A 317 (1984) 31.
7) B. Heusch et al. Z. Phys. A 312 (1983) 109 and 322 (1985) 309.
8) M.E. Faber, Phys. Rev. C 24 (1981) 1047.

4.2 A FISSION BARRIER STUDY IN ACTINIDES

T. Ohtsuki, H. Nakahara, Y. Nagame*, K. P. Tsukada,
N. Shinohara**, S. Baba*, K. Sueki, and H. Ikezoe***

Department of Chemistry, Faculty of Science,
Tokyo Metropolitan, University,
*Department of Radioisotopes, JAERI, **Department of Chemistry, JAERI, ***Department of Physics, JAERI

Although low energy nuclear fission has been investigated from the early days of the discovery of the phenomena, detail features of mass yield curves are necessary for the study of the mechanism. One of the most important information of the mass yiels is the fission barrier heights. The incident energy dependence of mass yields has been known to be different for symmetric mass division products and for asymmetric ones. This suggests the presence of two barrier heights corresponding to the two mass division modes[1].

In the present work, we have studied the mass distributions of fragments from the fissions of ^{232}Th, ^{233}U, ^{235}U, ^{238}U, ^{237}Np, ^{239}Pu, ^{242}Pu, ^{244}Pu, ^{241}Am, and ^{243}Am induced by protons in the energy range 9-16 MeV for the purpose of investigating the dependence of symmetric and asymmetric fission modes on excitation energy. The peak-to-valley ratios were obtained as a function of proton energy, and also analyzed as a function of the fissioning nucleus. The variation of barrier heights for the symmetric and asymmetric fissions was deduced. The difference of the barrier heights between the two modes is compared with static potential barriers calculated by Mőller and Nix[2].

The cross section for obtaining each fission product was evaluated from the observed γ-ray intensities, and the correction was made, if necessary for the charge distribution by assuming a gaussian charge distribution with the most probable charge Z_p of the unchanged charge distribution model. All the mass yield curves were asymmetric as expected. The results showed a strong dependence of fission yields on E_p in the

valley region (increased probability of the near-symmetric fission with increasing of excitation energy) in comparison with the peak region and the outer sides of the asymmetric peaks.

The yield ratios of typical asymmetric division products are independent on the incident proton energy and that is the same as the symmetric division products, while the yield ratios of asymmetric to symmetric division products are strongly dependent on energy. These observations suggest the existence of two distinctly different threshold energies, one related to the so-called symmetric fission and the other to the asymmetric fission.

For all nuclei studied it has been found that the peak-to-valley ratio decreases as the excitation energy of the compound nucleus is increased, and eventually the distribution becomes symmetric about $A_f/2$. The P/V ratios as a function of the mass of the compound nucleus (A_f) with a fixed excitation energy above the saddle point are shown in Fig. 1, in which the outer barrier heights reported by Back et al.[3] are used for the saddle point energy. Filled circles show the P/V ratios for the excitation energy of 9.5 MeV and filled triangles for 11.5 MeV. From the figure, it is found that yields of the symmetric mass division become more favored as the fissioning mass increases up to 245 or to the neutron number of the compound nucleus N=150. It is interesting to note that the P/V ratios seem to vary smoothly from the actinide region to the distinctly triple-humped Ra region[4] and even down to the Po region[5]. This smooth variation of the P/V ratio as a function of A_f indicates that some unknown causes of the asymmetric mass division, probably the shell effect at the saddle or at the scission or the dynamics from the saddle to scission, gradually become more effective as A_f increases up to the actinide region.

A quantative analysis was carried out for the ratio of probabilities of the symmetric and to the asymmetric fission in terms of a statistical model according to which the ratio Γ_a/Γ_s=P/V can be represented in the form[6]:

$$\ln(P/V)=C*((2\sqrt{a_a(E_x-E_a)})-(2\sqrt{a_s(E_x-E_s)}))$$

where C is a constant, E_x, the excitation energy of the fissioning nuclide, a_a and a_s, the level density parameters of the symmetric and asymmetric fission modes,respectively, and E_a and E_s the extra-energy above each

barrier. An assumption was also made that the level-density parameters do not depend on the excitation energy and that a_a=1.05A/8, a_s=1.15a_a. The differences in the evaluated extra-energy(E_s-E_a) required for the symmetric mass division to the asymmetric one as a function of neutron number are shown in Fig.2. The (E_s-E_a) value changes from a large positive value for N-150 to a large negative value for N-126, and the two barrier heights become comparable at N=136-137. This trend indicates that the shape of the mass distribution changes from symmetric mass distribution for the Bi and Po region, triple-humped for the Ra and Ac region and to double-humped for most of actinides systematically. The broken lines show the difference in heights between the symmetric 2nd barrier and the asymmetric 2nd barrier for even-Z fissioning nuclides calculated by Möller et al[2]. The observed (E_s-E_a) seem to fall within the energy range predicted by the potential energy calculation, and it may suggest that the symmetric mass division process experiences the static symmetric 2nd barrier and the asymmetric process goes through the static asymmetric barrier even though there is no theoretical justification for the former process.

References

1) A. Turkevich and J. B. Niday, Phys. Rev. 84, 52(1951).
2) P. Moller and J. R. Nix, Nucl. Phys. A229, 269(1974).
3) B. B. Back, O. Hansen, H. C. Britt, J. D. Garrett, and P. Leroux, Phys. and Chem. of Fission, Proceedings of a Symposium at Rochester (IAEA, Vienna), Vol.I, 3(1974).
4) E. Konecny, H. J. Specht, J. Weber, Phys. and Chem. of Fission, Proceedings of a Symposium at Rochester (IAEA, Vienna) Vol.II, 1(1974).
5) M. G. Itkis, V. N. Okolovich, A. Ya. Rusanov, and G. N. Smirenkin, Sov. J. Nucl. Phys. 41, 544(1985).
6) C. F. Tsang and J. B. Wilhelmy, Nucl. Phys. A184, 417(1972).

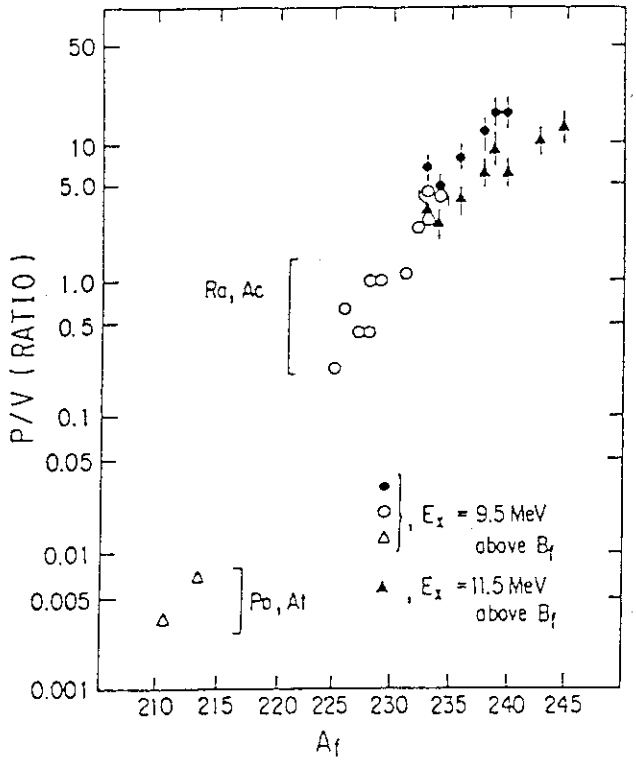

Fig.1 P/V ratios as a function of fissioning nuclides. Closed circles, open circles and open trianbles indicate the P/V ratio at the excitation energy E_X=9.5 MeV above asymmetric fission barriers. Closed triangles are for E_X=11.5. Closed symbols are the results obtained in this work, open circles are from ref.4, open triangles from ref.5.

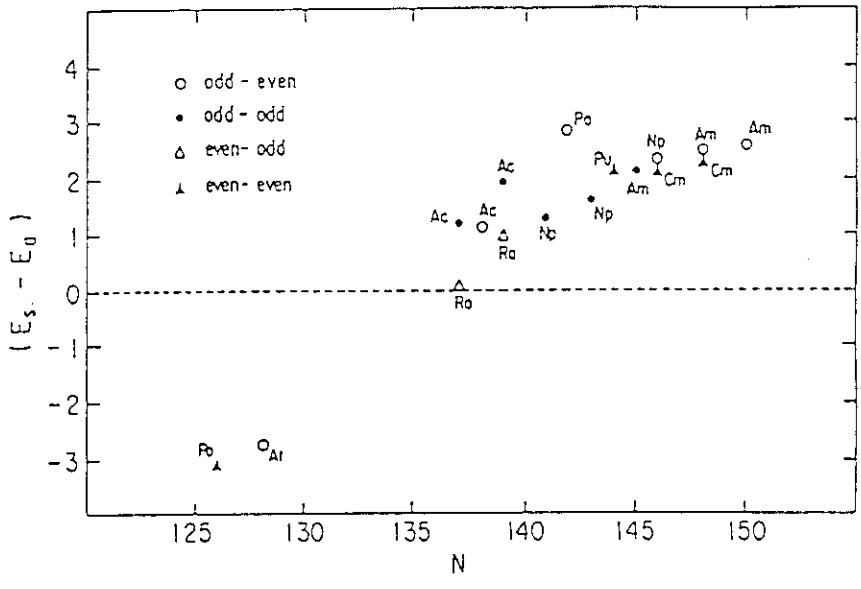

Fig.2 Difference in barrier heights(MeV) as a function of neutron number. The value for Ra and Ac isotopes are from ref.4 and those for Po and At isotopes are from ref.5.

4.3 BETA-DECAY STUDIES OF ^{123}La, ^{125}La AND ^{127}La WITH AN ON-LINE ISOTOPE SEPARATOR

Hideki IIMURA, Shin-ichi ICHIKAWA, Toshiaki SEKINE[‡],
Masumi OSHIMA[‡‡], Nobuo SHINOHARA,
Masahide MIYACHI[‡‡‡], Akihiko OSA[‡‡‡], Michihiro SHIBATA[‡‡‡],
Hiroshi YAMAMOTO[‡‡‡] and Kiyoshi KAWADE[‡‡‡]

Department of Chemistry, [‡]Department of Radioisotopes,
[‡‡]Department of Physics, JAERI and
[‡‡‡]Department of Nuclear Engineering, Nagoya University

Investigation of the nuclear structure of neutron deficient nuclei in the A=120-130 mass region has revealed many interesting features. The nuclei in this region, tend to loose γ-softness and their collective character grows rapidly with decreasing neutron number. As to odd-A Ba nuclei in-beam γ-ray spectroscopic studies lead to information on high-spin level structures.[1-3] However, experimental information on low-spin levels of these nuclei is very scarce. The knowledge of the excitation energies and transition probabilities of such levels are needed for understanding the collective behaviour of these nuclei. In the present work, we studied the level schemes of ^{123,125,127}Ba from the β-decays of ^{123,125,127}La using an on-line isotope separator (ISOL).

The experiments were performed at the tandem accelerator facility, using the reactions ^{92}Mo(^{35}Cl,2p2n)^{123}La with a 180-MeV ^{35}Cl beam and ^{nat}Mo(^{32}S,pxn)^{125,127}La with a 160-MeV ^{32}S beam. The thickness of the molybdenum targets was about 4 mg/cm^2. Reaction products were ionized in a surface-ionization ion source. The ionized activities were extracted from the ion source and mass-separated by an analyzing magnet. In order to obtain La activities free from the Cs and Ba isobars, monoxide compounds of La were extracted: the mass number M was set at M=A+16 (^{A}La^{16}O^{+}). The detailed description of this method is given in ref. 4. After mass separation, ^{123,125,127}La activities were implanted into an aluminum-coated mylar tape and periodically transported in front of detectors by a tape-transport system. Gamma-ray multi-spectrum measurements were performed with a low-energy photon HPGe detector (LEPS) and an 18% γ-X HPGe detector. The decay of each γ-line was traced by taking

16 spectra sequentially. These detectors were also used for X/γ-γ coincidence measurements. In addition, in order to measure half-lives of excited states, β-γ delayed coincidences were observed with a 1-mm-thick plastic scintillation detector and the LEPS.

As an example of the data obtained, levels and transitions in ^{125}Ba are shown in fig. 1. The excited states of ^{125}Ba were placed on the basis of the energies, intensities and coincidence relations of the γ-rays assigned to the decay of ^{125}La. The level scheme shows two different sets of levels with no interconnection. The position of the 0+X keV level was not determined. We have derived 13 new levels. The energies of these new levels are indicated with an asterisk in fig. 1. As to the spin and parity values for the ground state and the levels at 0+X, 67.2+X, 165.9+X, 168.6+X, 300.0+X, and 385.0+X keV we have adopted the previous ones.[5,6] From the intensity ratios of the K X-rays to the γ-rays in the coincidence spectra, the multipolarities of the 43.6- and 67.2-keV transitions have been determined to be M1+E2 and E1, respectively. Consequently, the parity of the 43.6-keV level has been assigned as positive; from the level systematics of the heavier Ba isotopes, the most probable spin of this level is 3/2. The 67.2-keV γ-ray was found to be delayed with a half-life of 2.76$\pm$0.14μs. This half-life value gives an E1 hidrance factor F_W=5.2X10^6 to this transition.

Further investigation, including the measurements of internal conversion electrons, is now in progress to obtain more complete level schemes of the isotopes.

References

1) N. Yoshikawa, J. Gizon and A. Gison: J. de Phys. 40 (1979) 209.
2) J. Gizon and A. Gizon: Z. Phys. A285 (1978) 259.
3) J. Gizon and A. Gizon: Z. Phys. A281 (1977) 99.
4) S. Ichikawa, T. Sekine, H. Iimura, M. Oshima and N. Takahashi: Nucl. Instr. and Meth. A274 (1989) 259.
5) A. C. Mueller, F. Buchinger, W. Klempt, E. W. Otten, R. Neugart, C. Ekstrom and J. Heinemeier: Nucl. Phys. A403 (1983) 234.
6) T. Tamura, Z. Matumoto and M. Oshima: Nucl. Data Sheets 32 (1981) 497.

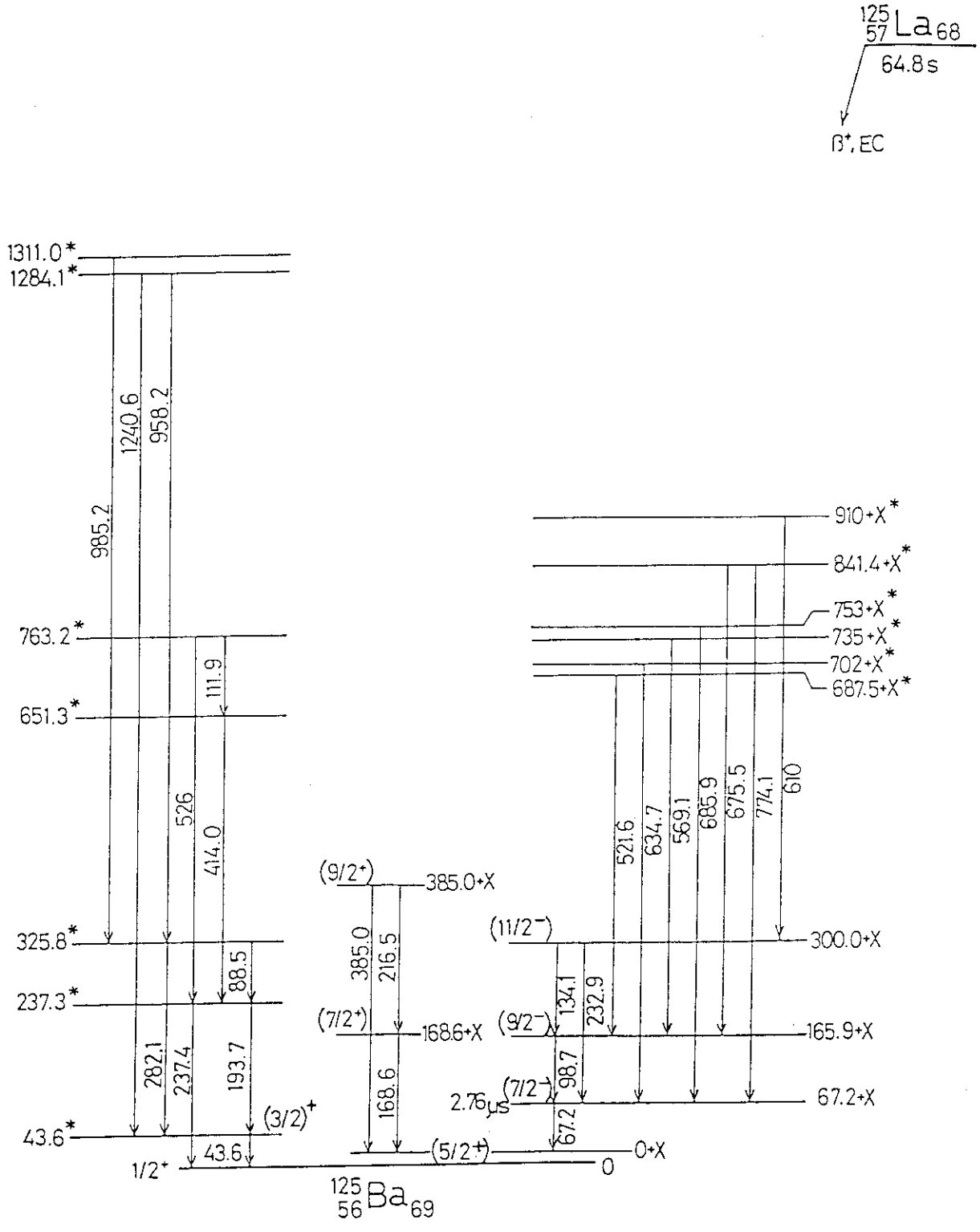

Fig. 1 Levels and transitions in ^{125}Ba.

4.4 A STUDY OF SHORT-LIVED ACTINIDES BY MEANS OF ON-LINE CHEMICAL SEPARATION SYSTEM

Nobuo SHINOHARA, Shin-ichi ICHIKAWA, Hideki IIMURA, Kazuaki TSUKADA, Sumiko BABA*, Tsutomu OTSUKI*, Hirokazu UMEZAWA*, Ichiro FUJIWARA** and Jorolf ALSTAD***

Department of Chemistry, *Department of Radioisotopes, JAERI, **Otemon Gakuin University, ***University of Oslo, Norway

Actinides produced by heavy-ion bombardments have short-lives and the production yields are quite low. In order to investigate the short-lived actinides, therefore, it is necessary to rapidly separate such a small amount of an aimed actinide from large amounts of other reaction products. For this purpose, we have developed an on-line chemical separation system which consists of a helium-jet transport system, a rapid solvent extraction system (SISAK),[1] and an automatic ion-exchange system.

Rapid solvent extraction system (SISAK)

For off-line experiment of the SISAK system, short-lived isotopes of ruthenium which were forming in the spontaneous fission of 1 mCi ^{252}Cf were separated and their gamma rays were measured. The recoil nuclei produced in the fission were thermalized through collision with helium atoms and attached to aerosol particles in the helium gas. The nuclei sticking in the particles were transferred through a Teflon capillary (2 mm diameter and 8 m long) to a degasser of the SISAK system to remove the gas, and dissolved in a solution of 5×10^{-5}M $RuCl_3$/0.2M H_2SO_4. Then, a solution of 0.015M $Ce(SO_4)_2$/0.2M H_2SO_4 preheated to about 80°C was added to oxidize ruthenium to RuO_4. The ruthenium oxide was separated from fission products by extracting it into carbon tetrachloride. Gamma-ray measurements were carried out on the organic solution after the solvent extraction and centrifugal separation from the aqueous phase. Figure 1 shows a schematic drawing of the SISAK experiment for the fast ruthenium separation.

Figure 2 gives the gamma-ray spectrum of the ruthenium fraction (organic phase) after the solvent extraction. Several gamma-ray peaks in the figure were assigned to the isotopes of ruthenium with mass numbers 108, 109, 110, 111 and 112 or to their daughter isotopes, with reference to

literature.[2,3] The gamma ray of 263.5 keV for ^{113}Ru given in the literature was not detected in our spectrum. The measurements of gamma-ray singles and gamma-gamma coincidence are in progress to constrcut the level schemes of the neutron-rich ruthenium isotopes.

There are few experimental data for neutron-deficient berkelium isotopes, especially ^{241}Bk isotope has not yet been identified. The ^{241}Bk isotope is possibly synthesized in (HI,xn) reactions. Estimating the cross section with the code ALICE,[4] the reaction systems of ^{11}B+^{235}U and ^{12}C+^{235}U were used for the identification of the neutron-deficient berkelium isotopes. Figure 3 shows the separation scheme using the SISAK for rapid berkelium separation. In an off-line test of chemistry using ^{252}Cf fission products, the extraction of cerium is the most likely in its IV valence in solution as well as berkelium. It was confirmed that the cerium is extracted into 0.3M HDEHP/heptane in C1 centrifuge and back-extracted into 4.5M H_2SO_4/ 0.05M $K_2Cr_2O_7$ in C2 centrifuge. The berkelium was supposed not to be back-extracted in the C2 position.

In the on-line experiments, alpha-ray measurements of catcher foil in ^{12}C+^{235}U system was carried

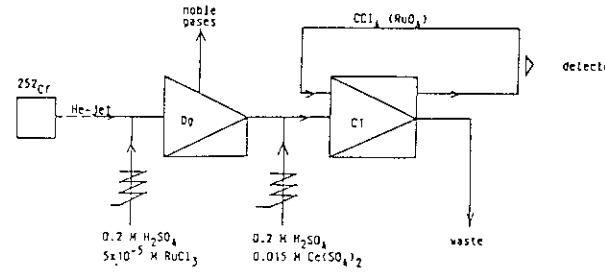

Fig.1 SISAK "circuit" for fast Ru separation. Flow rates: He-jet (0.8 kg/cm^2) 55 m/s, carrier solution (aq.1) 58 cm/s, Ce(IV)-solution (aq.2) 51 cm/s, CCl_4 (org. soln.) 108 cm/s. The aq.1 and aq.2 are preheated to about 80°C.

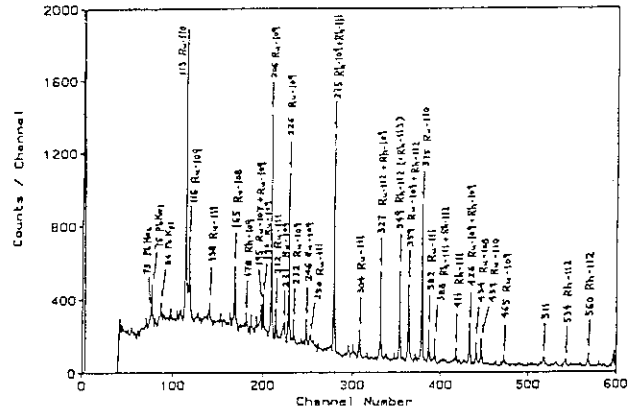

Fig.2 Gamma-ray spectrum of the ruthenium fraction after the solvent extraction with SISAK.

out at first and the californium isotopes of mass number $A \geq 241$ were observed. The identification of berkelium activity after the separation with SISAK was based on the X-ray of 109keV. However, the activities observed during the on-line experiments were high energy gamma-rays assigned to ^{19}O and ^{19}Ne (for Be backing of the target), and ^{28}Al and ^{29}Al (for Al backing), and no berkelium isotopes were identified so far.

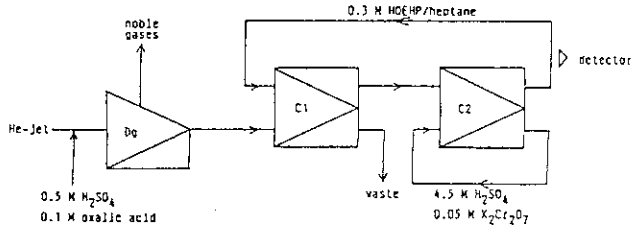

Fig.3 SISAK "circuit" for on-line sepaartion of Bk produced by the $^{11}B,^{12}C+^{235}U$ reaction system.

Automatic ion-exchange system

A personal computer controls the ion-exchange system: an injector is to dissolve the reaction products transferred with the helium-jet system and to inject the dissolved solution into an ion-exchange resin column; several tube pumps supply eluent solutions to the column, and 4- or 8-way valves and a solenoid valve change an eluent with another. The system can be automatically operated with a computer program. A nitrogen-gas tank with a pressure control valve is used as a controller of flow rate of the solutions in this system. After the ion-exchange separation, a necessary fraction is taken out and dried up to prepare a counting source for alpha- or gamma-ray spectrometry. Using the ^{252}Cf source, the dissolution yield of the spontaneous fission products into an acid solution was investigated at first, and consequently all of the nuclides transferred with the helium-jet system were dissolved in the acid solution. Fission product samalium was also separated with the automatic ion-exchange system, and $^{155\text{-}158}Sm$ ($T_{1/2}$: 5.5 min-9.4 h) were isolated. Figure 4 shows a diagram for the separation of samalium.[5] Required time for the dissolution, the separation and the source preparation of samalium was 7 min as whole.

Holmium and dysprosium isotopes produced from the $^{18}O+^{nat}Er$ reaction were separated with the ion-exchange system to identify $^{168,169}Ho$ and ^{168}Dy.

Although the chemical separation was repeated several ten times, the nuclides of holmium and dysprosium could not be observed. This indicates that their formation cross sections are less than 0.5 mb.

An automatic activity-measurement instrument, where the counting sources are prepared by quick evaporation of the chemically-separated fractions and immediately submitted for radioactivity measurements, is now developing.

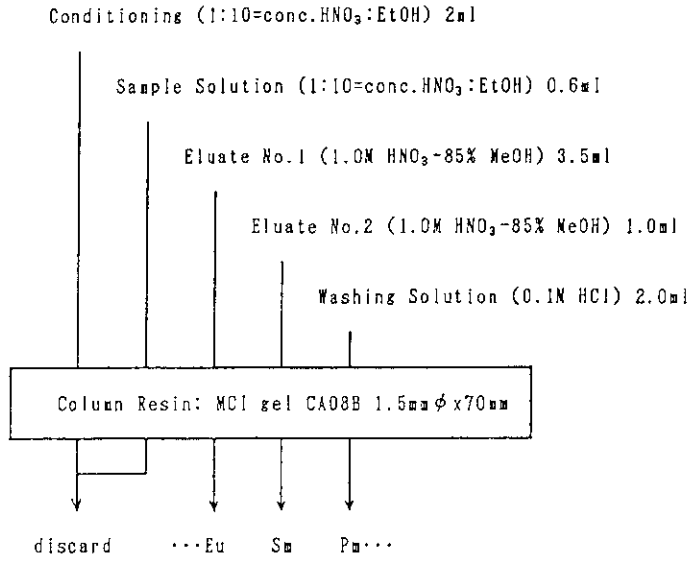

Fig.4 Diagram for rapid mutual separation of the rare earth elements (Eu, Sm and Pm). The operating temperature for the ion exchange, the flow rate of the eluents and N_2 gas pressure were $90\pm2^{\circ}C$ (in water bath), 1.5 ml/min and 20-30 kg/cm^2, respectively.

References

1) G. Skarnemark, et al.: Nucl. Instr. Methods, 171 (1980) 323.
2) N. Kaffrell, et al.: Nucl. Phys. 470 (1987) 141.
3) H. Penttila, et al.: Phys. Rev. C38, 931 (1988).
4) M. Blann: COO-3494-29 (1976).
5) S. Usuda, J. Radioanal. Nucl. Chem. 111 (1987) 399.

V NUCLEAR PHYSICS

5.1 CONTRIBUTION OF NUCLEON TRANSFER TO ELASTIC SCATTERING OF $^{28}Si+^{58,64}Ni$ NEAR THE COULOMB BARRIER

Yasuharu SUGIYAMA, Yoshiaki TOMITA, Hiroshi IKEZOE, Kazumi IDENO, Hiroshi FUJITA*, Tsuyoshi SUGIMITSU**, Norihisa KATO**, Shigeru KUBONO*** and Stephen LANDOWNE****

Department of Physics, JAERI, *Daiichi College of Pharmaceutical Sciences, **Department of Physics, Kyushu University, ***Institute for Nuclear Study, University of Tokyo, ****Physics Division, Argonne National Laboratory

Experiments on the quasielastic reaction for the systems $^{28}Si+^{58,64}Ni$ were carried out in order to clarify the heavy-ion reaction mechanism near the Coulomb barrier.[1,2] Momentum spectra from $^{28}Si+^{58,64}Ni$ quasielastic scattering were measured with a high resolution at the JAERI tandem accelerator by using the heavy-ion magnetic spectrograph[3] "ENMA". The spectrograph has the characteristic feature that the kinematic momentum shift k is well compensated, so that a high energy resolution is achieved over a wide range of k. Elastic and inelastic scattering angular distributions for $^{28}Si+^{58,64}Ni$ were measured in the energy range $E_{c.m.}$=50.0 - 76.5MeV. We used the advantages of the reversed kinematics in the backward angle range $\theta_{c.m.}$=85°-160° by bombarding a ^{28}Si target with ^{58}Ni and ^{64}Ni beams. Transfer cross sections were measured at $E_{c.m.}$=54.8MeV for $^{28}Si+^{58}Ni$ and at $E_{c.m.}$=50.0 and 54.8 MeV for $^{28}Si+^{64}Ni$, respectively. In order to measure elastic and inelastic scattering at forward angles, a ^{28}Si beam was incident on Ni targets. Quasielastic scattering cross sections of $^{28}Si+^{64}Ni$ were measured at $E_{c.m.}$=76.5MeV by using a 110MeV ^{28}Si beam.

The outgoing particles were momentum analyzed in the magnetic spectrograph ENMA and detected in the focal plane[4] with a 40cm long hybrid focal plane detector. The entrance slits of the spectrograph were opened 2.2° horizontally and vertically which corresponded to a solid angle of 1.6 msr. From a measurement of total energy E, energy loss δE and position $B\rho$ an unambiguous determination of mass, atomic number, Q value and atomic charge state q were possible. Four nuclei ^{29}Si, ^{30}Si, ^{27}Al and ^{26}Mg, which were produced from neutron-pickup or proton-stripping reactions, were observed in addition to elastically scattered ^{28}Si. Other reaction products could not be identified because of their small yields.

An energy spectrum obtained at θ_{lab}=40° from the elastic and inelastic scattering $^{28}Si(^{64}Ni, ^{64}Ni)^{28}Si$ is shown in Fig.1. The kinematic momentum shift, which amounts to δE=6.0MeV at θ_{lab}=40° for the present solid angle, is compensated well. An energy resolution of 0.24 MeV made it possible to resolve transitions to low-lying discrete levels. Elastic scattering angular distributions of $^{28}Si+^{58}Ni$ and $^{28}Si+^{64}Ni$ are shown by filled circles in Fig.2 and Fig.3, respectively. In Fig.4 angular distributions for energy-integrated cross sections of the one-nuetron pickup reactions are shown. Filled circles correspond to the results from the reaction $^{64}Ni(^{28}Si, ^{29}Si)^{63}Ni$ and filled triangles are the result from $^{58}Ni(^{28}Si, ^{29}Si)^{57}Ni$. It is seen that the transfer cross section of $^{28}Si+^{64}Ni$ is about an order of magnitude larger than that of $^{28}Si+^{58}Ni$ at $E_{c.m.}$≈75MeV.

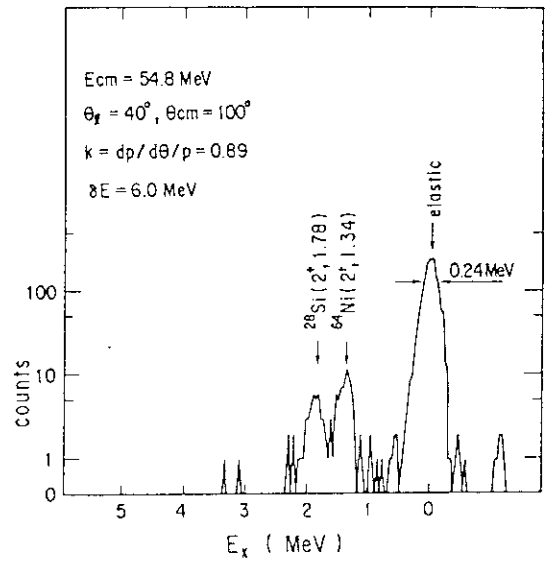

Fig.1 A spectrum obtained at θ_{lab}=40° from the elastic and inelastic scattering $^{28}Si(^{64}Ni, ^{64}Ni)^{28}Si$.

At first we carried out the coupled-channels culations including the inelastic excitations. The following spherical Woods-Saxon potential parameters[5] were used; V=50MeV, W=10MeV, r_0=r_I=1.2fm, a_0=a_I=0.65fm, r_C=1.32fm. THe form factor was the derivative of the Woods-Saxon potential. The coupling parameters used were as follows; β_n=-0.36, β_c=-0.379 for $^{28}Si(2^+)$ and β_n=0.2, β_c=0.182 for $^{58,64}Ni(2^+)$. The calculated results using the code Ptolemy[6] are shown by dashed-lines in Figs.2 and 3. It is seen that the single energy- and isotope-independent potential reproduces well the elastic scattering angular distributions of $^{28}Si+^{58}Ni$ at all energies. However the calculations deviate considerably from the measured elastic scattering cross sections for $^{28}Si+^{64}Ni$ at near-barrier energies of $E_{c.m.}$=52.4, 54.8 and 57.3 MeV , although the angular distribution at $E_{c.m.}$=76.5MeV is reproduced well.

We then carried out the coupled-channels calculations including the transfer channels additionally. The transfer reactions were treated in the same way as in the fusion calculations of ref.7. We took into

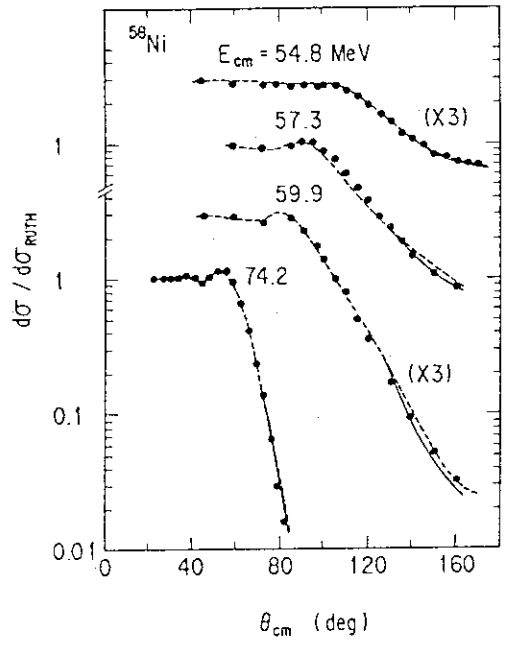

Fig.2 Elastic scattering angular distributions for $^{28}Si+^{58}Ni$ at different center of mass energies. The dashed lines are coupled-channels calculations including inelastic excitation. Solid lines are the calculations including the one-neutron transfer channel additionally.

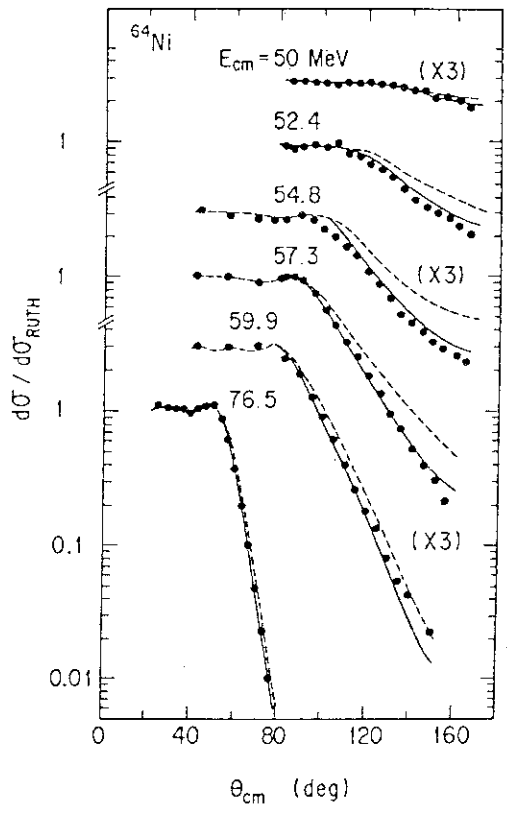

Fig.3 Same as Fig.2 but for $^{28}Si+^{64}Ni$.

account only one-neutron transfer channels for simplicity. The calculated results for the elastic are shown by solid lines in Figs.2 and 3. It is seen that the coupled-channels calculations including the transfer channel additionally reproduce the data very well. The one-neutron transfer cross sections are compared with the coupled-channels calculations in Fig.4. A reasonable overall agreement is obtained with this simple approximated method. A large difference of the transfer cross sections between the $^{28}Si+^{58,64}Ni$ cases at $E_{c.m.}\approx$75Mev is reproduced well.

In summary, we presented the results of elastic scattering and one-neutron transfer measurements in $^{28}Si+^{58,64}Ni$ at various energies arround the Coulomb barrier. A high resolution work was achieved by compensating the strong kinematic shift in a reversed kinematics and the elastic scattering cross section was measured over a wide range of scattering angles. The coupled-channels calculations were carried out

including one-neutron transfers in addition to inelastic scattering process. The data were reproduced wll using a single energy- and isotope-independent bare potential. The present result ,together with the one[7,8] of the fusion reaction, indicates that the coupled-channels method is a unified approach for describing the elastic, quasielastic and fusion cross sections at energies around the Coulomb barrier.

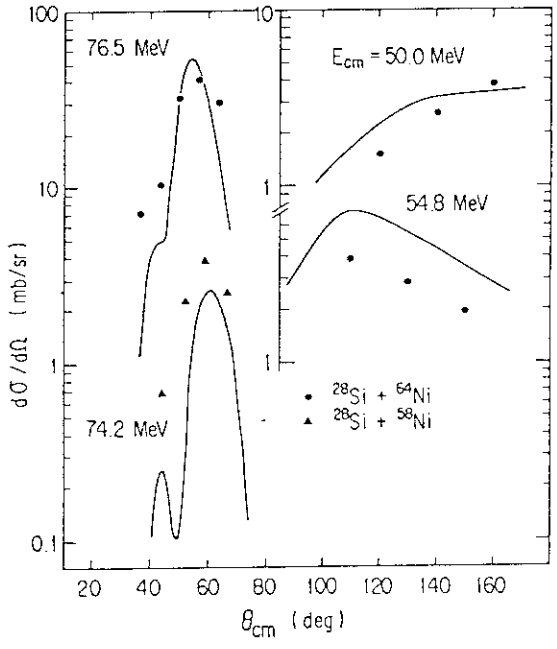

Fig.4 Angular distributions for energy-integrated cross sections of the one-neutron transfer reactions. Filled circles and triangles are the results from the reactions ^{64}Ni(^{28}Si, ^{29}Si)^{63}Ni and ^{58}Ni(^{28}Si, ^{29}Si)^{57}Ni, respectively. Solid lines are the coupled-channels calculations.

References

1) Y.Sugiyama et al., Phys. Rev. Lett.62 (1989) 1727.
2) Y.Sugiyama et al., Invited Papers of the JAERI International Symposium on Heavy-Ion Reaction Dynamics in Tandem Energy Region, edited by Y.Sugiyama et al. (University Academy Press, Tokyo,1988), p.85.
3) Y.Sugiyama et al., Nucl. Instrum. Methods 187(1981)25; Z.Phys. A322(1985)579; submitted to Nucl. Instrum. Methods.
4) E.Takekoshi et al., Nucl. Instrum. Methods A237(1985)512.
5) Y.Sugiyama et al., Phys. Lett. 176B(1986)302.
6) M.J.Rhoades-Brown et al., Phys. Rev. C21(1980)2417,2436.
7) S.Landowne et al., Phys. Rev. C35(1987)597.
8) A.M.Stefanini et al., Phys. Rev. C30(1984)2088.

5.2 MEASUREMENTS OF PRE–FISSION ^{4}He MULTIPLICITY TO INVESTIGATE THE TEMPERATURE DEPENDENCE OF LEVEL DENSITY PARAMETER

Hiroshi IKEZOE, Naomoto SHIKAZONO, Yuichiro NAGAME, Yasuharu SUGIYAMA, Yoshiaki TOMITA, Kazumi IDENO, Hiromichi NAKAHARA*, Tsutomu OHTSUKI*, Takayuki KOBAYASHI* and Keisuke SUEKI*

Department of Physics, JAERI, *Department of Chemistry, Faculty of Science, Tokyo Metropolitan University

The nuclear level density plays an important rule in the statistical treatment of the probabilities of evaporation and fission of an excited nucleus. The dependence of the level density parameter on the excitation energy is especially important. Up to now a few experimental data are available in connection with this point[1–3]. In the present work, we investigated the dependence of the level density parameter on the excitation energies in the range of 45 to 90 MeV. For the present purpose, the reaction of ^{19}F + ^{197}Au was used to produce the compound nucleus ^{216}Ra. The pre–fission ^{4}He multiplicity was measured as a function of the excitation energy of the compound nucleus. It was expected that ^{4}He was likely emitted from the excited compound nucleus ^{216}Ra before fission, because the daughter nucleus ^{212}Rn has the neutron magic number N=126. It was also expected that the ^{4}He emission should depend on the excitation energy of the daughter nucleus ^{212}Rn, in which the shell correction energies of the excited states rapidly disappear[4] as the excitation energy increases.

The energy spectra of ^{4}He in coincidence with the fission fragments are shown in Fig.1. The ordinate is defined as

$$d^2M/dE_\alpha d\Omega_\alpha = (d^3\sigma/dE_\alpha d\Omega_\alpha d\Omega_{fiss})/(d\sigma/d\Omega_{fiss}),$$

where $d\sigma/d\Omega_{fiss}$ is the inclusive cross section of the fission fragments. In general, there are three different sources for the ^{4}He emission, that is, the evaporations from fission fragments (FE), the compound nucleus emission (CE) and the pre–equilibrium process (PE). Since the ^{4}He in the coincidence measurements was detected at the backward angles, the contribution from the PE was negligible. The calculated energy spectra corresponding to the emission sources of the CE and the FE are shown in Fig.1 as the dotted and the dash–dotted lines, respectively.

The pre–fission multiplicity of ^{4}He obtained after the components of the FE were subtracted from the data are shown in Fig.2 as a function of the excitation energy U. The observed data were compared with the results of the statistical model calculation,

where the code PACE[5] was used assuming the liquid drop masses for the excited parent and daughter nuclei and the level density parameter $a = A/8\ MeV^{-1}$. The ratio a_f/a_n of the level density parameters at the saddle point and ground state deformations was varied to see the dependence of the calculated M on the excitation energy. It is obvious that the observed data are enhanced at the low excitation energy compared with the calculated results

In order to explain the observed enhancement, the dependence of a on the excitation energy was taken into account in the statistical model calculation. According to Ignatyuk[1], the level density parameter is expressed as

$$a(U) = \tilde{a}\ (1 + f(U)\delta E_s/U),$$
$$f(U) = 1 - \exp(-\gamma U),$$

where δE_s is the experimental value of the shell correction energy to the ground state mass formula,

$$\delta E_s = M_{exp}(Z,A) - M_{ld}(Z,A).$$

The experimental and the calculated mass defects with the liquid drop model of Myers–Swiatecki[6] are denoted by $M_{exp}(Z,A)$ and $M_{ld}(Z,A)$, respectively. The asymptotic value of a at high excitation energies is denoted by $\tilde{a}$ and γ is a parameter representing the degree of the shell smearing and to be fixed by the experimental data. The result of the calculation with $\gamma = 0.06$ is shown in Fig.2 as the solid line. The agreement with the data becomes better. This indicates that the enhancement of the pre–fission ^{4}He multiplicity at the energy region region $(45 - 60\ MeV)$ can be explained by the shell effect of the residual nucleus after the ^{4}He particle is evaporated. From the present measurement the parameter γ was determined to be $0.06^{+0.06}_{-0.03}$. This value is close to the value 0.05 estimated by Ignatyuk from the analysis of the neutron resonance data[1].

References

1. A. V. Ignatyuk, G. N. Smirenkin and A. S. Tishin, Sov. J. Nucl. Phys., **21** (1975) 255.
2. H. Baba, Nucl. Phys., **A159** (1970) 625.
3. V. S. Ramamurthy, S. S. Kapoor and S. K. Kataria, Phy. Rev. Lett., **125** (1970) 386.
4. A. Bohr and B. R. Mottelson, " Nuclear Structure" Vol. **2** (Benjamin, Reading, Mass,1975)
5. A. Gavron, Phys. Rev. **C21** (1980) 230.
6. W. D. Myers and W. S. Swiatecki, Ark. Fysik **36**, (1967)593.

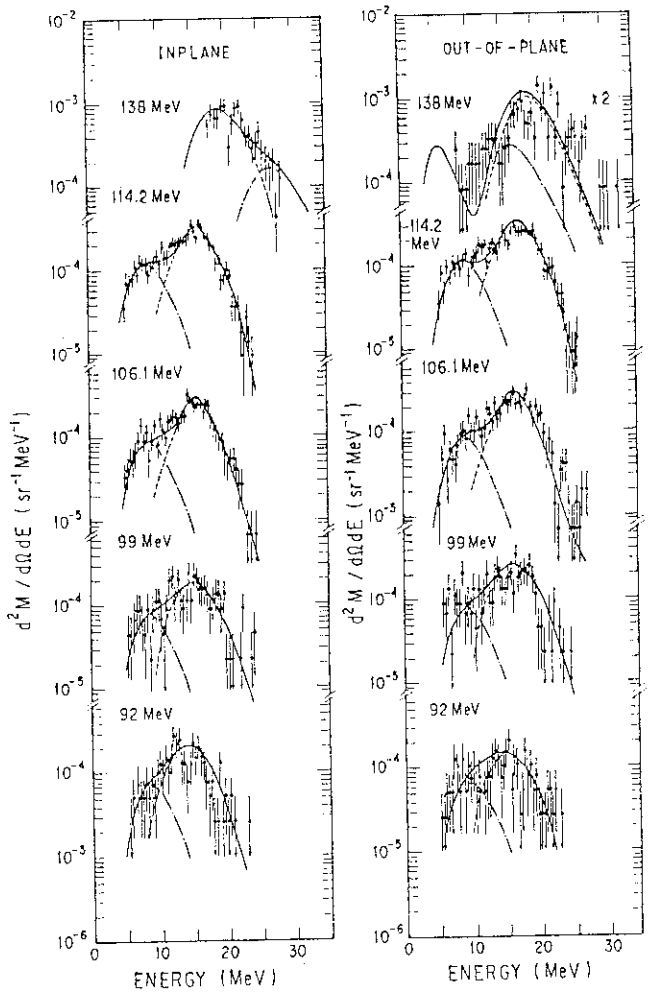

Fig.1 Energy spectra of ^{4}He in coincidence with the fission fragments. The dotted and the dash–dotted lines represent the calculated spectra corresponding to the emission sources of the CE and the FE, respectively. The out–of–plane data were measured at $\varphi = 60^{\circ}$.

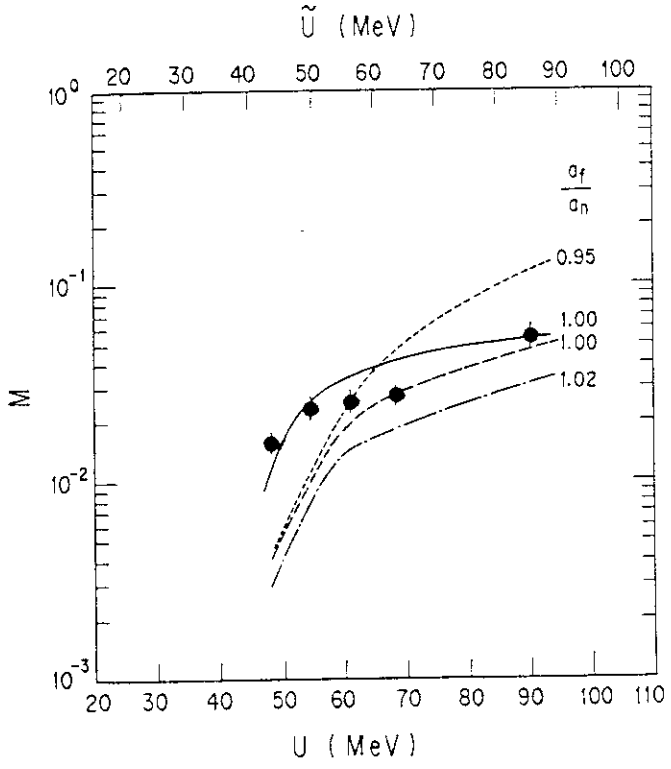

Fig.2 Pre–fission multiplicity of ^{4}He as a function of the excitation energy U. The upper scale $\tilde{U}$ is the excitation energy reckoned from the energy of the ground state as given by the liquid drop model. The results of the statistical model calculation assuming $a_f/a_n = 0.95$, 1.00 and 1.02 are shown in the dotted, the dashed and the dash–dotted lines, respectively. The solid line is the calculated result taking into account the excitation energy dependence of the level density parameter with $\gamma = 0.06$.

5.3 DETECTION OF THE ^{8}Be NUCLEI FROM THE REACTIONS ^{28}Si + ^{68}Zn AND ^{32}S + ^{64}Ni

Kazumi IDENO, Yoshiaki TOMITA, Yasuharu SUGIYAMA,
Hiroshi IKEZOE, Susumu HANASHIMA and Yuichiro NAGAME*

Department of Physics, *Department of Radioisotopes,
JAERI

In ^{16}O-induced heavy ion reactions the ^{8}Be nuclei occupy a large fraction of the reaction yields for light fragments[1]. In order to see the dominance of ^{8}Be nuclei for heavier projectile systems, we performed the measurement of the production cross section of ^{8}Be nuclei for the systems ^{28}Si + ^{68}Zn and ^{32}S + ^{64}Ni at the incident energies of 163 and 175 MeV, respectively. Both systems lead to the same composite components. The incident energies were chosen so that the two systems had approximately the same excitation energy and angular momentum. The ^{8}Be nucleus decays promptly into two α-particles ($t_{1/2} \approx 10^{-16}$ sec at ground state). We need a special detection system to identify it[2]. For this purpose we have constructed a two-dimensional position-sensitive detection system[3], which is composed of paired drift chambers as ΔE counters and two closely-spaced Si detectors (40x40 mm^2) as E counters.

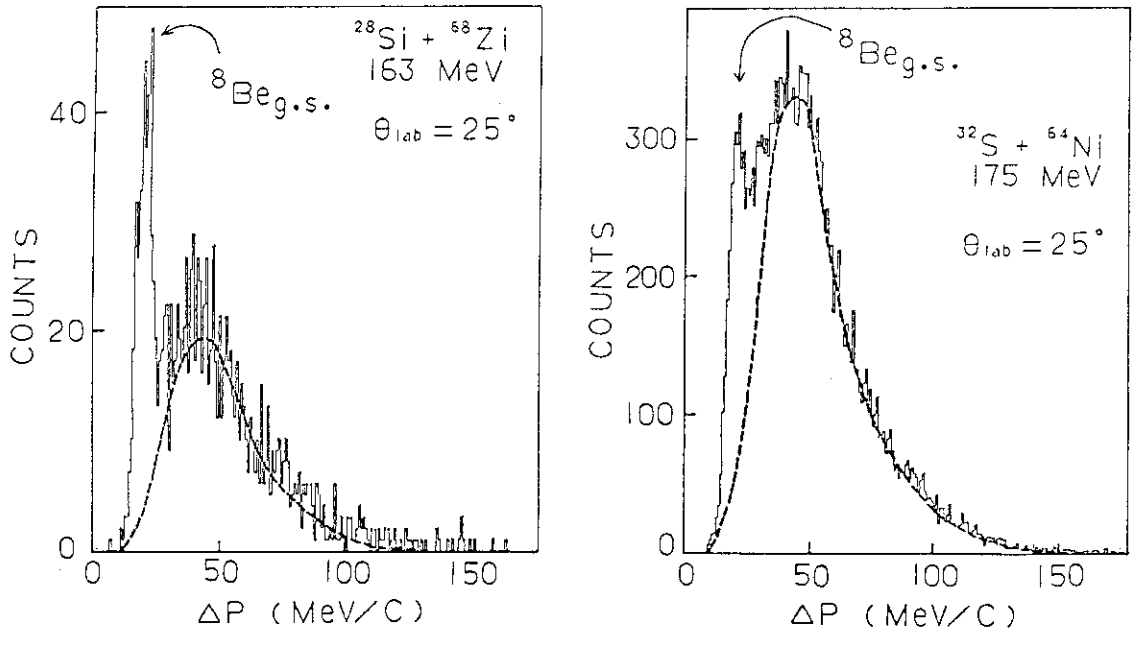

Fig. 1 Relative momentum between coincident α-particles

This system worked effectively for the measurement of continuous ^{8}Be spectra buried in the strong α-backgrounds. We also measured the cross section for the production of light stable fragments (Z = 3 - 6). Fig. 1 shows the measured distribution of the relative momentum between coincident α-particles at Θ_{lab} = 25 degree. The observed discrete peak at the lower end in the figure corresponds to the contribution from the ^{8}Be ground state. The background components are mainly due to the uncorrelated α-particles, whose average contribution is represented by a dashed curve. Both in the two systems, the ratio of the ^{8}Be component

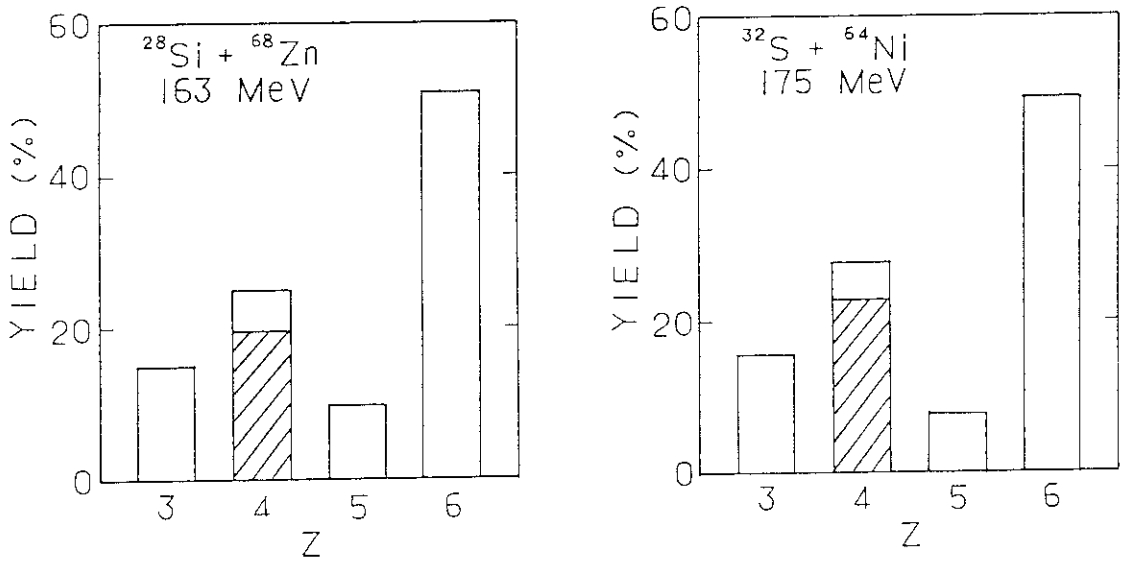

Fig. 2 Relative cross sections at Θ_{lab} = 30 degree for the observed light fragments. The open areas represent the ones for stable isotopes and the hatched area the one for the ^{8}Be$_{g.s.}$ nuclei.

to the background increased as the detection angle increased. Fig. 2 shows the yield ratios among the light fragments observed at Θ_{lab} = 30 degree. Almost the same ratios were observed up to the backward angle of Θ_{lab} = 50 degree. It is seen that the two systems behave similarly with respect to the relative yields. We also compared the spectra of the ^{8}Be nuclei with those of neighboring stable nuclei. All these nuclei showed a similar kinematical behavior among them. Further analyses are in progress.

References

1) M. E. Brandan et al.: J. Phys. G12 (1986) 391.

2) G. J. Wozniak et al.: Phys. Rev. C14 (1976) 815.

3) K. Ideno et al.: JAERI-M 88-181 (1988) 146.

5.4 SHIFT OF NEUTRON RESONANCE LEVELS IN PERIODIC STRUCTURE

Kazumi IDENO

Department of Physics, JAERI

Search for deviations from the statistical distributions of neutron resonance levels has been made in these decades[1-7]. Neutron resonance spectra are so complex that it is natural that such trial has started from finding simple level patterns: equidistant nature of level occurrence or periodic level distributions. In Ref. 5, we looked for common periodicities among medium and heavy nuclei. However, owing to the insufficient data at that time (1973), we could not make a systematic comparison among different nuclei. With an attempt to find out a trend of the periodicities, we have extended our original method[3] and made an extensive comparison among different nuclei, taking into account a recent progress in experimental data[8].

We searched for periodic structures using the correlation function A_{20}[1]. We analyzed nuclei with $D < 15$ eV in the energy region below 300 eV (I) and nuclei with $D < 250$ eV in the energy region below 5000 eV (II), where D is the average level spacing. The data are taken from Refs. 4 and 8. The nuclei ^{168}Er, ^{177}Hf and ^{179}Hf show a definite periodic structure in which a large part of levels are located among the periodic positions of a single sequence over a whole range of energy. These level energies are expressed as $E_i = n\varepsilon + \eta$, where n takes integers, ε is a period and η means a shift to the level sequence of $E_i = n\varepsilon$. These periods and shifts are listed in the following:

(I) ^{168}Er (I = 0): ε = 17.6 eV (ΔE = 6 eV) and η = -3.2 eV;
(II) ^{177}Hf (J = 3): ε = 4.37 eV (ΔE = 0.6 eV) and η = 0.8 eV;
^{179}Hf (I = 9/2): ε = 3.06 eV (ΔE = 0.6 eV) and η = -0.5 eV.

Here ΔE represents the resolution of the period, J is the spin of the levels and I the spin of the target nucleus. It is noted that $|\eta|$ is approximately equal to $(1/6)\varepsilon$ for each of the above nuclei.

When one nucleus has a periodic component with the same period ε as

that of a reference nucleus and its shift is η, a relative shift between the two nuclei is defined as

$$\Delta\eta = \eta_{ref} - \eta, \qquad (1)$$

where η_{ref} is the shift of the reference nucleus. The relative shift can be determined directly by using the function A_{20} for the superposed levels of the two nuclei[1]. In order to avoid inclusion of accidental effects in obtaining the relative shift, we calculated the probability of the occurrence of the observed correlation by simulations in each of the cases.

Relative shifts of the 17.6 eV components (E < 5 keV)

The ^{168}Er nucleus was taken as a reference. Fig. 1 shows the relative shifts of the 17.6 eV components for even rare earth nuclei. It is seen that all the relative shifts except for the ^{160}Gd nucleus center around η = 0 or (1/2)ε. Among the nuclei in the figure, the ^{160}Gd nucleus has the weakest correlation with the reference nucleus. The correlations are very strong for the other nuclei, and clustering of the relative shifts at the definite values cannot be expected for independent ensembles.

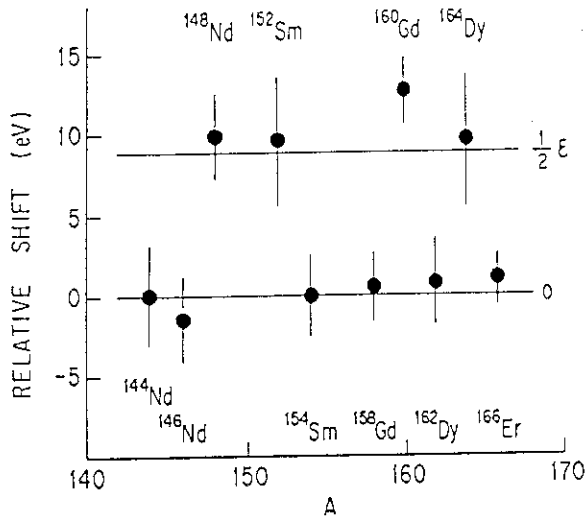

Fig. 1 Relative shifts of the 17.6 eV components.

Except for two nuclei of ^{144}Nd and ^{160}Gd, there is one-to-one correspondence between the change of isotopic components and the relative shift. An increase (or decrease) of two neutrons or two protons in a nucleus makes change its relative shift by one half of the period, and after two successive operations the relative shift returns to the original value. Outside of this mass range, however, such correspondence could not be seen clearly.

Relative shifts of the 4.37 eV components (E < 300 eV)

The ^{177}Hf nucleus with J = 3 levels was taken as a reference. The relative shifts for odd nuclei in the rare earth region behave in a complicated manner, but they show a regular pattern for the nuclei with a mass range of 232 to 242 as is seen from Fig.2. The nuclei from ^{232}Th to ^{238}U have the same relative shift of -(1/6)ε and the ^{242}Pu nucleus has a relative shift of zero. The relative shift of (1/2)ε appears among the nuclei ^{232}Th, ^{236}U and ^{240}Pu where isotopic components differ by even units. The ^{232}Th and ^{236}U nuclei have two periodic components with different shifts. For the ^{232}Th nucleus, the correlation at η = (1/2)ε is weaker than the one at η = -(1/6)ε; for the ^{236}U nucleus, the two components have about the same degree of correlation. It is noted that the 4.37 eV period is one fourth of the 17.6 eV period observed in the even rare earth nuclei.

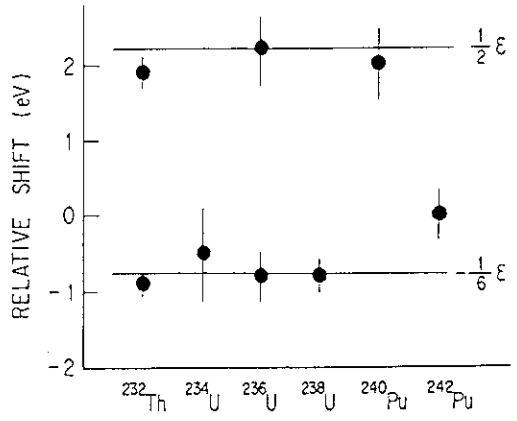

Fig. 2 Relative shifts of the 4.37 eV components.

Relative shifts of the 3.06 eV components (E < 300 eV)

The ^{179}Hf nucleus was taken as a reference. Figs. 3 shows the relative shifts for odd nuclei from ^{127}I to ^{177}Hf, whose levels have two possible spins J = I ± 1/2. In this mass range, most of the relative shifts show a correlated behavior with respect to the values of target spin; the nuclei with I= 1/2 and 5/2 have the relative shift of (1/2)ε and the nuclei with I = 7/2, except for the ^{147}Sm nucleus, have the relative shift of (1/6)ε. The nuclei with I = 3/2 (^{157}Gd and ^{159}Tb) have either η = (1/6)ε or (1/2)ε, and in this case the correlation with the target spin is not definite. For the six nuclei where spin assignments were made to most of the levels, we obtained the relative shifts for the levels with fixed spin J. Fig. 4 shows these relative shifts. In the cases of ^{165}Ho and ^{177}Hf the relative shifts are separated into two values according to the spins J. In the ^{165}Ho nucleus the correlation is stronger for the J = 3 levels than for the J = 4 levels, while in the

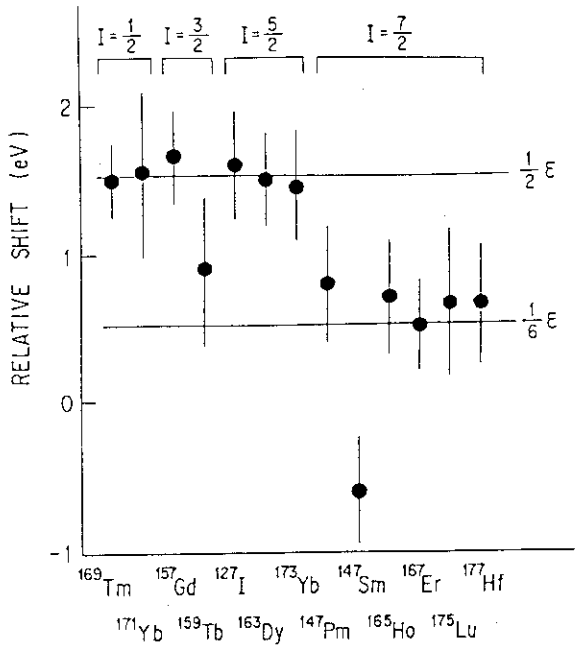

Fig. 3 Relative shifts of the 3.06 eV components.

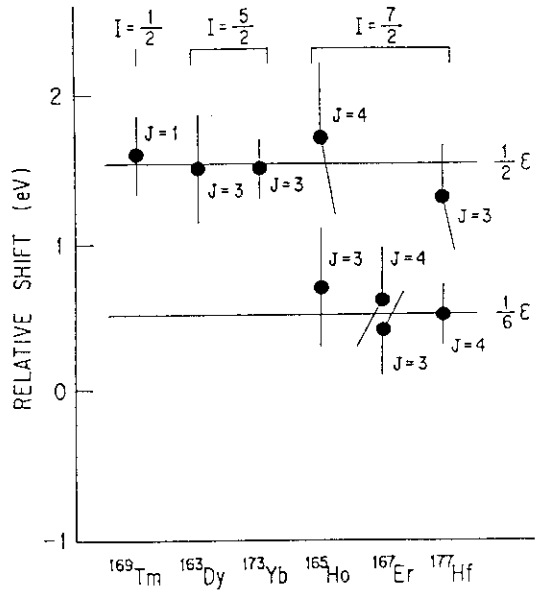

Fig. 4 Relative shifts of the 3.06 eV components for spin J.

^{177}Hf nucleus the correlation is stronger for the J = 4 levels than for the J = 3 levels.

The periodic structures typically seen in the nuclei ^{168}Er, ^{177}Hf and ^{179}Hf seem to be mutually correlated with the level occurrence of other nuclei not only through the periods, but also through the relative shifts.

References

1) K. Ideno: Proc. Int. Conf. on Nuclear Data for Science and Technology (Mito, 1988) p. 783.
2) S. I. Suchoruchkin: Sov. J. Nucl. Phys: 10 (1970) 285; Statistical Properties of Nuclei (Plenum Press, N.Y., 1972) p. 215.
3) K. Ideno and M. Ohkubo: J. Phys. Soc. Jpn. 30 (1971) 620.
4) C. Coceva et al.: Statistical Properties of Nuclei (Plenum Press, N.Y., 1972) p. 447.
5) K. Ideno: J. Phys. Soc. Jpn. 37 (1974) 581.
6) F. N. Belyaev et al.: Sov. J. Nucl. Phys.: 27 (1978) 157.
7) K. Ideno: Proc. Int. Sym. on Highly Excited States in Nuclear Reactions (Osaka Univ., Osaka, 1980) p.83.
8) S. F. Mughabghab et al.: Neutron Cross Sections, Vol.1, Part A (1981), Part B (1984) (Academic Press, N.Y.).

5.5 ELECTROMAGNETIC TRANSITION PROBABILITIES IN THE NATURAL–PARITY ROTATIONAL BAND OF ^{157}Gd

Masumi OSHIMA, Shin–ichi ICHIKAWA,[*] Hideki IIMURA,[*] Hideshige KUSAKARI,[**] Takashi INAMURA,[***] Akira HASHIZUME[***] and Masahiko SUGAWARA[****]

[*]Department of Physics, [*]Department of Chemistry, JAERI, [**]Faculty of Education, Chiba University, Yayoi–cho, Chiba 260, [***]RIKEN, Wako–shi, Saitama 351–01 and [****]Chiba Institute of Technology, Shibazono, Narashino, Chiba 275

In a series of the study of rotational perturbation effects in odd nuclei,[1–4] the nucleus ^{157}Gd has been investigated through multiple Coulomb excitation. Ground–state rotational–band members from $17/2^-$ to $23/2^-$ states have been newly identified in ^{157}Gd.

The experiment was performed using a Ni beam of 240 MeV obtained from the tandem accelerator. Targets used were self–supporting metallic ^{157}Gd, and 93.3 % isotopically enriched: one is about 30 mg/cm^2, and the other about 3 mg/cm^2 in thickness. Deexcitation γ rays were measured with Compton suppressed Ge detectors by using the thick target; $\gamma\gamma$ coincidences, γ–ray angular distributions, and nuclear lifetimes were determined by the recoil distance method using the thin target.

As is shown in Fig. 1, energy levels are clearly dependent on the signature r, that is defined as[5]

$$r = \exp(-i\pi\alpha)$$

where $\alpha = +1/2$ for I = 1/2, 5/2, 9/2,$\cdots$, and $\alpha = -1/2$ for I = 3/2, 7/2, 11/2,$\cdots$. On the contrary, reduced M1 transition probabilities, B(M1; I→I–1), do not show significant dependence on the signature.(See Fig. 2.) Usually the B(M1; I→I–1) is much sensitive to the signature, compared to the energy level.

The present result suggests that the configuration mixing strongly affects the signature dependence of the B(M1) values. Theoretical analysis in terms of a microscopic model is in progress.

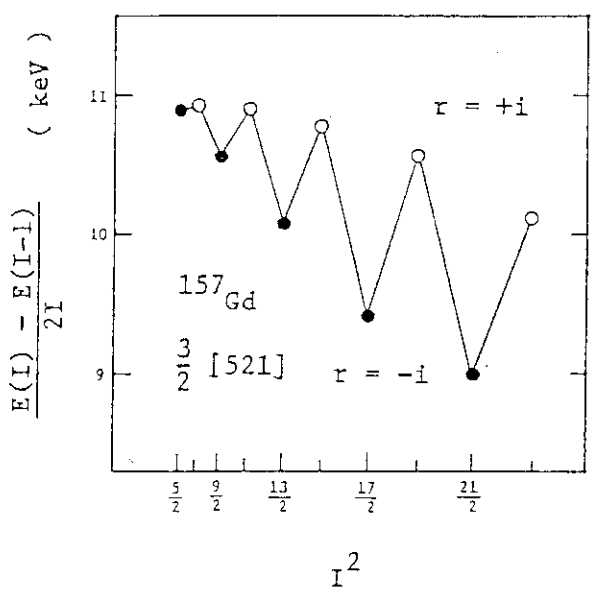

Fig. 1 Energy difference vs. I^2 within the 3/2–[521] rotational band of ^{157}Gd. Closed circles denote the signature $r = -i$, and open ones the signature $r = +i$.

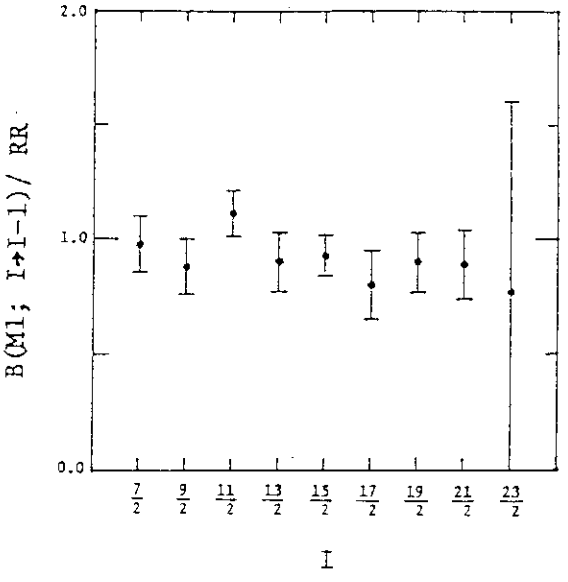

Fig. 2 B(M1;I→I–1) values for the ground–state rotational band of ^{157}Gd.

References

1) M.Oshima et al., Nucl. Phys. A436, 518 (1985).
2) M.Oshima et al., Phys. Rev. C 37, 2578 (1988).
3) E.Minehara et al., Phys. Rev. C 35, 858 (1987).
4) M.Oshima et al., Phys. Rev. C 39, 645 (1989).
5) M.J.A. de Voigt et al., Rev. Mod. Phys. 55, 949 (1983).

5.6 ELECTROMAGNETIC TRANSITION PROBABILITIES IN THE NATURAL–PARITY ROTATIONAL BAND OF ^{173}Yb

Masumi OSHIMA, Shin–ichi ICHIKAWA,[*] Hideki IIMURA,[*] Eisuke MINEHARA, Masayuki MATSUZAKI,[**] Hideshige KUSAKARI,[***] Takashi INAMURA,[****] Akira HASHIZUME,[****] and Masahiko SUGAWARA[*****]

Department of Physics, [*]Department of Chemistry, JAERI, [**]Institute of Physics, University of Tsukuba, Tsukuba, Ibaraki 305, [***]Faculty of Education, Chiba University, Yayoi–cho, Chiba 260, [****]RIKEN, Wako–shi, Saitama 351–01 and [*****]Chiba Institute of Technology, Shibazono, Narashino, Chiba 275

Electromagnetic transition probabilities have been studied putting emphasis on the rotational bands based on high–j orbitals such as $h_{11/2}$ or $i_{13/2}$.[1–7] These high–j orbitals have a unique–parity character and their wave functions are more definite than those of natural–parity orbitals. Rotational perturbations are strong for the unique–parity bands and considerable signature dependence (zigzag pattern) has been observed for the quasiparticle energies and the B(M1) values. The phase rule[8] for the zigzag patterns is well established for the unique–parity bands.

In the natural–parity rotational band of ^{163}Dy, the phase of the zigzag in the B(M1) values is opposite to what is expected for the dominant $j = 9/2$ configuration,[9,10] while the quasiparticle energy splitting and the absolute value of the B(M1) are in agreement with the dominant $j = 9/2$ character. This "inverted" signature dependence was shown in terms of the rotating shell model to originate from the characteristic coherence between the orbital and spin contributions in the spin–down ($\Omega = \Lambda - 1/2$) dominant one–quasiparticle states.[10,11] In order to confirm such a mechanism, the counterpart, i.e., the spin–up ($\Omega = \Lambda + 1/2$) dominant configuration is studied.

We made a Coulomb–excitation experiment on ^{173}Yb whose ground–state rotational band is based on the natural–parity Nilsson state $\nu\, 5/2\,[512]$. We have assigned levels up to $J^{\pi} = (27/2^{-})$ and measured γ–ray branchings, E2/M1 mixing ratios and nuclear lifetimes, and determined the absolute intraband transition probabilities up to the $25/2^{-}$ state as shown in Figs. 1–3. The experimental details have been presented elsewhere.[12] Here we report results of the theoretical analysis.

Microscopic calculation was performed based on the rotating shell model.[13] In

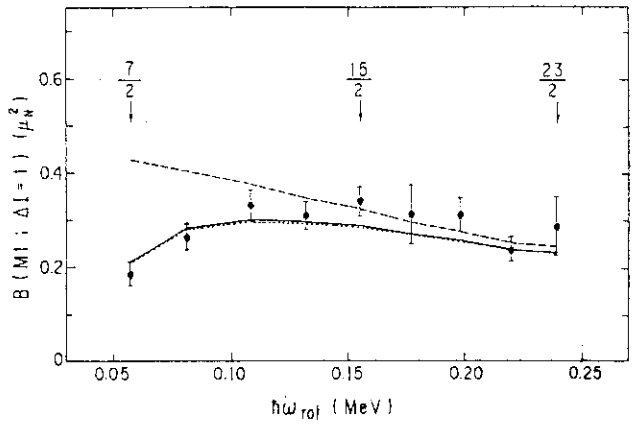

Fig.1 B(M1;I → I−1) values for the ground−state rotational band of ^{173}Yb. The solid (broken) line shows the calculation with (without) the geometrical factor. The dotted line includes the γ vibration besides the geometrical factor.

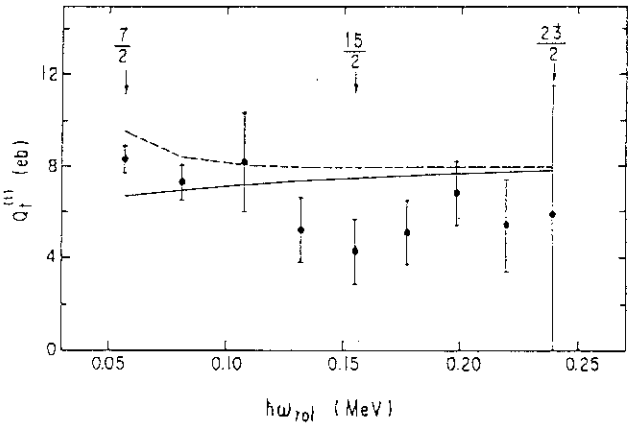

Fig.2 $\Delta I = 1$ transition quadrupole moments for the ground−state rotational band of ^{173}Yb. The notations for the solid and broken lines are the same as in Fig. 1.

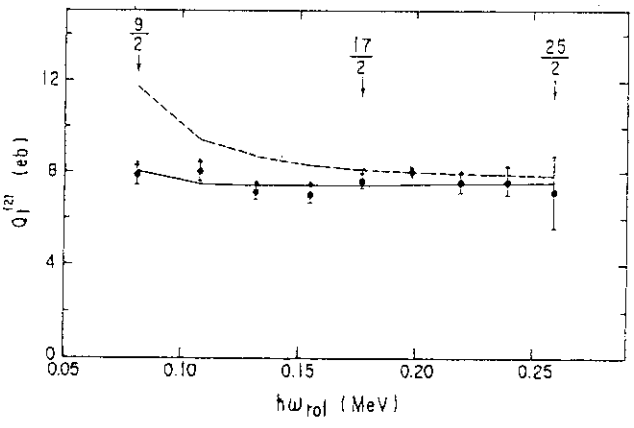

Fig.3 $\Delta I = 2$ transition quadrupole moments for the ground−state rotational band of ^{173}Yb. The notations for the solid and broken lines are the same as in Fig. 1.

this framework following important physical mechanisms are taken into account: static and dynamic triaxial deformations which are estimated to be important in the case of unique−parity orbitals,[14] the many−j mixing effect which is inevitable in treating natural−parity orbitals,[10,11] and many−quasiparticle configurations[15] which may become yrast at very high spins. On the other hand, this framework becomes worse at low−spin states because of its semiclassical nature. In order to overcome this defect in

a simple manner, we adopted the "geometrical factors" proposed by Dönau.[16]

The parameters used in the numerical calculation were as follows. We used the single–particle space consisting of the N_{osc} = 4–6 shells for neutrons and the N_{osc} = 3–5 shells for protons. It means that our model space includes all the j–components which might be contained in the odd–quasineutron orbital under consideration. Quadrupole deformation parameter $\delta = 0.28$ was chosen so as to approximately reproduce the observed quadrupole moments of neighboring even–even nuclei. Gamma–vibrational phonons ($r = \pm 1$) were taken into account up to double excitations. The calculated results with and without the geometrical factors are presented in Figs. 1–3.

The observed quantities, B(M1), B(E2; ΔI=1), and B(E2; ΔI=2), show almost no signature dependence as shown in Figs. 1–3. This appears natural for spin–up ($\Omega = \Lambda + 1/2$) dominant one–quasiparticle bands with natural parity[11] and our calculation reproduces them very well. The spin–up character in the present case is mainly due to the $f_{7/2}$ spherical–shell–model state. Namely, the orbital under consideration ν 5/2 [512] is the counterpart to the ν 5/2 [523] occupied by the last odd particle of ^{163}Dy , whose dominant component is $h_{9/2}$ after an avoided crossing.[10]

The B(M1) value is determined by $| g_j - g_{RPA} |$ in the rotating shell model when one of the spherical–shell–model state j is dominant in the deformed wave function. Here g_j is the Schmidt value and g_{RPA} is calculated as[11]

$$g_{RPA} = \frac{<\mu_x>}{<J_x>}.$$

Consequently the absolute values of B(M1) are large (small) when g_j is negative (positive) in one–quasiparticle bands where g_{RPA} is positive. Besides the effect taken into account by the rotating shell model, the vibrational contributions are expected to affect the B(M1) value depending on the shell structure.[10] Here we discuss the role of γ vibration in the present case.

The phenomenological g_R is extracted from experimental data using a model without the vibrational contributions.[17] When the contributions are negligible, the calculated g_{RPA} and the phenomenological g_R should coincide with each other and the B(M1) value should be reproduced within the rotating shell model. This is true in the present case of ^{173}Yb (Fig. 1) where the calculated g_{RPA} varies from 0.292 to 0.283

as the rotational frequency increases, whereas the phenomenological g_R is 0.277 ± 0.017.[18] The result is consistent with the fact that the collectivity of γ vibration is very weak around the nucleus ^{173}Yb due to the subshell structure in the Nilsson orbitals.[17] In contrast, the calculated values of g_{RPA} for ^{163}Dy were considerably larger than the phenomenological g_R and consequently the calculated B(M1) values were larger than the experimental ones.[10] But this discrepancy has been solved by taking the γ–vibrational effects into account.[10]

Transition quadrupole moments deduced from the B(E2) values are shown in Figs. 2 and 3. Our rotating–shell–model calculation reproduces them well. This means that the adopted deformation parameter is adequate. The effects of the γ vibration on them have been found negligible.

References

1) G.B.Hagemann et al., Nucl. Phys. A424, 365 (1984); D.C.Radford et al., in contrib. to the workshop on Nuclear Structure, The Niels Bohr Institute, May, 1988.
2) M.Oshima et al., Nucl. Phys. **A436**, 518 (1985).
3) K.Honkanen et al., in Proc. of the American Chemical Society Meeting (1986).
4) J.Gascon et al., Nucl. Phys. **A467**, 539 (1987).
5) C.–H.Yu et al., Nucl. Phys. **A489**, 477 (1988).
6) P.Frandsen et al., Nucl. Phys. **A489**, 508 (1988).
7) M.Oshima et al., Phys. Rev. C **37**, 2578 (1988).
8) I.Hamamoto, Phys. Lett. **106B**, 281 (1981); in Proceedings of the Niels Bohr Centennial Conference on Nuclear Structure, Copenhagen 1985, ed. R.Broglia, G.B.Hagemann, and B.Herskind (North–Holland, Amsterdam–London, 1985) p.129.
9) E.Minehara et al., Phys. Rev. C **35**, 858 (1987).
10) M.Oshima et al., Phys. Rev. C **39**, 645 (1989).
11) M.Matsuzaki, Phys. Rev. C **39**, 691 (1989).
12) M.Oshima et al., JAERI–M Report 88–181 (1988) 134; and submitted to Phys. Rev. C.
13) M.Matsuzaki et al., Prog. Theor. Phys. **79**, 836 (1988).
14) M.Matsuzaki, Nucl. Phys. **A491**, 433 (1989); and references therein.
15) M.Matsuzaki et al., Prog. Theor. Phys. **77**, 1302 (1987).
16) F.Dönau, Nucl. Phys. **A471**, 469 (1987).
17) A.Bohr and B.R.Mottelson, Nuclear Structure Vol. 2 (Benjamin, New York, 1975).
18) F.Boehm et al., Phys. Lett. **22**, 627 (1966).

5.7 LIFETIMES AND G-FACTORS OF EXCITED STATES IN ^{106}Sn

Tetsuro ISHII, Mitsuhiko ISHII,
Yuichi SAITO*, Mituo NAKAJIMA* and Masao OGAWA*

Department of Physics, JAERI, *Tokyo Institute of Technology, Yokohama

We have established the level scheme up to the $14^{\pm}$ state in ^{106}Sn in the previous experiment[1] as shown in fig.1; the lower 2^+, 4^+ and 6^+ states come from a broken pair of neutrons and the others, probably, have higher seniorities. In order to confirm the nature of these states, we have measured the lifetimes and the g-factors of some of them.

Excited states in the nucleus ^{106}Sn were populated via the reaction ^{51}V(^{58}Ni,1p2n) with a 217MeV ^{58}Ni beam from the JAERI tandem accelerator. The γ-rays of ^{106}Sn were sorted with a help of the Si-Box.[2] The lifetime measurement has been done by the recoil distance method as well as the centroid-shift method of TAC spectra between particles and γ-rays. In the former we employed three stacks of foils: ^{51}V 2.4mg/cm^2 thick and Cu 9mg/cm^2 thick with separations of 1.0, 0.5 and 0.25mm. The lifetimes have been measured to be 2.3±0.5ns(6^+), 40±10ps(10^+) and 20±10ps($14^{\pm}$). The B(E2) values of the 6^+ and 10^+ states are estimated to be 3.1 W.u. and 3.9 W.u.,respectively.

The g-factors have been measured by the method of the integral perturbed angular distribution. The target used was a ^{51}V foil 2.7mg/cm^2 thick backed with Gd 7.9mg/cm^2

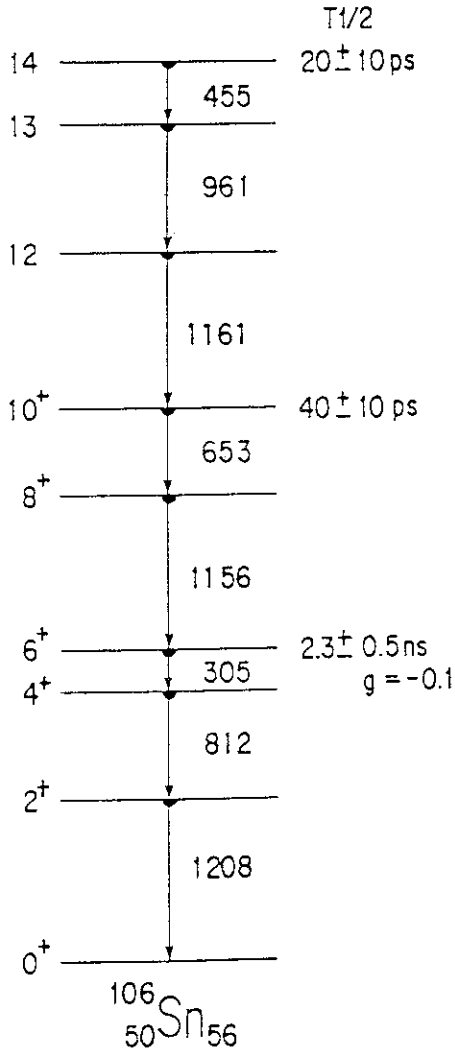

Fig.1 Level scheme of ^{106}Sn. The transition energies are given in units of keV.

thick. The ^{106}Sn nuclei were implanted into the Gd backing which was cooled and magnetized up or down. The perturbed γ-rays angular distributions have been observed by two Ge detectos placed at $\pm 50^{\circ}$ to the direction of the beam. The ^{106}Sn nucleus precessed by -4° in the 6^+ state. By comparison between Stone's data[3] in Fe host and ours in Gd host[4], the internal magnetic field of Sn in Gd was estimated to be -40kG. Together with the lifetime measured, we have obtained $g(6^+) \simeq -0.1$. This negative and small g-factor indicates that the 6^+ states is composed of a dominent component of $|\nu g_{7/2} \cdot \nu d_{5/2}>$ with a small admixture of $(\nu g_{7/2})^2$; $g(|\nu g_{7/2} \cdot \nu d_{5/2}>)=-0.072$ and $g(|(\nu g_{7/2})^2>)=+0.42$. Furthermore a small rotation($< 1^{\circ}$) was observed for the 8^+ state of ^{106}Sn having experienced the transient magnetic field. This suggests that higher excited states proceeding the $14^{\pm}$ state have a small g-factor and are probably neutron-like. So are the states with spins 10^+ to $14^{\pm}$ because no long-lived isomer intervenes among them.

References

1) T. Ishii et al., JAERI-M 88-181 131(1988)
2) M. Ishii et al., in Nuclei off the line of Stability(ed. R. A. Meyer and D. S. Brenner, A.C.S., Washington D.C., 1986) ch. 75
3) Stone,N. J., in Nuclei off the line of Stability(ed. R. A. Meyer and D. S. Brenner, A.C.S., Washington D.C., 1986) p.350
4) T. Ishii et al., to be submitted to Z. Physik, 'Static Hyperfine Interaction in Ba and Light Rare-Earth Ions Recoil-Inplanted into Gd Host'

5.8 NUCLEAR STRUCTURE OF ^{105}In

Tetsuro ISHII, Mitsuhiko ISHII,
Yuichi SAITO*, Mituo NAKAJIMA* and Masao OGAWA*

Department of Physics, JAERI, *Tokyo Institute of Technology, Yokohama

We have studied the nuclear structure of ^{105}In . ^{105}In nuclei were produced by bombarding ^{51}V with a 217MeV ^{58}Ni beam from the JAERI tandem accelerator. The p–γ and p–γ–γ coincidences have been taken by selecting the exit channel to ^{105}In with a help of the Si–Box.[1] The level scheme obtained is shown in fig.1. The spin–parity assignment is based on the level scheme of the nucleus ^{107}In[2] because there exists one to one correspondence in the γ–γcoincidences between most of γ–rays from these two nuclei. The lower three excited states with spins $13/2^+$, $17/2^+$ and $21/2^+$ consist of the proton hole $\pi(g_{9/2})^{-1}$ coupling with the 2^+, 4^+ and 6^+ states in ^{106}Sn, respectively.

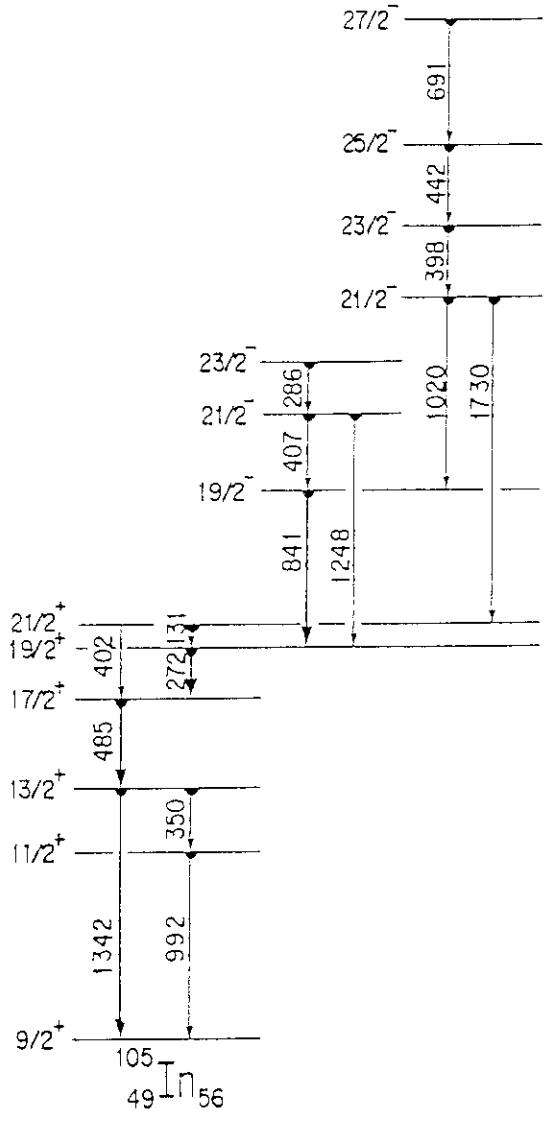

Fig.1 Level scheme of ^{105}In.

References

1) M.Ishii et al., in Nuclei off the line of Stability(ed. R.A. Meyer and D.S. Brenner, A.C.S., Washington D.C., 1986) ch.75
2) E. Andersson et al., Phys. Rev. C24(1981)917

5.9 INVARIANT FISSION PATH IN THE MULTI–DIMENSIONAL PARAMETER SPACE

Akira IWAMOTO and Toshiki. KINDO

Department of Physics, JAERI

The spontaneous fission is considered as a multi–dimensional penetration problem in the parameter space. We do not, however, have the standard method to treat this problem. The adiabatic model, which defines the fission path as the valley line in the fission potential, is frequently used as an approximation. Some groups[1,2] pointed out, however, that the action integral along the adiabatic path dose not lead to the minimum action. In addition, the adiabatic model has a serious defect that the path and the action along it depend on the choice of the coordinate system[3]. On the other hand, the methods used in Refs.1 and 2 involve considerable amount of calculations and are almost impossible to be applied to the three– or more–dimensional problem with good accuracy. We consider two models for the calculation of the fission half–life which are invariant with respect to the coordinate transformation. First one is the application of the model of Schmid[4]. Another one is the invariant adiabatic model[3], which has a feature of the adiabatic model and is invariant with respect to the coordinate transformation.

We treat only the symmetric fission and neglect the shell effect on the potential and mass tensors. The shape parameters are taken from the two–center shell model in which we use two parameters, center separation z and the spheroidal deformation parameter of fragments δ. The potential energy is calculated by the Yukawa–plus–exponential model[5] and the mass tensors by the Werner–Wheeler method[6].

We start from the Schrödinger equation,

$$\mathcal{H}\psi(z,\delta) = E\psi(z,\delta), \tag{1}$$

where E is the energy eigenvalue and the Hamiltonian $\mathcal{H}$ is assumed as

$$\mathcal{H} = -\frac{\hbar^2}{2}\frac{\partial}{\partial x^i}(M^{-1})^{ij}(z,\delta)\frac{\partial}{\partial x^j} + V(z,\delta), \tag{2}$$

where $x^i = z$ or δ. Here we generalized the assumption of constant masses used by Schmid[4] to the the coordinate–dependent mass tensors for use in the fission study. In the classically forbidden region, we put the wave function in the $\hbar$–expansion form and insert it

into eq.(1). Equating the terms of equal power of $\hbar$, we obtain in the leading order the eikonal equation. This equation can be solved by the method of characteristics. Following the method of Schmid[4], we can find numerically the escape path which gives a minimum action integral among the possible paths. From the derivation of this model, it is clear that the escape path is invariant with respect to the coordinate transformation. To distinguish this path from other paths which will be given below, we call this path as the invariant dynamical path.

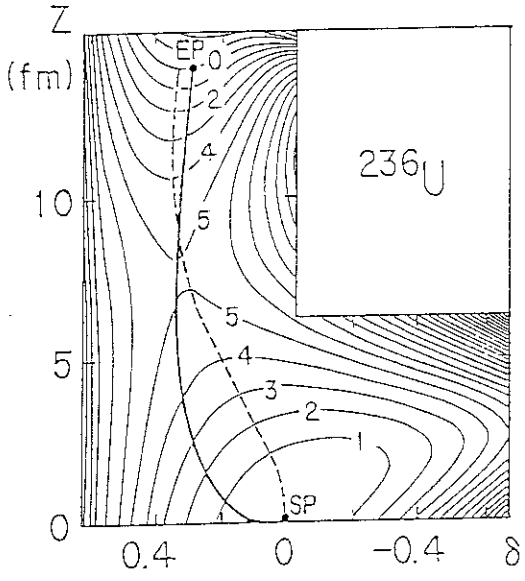

Fig.1 The potential energy surface for the fission of ^{236}U. The equipotential surfaces shown by thin solid lines are plotted in units of MeV. The solid line is the escape path and the dashed line is the usual adiabatic path for the spontaneous fission. The invariant adiabatic path is not shown because it almost coincides with the escape path for this nucleus.

Our Werner–Wheeler mass is an approximation to the incompressible and irrotational flow mass. In the fission study, it is necessary to introduce the factor $k \approx 7$[7] to renormalize the mass. We introduce the fitting parameter k to the mass corresponding to the fissioning motion[3].

In Fig.(1), the potential energy and fission paths for the spontaneous fission of ^{236}U are shown. The solid line is the escape path and the dashed line is the usual adiabatic path which is defined as the line passing the saddle point and is always orthogonal to the equipotential surface. From this figure, we see a large difference between two fission paths. The origin of this difference is the effect of kinetic energy which is neglected in the adiabatic treatment.

The WKB action S is written in the form,

$$S = \int ds \, [2\{V(\vec{x}(s))-E\} \cdot \frac{dx^i(s)}{ds} M_{ij} \frac{dx^j(s)}{ds}]^{\frac{1}{2}} . \qquad (3)$$

where s is an arbitrary parameter and the integration is performed along a fixed path. If we choose the escape path for the integration and denote the action integral by S_{es}, the

fission half–life $T_{\frac{1}{2}}$ is expressed as,

$$T_{\frac{1}{2}} = \left(\frac{2\pi}{\omega}\right) exp(-2S_{es}/\hbar), \tag{4}$$

where ω is the typical frequency of the nuclear surface vibration and is fixed as $\hbar\omega/2 =$ 0.5MeV in the following numerical calculations.

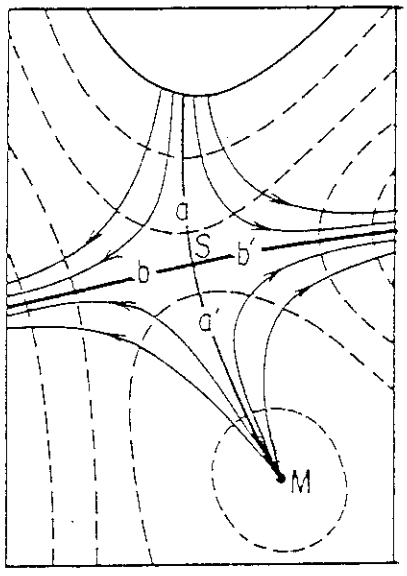

Fig.2 The figure showing the concept of the invariant adiabatic path. M represents the minimum (ground state deformation) point and S represents the saddle point of the potential. The dashed lines are the equipotential surfaces and a solid line in the upper part is the equipotential surface whose energy is the same as point M. Thin solid lines with arrows are solutions of eq.(5). The line a–a' defines the invariant adiabatic path.

To obtain the escape path numerically is, however, not easy. Therefore, we propose an alternative model which is invariant with respect to the coordinate transformation and at the same time, is easy to calculate. To define it, we start by solving the equation,

$$M_{ij}\frac{dx_j}{ds} = \frac{\partial V}{\partial x^i}. \tag{5}$$

Here s stands for an arbitrary parameter. As was shown in eq.(3), the WKB action does not depend on s but depends only on the shape of the trajectory determined from eq.(5). We show in Fig.2, the solution of this equation for a simple potential which has one minimum and one saddle point. The dashed lines in this figure are the equipotential energy surfaces and the solid lines with arrows are the solution of eq.(5). Paths obeying this equation have two asymptotes and we define the asymptote a–a' as the new adiabatic path. This adiabatic path is invariant with respect to the coordinate transformation,

$$x^i \to q^i,$$

$$M_{ij} \to \mathcal{M}_{kl} = \frac{\partial x^i}{\partial q^k}\cdot M_{ij}\cdot\frac{\partial x^j}{\partial q^k}. \tag{6}$$

The WKB action for this adiabatic path can be calculated by eq.(3) and the corresponding life time is obtained by using eq.(4). New adiabatic action is invariant with respect to the

coordinate transformation and we call this path as the invariant adiabatic path.

WKB actions were calculated along two invariant paths (dynamical and adiabatic) and along the usual adiabatic path for the spontaneous fission of ^{236}U and ^{212}Po. For ^{236}U, the "experimental" action, which is calculated from eq.(4) by using the fission half-life data is about 53ħ. The value of k=23 for ^{236}U is necessary for the invariant actions (they differ within 1%) to agree with the experimental data and k=15, for the usual adiabatic action to agree with the data. For ^{212}Po, k=20 is rather arbitrary chosen. In this case, calculations show that two invariant paths give the values of actions 88ħ and 90ħ, respectively. They deviate only 2% but the usual adiabatic path gives the value 114ħ.

In conclusion, we showed that the method of Schmid works well for the calculation of the fission half-life if we treat the mass tensors as coordinate-dependent quantities. The method gives us the fission path which minimizes the action integral and which is invariant with respect to the coordinate transformation. An alternative model we proposed is a new adiabatic model, in which the path is also invariant with respect to the coordinate transformation. In addition, the path is a good approximation to the minimum action path. *We insist that this definition of the adiabatic path should be used in place of the commonly used adiabatic path which is coordinate dependent.* Two methods we proposed are applicable for the decay process in the strongly-coupled multi-dimensional parameter space which can not be reduced into the product of one-dimensional subspace.

References

1. M. Brack et.al., Rev.Mod.Phys.44 (1972) 320.
2. A. Baran et.al., Nucl.Phys.A361 (1981) 83.
3. T. Kindo and A. Iwamoto, Phys.Lett.B. in press.
4. A. Schmid, Ann.Phys.170 (1986) 333.
5. H.J. Krappe, J.R. Nix and A.J. Sierk, Phys.Rev.C20 (1979) 992.
6. K.T.R.Davies, A.J. Sierk and J.R. Nix, Phys.Rev.C13 (1976) 2385.
7. J. Rundrup et.al., Nucl.Phys.A217 (1973) 221.

5.10 STRUCTURE OF ACTINIDE NUCLEI AND THE *SPDF* BOSON MODEL

Michiaki SUGITA and Takaharu OTSUKA*

Department of Physics, JAERI, *Department of Physics, University of Tokyo*

We have investigated the structure of the actinide nuclei and the α decay in terms of the *spdf* boson model [1-5]. In the present article, we will mainly discuss $K^{\pi}=0^{+}$ bands. On the other topics concerned with the *spdf* boson model, refer to Ref.[1-3].

In some actinide nuclei, one finds an excited $K^{\pi}=0^{+}$ band which has the following unusual properties:

(i) The moment of inertia is larger by a factor of ≈1.5 than that of the ground band, while the excitation energy is as low as the energy of the γ bands.

(ii) The α–decay width to this band is relatively large (hindrance factor ≈10).

[We have called this band *super* β band to distinguish it from the *usual* β bands [4].]

We have studied side bands of the actinide nuclei, including this band, in terms of the *spdf* boson model [1-3]. We take ^{228}Th as an example. The energy and the wave function are obtained by the *angular–momentum* and *parity* projected Tamm–Dancoff approximation [4], where all possible K–values are included in the standard diagonalization procedure. Therefore, all states are exactly orthogonal, while K–values can stand only for major component in general.

By using the Hamiltonian containing six free parameters [4], the theoretical energy levels in Fig. 1 are obtained. There are two excited $K^{\pi}=0^{+}$ bands in the calculated bands; the one with higher energy is the usual β band which has the same moment of inertia as the ground band, whereas the lower one has a larger moment of inertia.

The lower one corresponds to the observed $K^{\pi}=0^{+}$ band at Ex=832 keV [6]. Although the usual β band has not been confirmed experimentally, the fourth 2^{+} state at Ex=980 keV seems to be a good candidate for the 2^{+}_{β} band member[6]. The agreement between theory and experiment is quite good for all bands in Fig. 1. It is of much interest to locate the other members of the usual β band experimentally.

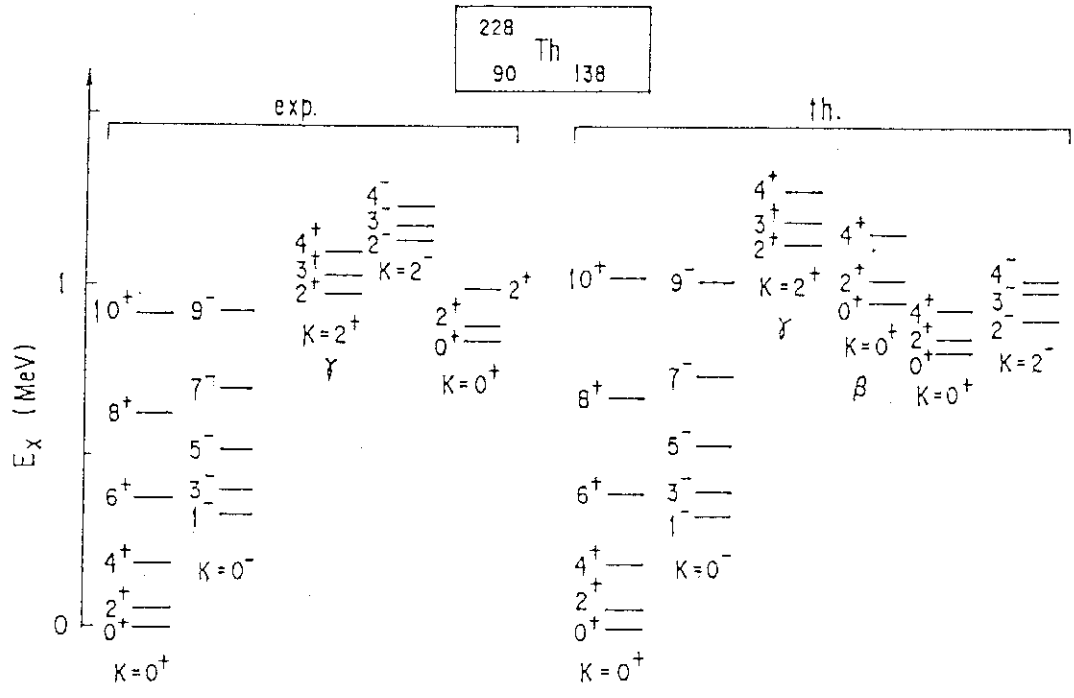

Fig. 1 Experimental (exp.) [ref. 6] and theoretical (th.) energy levels of ^{228}Th.

The α–decay widths to the 0^{+} states of the super and the usual β band are evaluated with the following operator [4,5]:

$$\hat{T}(\alpha,L=0) = \alpha_0 (\tilde{s}_{\pi}\cdot\tilde{s}_{\nu}) + \alpha_1 (\tilde{p}_{\pi}\cdot\tilde{p}_{\nu}) + \alpha_2 (\tilde{d}_{\pi}\cdot\tilde{d}_{\nu}) + \alpha_3 (\tilde{f}_{\pi}\cdot\tilde{f}_{\nu})$$

where α's are parameters and $(\cdot)$ stands for the scalar product. We have calculated the α–decay width for ^{232}U $\rightarrow$ ^{228}Th + α. The resultant hindrance factor is 15 for the *super* β band, whereas it is 69 for the *usual* β band. Experimentally [7], the value for the former is about 10, which does not differ much from the calculation. The hindrance factor for the usual β band has not been measured yet, but is expected to be large[7].

The expectation values of the sum of the p and f bosons are 0.2, 1.3 and 1.5 for the 0_1^+, 0_1^- and 0_2^+ states, respectively. As expected, the 0_1^+ state contains small amount of the negative–parity bosons, while the values for the 0_1^- and 0_2^+ states are similar. Because of this, the present description of the 0_2^+ (*i.e., super* β) band contradicts the naive picture that it is the double excitation state of the octupole phonon. In fact, the observed anharmonicity is too strong to accept the *double–phonon* ansatz.

In summary, we would like to emphasize that the *spdf* boson model can provide us with a comprehensive description of various interesting aspects of actinide nuclei within a single framework.

References

1) T. Otsuka and M. Sugita, Phys. Lett. **B209** (1988) 140
2) T. Otsuka and M. Sugita, Proceedings of the International Conference on *Contemporary Topics in Nuclear Structure Physics*, P.385 (Cocoyoc, Mexico, June 9–14, 1988)
3) T. Otsuka and M. Sugita, JAERI–M 88–100, P.27 (Report on the Joint Seminar on *Heavy–ion Nuclear Physics and Nuclear Chemistry in the Energy Region of Tandem Accelerators* (III))
4) T. Otsuka and M. Sugita, J. Phys. Soc. Japan **58** (1989) Suppl. P.530 (Proceedings of the Fifth Int. Conf. *Clustering Aspects in Nuclear and Sub–nuclear Systems*, Kyoto, July 25–29, 1988)
5) M. Sugita and T. Otsuka, Proceedings of the International Symposium on *Developments of Nuclear Cluster Dynamics*, P.88 (Sapporo, Japan, 1–3 August 1988)
6) J. Dalmasso *et al.*, Phys. Rev. **C3** (1987) 2510
7) W. Kurcewicz *et al.*, Nucl. Phys. **A289** (1977) 1

Ⅵ NEUTRON PHYSICS

6.1 SCATTERING OF 28.15 MeV NEUTRONS FROM ^{12}C

Yoshimaro YAMANOUTI, Masayoshi SUGIMOTO, Satoshi CHIBA,
Motoharu MIZUMOTO, Yukinobu WATANABE*
and Kazuo HASEGAWA**

Department of Physics, JAERI, *Department of Nuclear Engineering, Kyushu University, ** Department of Nuclear Engineering, Tohoku University

Neutron scattering cross sections in the energy range above 20 MeV are of great importance for deeper understanding of the nucleon-nucleus interaction. For the neutron scattering on ^{12}C in the energy range above 20 MeV, elastic and inelastic scattering at incident energies of 20.8, 22, 24 and 26 MeV[1], and at an incident energy of 21.6 MeV[2] has been studied, and differential cross sections for elastic scattering at 40 MeV have been reported[3]. In this work differential cross sections for elastic and inelastic scattering of neutrons on ^{12}C were measured at an incident enery of 28.15 MeV in order to study the reaction mechanism for the neutron scattering in the energy region around 30 MeV and the collective nature of ^{12}C. These experimental data were analyzed by the optical model and the coupled-channel(CC) theory, and compared with proton scattering in the framework of the Lane model.

The measurements were performed with the pulsed beam time-of-flight technique. A pulsed beam of protons with a repetition rate of 4 MHz and with a burst duration of about 2 nsec was provided by the JAERI tandem electrostatic accelerator. Neutrons were generated by the $^{7}Li\ (p,n)\ ^{7}Be$ reaction. A lithium-metal target with proton energy loss of 450 KeV was used as a neutron producing target. The neutron detector is a 20 cm in diam by 35 cm thick NE213 liquid scintillator viewed by RCA 8854 photo-multiplier tubes at the front and rear scintillator faces. Neutrons were observed by an array of these four neutron detectors for efficient measurements of scattered neutrons.

Fig.1 shows a neutron time-of-flight spectrum obtained at 60°. The efficiency of the neutron detector was determined by measuring the angular distribution of neutrons from the $^{1}H(n,n)\ ^{1}H$ reaction. The differential cross sections were normalized to the known n-p scattering differential cross sections by measuring neutrons scattered from

a 12 cm in diam by 4 cm long polyethylene scatterer. The resulting differential cross sections were corrected for dead time in the data acquisition system, and also for multiple scattering and flux attenuation in the scattering sample. Differential cross sections were obtained for the elastic scattering and the inelastic scattering leading to the excited states at 4.439 MeV(2^+) and 9.641 MeV(3^-) over the angular range from 20° to 140° in 10° steps. The experimental cross sections are shown in figs.2 and 3 together with theoretical predictions.

The data were analyzed first by the optical model. The compound nuclear contribution estimated by the Hauser-Feshbach formalism is small compared with the experimental cross sections at the incident energy of 28.15 MeV.

The CC calculations based on the rotational model and the vibrational model were performed with the codes ECIS79 and JUPITOR1. In the rotational model calculations, CC calculations with the quadrupole deformation only, and with the quadrupole and hexadecapole deformation were carried out. In the CC calculations optical potential parameters except the spin orbit term, and the deformation parameters were adjusted to get the best fit to the experimental cross sections for the elastic and inelastic scattering. The theoretical curves of the CC calculations are shown in figs.2 and 3. The rotational model calculation with the oblate quadrupole and hexadecapole deformation gives slightly better fit to the experimental cross sections for the elastic and inelastic scattering on ^{12}C than the vibrational model. The present result is consistent with that obtained in the energy range from 20.8 to 26 MeV[1].

A proton potential obtained in proton scattering[4] was transformed into a neutron potential in the Lane model, and its ability to predict the present neutron cross sections for elastic and inelastic scattering was checked in CC calculations. The same deformation parameters as those obtained in the proton scattering were used. The CC calculation reproduces well the present neutron cross sections for the elastic scattering and the inelastic scattering to the first 2^+ state.

References

1) A.Meigooni, R.W.Finlay and J.S.Petler: Nucl Phys. A445 (1985) 304
2) N.Olsson et al: Nucl.Phys. A472 (1987) 237
3) R.P.DeVito: Ph.D. thesis, Michigan State University (1979)
4) R.DeLeo et al: Phys.Rev. C28 (1983) 1443

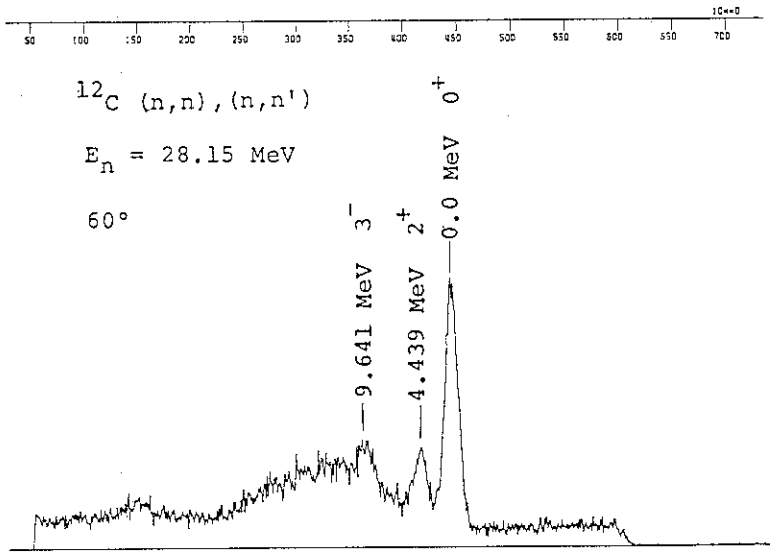

Fig.1 A time-of-flight spectrum of elastic and inelastic scattering of 28.15 MeV neutrons from ^{12}C at 60°.

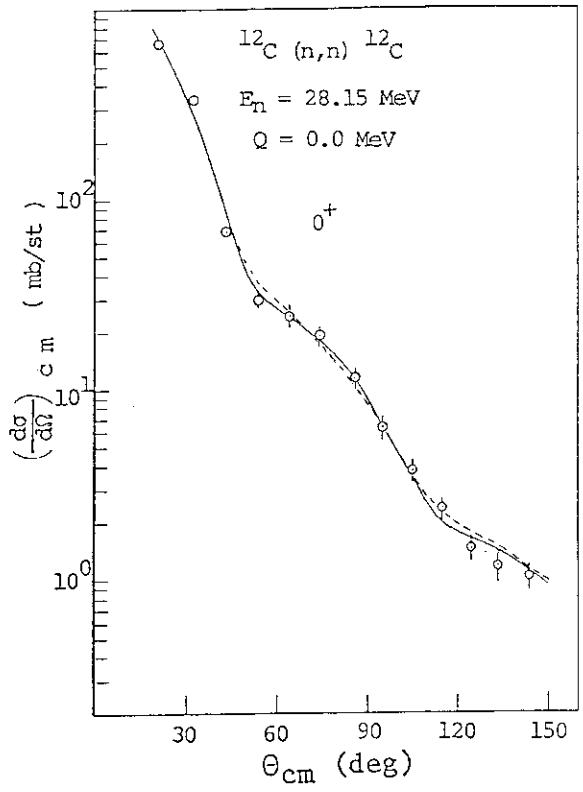

Fig.2 Elastic scattering cross sections and CC calculations. solid line: rotational model with oblate quadrupole and hexadecapole deformation, dashed line:vibrational model

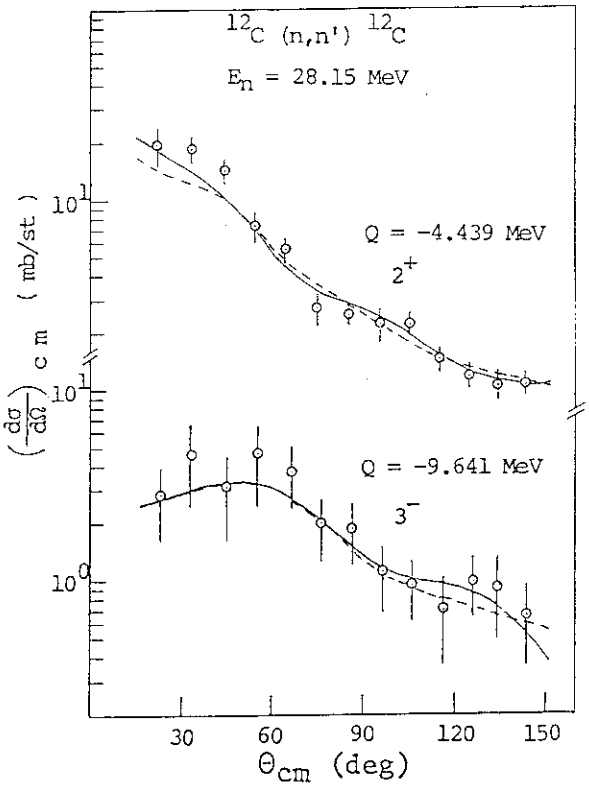

Fig.3 Inelastic scattering data and CC calculations. solid line: rotational model with oblate quadrupole and hexadecapole deformation, dashed line: vibrational model

6.2 GAMMA-RAY PRODUCTION CROSS SECTIONS OF Al,Si,Fe,Pb AND Bi AT 10 AND 11.5 MeV

Motoharu MIZUMOTO, Kazuo HASEGAWA*, Satoshi CHIBA, Masayoshi SUGIMOTO, Yoshimaro YAMANOUTI, Masayuki IGASHIRA**, Toshiro UCHIYAMA**, Hideo KITAZAWA**

Department of Physics, JAERI, *Faculty of Engineering, Tohoku University, **Research Laboratory for Nuclear Reactor, Tokyo Institute of Technology

Introduction

Gamma-ray production cross sections have been measured for structural materials such as Al, Si, Fe, Pb and Bi at the neutron energies of 10 and 11.5 MeV. In last year 1987, we have measured the similar data at the lower energy of 7.8 MeV[1]. Gamma-ray data are very important to calculate radiation shielding and γ-rays heating for fusion reactors. Experimental data, however, are still scarce in the neutron energy region between 5 and 14 MeV, where adequate neutron sources have not been available. Previous measurements were only obtained with the white neutron source at the ORNL electron linear accelerator[2].

Continuum γ-rays from reactions of inelastic scattering (n,n'γ), neutron capture (n,γ) and charged particle (n,pγ) and (n,$\alpha\gamma$) have been observed in our measurements. The energy dependence of some discrete γ-rays due to the (n,n'γ) have been also newly obtained.

The γ-ray production data for JENDL-3 (Japanese Evaluated Nuclear Data Library -Version 3) have been evaluated for these nuclei[3] by taking into account such various reactions. Our data were used for the check of the validity of the evaluated files.

Experiment and Analysis

The present experiments were made at the energies of 10 and 11.5 MeV with two neutron sources of $^{2}H(d,n)^{3}He$ and $^{1}H(^{11}B,n)^{11}C$ reactions, respectively. In particular, the latter source was found to be very interesting and useful for our experiments[4]. Fig. 1 shows the time-of-flight spectrum of the neutron source which is kinematically collimated into

a forward angle and has very low background components.

The γ-ray detector was a 7.6 cm diam. x 15.2 cm long NaI(Tl) detector, which was set in a 25.4 cm diam. x 25.4 cm long NaI(Tl) annular detector. These two detectors were operated in an anti-coincidence mode to suppress Compton backgrounds and neutron capture γ-rays in the detector. The TOF technique of the γ-ray detection was used to improve the signal to background ratio.

The neutron spectra were measured by employing two sets of 5 cm diam. x 1.27 cm thick NE213 detectors located at a forward angle and either 59° (for d-D neutron) or 29.2° (for ^{11}B-H neutron). The standard cross section of Al(n,α) reaction was also used to normalize the absolute neutron flux for the ^{11}B-H neutrons, for which the activation of ^{24}Na with a half life of 15 hours was measured with Na(Tl) and Ge detectors.

The response functions of the γ-ray detector were determined with the discrete γ-rays from the standard sources of ^{60}Co, ^{137}Cs and ^{22}Na. and the several discrete γ-rays from the 992 keV resonances of ^{27}Al(p,γ) and the 935 keV resonance of ^{19}F(p,γ) using the proton beam at the TIT pelletrons[5]. The inelastic γ-rays from the ^{12}C(n,n'γ) and ^{16}O(n,n'γ) reactions were also utilized.

After subtracting the backgrounds, γ-ray spectra were unfolded using the computer program FERDOR. Corrections were applied for attenuation and multiple scattering of neutrons and γ-rays by the Monte Carlo program.

Results and discussion

The results at 11.5 MeV are shown in Figs. 2-5 together with the data taken at ORELA[2]. (The data at 10 MeV are not included in the present report due to the limited space). The overall agreement of the spectrum shape is good both for the data at 10 and 11.5 MeV. The careful comparisons, however, show that their peak areas in the lower γ-ray energy region are generally larger than the present data.

Fig. 6 shows the examples of the energy dependence for the discrete γ-rays of Si, Fe and Pb. Though our data are only available above 10 MeV, agreement among the experimental data is good.

The JENDL-3 data are also compared in the figures. The evaluations represents the present experimental data reasonably well with some data which may have to be modified based on the our data.

References

1. M. Mizumoto et al., Proc. Int. Conf. on Nuclear Data for Science and Technology, Mito,1988, p197-200
2. J.K. Dickens et al., Nucl. Sci. Eng. 62 (1977) 515
3. JENDL CG (Nuclear Data Center), JENDL-3T Private communication (1989)
4. S. Chiba et al., to be published in NIM, Section A, (1989)
5. K. Hasegawa and M. Mizumoto, JAERI-M 89-042, 1989.

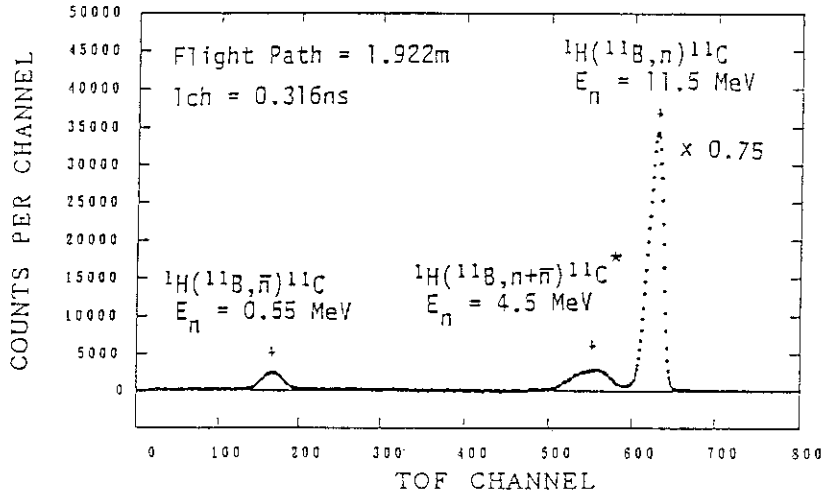

Fig.1 TOF spectrum of $^{1}H(^{11}B,n)^{11}C$ neutron source

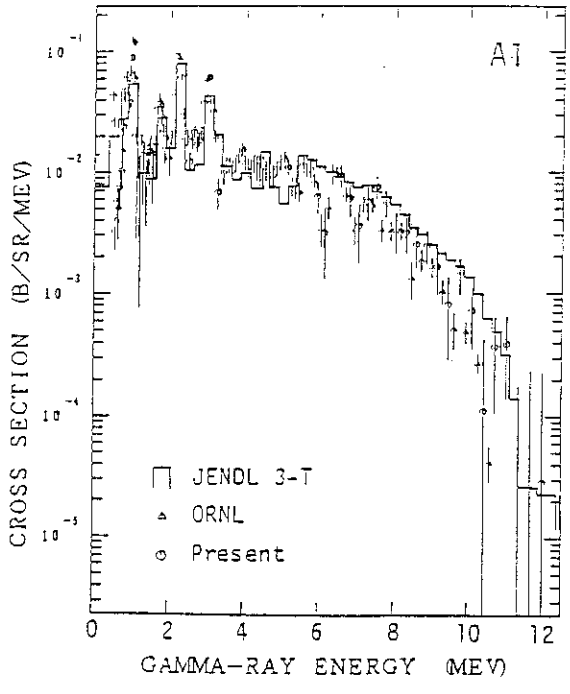

Fig.2 Gamma-ray spectrum of Al

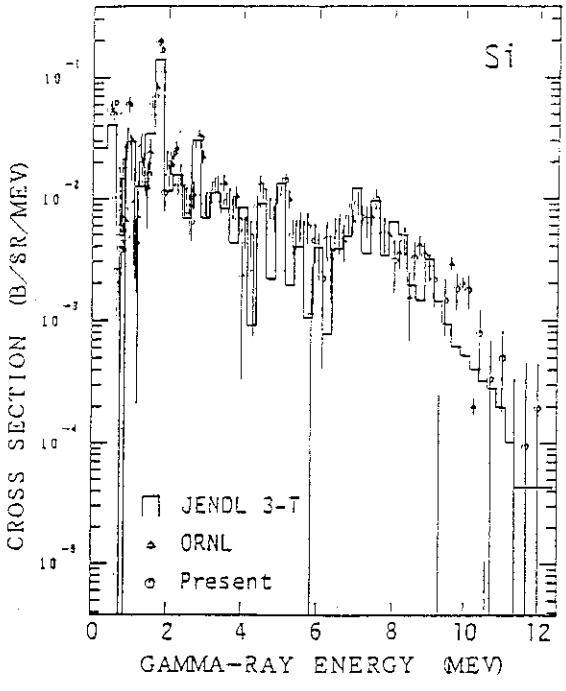

Fig.3 Gamma-ray spectrum of Si

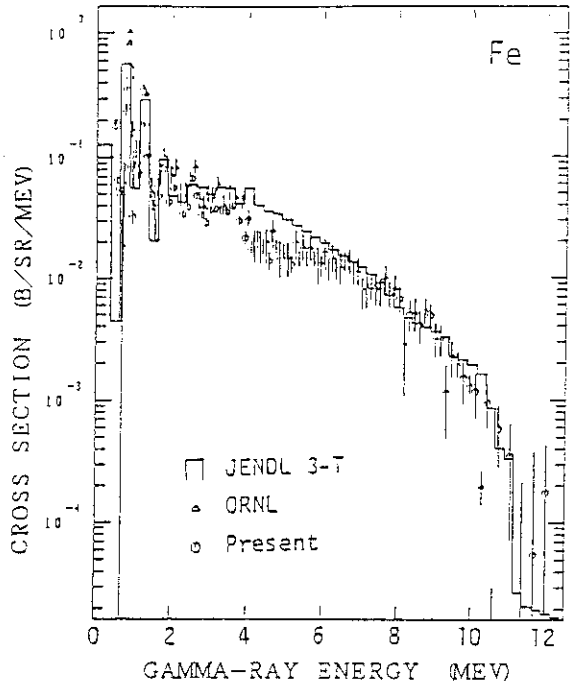

Fig.4 Gamma-ray spectrum of Fe

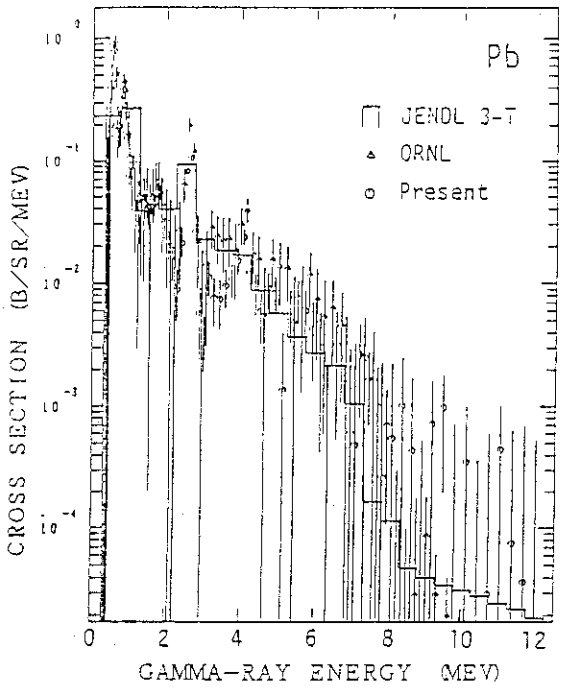

Fig.5 Gamma-ray spectrum of Pb

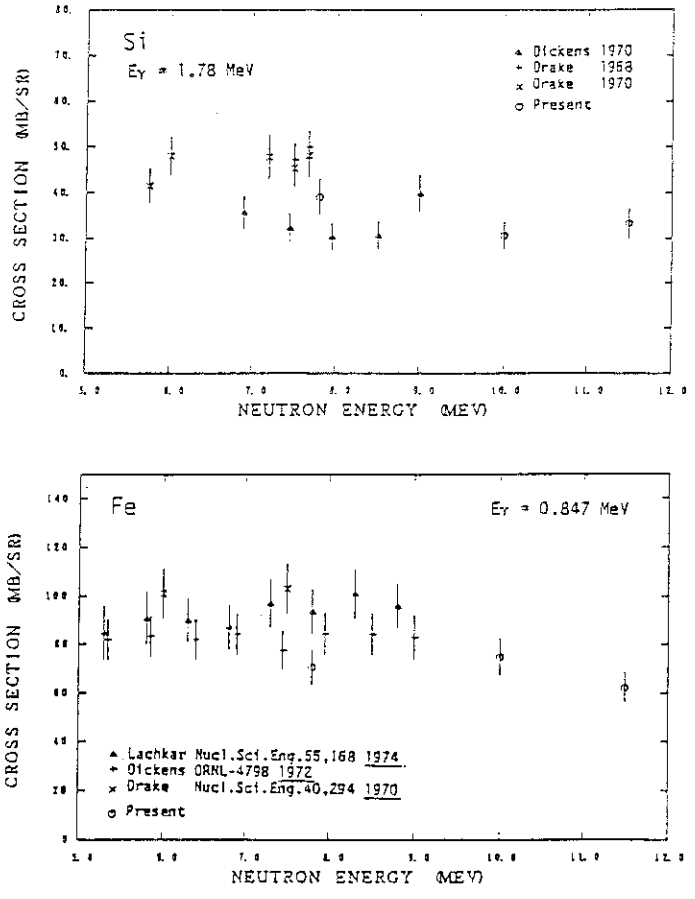

Fig. 6 Discrete gamma-ray production cross sections

Ⅶ PUBLICATIONS

Journal/Proceedings

1. Aruga, T., Takamura, S., Hoshiya, T. and Kobiyama, M.
   Effects of He Ion Irradiation on Superconductivity of Bi-Sr-Ca-Cu-O Films
   Jpn. J. Appl. Phys. 28 (1989) in press.
   V

2. Baba, S., Hata, K., Ichikawa, S., Sekine, T., Nagame, Y., Yokoyama, A., Shoji, M., Saito, T., Takahashi, N., Baba, H. and Fujiwara, I.
   Evaporation Residue Formation Competing with the Fission Process in the $^{197}Au + ^{16}O$, ^{12}C Reactions and Fission Barriers at a Specified J Window
   Z. Phys. A 331 (1988) 53.
   T

3. Fujita, H., Kato, N., Sugimitsu, T. and Sugiyama, Y.
   Three-Body Coupled Channel Analysis of $^{19}F + ^{12}C$ and $^{19}F + ^{16}O$ Elastic and Inelastic Scattering
   Proc. of the JAERI Int. Sym. on Heavy-Ion Reaction Dynamics in Tandem Energy Region, (Hitachi 1988), p.157.
   T

4. Harami, T., Kabasawa, M., Nakayama, K., Yanagida, K., Yokomizo, H. and Suzuki Y.
   An Analytical Study on Small Storage Ring JSR
   Proc. Sym. on the Accelerator Technology for the High Brilliance Synchrotoron Radiation Sources, (Tokyo, 1988) p.299.

5. Hasegawa, K. and Mizumoto, M.
   Detector System for Gamma-ray Production Cross Section Measurement and Data Analysis.
   JAERI-M 89-042 (1989).
   T

6. Ideno, K.
   Shift of Neutron Resonance Levels in Periodic Structure
   Proc. of Int. Conf. on Nuclear Data for Science and Technology (Mito, 1988) p.783.
   T

7. Ikezoe, H., Shikazono, N., Tomita, Y., Sugiyama, Y., Ideno, K., Nagame, Y., Nakahara, H., Ohtsuki, T., Kobayashi, T.
Charged Particle Emission from Fission Process
Proc. of the JAERI Int. Sym. on Heavy-Ion Reaction Dynamics in Tandem Energy Region (Hitachi 1988), p.275.
T

8. Ishii, Y., Noda, K. and Watanabe, H.
Volume Change of Lithium Oxide by Lithium Ion Irradiation
Advances in Ceramics, Proc. 2nd Sym. Fabrication and Properties of Lithium Creamics.
American Ceramic Society, Apr. 23-27, 1989 (Indianapolis), submitted.
T

9. Ito, Y., Sueoka, O., Hirose, M., Hasegawa, M., Takamura, S., Hyodo, T. and Tabata, T.
Production of Intense Positron Beam using 100 Mev Linac "Positron Annihilation"
Proc. 8th Int. Conf. Positron Annihilation, Dorikens, L., Dorikens, M. and Segers, D., eds., (World Scientific, 1989) p.583-585.

10. Iwamoto, A. and Takigawa, N.
On the Subbarrier Fusion of $^{74}Ge + ^{74}Ge$
Report of the Joint Seminor on Heavy-Ion Nuclear Physics and Nuclear Chemistry in the Energy Region of Tandem Accelerators (III) JAERI-M 88-100, p.120.

11. Iwamoto, A. and Takigawa, N.
Effect of the Shell Structure on the Potential Barrier for the Subbarrier Fusion Reactions
Proc. of the JAERI Int. Sym. on Heavy-Ion Reaction Dynamics in Tandem Energy Region (Hitachi 1988) p.29.

12. Iwamoto, A. and Takigawa, N.
Anomalous Enhancement of the Subbarrier Fusion Cross Section by Cooperative shell and Deformation Effects
Phys. Lett. B219 (1989) 176.

13. Iwase, A., Masaki, N., Iwata, T., Nihira, T. and Sasaki, S.
Effect of 120 Mev ^{16}O Ion Irradiation at Low Temperatures on Superconducting Properties of $YBa_2Cu_3O_{7-x}$ and $La_{1.8}Sr_{0.2}CuO_4$.
Jpn. J. Appl. phys. 27 (1988) L2071.
T

14. Iwase, A., Sasaki, S., Iwata, T., and Nihira, T.
Defect Production and Defect Saturation Behavior in Nickel Irradiated with Heavy Ions in the Energy Range 84-120 Mev
J. Nucl. Mater. 155-157 (1988) 1188.
V T

15. Iwase, A.
Effect of Electron-Excitation on Radiation Damage in Ion-Irradiated FCC Metals.
Thesis, University of Tokyo (1989)
JAERI-M 89-071 (1989).
V T

16. Iwata, T. and Iwase, A.
Damage Production and Annealing in Ion-Irradiated FCC Metals
Rad. Eff. in press.
V T

17. Kawarasaki, Y., Ohkubo, M., Shikazono, N. and Mashiko, K.
Linac for a Free Electron Laser Oscillator: Design Consideration on the Injector System
Nucl. Instr. and Meth. A272 (1988) 206

18. Kikuchi, A., Naramoto, H., Ozawa, K. and Kazumata, Y.
Damage Profiles in Alkali Halides Irradiated with High-Energy Heavy Ions
Nucl. Instr. and Meth. B39 (1989) 724.
T

19. Komaki, Y., Ishikawa, N., Sakurai, T. and Iwasaki, M.
Polyvinylidene Fluoride Microfilter by the $^{35}Cl^{9+}$, $^{58}Ni^{10+}$, and $^{63}Cu^{11+}$ Ions Bombardments and Alkali Etching
Nucl. Inst. and Meth. B34 (1988) 332
T

20. Komaki, Y., Matsumoto, Y., Ishikawa, N. and Sakurai, T.
Heavy Ion Track Microfilter of Polyimide Film
Polymer Communications, 30 (1989) 43.
T

21. Kusakari, H., Oshima, M. and Ono, Y.
Multiple Coulomb Excitation of Nd-Sm Nuclear Region
Report of the Joint Seminor on Heavy-Ion Nuclear Physics and Nuclear Chemistry in the Energy Region of Tandem Accelerators (III) JAERI-M Report 88-100 (1988) p.4.
T

22. Minehara, E.
RF Properties of High Tc Superconductor Prepared by Plasma-Spray Painting Method
Extended Abstracts of 5th International Workshop on Future Electron Devices/Topical Meeting on High Temperature Superconducting Electron Devices (Miyagi-Zao, 1988).

23. Minehara, E., Nagai, R., and Takeuchi, M.
Plasma Spray Painting for Metal Oxide High Tc Superconductors
Proceeding of Surface Engineering International Conference (Tokyo, 1988).

24. Minehara, E., Nagai, R., and Takeuchi, M.
The TM_{010} Microwave Cavity Made of $YBa_2Cu_3O_{7-\delta}$
Jpn. J. Appl. Phys. 28 (1989) L100-L101.

25. Minehara, E., Nagai, R., and Takeuchi, M.
RF Properties of High Tc Superconducting Microwave Elements Fabricated by Plasma-Spray Painting, and Bulk-Material Machining Methods
J. Electrochem. Soc., 136 (1989), 239C.

26. Minehara, E., Nagai, R., and Takeuchi, M.
Quality Factor Performance for the S-band TM_{010} Microwave Cavity Made of $YBa_2Cu_3O_{7-\delta}$
to be published.

27. Mitamura, T., Kawatsura, K., Koterazawa, K., Iwasaki, H., Nakai, Y., and Terasawa, M.
Ion Beam Analysis of Single Crystal Austenitic Stainless Steel
Proceedings of 7th Symposium on Ion Beam Technology, Hosei Univ. (Hosei University, 1989) p.179.
V

28. Mizumoto, M., Hasegawa K., Chiba, S., Yamanouti Y., Kawarasaki, Y., Igashira, M., Uchiyama, T., and Kitazawa, H.
Gamma-ray Production Cross Sections of Some Structural and Shielding Materials
Proc. Int. Conf. on Nuclear Data for Science and Technology, (Mito, 1988) p.197-200.
T

29. Mizumoto, M.
Neutron Resonance Parameters of ^{135}Ba, ^{137}Ba and ^{138}Ba
J. Nucl. Sci. Technol. 25 (1988) 757.
L

30. Mizumoto, M. and Sugimoto, M.
Influence of Water Absorption in a Sample for Neutron Capture Cross Section Measurement
Nucl. Instr. Meth. in press.
L

31. Nagame, Y., Ikezoe, H., Baba, S., Hata, K., Sekine, T., Ichikawa, S., Ideno K., Yokoyama, A., Hatsukawa, Y. and Ohtsuki, T.
Symmetric and Asymmetric Mass Divisions of the Compound Nucleus ^{105}Ag
Proc. JAERI Int. Sym. on Heavy-Ion Dynamics in Tandem Energy Region (Hitachi 1988) p.265.
T

32. Nagame, Y., Nakamura, Y., Takahashi, M., Sueki, K. and Nakahara, H.
Pre-equilibrium Process in ^{3}He-Induced Reactions on ^{59}Co, ^{109}Ag, ^{181}Ta and ^{209}Bi
Nucl. Phys. A 486 (1988) 77.

33. Nagame, Y., Nakahara, H. and Furukawa, M.
Excitation Functions for α and ^{3}He Particles Induced Reactions on Zinc
Radiochimica Acta 46 (1989) 5.

34. Nakahara, H., Ohtsuki, T., Hamajima, Y. and Sueki K.
Systematic Study of Mass Divisions Mechanism in Low-Energy Nuclear Fission
Radiochim. Acta 43, 77 (1988).
T

35. Naramoto, H., Kawatsura, K., Sataka, M., Sugizaki, Y., Nakai, Y., Ozawa, K., Yamaguchi, S., Fujino, Y., and Aoki, M.
Lattice Location of Deuterium in Nb-Mo with Ion Beams
Nucl. Instr. and Meth. in Phys. Research B33 (1988) 595.
T V

36. Noda, K., Ishii, Y., Matsui, H., Ohno, H., Hirano, S., Watanabe, H.
Irradiation Damage in Solid Breeder Materials
J. Nucl. Mater. 155-157 (1988) 568.
T

37. Noda, K., Ishii, Y., Matsui, H., Ohno, H., Watanabe, H.
A Study of Tritium Behavior in Lithium Oxide by Ion Conductivity Measurements
J. Fusion Engineering and Design, in press.
T

38. Noda, K., Ishii, Y., Ohno, H., Watanabe, H., Matsui, H.
Irradiation Effects on Ion Conductivity of Lithium Oxide
Advances in Ceramics, Proc. 2nd Sym. Fabrication and Properties of Lithium Ceramics
American Ceramic Society, (Indianapolis 1989), submitted.

39. Ohkubo, M.
Design Considerations of the JAERI superconducting Linac for Free Electron Laser
Proceedings of the Work Shop on Free Electron Laser
JAERI-M 88-149, p.60.

40. Ohkubo, M.
View points of the Laser Development for Nuclear Energy and the Development of the Free Electron Laser
Atomic Energy Information Center, Publication No. 8809405, p.61.

41. Ohkubo, M.
Report of the 1988 Linac Conference and the Visit to several Accelerator Laboratories
JAERI-memo 01-042, p.83.

42. Ohkubo, M., Kawarasaki, Y., Shikazono, N., Mashiko, K., Sugimoto, M., Sawamura, M., Yoshikawa, H. and Takabe, M.
A Linac for Free Electron Laser at JAERI
Proc. of the 1988 Linear Accelerator Conference, Virginia, U.S.A.
(to be published).

43. Ohkubo, M., Kawarasaki, Y., Shikazono, N., Mashiko, K., Sugimoto, M., Sawamura, M., Yoshikawa, H. and Takabe, M.
Free Electron Laser Project at JAERI
Proc. of the 13th Linear Accelerator Meeting in Japan p.158.

44. Ohtsuki, T., Sueki, K., Hamajima, Y., Hatsukawa, T., Tsukada, K., Kobayashi, T., Nakahara, H., Nagame, Y. and Shinohara, N.
A Systematic Study of Mass Yield Curves in Proton-Induced Fission of Actinides
Proceedings of International Symposium on Advanced Nuclear Energy Research at Ooarai (Fib. 15-16, 1989), to be published.
T

45. Ohtsuki, T., Sueki, K., Hamajima, Y., Nakahara, N., Nagame, Y., Shinohara, N. and Ikezoe, H.
A Systematic Study of Mass Yield Curves in Low Energy Fission of Actinides
Proceedings of 50 Years with Nuclear Fission at Maryland (USA). (April 25-28, 1989), to be published.
T

46. Okamoto, H. and Sawamure, M.
Measurements of Permanent Magnet Pieces and PMQ Lens
Proceedings of the Free Electron Laser Workshop. 1988 JAERI, JEARI-M Report 88-149 (1988).

47. Oshima, M., Minehara, E., Ichikawa, S., Iimura, H., Inamura T., Hashizume, A. and Kusakari, H.
Electromagnetic Transition Probabilities for One-Quasineutron Natural-Parity Rotational Bands
Report of the Joint Seminor on Heavy-Ion Nuclear Physics and Nuclear Chemistry in the Energy Region.of Tandem Accelerators (III) JAERI-M Report 88-100 (1988) p.10.
T

48. Oshima, M., Minehara, E., Ichikawa, S., Iimura, H., Inamura, T., Hashizume, A., Kusakari, H. and Iwasaki, S.
Signature Dependence of M1 and E2 Transition Probabilities for the $i_{13/2}$ Rotational Band in ^{161}Dy
Phys. Rev. C37 (1988) 2578.
T

49. Oshima, M., Inamura, T., Hashizume, A., Kusakari, H., Sugawara, M., Minehara, E., Ichikawa S. and Iimura, H.
Multiple Coulomb Excitation of ^{157}Gd
RIKEN Accel. Progr. Rep. Vol. 22 (1988) in press.
T

50. Oshima, M., Inamura, T., Hashizume, A., Kumagai, H., Kusakari, H., Sugawara, M., Minehara, E., Ichikawa S. and Iimura, H.
A Candidate for $K^{\pi} = 4^{+}$ Double-Gamma Vibrational Band Head in ^{168}Er
RIKEN Accel. Progr. Rep. Vol. 22 (1988) in press.
T

51. Oshima, M.
Signature Dependence of Electromagnetic Transition Probabilities in Odd-A Nuclei
Genshikaku Kenkyu Vol.33 No.6 (1989) 133.
T

52. Oshima, M., Minehara, E., Kikuchi, S., Inamura, T., Hashizume, A., Kusakari, H. and Matsuzaki, M.
Rotational Perturbation to the Natural-Parity Rotational Band of 163Dy
Phys. Rev. C39 (1989) 645.
T

53. Otsuka, T. and Sugita, M.
Unified Description of Quadrupole-Pctupole Collective States in Nuclei
Phys. Lett. B209 (1988) 140.

54. Otsuka, T. and Sugita, M.
Proton-Neutron s-d-g Boson Model and Spherical-Deformed Phase Transition
Phys. Lett. B215 (1988) 205.

55. Otsuka, T. and Sugita, M.
Unified Description of Quadrupole-Octupole States in Nuclei
Proc. of the Int. Conf. on Contemporary Topics in Nuclear Structure Physics, p.385 (Cocoyoc, Mexico, June 9-14, 1988).

56. Otsuka, T. and Sugita, M.
Alpha Decay from Quadrupole-Octupole Collective States of Actinide Nuclei
J. Phys. Soc. Japan 58 (1989) Suppl., p.530.
Proc. of the Fifth Int. Conf. Clustering Aspects in Nuclear and Subnuclear Systems, (Kyoto, July 25-29, 1988).

57. Otsuka, T. and Sugita, M.
Proton-Neutron s-d-g IBM and Spherical-Deformed Phase Transition
Report on the Joint Seminar on Heavy-ion Nuclear Physics and Nuclear Chemistry in the Energy Region of Tandem Accelerators (III)
JAERI-M 88-100, p.19.

58. Otsuka, T. and Sugita, M.
A Unified Description of $K^{\pi} = 0^{+}$ and $K^{\pi} = 0^{-}$ Bands from Octupole Vibrational to Octupole Deformed Nuclei
Report on the Joint Seminar on Heavy-ion Nuclear Physics and Nuclear Chemistry in the Energy Region of Tandem Accelerators (III)
JAERI-M 88-100 p.27.

59. Sugita, M. and Otsuka, T.
Alpha Decay of Actinide Nuclei and the SPDF Boson Model.
Proceedings of the International Symposium on Developments of Nuclear Cluster Dynamics (Sapporo, 1988) p.88.

60. Sugita, M.
Triaxial Deformation in Finite Systems
Genshikaki Kenkyu Vol.33 (1989) No.6 p.171.

61. Sugita, M., Otsuka, T. and Gelberg, A.
Devydov-Filippov Limit of the IBM
Nucl. Phys. A493 (1989) 350.

62. Sugiyama, Y., Tomita, Y., Ikezoe, H., Ideno, K., Jujita, H., Sugimitsu, T., Kato, N. and Kubono, S.
Effect of Transfer Reactions Observed in Elastic Scattering of $^{28}Si+^{58,64}Ni$ near the Coulomb Barrier
Proc. of the JAERI Int. Sym. on Heavy-Ion Reaction Dynamics in Tandem Energy Region, (Hitachi, 1988), p.85.

T

63. Sugiyama, Y., Iwamoto, A. and Ikezoe, H. (Editors)
Proc. of the JAERI Int. Sym. on Heavy-Ion Reaction Dynamics in Tandem Energy Region (Hitachi, 1988).
T

64. Sugiyama, Y., Tomita, Y., Ikezoe, H., Ideno, K., Jujita, H., Sugimitsu, T., Kato, N., Kubono, S. and Landowne, S.
Contribution of Nuclear Transfer to the ELastic Scattering of $^{28}Si+^{58,64}Ni$ near the Coulomb Barrier
Phys. Rev. Lett. 62 (1989) 1727.
T

65. Takahiro, K., Nakajima, H., Yamaguchi, S., Jujino, Y., and Naramoto, H.
Retention and Release of Deuterium Implanted into VCx(x=0.44-0.95)
Nucl. Instr. and Meth. B33 (1988) 734.
V

66. Takeuchi, S.
Development of the JAERI Tandem Superconducting Booster
Proc. of the First Workshop on Tankem Accelerators and Associated Technology (Tokyo, 1988) 66.

67. Takeuchi, S., Ishii, T. and Ikezoe, H.
Niobium Superconducting Quarter Wave Resonators as a Heavy Ion Acceleratinf Structure
Nucl. Instr. and Meth. to be published.

68. Tomita, Y., Ishii, T., Takeuchi, S., Kikuchi S. and Minehara E.
Beam Optics of a Superconducting Booster for the JAERI Tandem Accelerator
JAERI-M 88-155 (1988).

69. Yokomizo, H., Sasaki, S., Harami, T., Yanagida, K., Konishi, H., Mashiko, K., Kawarasaki, Y., Ohkubo, M., Harada, Y., Sasamoto, N., Ashida, K., Harada, S., Hashimoto, H., Iizuka, M., Kabasawa, M., Nakayama, K., Yamada, K. and Suzuki, Y.
Design of A Small Storage Ring in JAERI
Proc. of the European Particle Accelerator Conference (Rome, 1988).

70. Yokomizo, H., Yanagida, K., Sasaki, S., Harami, T., Konishi, H., Mashiko, K., Ashida, K., Harada, S., Hashimoto, H., Iizuka, M., Kabasawa, M., Nakayama, K., Yamada, K. and Suzuki Y.
Construction of A Compact Electron Storage Ring JSR
Rev. Sci. Instrum., 1989.

71. Yokota, Y., Nakagawa, T., Ogihara, M., Komatsubara, T., Fukuchi, Y., Suzuki, K., Galster, W., Nagashima, Y., Furuno, K., Lee, S. M., Mikumo, T., Ideno, K., Tomita, Y., Ikezoe, H., Sugiyama, Y. and Hanashima, S.
Energy Damping Feature in Light Heavy-Ion Reactions
Z. Phys. A (1989) in press.
T

72. Yokoyama, A., Saito, T., Shoji, M., Baba, H., H., Baba, S., Hata, K., Sekine, T. and Ichikawa, S.
Nucleon Transfer in Highly Mass-Asymmetric Reaction Systems between ^{197}Au and Relatively Light Projectiles in the Energy Region below 10 MeV/u I. Target-like Products Z. Phys. A332 (1989) 61.
Z. Phys. A332 (1989) 61.
T

73. Yokoyama, A., Saito, T., Baba, H., Hata, K., Nagame, Y., Ichikawa, S., Baba, S., Sinohara, A. and Imanishi, N.
Nucleon Transfer in Highly Mass-Asymmetric Reaction Systems between ^{197}Au and Relatively Light Projectiles in the Energy Region below 10 MeV/u II. Projectile (^{19}O)-like Products Z. Phys. A 332 (1989) 71.
T

74. Yoshikawa, H., and Mashiko, K.
An Electron Gun for JAERI-FEL
Proceedings of the 13th Linear Accelerator Meeting in JAPAN (Electrotechnical Laboratory), Sept. 7-9, 1988 p.115.

Scientific Meetings

1. Fujita, H., Kato, N., Sugimitsu, T. and Sugiyama, Y.
   Three-Body Coupled Channel Analysis of $^{19}F+^{12}C$ and $^{19}F+^{16}O$ Elastic and Inelastic Scattering
   International Conference on Cluster '88, Kyoto (July 25-29, 1988).
   T

2. Hasegawa, K., Mizumoto, M., Yamanouchi, Y., Chiba, S., Igashira, M., Uchiyama, T. and Kitazawa, H.
   Measurements of Gamma-ray Production Cross Sections of Al, Si, Fe, Pb and Bi at the Incident Neutron Energy of 10 MeV
   Autumn Meeting of the Atomic Energy Society of Japan in Kobe (Oct. 8-10, 1988).
   T

3. Hasegawa, K., Mizumoto, M., Yamanouchi, Y., Chiba, S., Sugimoto, M., Igashira, M., Kitazawa, H., Uchiyama, T.
   Measurements of Gamma-ray Production Cross Sections at E_n=11.5 MeV Using $^{1}H(^{11}B,n)^{11}C$ reaction
   Annual Meeting of the Atomic Energy Society of Japan in Ohsaka (Apr. 5-7, 1989).
   T

4. Hoshiya, T., Takamura, S. and Aruga, T.
   Effects of He Ion Irradiation on Superconductivity of Bi-Sr-Ca-Cu-O Films
   Spring Meeting of the Japan Society of Applied Physics in Chiba (Apr. 1-4, 1989).
   V

5. Ideno, K., Tomita, Y., Sugiyama, Y., Ikezoe, H., Hanashima, S. and Nagame, Y.
   Detection of ^{8}Be nuclei from the Reactions $^{32}S + ^{64}Ni$ and $^{28}Si + ^{68}Zn$
   Autumn Meeting of the Physical Society of Japan in Matsuyama (Oct. 6, 1988).
   T

6. Iimura, H., Ichikawa, S., Oshima, M., Sekine, T., Shinohara, N., Miyachi, M., Osa, A., Shibata, M., Yamamoto, H. and Kawade, K.
Decays of ^{125}La and ^{127}La
Autumn Meeting of the Physical Society of Japan in Matsuyama (Oct. 3-6, 1988).
T

7. Ikezoe, H., Shikazono, N., Tomita, Y., Sugiyama, Y., Ideno, K., Nagame, Y., Ohtsuki, T., Nakahara, H., Sueki, K. and Kobayashi, T.
Charged particle Emission from Fission Process
Autumn Meeting of the Physical Society of Japan in Ehime (Oct. 3-6, 1988).
T

8. Ishii, T., Ishii, M., Saito, Y., Nakajima, M. and Ogawa, M.
Nuclear Structure of ^{106}Sn
Autumn Meeting of the Phiysical Society of Japan in Mastuyama (Oct. 3-6, 1988).
T

9. Ishii, Y., Noda, K. and Watanabe, H.
Volume Change of Lithium Oxide by Lithium Ion Irradiation
2nd Sym. Fabrication and Properties of Lithium Creamics, American Ceramic Society in Indianapolis (Apr. 23-27, 1989).
T

10. Iwamoto, A. and Takigawa, N.
Anomaly of the Subbarrier Fusion Cross Section in ^{74}Ge+^{74}Ge Scattering
Fifth Int. Conf. on Clustering Aspects in Nuclear and Subnuclear Systems, Kyoto (July 25-29, 1988).

11. Iwamoto, A. and Takigawa, N.
Effect of the Nuclear Structure on Subbarrier Fusion Reaction
Autumn Meeting of the Physical Society of Japan in Matsuyama (Oct. 3-6, 1988).

12. Iwamoto, A.
Nuclear Fission as a Multi-Dimensional Quantum Decay Problem
Topical Meeting on Non-Linear Dynamics of the Nuclear Collective Motion, Kyoto (Dec. 5-7, 1988).

13. Iwamoto, A.
Subbarrier Fusion Reaction: Shell Effect at the Barrier and Penetration in Multi-Dimensional Space
Int. Conf. on Nuclear Reaction Mechanism, Calcutta (Jan. 3-9, 1989)

14. Iwase, A., Iwata, T., Sasaki, S., and Nihira, T.
PKA Dependence of Damage Production and Damage Structure in FCC Metals Irradiated with Energetic Ions
Spring Meeting of the Physical Society of Japan in Koriyama (Apr. 3, 1988).
V T

15. Iwase, A., Iwata, T., Nihira, T., and Sasaki, S.
Radiation Annealing in Nickel and Copper by 100 MeV Iodine Ions.
Autumn Meeting of the Physical Society of Japan in Hiroshima (Oct. 4, 1988).
V T

16. Iwase, A., Masaki, N., Iwata, T. and Nihira, T.
Ion Irradiation Effect on Oxide superconductors.
Spring Meeting of the Physical Society of Japan in Hiratsuka (Mar. 29, 1989).
T

17. Kawarasaki, Y.
Japanese Activities on Storage Ring and RF Linac FEL Development
The 10-th International FEL Conference in Jerusalem, Israel (Aug. 29-Sept. 2, 1988).

18. Kawarasaki, Y., Ohkubo, M., Shikazono, N., Mashiko, K., Sugimoto, M., Sawamura, M., Yoshikawa, H. and Takabe, M.
Linac for a Free Electron Laser Oscillator
The 10-th International FEL Conference in Jerusalem, Israel (Aug. 29-Sept. 2, 1988).

19. Kawarasaki, Y.
Overview of the Accelerators for Free Electron Laser Oscillators and the Design Considerartion on the JAERI Superconducting Linac
International Symposium on Applied Electromagnetics in Materials in Tokyo (Oct. 3-5, 1988).

20. Kawatsura, K., Yamazaki, Y., Komaki, K., Kanai, Y., Sataka, M., Naramoto, H., Nakai, Y., Kuroki, K., Fujimoto, F., Kambara, T., Awaya, Y., and Stolterfoht, N.
Zero-Degree Electron Spectroscopy in Energetic Ion-Atom Collisions (I)
Annual Meeting of the Physical Society of Japan in Hiratsuka (Mar. 28-31, 1989).
T

21. Kawatsura, K., Sataka, M., Naramoto, H., Nakai, Y., Yamazaki, Y., Komaki, K., Kuroki, K., Kanai, Y., Kambara, T., Awaya, Y. and Stolterfoht, N.
Angular Momentum Distribution of Autoionizing Rydberg States Produced by 64 MeV S Ions in Collisions with C Foils
13th Int. Conf. on Atomic Collisions in Solids in Aarhus (Aug. 7-11, 1989).
T

22. Kindo, T. and Iwamoto, A.
Dynamical Fission Path as Multidimensional Quantum Decay Problem
Fifth Int. Conf. on Clustering Aspects in Nuclear and Subnuclear Systems, Kyoto (July 25-29, 1988).

23. Kindo, T. and Iwamoto, A.
Nuclear Fission as a Multi-Dimensional Quantum Decay Problem
Autumn Meeting of Physical Society of Japan in Matsuyama (Oct. 3-6, 1988).

24. Kusakari, H., Oshima, M., Sugawara, M., Ono, Y., Inamura, T., Hashizume, A., Minehara, E., Ichikawa, S. and Iimura, H.
Multiple Coulomb Excitation of Er and Nd nuclei
Spring Meeting of Physical Scciety of Japan in Hiratsuka (Mar. 28-31, 1989).
T

25. Maeta, H., Larson, B.C., Sjoreen, T.P., Oen, O.S and J.D. Lewis, J.D.
Interstitial and Vacancy Loops in Ion-Irradiated Copper
Autumn Meeting 88 of MRS Boston, USA (Nov. 1988).

26. Minehara, E., Nagai, R. and Takeuchi, M.
Possible Application of High Tc Superconductors to Accelerator Components
The 13th Linear Accelerator Meeting in Japan, Tsukuba (Sept. 7-9).

27. Minehara, E., Nagai, R. and Takeuchi, M.
High Tc Superconducting Magnetic Shield for Nb Superconducting Cavity Resonator
Autumn Meeting of the Physical Society of Japan in Matsuyama (Oct. 3-6, 1988).

28. Minehara, E., Nagai, R. and Takeuchi, M.
Fabrication and RF Properties for High Tc Superconducting Waveguide, Coaxial Cable, and Cavity Resonator made of $YBa_2Cu_3O_{7-\delta}$
Spring Meeting of the Physical Society of Japan in Hiratsuka (Mar. 28-31, 1987).

29. Minehara, E., Obana, H., Nagai, R. and Takeuchi, M.
Fabrication of High Tc Superconductor utilizing Oxygen Gas Plasma Spray Painting with Aqueous Spraying Materials
Spring Meeting of the Japan Society of Applied Physics and Related Societies in Chiba (Apr. 1-4, 1989).

30. Ming-Jing, D. Takahashi, N., Yokoyama, A., Baba, H., Baba, S., Hata, K. and Nagame, Y.
^{12}C-Induced Fission of ^{233}U, ^{235}U and ^{238}U
The 32th Sym. on Radiochemistry in Tokai (Oct. 3-5, 1988).
T

31. Mitamura, T., Kawatsura, K., Koterazawa, K., Iwasaki, H., Nakai, Y. and Terasawa, M.
Ion Beam Analysis of Single Crystal Austenitic Stainless Steel
7th Symposium on Ion Beam Technology, Hosei univ. at Hosei University in Koganei (Dec. 9-10, 1988).
V

32. Mizumoto, M.
On the Concept of an Energy Selective Neutron Source for Materials Irradiation Studies
IFMIF Work Shop for the International Energy Agency in San Diego (Feb. 10-13, 1989).

33. Nagai, R., Shimoizumi, M., Takeuchi, M. and Minehara, E.
Fabrication of High Tc Superconductor utilizing Oxygen Gas Plasma Spray Painting Method
Autumn Meeting of the Japan Society of Applied Physics and Related Societies in Toyama (Oct. 4-7, 1988).

34. Nagame, Y., Ikezoe, H., Baba, S., Hata, K., Sekine, H., Ichikawa, S., Ideno, K., Yokoyama, A., Hatsukawa, Y. and Ohtsuki, T.
Large Fragment Emission from the Highly Excited Compound Nucleus ^{105}Ag
The 32th Symposium on Radiochemistry in Tokai (Oct. 3-5, 1988).
T

35. Naramoto, H. and Kazumata, Y.
Ion Beam Analysis of Solid Materials
Int. Sym. on Advanced Nuclear Energy Research "Near-Future Chemistry in Nuclear Energy Field" in Ooarai (Feb. 1989).
T V

36. Noda, K., Ishii, Y., Matsui, H., Ohno, H., Watanabe, H.
A Study of Tritium Behavior in Lithium Oxide by Ion Conductivity Measurements
1st Int. Sym. Fusion Nuclear Technology in Tokyo (Apr. 10-19, 1988).
T

37. Noda, K., Ishii, Y., Ohno, H., Watanage, H. and Matsui, H.
Irradiation Effects on Ion Conductivity of Lithium Oxide
2nd Sym. Fabrication and Properties of Lithium Ceramics, American Ceramic Society in Indianapolis (Apr. 23-27, 1989).

38. Oshima, M., Ichikawa, S., Iimura, H., Minehara, E., Kusakari, H., Inamura, T., Hashizume, A. and Sugawara, M.
The Ground-State Rotational Bands of ^{157}Gd and ^{173}Yb
Autumn Meeting of the Physical Society of Japan in Matsuyama (Oct. 3-6, 1988).
T

39. Oshima, M.
Signature Dependence of Electromagnetic Transition Probabilities in Odd-A Nuclei
INS Sym. on Rotation and Vibration of Atomic Nuclei Tokyo, (Dec. 8-9, 1988)
T

40. Ohtsuki, T., Hatsukawa, Y., Sueki, K., Nakahara, H., Shinohara, N. and Nagame, Y.
Mass Division of Proton-Induced Fission in Actinides
Spring Meeting of the Physical Society of Japan in Kohriyama (Apr. 1-3, 1988).
T

41. Ohtsuki, T., Sueki, K., Hatsukawa, Y., Nakahara, H., Shinohara, N. and Nagame Y.
Low-Energy Nuclear Fission of Actinide Elements
Fifth Int. Conf. on Clustering Aspects in Nuclear and Subnuclear Systems in Kyoto (Jul. 25-29, 1988).
T

42. Sawamura, M.
Beam Dynamics of JAERI FEL Linac
7th Meeting of Light Source Development, Institute for Molecular Science, (Feb. 14, 1989).

43. Shinohara, N., Ichikawa, S., Iimura, H. and Tsukada, K.
Separation and Measurement of Short-Lived Nuclides with SISAK
The 32nd Symposium on Radiochemistry in Tokai (Oct. 3-5, 1988).
T

44. Shinohara, N., Alstad, J., Baba, S., Fujiwara, I., Ichikawa, S., Iimura, H., Otsuki, T., Tsukada, K. and Umezawa, H.
A Study of Short-lived Ruthenium Isotopes Produced in the Spontaneous Fission of ^{252}Cf using SISAK
Int. Sym. on Advanced Nucl. Ener. Res. "Near-Future Chem. in Nucl. Ener. Field" in Oarai (Feb, 15-16, 1989).
T

45. Sugimoto, M.
Design of the Electrode Shape of the Injection gun for the JAERI Free Electron Laser
Proc. of the 13th Linear Accelerator Meeting in Japan, in Tsukuba (Sept. 7-9, 1989).

46. Sugita, M. and Otsuka, T.
The spdf Boson Model and Phase Transition from Y_3 Deformed to Y_3 Vibrational Spring Meeting of the Physical Society of Japan in Kooriyama (Apr. 1, 1988).

47. Sugita, M., Otsuka, T. and Gelberg, A.
Devydov-Filippov Limit of the IBM
Autumn Meeting of the Physical Society of Japan in Matsuyama (Oct. 6, 1988).

48. Sugita, M.
Deformation and Shape-Coexistence in a Mass Range around A=80
Autumn Meeting of the Physical Society of Japan in Matsuyama (Oct. 6, 1988).

49. Sugiyama, Y., Tomita, Y., Ikezoe, H., Ideno, K., Fujita, H., Sugimitsu, T., Kato, N. and Kubono, S.
Effect of Transfer Reactions Observed in Elastic Scattering of $^{28}Si+^{58,64}Ni$ near the Coulomb Barrier
Autumn Meeting of the Physical Society of Japan in Matsuyama (Oct. 1988).
T

50. Takeuchi, S., Ishii, T., Ikezoe, H., Ohkubo, M. and Ishii, M.
Development of the JAERI Tandem Superconducting Booster
Autumn Meeting of the Physical Society of Japan in Matsuyama (Oct. 1988).
T

51. Tsukada, K., Sueki, K., Kobayashi, T., Otsuki, T., Nakahara, H., Shinohara, N., Ichikawa, S., Kobayashi, Y. and Hoshi, M.
Development of On-line Rapid Chemical Separation System (II)
The 32nd Symposium on Radiochemistry in Tokai (Oct. 3-5, 1988).
T

52. Yamanouchi, Y., Sugimoto, M., Chiba, S., Mizumoto, M., Watanabe, Y. and Hasegawa, K.
Elastic and Inelastic Scattering of 28.15 MeV Neutrons from ^{12}C.
Autumn Meeting of the Physical Society of Japan in Matsuyama (Oct. 1988).
T

53. Yamanouchi, Y., Sugimoto, M., Chiba, S., Mizumoto, M., Watanabe, Y. and Hasegawa, K.
Neutron Scattering Cross Sections and Partial Kerma Factor on ^{12}C
Annual Meeting of the Atomic Energy Society of Japan in Osaka (Apr. 4-6, 1989).
T

54. Yoshikawa, H., Sawamura, M., and Sugimoto, M.
Design Study of JAERI-FEL
OQD-89-18. Conference of Photo-quantum Device, IEEJ (1989).

Ⅷ PERSONNEL AND COMMITTEES

(April 1988－March 1989)

(1) Personnel

Department of Physics			
	Naomoto Yoichi	Shikazono Suto	Director Administrative Manager
Accelerators Division			
Scientific Staff	Chiaki	Kobayashi*	
	Shiro	Kikuchi	
	Suehiro	Takeuchi	
	Eisuke	Minehara	
	Susumu	Hanashima	
Technical Staff (Tandem, V.D.G)	Isao	Ohuchi	
	Yutaka	Sato	
	Tadashi	Yoshida	
	Susumu	Kanda	
	Katsuzo	Horie	
	Satoshi	Tajima	
	Yoshihiro	Tsukihashi	
	Shinichi	Abe	
	Shuhei	Kanazawa	
	Takashi	Agematsu	
Technical Staff (Linac)	Katuo	Mashiko**	
	Yukio	Nobusaka	
	Tokio	Shoji	
	Nobuhiro	Ishizaki	
	Hidekazu	Tayama	
Nuclear Physics Laboratory			
Scientific Staff	Mitsuhiko	Ishii*	

* Head

** Leader, Technical Staff

Nuclear Physics Laboratory (continued)

Scientific Staff	Yoshiaki	Tomita
	Yasuharu	Sugiyama
	Akira	Iwamoto
	Kazumi	Ideno
	Hiroshi	Ikezoe
	Masumi	Ohshima
	Tetsuro	Ishii
	Michiaki	Sugita

Linac Laboratory

Scientific Staff	Yuuki	Kawarasaki*
	Makio	Ohkubo
	Motoharu	Mizumoto
	Yoshimaro	Yamanouchi
	Masayoshi	Sugimoto
	Satoshi	Chiba

Solid State Physics Laboratory I

Scientific Staff	Yukio	Kazumata*
	Hiroshi	Naramoto
	Hiroshi	Tomimitsu

Solid State Physics Laboratory II

Scientific Staff	Tadao	Iwata*
	Saburo	Takamura
	Hiroshi	Maeta
	Mitsuo	Watanabe
	Teruo	Kato
	Akihiro	Iwase
	Terufumi	Yokota

* Head

Solid State Physics Laboratory III

Scientific Staff	Masanobu	Sakamoto

Atomic and Molecular Physics Laboratory

Scientific Staff	Yohta	Nakai*
	Kiyoshi	Kawatsura
	Masao	Sataka

Synchrotorn Radiation Research Laboratory

Scientific Staff	Yasuo	Suzuki*
	Hideaki	Yokomizo
	Taikan	Harami
	Shigemi	Sasaki
	Hiroyuki	Konishi
	Kenich	Yanagida

Department of Chemistry

Nuclear Chemistry Laboratory

Scientific Staff	Michio	Hoshi*
	Shin-ichi	Ichikawa
	Nobuo	Shinohara
	Hidenori	Iimura
	Yoshii	Kobayashi

Analytical Chemistry Laboratory

Scientific Staff	Yuji	Baba
	Toshio	Suzuki

Physical Chemistry Laboratory

Scientific Staff	Mutsuhide	Komaki
	Jiro	Ishikawa

Solid State Chemistry Laboratory

Scientific Staff	Teikichi	Sasaki*
	Shigemi	Furuno
	Takeshi	Soga

Kiichi Hojou

Laser Chemistry Laboratory

Scientific Staff Shin-ichi Ohno*

Katsutoshi Furukawa

* Head

Department of Radioisotopes

Isotope Research and Development Division

Scientific Staff	Sumiko	Baba
	Hiromitsu	Matsuoka
	Kentaro	Hata
	Toshiaki	Sekine
	Yuichiro	Nagame
	Takami	Sorita
	Mishiroku	Izumo

Department of Fuels and Materials Research

Radiation Effects and Analysis Laboratory

Scientific Staff	Akimichi	Hishinumua*
	Takeo	Aruga
	Shozo	Hamada
	Tomotsugu	Sawai
	Katsumaro	Fukai

Material Processing and Qualification Laboratory

Scientific Staff	Hitoshi	Watanabe*
	Kenji	Noda
	Yoshinobu	Ishii

Material Innovation Laboratory

Scientific Staff	Hideo	Ohno*
	Takanori	Nagasaki
	Yoshio	Katano

* Head

Department of Health Physics

Technical Staff	Shoji	Izawa*
	Toshihiro	Miyamoto
	Katsunori	Sawahata

* Chief Radiation Control Division II

(2) Tandem Steering Committee

(Chairman)	Kazumi	Iwamoto	(Deputy Director General, Tokai Research Establishment)
	Yoshihiko	Kaneko	(Director, Department of Reactor Engineering)
	Tatuo	Kondo	(Director, Department of Fuels and Materials Research)
	Naomoto	Shikazono	(Director, Department of Physics)
	Enzo	Tachikawa	(Director, Department of Chemistry)
	Masatoshi	Tanaka	(Apr.1988-Dec.1988,:Director, Department of Thermonuclear Fusion Research. Jan.1989-:Director General, Naka Fusion Research Establishment.)
	Eiji	Shikata	(Director, Department of Radioisotopes)
(Secretary)	Chiaki	Kobayashi	(Head, Accelerators Division)
(Secretary)	Yoichi	Suto	(Administrative Manager, Department of Physics)

(3) Tandem Consultative Committee

(Chairman)	Takumi	Asaoka	(Director General, Tokai Research Establishment)
(Vice Chairman)	Kazumi	Iwamoto	(Deputy Director General, Tokai Research Establishment)
(Vice Chairman)	Naomoto	Shikazono	(Director, Department of Physics)
	Hiromichi	Kamitsubo	(Principal Scientist, Institute of Physical and Chemical Research)
	Kōji	Nakai	(Professor, National Laboratory for High Energy Physics)
	Hiroyasu	Ejiri	(Professor, Osaka University)
	Shiori	Ishino	(Professor, University of Tokyo)
	Hiroyuki	Tawara	(Associate Professor, Institute of Plasma Physics, Nagoya University)
	Kohzoh	Masuda	(Professor, University of Tsukuba)
	Shiro	Iwata	(Professor, Kyoto University)
	Ichiro	Fujiwara	(Professor, Otemon Gakuin University)
	Kenji	Sumita	(Professor, Osaka University)
	Naohiro	Hirakawa	(Professor, Tohoku University)
	Kousuke	Yagi	(Professor, the University of Tsukuba)
	Syunpei	Morinobu	(Associate Professor, Rerearch Center for Nuclear Physics Osaka University)
	Hiromichi	Nakahara	(Professor, Tokyo Metropolitan University)
	Sadae	Yamaguchi	(Professor, The Perearch Institiule for Iron, Steel and other Metals, Tohoku University)
(Secretary)	Chiaki	Kobayasihi	(Head, Accelerators Division)
	Yoichi	Suto	(Administrative Manager, Department of Physics)

Koichi	Umezawa	(Director, Department of Radioisotopes)
Tadao	Iwata	(Head, Solid State Physics Laboratory II)
Yohta	Nakai	(Head, Atomic and Molecular Physics Laboratory)

(4) Tandem Program Advisory Committee

(Chairman)	Naomoto	Shikazono	(Director, Department of Physics)
	Hirokazu	Umezawa	(Director, Department of Radioisotopes)
	Shoji	Izawa	(Chief, Radiation Control Group, Department of Health Physics)
	Hitoshi	Watanabe	(Head, Material Processing and Qualification Laboratory)
	Yohta	Nakai	(Head, Atomic and Molecular Physics Laboratory , Department of Physics)
	Yuuki	Kawarasaki	(Head, Linac laboratory, Deparrment of Physics)
	Chiaki	Kobayashi	(Head, Accelerators Division, Department of Physics)
	Shiro	Kikuchi	(Accelerators Division, Department of Physics)
	Tadashi	Yoshida	(Accelerators Division, Department of Physics)

Ⅸ CO-OPERATIVE RESEARCHES

	Title	Co-Operation Institution
2.1	High-Resolution Zero-Degree Electron Spectroscopy(I)	College of General Education, The University of Tokyo*
2.2	Ion Channeling Spectroscopy of Single Crystal Austenitic Stainless Steel	Faculty of Engeneering, Himeji Institute of Technology*
2.3	Perturbed Angular Correlation Measurement Using Pd-100/Rh-100 Nuclear Probes	Institute for Materials Research, Tohoku University*
3.1	Ion Conductivity of Lithium Oxide Irradiated with Oxygen and Lithium Ions	Faculty of Engineering, Nagoya University*
3.3	Damage Structure Obtained by Cross-Sectional Observation in He-Ion Irradiated SiC	Hitachi Research Laboratory, Hitachi Ltd.
3.4	Electron Microscopic Observation of Lithium Aluminate Irradiated with Oxygen Ions	Faculty of Engineering, Nagoya University*
3.5	Defect Production by Electron Excitation in FCC Metals Irradiated with High Energy Heavy Ions	Faculty of Engineering, Ibaraki University*
3.6	A Study of X-ray Diffraction on Irradiated GaAs Crystals	Faculty of Engineering, Tamagawa University*
4.1	Complex Fragment Emission in the Reaction $^{37}Cl+^{68}Zn$	Department of Chemistry, Tokyo Metropolitan University*
4.2	Fission Barrier Study in Actinides	Faculty of Science, Tokyo Metropolitan University
4.3	Beta-Decay Studies of ^{123}La and ^{127}La with an on-Line Isotope Separator	Department of Nuclear Engineering, Nagoya University*

4.4	A Study of Short-Lived Actinides by Means of on-Line Chemical Separation System	Otemon Gakuin University*
5.1	Contribution of Nucleon Transfer to Elastic Scattering of $^{28}Si+^{58,64}Ni$ Near the Coulomb Barrier	Department of Physics, Kyushu University*
5.2	Measurements of Pre- Fission ^{4}He Multiplicity to Investigate the Temperature Dependence of Level Density Parameter	Department of Chemistry, Faculty of Science, Tokyo Metropolitan University
5.5	Electromagnetic Transition Probabilities in the Natural-Parity Rotational Band of ^{157}Gd	Faculty of Education, Chiba University
5.6	Electromagnetic Transition Probabilities in the Natural-Parity Rotational Band of ^{173}Yb	Faculty of Education, Chiba University
5.7	Lifetimes and G-Factors of Excited States in ^{106}Sn	Tokyo Institute of Technology*
5.8	Nuclear Structure of ^{105}In	Tokyo Institute of Technology*
5.10	Structure of Actinide Nuclei and the SPDF Boson Model	Department of Physics, University of Tokyo
6.1	Scattering of 28.15 MeV Neutrons from ^{12}C	Department of Nuclear Engineering, Kyushu University*
6.2	Camma-Ray Production Cross Sections of Al,Si,Fe,Pb and Bi at 10 and 11.5 MeV	Research Laboratory for Nuclear Reactor, Tokyo Institute of Technology*

* Travel Expenses are supplied by JAERI